

Towards integrated PV applications: development of lightweight silicon heterojunction solar modules and their damp-heat and UV stability

Kai Zhang

Energie & Umwelt / Energy & Environment
Band / Volume 713
ISBN 978-3-95806-929-9

Mitglied der Helmholtz-Gemeinschaft

JÜLICH
Forschungszentrum

Towards integrated PV applications: development of lightweight silicon heterojunction solar modules and their damp-heat and UV stability

Von der Fakultät für Elektrotechnik und Informationstechnik der Rheinisch-Westfälischen Technischen Hochschule Aachen zur Erlangung des akademischen Grades eines Doktors der Ingenieurwissenschaften genehmigte Dissertation

vorgelegt von

Kai Zhang, M. Eng.

aus Gansu, China

Berichter: Univ.-Professor Dr. rer. nat. Uwe Rau
Univ.-Professor Dr. rer. nat. Ulrich Wilhelm Paetzold

Tag der mündlichen Prüfung: 13.04.2026

Diese Dissertation ist auf den Internetseiten der Universitätsbibliothek online verfügbar.

Forschungszentrum Jülich GmbH
Institute of Energy Materials and Devices (IMD)
Photovoltaik (IMD-3)

Towards integrated PV applications: development of lightweight silicon heterojunction solar modules and their damp-heat and UV stability

Kai Zhang

Schriften des Forschungszentrums Jülich
Reihe Energie & Umwelt / Energy & Environment Band / Volume 713

ISSN 1866-1793 ISBN 978-3-95806-929-9

Bibliografische Information der Deutschen Nationalbibliothek.
Die Deutsche Nationalbibliothek verzeichnet diese Publikation in der
Deutschen Nationalbibliografie; detaillierte Bibliografische Daten
sind im Internet über http://dnb.d-nb.de abrufbar.

Herausgeber und Vertrieb:	Forschungszentrum Jülich GmbH Zentralbibliothek, Verlag 52425 Jülich Tel.: +49 2461 61-5368 Fax: +49 2461 61-6103 zb-publikation@fz-juelich.de www.fz-juelich.de/zb
Umschlaggestaltung:	Grafische Medien, Forschungszentrum Jülich GmbH
Titelbild:	KI-gestütztes Design
Druck:	Grafische Medien, Forschungszentrum Jülich GmbH
Copyright:	Forschungszentrum Jülich 2026

Schriften des Forschungszentrums Jülich
Reihe Energie & Umwelt / Energy & Environment, Band / Volume 713

D 82 (Diss. RWTH Aachen University, 2026)

ISSN 1866-1793
ISBN 978-3-95806-928-2 (Print)
ISBN 978-3-95806-929-9 (E-Book)

Vollständig frei verfügbar über das Publikationsportal des Forschungszentrums Jülich (JuSER)
unter www.fz-juelich.de/zb/openaccess.



This is an Open Access publication distributed under the terms of the Creative Commons Attribution License 4.0,
which permits unrestricted use, distribution, and reproduction in any medium, provided the original work is properly cited.

Contents

Abstract **1**

Zusammenfassung **5**

1 Introduction **9**

2 Fundamentals and literature review **13**

2.1 Silicon heterojunction solar cells 13

2.1.1 Evolution 13

2.1.2 Strengths and challenges 14

2.2 Evolution of encapsulant materials 16

2.3 Challenges for lightweight SHJ solar modules 17

2.3.1 Lightweight c-Si-based solar modules 17

2.3.2 Reliability and durability 20

3 Experimental methods **27**

3.1 Design and fabrication of the lightweight SHJ solar modules 27

3.1.1 Preliminary design 27

3.1.2 Optimized design 31

3.2 Accelerated aging test 33

3.2.1 DH aging test 33

3.2.2 UV aging test 34

3.3 Characterization 35

3.3.1 Optical properties 35

3.3.2 Electrical properties 37

3.3.3 Optoelectronic properties 37

3.3.4 Microstructural properties 43

3.3.5 Physical properties 44

3.3.6 Chemical properties 45

4 Insights into DHID of lightweight SHJ solar modules with different TCOs **49**

4.1 DH stability of lightweight and glass SHJ solar modules with different TCOs 49

4.1.1 Preparation of tested solar module samples 49

4.1.2 DH test results . . . 51
4.2 DHID mechanism of SHJ solar cells with different TCOs . . . 53
4.2.1 Optoelectronic properties of SHJ solar cells . . . 53
4.2.2 Electrical properties of TCO films . . . 56
4.3 Improved DH resistance: the role of the capping layer . . . 59
4.3.1 AZO-incorporated SHJ solar cell with a capping layer . . . 59
4.3.2 DH stability of AZO-incorporated lightweight SHJ solar modules featuring a capping layer . . . 60
4.4 Improved DH resistance: the role of the interconnection foil . . . 71
4.4.1 CTM loss analysis of lightweight SHJ solar modules using two different interconnection foils . . . 71
4.4.2 DH stability of AZO-incorporated lightweight SHJ solar modules with different interconnection foils . . . 73

5 Influence of encapsulation materials on the DH stability of lightweight SHJ solar modules 77
5.1 Effect of encapsulants on the DH stability of lightweight SHJ solar modules 78
5.1.1 Physical properties of different encapsulants . . . 78
5.1.2 Configurations of solar modules with different encapsulants . . . 82
5.1.3 DH stability of lightweight SHJ solar modules with different encapsulants . . . 85
5.2 Optimized DH stability of lightweight solar modules with different front sheets . . . 100
5.2.1 Configurations of solar modules with different front sheets . . . 100
5.2.2 DH stability of lightweight SHJ solar modules with different front sheets . . . 104
5.3 Equivalence between accelerated DH aging and field conditions . . . 105
5.3.1 Accelerated degradation model . . . 106
5.3.2 Determination of acceleration factors . . . 107

6 Insights into UVID in lightweight SHJ solar modules with different encapsulants 111
6.1 UV stability of encapsulation materials . . . 111
6.1.1 UV stability of front sheet materials . . . 112
6.1.2 UV stability of encapsulants . . . 113
6.2 UVID behavior of lightweight SHJ solar modules with different encapsulants 116
6.2.1 Configurations of solar modules with different encapsulants . . . 116
6.2.2 UVID mechanism of lightweight SHJ solar modules with different encapsulants . . . 119

6.3 UVID of SHJ solar modules with downshifting encapsulants 127
6.3.1 Interpretation of the UVID mechanism of lightweight SHJ solar modules with downshifting encapsulants 128
6.3.2 UVID of SHJ solar modules with downshifting encapsulants: influence of solar module structure 128
6.4 A strategy for enhancing the performance and UV stability of lightweight SHJ solar modules 131
6.4.1 Dual-layer encapsulation approach 131
6.4.2 Performance and stability of solar modules with dual-layer encapsulation design 132

7 Summary and outlook **137**
7.1 Summary 138
7.1.1 Damp-heat stability of lightweight SHJ solar modules 138
7.1.2 UV stability of lightweight SHJ solar modules 140
7.2 Outlook 141
7.2.1 Pathways toward durable, lightweight SHJ solar modules 141
7.2.2 Perovskite/SHJ tandem lightweight solar modules 143

A Appendix **145**

B Symbols and abbreviations **149**

C List of publications **157**

D Curriculum vitae **159**

References **161**

Acknowledgements **177**

Abstract

Lightweight solar modules are essential for diversifying the solar energy supply due to their lower weight compared with traditional glass solar modules. This opens up vast new scenarios for solar modules, especially for roofs with low load capacity, and vehicle-integrated photovoltaic (VIPV), significantly boosting the capacity of renewable energy. Silicon heterojunction (SHJ) solar cells have been recognized as one of the most advanced technologies for improving solar power generation. They can achieve a high power conversion efficiency (η) owing to their excellent surface passivation to minimize surface recombination, resulting in a higher open-circuit voltage (V_{oc}) and fill factor (FF) compared to other crystalline silicon (c-Si)-based solar cell technologies, such as the aluminum back-surface field (Al-BSF) solar cell and passivated emitter rear contact (PERC) solar cell. Additionally, SHJ solar cells are highly compatible with integrated photovoltaic (PV) applications due to their thinner wafer thickness and symmetrical structure, which ensures identical stress distribution across the front and rear sides. Integrated PV typically operates under limited ventilation conditions, and the low power-temperature coefficient of SHJ solar cells results in significantly reduced power degradation in high-temperature environments. This makes them particularly advantageous in such scenarios. Therefore, a combination of SHJ solar cell technology with a lightweight solar module configuration would be a good attempt.

However, several challenges are associated with the development and deployment of lightweight SHJ solar modules. On the one hand, SHJ solar cells are more sensitive to moisture than other solar cell technologies, such as PERC solar cell technology, because the amorphous/crystalline interface is susceptible to moisture, due to the oxidation of the hydrogenated amorphous silicon (a-Si:H) passivation layer. Different transparent conductive oxides (TCOs), such as indium tin oxide (ITO) and aluminum-doped zinc oxide (AZO), have varying resistance to moisture. The SHJ solar cells are degraded by moisture ingress with increasing temperature, causing damp-heat-induced degradation (DHID), which decreases the solar module's power output in the long run. Ultraviolet (UV) radiation has been identified as another critical reliability issue for SHJ solar cells and modules. This poses a serious concern when SHJ solar modules are operating in the field, particularly for lightweight solar module configurations, where flexible

polymer-based front sheets may provide reduced shielding against UV radiation. On the other hand, a reliable encapsulation solution is currently only available for glass/glass solar module structures, and it is not yet ready for front sheet/back sheet solar module structures.

It is crucial to address these challenges to develop and commercialize lightweight SHJ solar modules that meet the required performance and durability standards for diverse applications. This thesis aims to develop high-performance lightweight solar modules based on SHJ solar cells, with a particular focus on improving resistance to damp-heat (DH) and mitigating the effects of UV radiation.

In the first part of this work, the DH stability of the specific lightweight SHJ mini-modules based on ITO or AZO films was investigated through an accelerated DH aging test. The efficiency of the AZO module decreased by $58.57\%_{\mathrm{rel}}$, which was dominated by a large increase in series resistance (R_{s}) and a significant decrease in FF. It is identified that the AZO film is more vulnerable to moisture than the ITO film under damp and heat conditions, which is attributed to the hydrophilic property of the AZO film. The AZO film was damaged by the combined effects of moisture ingress and delamination of the interconnection foil. The poor adhesion of the AZO layer to the interconnection foil accelerates the penetration of moisture, leading to severe degradation of the AZO layer. Consequently, moisture has a greater chance of percolating through the damaged AZO layer into the a-Si:H passivation layer, causing passivation degradation, which leads to an increase in recombination, resulting in a decrease in V_{oc} of the solar modules. Therefore, a capping layer strategy was proposed to improve the moisture resistance of the AZO-incorporated solar module. Notably, capping the AZO with an ITO layer reduced the efficiency loss of the ITO/AZO/ITO solar module to $18.92\%_{\mathrm{rel}}$, suggesting that the ITO capping layer could enhance moisture resistance and improve DH stability. Thus, it is expected to be a promising protective capping layer for AZO-incorporated SHJ solar cells and modules. Furthermore, a comparison of lightweight AZO solar modules with two different interconnection foils (IF1 and IF2) revealed that the adhesion between the polymer interconnection foil and the AZO layer is essential for the DH stability of the lightweight AZO solar modules.

In the second part of this work, lightweight SHJ mini-modules were fabricated using SHJ solar cells with different encapsulation materials and architectures. These solar modules have a low area density (~ 2 kg/m^2), which is about eight times lighter than traditional glass-based solar modules, while preserving a high power-to-weight ratio (~ 70 W/kg). The DH stability of the lightweight SHJ mini-modules encapsulated with various encapsulants was investigated through a 1000 h accelerated DH aging test. A comprehensive analysis of lightweight solar module degradation was carried out, with a focus on

the optoelectronic properties of solar modules, as well as the chemical properties of the polymer encapsulants. The efficiency loss in lightweight SHJ solar modules following the DH test varied significantly, ranging from $3.22\%_{\mathrm{rel}}$ to $54.06\%_{\mathrm{rel}}$, with the extent of the loss depending strongly on the type of encapsulation material used. The increase in R_{s} is the main cause of the decrease in solar module efficiency. The degradation mechanisms specific to each solar module have also been revealed. The solar module encapsulated with EPE (EVA/POE/EVA) showed the greatest efficiency degradation due to a significant increase in R_{s}. This can be attributed to two main factors: wires detaching from the ribbons due to solder joint failure, and interconnection failure of wires detaching from the fingers. The thermoplastic polyolefin (TPO)-encapsulated solar module was found to have the lowest degradation efficiency of $3.22\%_{\mathrm{rel}}$ after 1000 h of DH due to its low water permeability and high thermal stability. This indicated that TPO is a promising encapsulant for moisture-sensitive solar cells. Based on Arrhenius-based modeling, 1000 h of DH testing at 85 °C, 85% RH is estimated to correspond to approximately 1.1 years of exposure under typical field conditions for the ethylene tetrafluoroethylene (ETFE)/polyolefin-based aluminum back sheet (Al-bs) lightweight SHJ solar module with TPO encapsulants, during which about $5\%_{\mathrm{rel}}$ efficiency degradation was observed. Additionally, a degradation of the downshifting (DS) effect was also found in solar modules encapsulated with downshifting encapsulants. An optimized, damp-heat-stable, lightweight SHJ solar module was successfully fabricated by using polyethylene terephthalate (PET)-based material instead of ETFE as the front sheet, polyolefin-based aluminum as the back sheet, and TPO as the encapsulant. The efficiency degradation of the solar module was only $0.47\%_{\mathrm{rel}}$ after 1000 h of the DH test. Its DH stability is almost identical to that of the glass/back sheet solar module.

In the third part of this work, a comprehensive investigation of the UV-induced degradation (UVID) behavior of lightweight SHJ solar modules utilizing different types of encapsulants with different UV transmittance: UV-blocking, UV-transmitting, and UV-downshifting is presented. After indoor UV exposure of 120 kWh/m², equivalent to 30 months of outdoor exposure in Jülich, Germany, solar modules incorporating these encapsulants exhibited relative efficiency losses of 2.17%, 9.25%, and 6.15%, respectively. The decrease in efficiency was mainly attributed to a reduction in the *FF* of the solar modules, accompanied by a diminished pseudo fill factor (p*FF*). Based on detailed *FF* and p*FF* loss analyses, we found that p*FF* loss was the major cause of *FF* loss, which is attributed to the deterioration of the passivation properties due to UV radiation. And the influence of R_{s}-related *FF* losses increased, which is attributed to the deterioration of the interconnection foil rather than the UV radiation itself. Additionally, while downshifting encapsulants helped mitigate UV damage, we observed a diminished DS effect in lightweight solar module configurations, potentially due to photo-oxidation. Utiliza-

tion efficiency of DS decreases from around $34\%_{abs}$ to $21\%_{abs}$ after 120 kWh/m^2 of UV exposure. Therefore, a novel encapsulation architecture combining UV-downshifting and UV-blocking encapsulants was proposed to ensure the UV utilization and stability of lightweight SHJ solar modules. Solar modules featuring this innovative dual-layer structure preserved over 98% of their initial performance after UV exposure, demonstrating a promising new approach for enhancing UV stability. The comprehensive investigation provides substantial insights into the degradation mechanism of lightweight SHJ solar modules under UV exposure and offers practical strategies in the progress of improving their durability and performance.

Zusammenfassung

Leichtbau-Solarmodule sind im Vergleich zu herkömmlichen Glas-Solarmodulen entscheidend für die Diversifizierung der Solarstromproduktion. Durch das geringere Gewicht dieser Solarmodule eröffnen sich zahlreiche neue Einsatzszenarien, insbesondere für Dächer mit geringer Tragfähigkeit sowie für fahrzeugintegrierte Photovoltaik (VIPV). Dadurch kann die Kapazität erneuerbarer Energien deutlich gesteigert werden. Silizium-Heterostruktur-Solarzellen (SHJ-Solarzellen) werden als eine der fortschrittlichsten Technologien zur Steigerung der Solarstromerzeugung angesehen. Dank ihrer exzellenten Oberflächenpassivierung, die Oberflächenrekombination minimiert, erreichen sie im Vergleich zu anderen kristallinen Silizium-Solarzelltechnologien, wie Al-BSF (Aluminium Back Surface Field) und PERC (Passivated Emitter Rear Contact), eine höhere Leerlaufspannung (V_{oc}) und einen höheren Füllfaktor (FF). Dies führt zu einem hohen Energieumwandlungswirkungsgrad (η). Außerdem sind SHJ-Solarzellen aufgrund ihrer geringeren Waferdicke und der symmetrischen Struktur, die eine identische Spannungsverteilung auf der Vorder- und Rückseite sicherstellt, besonders gut für integrierte Photovoltaikanwendungen geeignet. In Gebäude oder Fahrzeuge integrierte Photovoltaik wird typischerweise unzureichend belüftet. Da SHJ-Solarzellen einen niedrigen Leistungs-Temperaturkoeffizienten haben, ist die Leistungsdegradation in Umgebungen mit hohen Temperaturen deutlich reduziert. Dies macht sie in solchen Einsatzszenarien besonders vorteilhaft. Daher ist die Kombination der SHJ-Solarzelltechnologie mit Leichtbau-Solarmodulkonfigurationen ein vielversprechender Ansatz.

Allerdings sind mit der Entwicklung und Einführung leichter SHJ-Solarmodule mehrere Herausforderungen verbunden. Einerseits sind SHJ-Solarzellen feuchtigkeitsempfindlicher als andere Solarzelltechnologien, wie beispielsweise die PERC-Technologie, da die amorph-kristalline Grenzfläche aufgrund der Oxidation der wasserstoffhaltigen Silizium-Passivierungsschicht aus amorphem Silizium (a-Si:H) anfällig gegenüber Feuchtigkeit ist. Verschiedene transparente leitfähige Oxide (TCO), wie Indium-Zinn-Oxid (ITO) und aluminiumdotiertes Zinkoxid (AZO), weisen eine unterschiedliche Feuchtigkeitsbeständigkeit auf. Durch Feuchtigkeitseintritt degradieren die SHJ-Solarzellen mit zunehmender Temperatur. Diese feuchte- und hitzebedingte Degradation (DHID) verringert langfristig die Modulleistung.Allerdings sind mit der Entwicklung und Einführung leichter

SHJ-Solarmodule mehrere Herausforderungen verbunden. Einerseits sind SHJ-Solarzellen feuchtigkeitsempfindlicher als andere Solarzelltechnologien, wie beispielsweise die PERC-Technologie, da die amorph-kristalline Grenzfläche aufgrund der Oxidation der wasserstoffhaltigen Silizium-Passivierungsschicht aus amorphem Silizium (a-Si:H) anfällig gegenüber Feuchtigkeit ist. Verschiedene transparente leitfähige Oxide (TCO), wie Indium-Zinn-Oxid (ITO) und aluminiumdotiertes Zinkoxid (AZO), weisen eine unterschiedliche Feuchtigkeitsbeständigkeit auf. Durch Feuchtigkeitseintritt degradieren die SHJ-Solarzellen mit zunehmender Temperatur. Diese feuchte- und hitzebedingte Degradation (DHID) verringert langfristig die Modulleistung. Eine weitere Herausforderung für SHJ-Solarzellen und -module ist die ultraviolette (UV) Strahlung. Diese stellt ein ernstes Problem für den Feldbetrieb von SHJ-Leichtbaumodulen dar, insbesondere bei Modulkonfigurationen mit flexiblen polymerbasierten Frontfolien, die einen geringeren Schutz gegen UV-Strahlung bieten können. Eine zuverlässige Verkapselungslösung steht derzeit nur für Glas/Glas-Modulstrukturen zur Verfügung; für Modulstrukturen mit Front sheet/Back sheet-Konfiguration ist sie noch nicht ausgereift.

Die Bewältigung dieser Herausforderungen ist entscheidend, damit leichte SHJ- Solarmodule mit den erforderlichen Leistungs- und Stabilitätsanforderungen für vielfältige Anwendungen entwickelt und kommerzialisiert werden können. Ziel der vorliegenden Arbeit ist die Entwicklung leistungsstarker Leichtbau-Solarmodule auf Basis von SHJ-Solarzellen, wobei der Schwerpunkt auf der Verbesserung der Beständigkeit gegenüber Feuchtigkeit und hohen Temperaturen (Damp-Heat, DH) sowie auf der Minderung der Auswirkungen von UV-Strahlung liegt.

Im ersten Teil dieser Arbeit wurde die DH-Stabilität leichter SHJ-Mini-Module mit ITO- oder AZO-Schichten mittels eines DH-tests zur beschleunigten Alterung untersucht. Der Wirkungsgrad des AZO-Moduls verringerte sich um 58,57$\%_{\mathrm{rel}}$. Dies war hauptsächlich auf einen stark gestiegenen Serienwiderstand (R_{s}) und einen deutlich reduzierten *FF* zurückzuführen. Es wurde festgestellt, dass die AZO-Schicht unter DH-Bedingungen feuchtigkeitsempfindlicher ist als die ITO-Schicht, was den hydrophilen Eigenschaften der AZO-Schicht zuzuschreiben ist. Die AZO-Schicht wurde durch das Zusammenwirken von Feuchtigkeitseintritt und Delamination der Interconnection-Folie geschädigt. Die schlechte Haftung der AZO-Schicht an der Interconnection-Folie beschleunigt das Eindringen von Feuchtigkeit und führt zu einer starken Degradation der AZO-Schicht. Infolgedessen kann Feuchtigkeit leichter durch die geschädigte AZO-Schicht in die a-Si:H-Passivierungsschicht eindringen und diese degradieren, was zu einer erhöhten Rekombination und damit zu einer Verringerung der V_{oc} der Module führt. Um die Feuchtigkeitsbeständigkeit von Solarmodulen mit AZO-Schicht zu verbessern, wurde eine Abdeckschicht abgeschieden. Insbesondere reduzierte das Abdecken der AZO-Schicht mit einer ITO-Schicht den Wirkungsgradverlust des ITO/AZO/ITO-Solarmoduls auf 18,92$\%_{\mathrm{rel}}$, was darauf hinweist, dass die

ITO-Abdeckschicht die Feuchtigkeitsbeständigkeit erhöht und die DH-Stabilität verbessert. Sie ist daher eine vielversprechende Schutzschicht für SHJ-Solarzellen und -module mit AZO-Schicht. Darüber hinaus zeigte ein Vergleich leichter AZO-Solarmodule mit zwei verschiedenen Interconnection-Folien (IF1 und IF2), dass die Haftung zwischen der Polymer-Interconnection-Folie und der AZO-Schicht entscheidend für die DH-Stabilität der leichten AZO-Solarmodule ist.

Im zweiten Teil dieser Arbeit wurden leichte SHJ-Mini-Module unter Verwendung von SHJ-Solarzellen mit verschiedenen Verkapselungsmaterialien und -architekturen gefertigt. Diese Module weisen ein geringes Gewicht pro Fläche (~ 2 kg/m^2) auf, sind damit etwa achtmal leichter als herkömmliche glasbasierte Solarmodule und besitzen gleichzeitig eine hohe Leistungsdichte (~ 70 W/kg). Die DH-Stabilität der leichten SHJ-Mini-Module, die mit verschiedenen Verkapselungsmaterialien versehen wurden, wurde mittels eines DH-Tests über 1000 Stunden zur beschleunigten Alterung untersucht. Es wurde eine umfassende Analyse der Degradation der Leichtbau-Module durchgeführt, wobei der Schwerpunkt sowohl auf den optoelektronischen Eigenschaften der Solarmodule als auch auf den chemischen Eigenschaften der Verkapselungsmaterialien lag. Der Wirkungsgradverlust der leichten SHJ-Solarmodule nach dem DH-Test variierte erheblich und reichte von 3,22%$_{\text{rel}}$ bis 54,06%$_{\text{rel}}$. Das Ausmaß des Verlusts hing stark vom eingesetzten Verkapselungsmaterial ab. Die Zunahme des R_{s} war die Hauptursache für den Wirkungsgradabfall der Solarmodule. Die jeweiligen Degradationsmechanismen der einzelnen Solarmodule wurden ebenfalls identifiziert. Das mit EPE (EVA/POE/EVA) verkapselte Solarmodul zeigte aufgrund eines deutlichen Anstiegs des R_{s} die stärkste Wirkungsgraddegradation. Dies lässt sich im Wesentlichen auf zwei Faktoren zurückführen: das Ablösen der Drähte von den Bändern infolge von Lötstellenversagen sowie das Versagen der Verschaltung durch das Ablösen der Drähte von den Fingern. Das mit thermoplastischem Polyolefin (TPO) verkapselte Modul wies nach 1000 h DH mit 3,22%$_{\text{rel}}$ den geringsten Wirkungsgradverlust auf, was auf die geringe Wasserpermeabilität und die hohe thermische Stabilität von TPO zurückzuführen ist. Dies zeigt, dass TPO ein vielversprechendes Verkapselungsmaterial für feuchtigkeitsempfindliche Solarzellen ist. Gemäß einem Arrhenius-basierten Modell entspricht ein DH-Test bei 85 °C und 85% relativer Luftfeuchte über 1000 h einer Exposition von etwa 1,1 Jahren unter typischen Feldbedingungen für das leichte ETFE/Polyolefin-basierte Aluminium-Backsheet SHJ-Solarmodul mit TPO-Verkapselung. Für diesen Zeitraum wurde ein Wirkungsgradverlust von etwa 5%$_{\text{rel}}$ beobachtet. Zusätzlich wurde in mit Downshifting-Verkapselungsmaterialien versehenen Solarzellenmodulen eine Degradation des Downshifting-Effekts festgestellt. Ein optimiertes DH-stabiles Leichtbau-SHJ-Solarmodul wurde erfolgreich hergestellt, indem statt ETFE ein auf Polyethylenterephthalat (PET) basierendes Material als Frontsheet, ein Polyolefin-basiertes Aluminium-Backsheet und TPO als Verkapselungsmaterial verwendet wurden. Der Wir-

kungsgradverlust dieses Moduls betrug nach 1000 h DH-Test lediglich 0,47%$_{\text{rel}}$. Seine DH-Stabilität ist damit nahezu identisch mit der eines Glas/Backsheet-Moduls.

Im dritten Teil dieser Arbeit wird eine umfassende Untersuchung des durch UV-Strahlung induzierten Degradationsverhaltens (UVID) leichter SHJ-Solarmodule vorgestellt. Dazu werden Verkapselungsmaterialien verwendet, die die UV-Strahlung entweder blockieren oder durchlassen oder in den blauen Wellenlängenbereich verschieben (Downshifting). Nach einer Indoor-UV-Bestrahlung von 120 kWh/m^2, was etwa 30 Monaten Außenexposition in Jülich, Deutschland entspricht, zeigten Solarmodule mit diesen Verkapselungsmaterialien relative Wirkungsgradverluste von 2,17%, 9,25% bzw. 6,15%. Der Wirkungsgradrückgang war hauptsächlich auf eine Reduktion des *FF* der Module zurückzuführen, begleitet von einem verminderten Pseudo-Füllfaktor (p*FF*). Basierend auf einer detaillierten Analyse der *FF*- und p*FF*-Verluste zeigte sich, dass der Verlust des p*FF* die Hauptursache für den *FF*-Verlust war, was auf eine Verschlechterung der Passivierungseigenschaften infolge der UV-Bestrahlung zurückgeführt wird. Darüber hinaus nahm der Einfluss der R_{s}-bedingten *FF*-Verluste, was auf eine Verschlechterung der Interconnection-Folie und nicht unmittelbar auf die UV-Strahlung selbst zurückgeführt wird. Obwohl Downshifting-Verkapselungsmaterialien die UV-Schädigung mildern konnten, wurde in Leichtbau-Solarmodulkonfigurationen ein verringerter Downshifting-Effekt beobachtet, was möglicherweise auf Photonenoxidation zurückzuführen ist. Die Nutzungseffizienz des Downshifting-Effekts sank nach 120 kWh/m^2 UV-Bestrahlung von etwa 34%$_{\text{abs}}$ auf 21%$_{\text{abs}}$. Daher wurde eine neuartige Verkapselungsarchitektur vorgeschlagen, in der UV-Downshifting- und UV-blockierende Verkapselungsmaterialien kombiniert werden, um sowohl die UV-Nutzung als auch die Stabilität leichter SHJ-Solarmodule zu gewährleisten. Solarmodule mit dieser innovativen Doppelschichtstruktur behielten nach UV-Bestrahlung mehr als 98% ihrer Anfangsleistung bei und demonstrieren damit einen vielversprechenden neuen Ansatz zur Verbesserung der UV-Stabilität. Die umfassende Untersuchung liefert wesentliche Einblicke in die Degradationsmechanismen leichter SHJ-Solarmodule unter UV-Einwirkung und bietet praxisnahe Strategien für die Verbesserung ihrer Langzeitstabilität und Leistung.

1 Introduction

Energy is the cornerstone of human society. Currently, fossil fuels remain the primary energy source meeting humanity's ever-growing demand. However, their usage releases harmful pollutants into the environment, contributing significantly to global warming and climate anomalies. To mitigate global climate change, a comprehensive decarbonization of our energy systems is essential. We must identify and implement strategies that ensure reliable energy provision to society, while substantially reducing emissions of carbon dioxide (CO_2) and other greenhouse gases (GHGs).

Currently, GHGs emissions in the power generation sector are declining due to the accelerated adoption of renewable energy sources such as photovoltaic (PV) and wind power. In 2024, PV generated 6.9% (2,132 TWh) of global electricity [1]. The globalization of the PV market is becoming increasingly evident year by year. No other energy technology demonstrates the same degree of modularity and versatility as PV systems, which can be installed in a highly distributed manner. PV applications, whether standalone or grid-connected, offer an extensive range of power capacities, from tenths of watts up to hundreds of megawatts. According to the International Energy Agency (IEA), the global cumulative PV capacity had reached around 2.16 TW by the end of 2024 [2]. Global solar module manufacturing capacity grew from ~ 650 - 750 GW/year in late 2023 to about 1 TW/year in early 2024 [3]. And it is projected to reach ~ 1.8 TW/year by the end of 2025 [4].

Traditional glass-based crystalline silicon (c-Si) solar modules, while effective, are often heavy, rigid, and challenging to integrate into various applications, particularly where structural load and flexibility are primary considerations. The glass/glass solar module normally has an area density in the range of 14 - 20 kg/m^2, and the glass/back sheet solar module has an area density in the range of 12 - 16 kg/m^2 [5–7]. In recent years, researchers have been working on the development of lightweight solar modules by substituting the cover glass with ultra-thin glass [8] or even lighter materials such as polymer foils [5, 6, 9–13], and the metal-frame is not need either, which could reduce their area density down to ~ 2 kg/m^2. Lightweight solar modules with front sheet/back sheet configurations represent an innovative advancement designed to overcome the constraints faced

by glass-based solar modules. They offer flexibility, reduced weight, and ease of integration into diverse structures such as vehicle-integrated photovoltaics (VIPV), portable devices, transportation, and aerospace applications. The development of lightweight solar modules not only expands the versatility and accessibility of solar technology but also significantly reduces installation costs and structural reinforcement requirements. Despite these advantages, challenges such as maintaining high efficiency, durability, and long-term stability under varying environmental conditions remain critical areas of research. Therefore, understanding the materials, design strategies, and performance metrics associated with lightweight solar modules is essential to unlocking their full potential in the renewable energy landscape.

Silicon heterojunction (SHJ) solar cells, characterized by their high efficiency, symmetric architecture, and excellent temperature stability, offer significant potential for the development of lightweight solar modules. It can achieve a high power conversion efficiency (η) owing to its excellent surface passivation to minimize surface recombination, resulting in a higher open-circuit voltage (V_{oc}) and fill factor (FF) compared to other c-Si-based solar cell technologies, such as the aluminum back-surface field (Al-BSF) solar cell and passivated emitter rear contact (PERC) solar cell. Most recently, Trinasolar reported a record-breaking power conversion efficiency of 27.08% for a 210 $\times$ 105 mm^2 bifacial SHJ solar cell in December 2024 [14].

However, the development and deployment of lightweight SHJ solar modules face several notable challenges. Firstly, SHJ solar cells are inherently more sensitive to moisture compared to other photovoltaic technologies, such as PERC technology, because the amorphous/crystalline interface is susceptible to moisture, due to the oxidation of the hydrogenated amorphous silicon (a-Si:H) passivation layer. Various transparent-conductive oxides (TCOs), including indium tin oxide (ITO) and aluminum-doped zinc oxide (AZO), exhibit differing degrees of moisture resistance [15–19]. Moisture ingress, particularly under elevated temperatures, leads to damp-heat-induced degradation (DHID) in SHJ solar cells, ultimately reducing the solar module's power output over time [20]. Secondly, effective encapsulation solutions are currently limited to glass solar module configurations, with no sufficiently reliable solutions yet available for front sheet/back sheet configurations. In conventional glass/back sheet or glass/glass solar modules, the front glass acts as a primary barrier against environmental stressors. However, lightweight solar modules, which typically utilize polymer-based layers, suffer from higher water vapor transmission rates (WVTR) compared to traditional glass/back sheet or glass/glass designs. As a result, they are inherently more vulnerable to DHID. To mitigate this, both front and back sheets must offer enhanced protection, necessitating materials with significantly lower permeability. These components, particularly the polymeric elements of solar modules, play a vital role in the durability and reliability of these devices [21, 22]. In this context,

the choice of polymeric components becomes crucial for ensuring long-term durability and reliability. The compatibility and material properties of encapsulants must be carefully matched with the specific solar cell technology, and any introduction of new materials or combinations requires comprehensive reliability testing [23]. Thirdly, ultraviolet (UV) radiation has been identified as another major reliability concern for SHJ solar modules [24–26]. This is especially critical for lightweight solar module configurations, where flexible, polymer-based front sheets often provide inadequate shielding against UV exposure. Prolonged UV irradiation can degrade both the encapsulants and solar cells, compromising the performance and longevity of the solar modules. In light of these challenges, the long-term reliability and protection of SHJ solar modules, particularly lightweight variants, depend on optimized encapsulation strategies. These must effectively guard against environmental stressors such as moisture and UV radiation to preserve the integrity of sensitive interfaces within the device.

Addressing these challenges is essential for the successful development and commercialization of lightweight SHJ solar modules that meet the stringent performance and durability requirements for a wide range of applications. This thesis aims to develop high-performance lightweight solar modules based on SHJ solar cells, with a particular focus on improving resistance to damp-heat (DH) and mitigating the effects of UV radiation.

Chapter 2 presents a comprehensive literature review on the evolution of SHJ solar cells and encapsulation materials, along with the challenges associated with the development and application of lightweight SHJ solar modules. Section 2.1 outlines the historical development of SHJ solar cells, emphasizing their advantages and associated challenges. Section 2.2 reviews the evolution of encapsulant materials, detailing the properties and characteristics of each. Section 2.3 discusses the challenges in developing lightweight SHJ solar modules, with particular focus on reliability issues arising from moisture ingress and UV radiation.

Chapter 3 describes the experimental setup and characterization techniques employed throughout this research. Section 3.1 details the design and fabrication process of lightweight SHJ solar modules. Section 3.2 introduces the accelerated aging tests involved in this study. Section 3.2 provides a brief description of the characterization methods for both silicon solar cells/modules and the polymer encapsulation materials.

Chapter 4 investigated the DH stability of lightweight SHJ mini-modules fabricated with three different TCO films through accelerated DH aging tests. Section 4.1 compares the DH stability of lightweight and glass-based SHJ solar modules using ITO and AZO, demonstrating the vulnerability of AZO-incorporated lightweight SHJ solar modules to moisture. Section 4.2 analyzes the DHID mechanism in SHJ solar cells with ITO and AZO,

examining their optoelectronic properties as well as the electrical properties and morphology of TCO films. Section 4.3 explores the DHID mechanism of AZO-incorporated lightweight solar modules, which is highly related to the adhesion of the polymer interconnection foil (IF) to the AZO layer and moisture penetration. It also highlights the critical role of the capping layer in improving the DH stability of the AZO-incorporated solar cells and lightweight solar modules. Section 4.4 further investigates the role of the interconnection foil in the DHID of the AZO-incorporated lightweight solar modules. An optimized interconnection foil was used to improve the DH stability of AZO-incorporated lightweight solar modules.

Chapter 5 focuses on the DH stability of lightweight SHJ mini-modules with various encapsulants and architectures, evaluated through a 1000-hour accelerated DH aging test. Section 5.1 investigated the effect of encapsulants on the DH stability of lightweight SHJ solar modules. A comprehensive analysis of solar module degradation was conducted, focusing on the optoelectronic properties of the solar modules and the chemical properties of the polymer encapsulants. Section 5.2 reports the successful fabrication of an optimized, damp-heat-stable, lightweight SHJ solar module by selecting an optimal front sheet and encapsulant combination. After 1000 hours of DH exposure, the solar module exhibited only $0.47\%_{\mathrm{rel}}$ efficiency loss, achieving stability comparable to conventional glass/back sheet solar modules.

Chapter 6 provides insights into the UV-induced degradation (UVID) of lightweight SHJ solar modules incorporating different encapsulants with different UV transmittance, involving UV-blocking, UV-transmitting, and UV-downshifting. Section 6.1 investigates the UV stability of polymer front sheets and encapsulants after 120 $\mathrm{kWh/m^2}$ of UV exposure, focusing on the changes of their optical properties. Section 6.2 elucidates the UVID mechanism by comprehensively analyzing the optoelectronic properties of lightweight SHJ solar modules utilizing encapsulants with different UV-transmission properties. Section 6.3 explains the degradation of the downshifting (DS) effect due to photo-oxidation in lightweight solar modules and further illustrates the influence of the solar module structure on the degradation of the downshifting effect. Section 6.4 proposes a dual-layer encapsulation strategy that significantly improves UV resistance and preserves over 98% of the solar module's initial performance after UV exposure.

Chapter 7 summarizes the key findings and conclusions of this thesis, and outlines future research directions aimed at further enhancing the performance and reliability of lightweight SHJ solar modules, as well as advancing the development of the next generation of lightweight solar modules.

2 Fundamentals and literature review

This chapter introduces the fundamentals of SHJ solar cells and solar module technology, and provides a review of the literature on the evolution of SHJ solar cells and encapsulation materials. It also discusses the potential challenges in developing and applying lightweight SHJ solar modules.

2.1 Silicon heterojunction solar cells

2.1.1 Evolution

The SHJ solar cells have been recognized as one of the most advanced technologies for improving solar power generation [27–30]. The development of SHJ solar cells has undergone significant advancements over the past decades. The concept of heterojunction technology applied in photovoltaics traces back to the heterojunction transistor proposed by Shockley in 1948 [31]. The first experimental study of a heterojunction formed between doped a-Si:H and c-Si was reported by Fuhs et al. in 1974 [32]. In 1983, Hamakawa et al. integrated an a-Si:H/poly-Si heterojunction into a tandem junction solar cell, known as the "Honeymoon" cell [33, 34]. By the late 1980s, Sanyo began actively researching this technology and fabricated a solar cell by directly depositing a p-type a-Si:H layer onto an n-type c-Si substrate, achieving a conversion efficiency of 12.3% [35]. In 1992, Sanyo introduced an intrinsic a-Si:H (i-layer) between the c-Si and p-type a-Si:H layers to effectively passivate the dangling bonds on the c-Si surface. This innovation increased the efficiency to 14.8% and led to the establishment of the Heterojunction with Intrinsic Thin-layer (HIT®) structure, for which a patent was filed in 1993 [35]. In 1997, Sanyo commenced the industrial production of a-Si:H/c-Si hybrid solar cells. By 2000, large-area devices (>100 cm^2) exceeded 20% efficiency [36]. Continued material and process optimizations culminated in an efficiency of 23% with a 98 μm thin wafer in 2009 [37]. In 2014, Panasonic achieved 24.7% efficiency for both-side-contacted SHJ cells [38] and 25.6% with an interdigitated back contact (IBC) SHJ structure [39]. In 2015, Kaneka Corporation reported a record efficiency of 25.1% for both-side-contacted SHJ cells, surpassing the best-performing homojunction passivated emitter rear contact (PERC) solar

cells at the time [40]. Further progress was made in 2017 when Kaneka pushed the efficiency of SHJ-IBC solar cells to 26.7% by significantly reducing parasitic absorption from a-Si:H and TCO layers, setting a new world record for silicon solar cells [41]. This record was surpassed in 2022 by LONGi, which achieved 26.81% efficiency in both-side-contacted SHJ cells [42]. Furthermore, LONGi achieved a certified efficiency of 27.30% for a solar cell featuring Heterojunction Back Contact (HBC) structures [43]. Most recently, in December 2024, Trinasolar reported a record-breaking power conversion efficiency of 27.08% for a 210 $\times$ 105 mm^2 bifacial SHJ solar cell [14, 44].

Regarding the development of flexible solar cells, Liu et al. developed a large area ($>$ 240 cm^2) and a high efficiency ($>$ 24%) flexible solar cell by using edge-blunting passivation technology in August 2022 [45]. This technology improves the flexibility of silicon wafers by blunting the pyramidal structure in the marginal regions. In the same year, LONGi developed a flexible SHJ solar cell with a large area of 274.4 cm^2 and a minimum thickness of 57 μm. This solar cell has a very high power-to-weight ratio of 1.9 W/g [45]. The development of flexible solar cell technology provides a practical basis for fabricating lightweight, low-cost, high-efficiency SHJ solar modules [46].

2.1.2 Strengths and challenges

Figure 2.1(a) illustrates the schematic structure of an n-type rear-emitter SHJ solar cell, and Figure 2.1(b) displays the actual SHJ solar cell. The device employs a lightly doped n-type c-Si wafer as the absorber, featuring a randomly textured surface to facilitate effective light trapping. Ultrathin intrinsic hydrogenated amorphous silicon (a-Si:H(i)) layers are deposited on both wafer sides via plasma-enhanced chemical vapor deposition (PECVD) to provide excellent chemical passivation and to suppress interface recombination. A highly doped n-type a-Si:H(n) emitter is formed on the illuminated front side, creating an electron-selective contact that efficiently extracts photogenerated electrons. On the rear side, a p-type a-Si:H(p) layer establishes a back surface field (BSF) that repels minority carriers and facilitates hole collection. Additionally, transparent conductive oxide (TCO) layers are applied onto the doped a-Si:H layers using physical vapor deposition (PVD). The TCO layers enhance lateral carrier collection and ensure optimal electrical contact with the screen printing metal grid.

SHJ solar cells can achieve high efficiencies owing to the high quality interface between the c-Si wafer and the a-Si layer (a-Si/c-Si interface), which minimizes the minority carrier recombination at the surface, resulting in a higher V_{oc} and FF compared to other c-Si-based technologies, such as Al-BSF and PERC [43, 46, 48, 49]. In addition, the ideal passivated surfaces and the low temperature used during SHJ solar cell processing allow

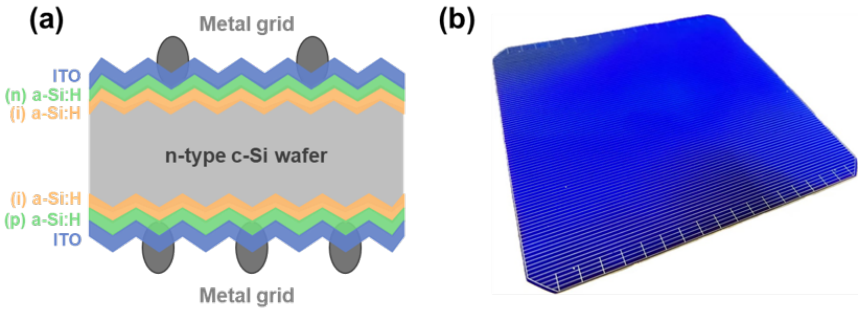


Figure 2.1: (a) Schematic structure of an n-type rear-emitter silicon heterojunction (SHJ) solar cell; (b) Image of the actual SHJ solar cell developed in FZJ [47].

for a thinner wafer to be used, making it suitable for lightweight PV applications. The SHJ device features a symmetrical structure and can naturally achieve high bifaciality ($> 90\%$) [36, 50]. Higher power output was therefore obtained for the SHJ bifacial solar modules under realistic operating conditions, compared with PERC modules [51, 52]. In addition, rear-junction SHJ bottom cells pair naturally with perovskite [53] or III-V compounds [54] top cells to form tandem devices [55, 56]. This is because the front is covered in TCO and is free of metal grids, which simplifies optical coupling [46].

Despite the numerous advantages of SHJ solar cell technology, several challenges remain. One of the primary limitations compared to other photovoltaic concepts is the reliance on a TCO layer, typically ITO, to facilitate lateral charge carrier transport. ITO is widely used in industry due to its excellent optoelectronic properties [20], but it also introduces significant drawbacks. A major concern is the dependence on scarce and expensive elements such as indium (In), which could pose a bottleneck for large-scale manufacturing and long-term sustainability of SHJ technology. To mitigate this issue, considerable research efforts have been directed toward developing alternatives to indium-based TCOs in recent years. Promising approaches under investigation include indium-free TCOs, indium-reduced (indium-less) TCOs, and even TCO-free architectures [57–60]. Among these, one of the most actively explored options is replacing ITO with AZO [46], which offers a more abundant and cost-effective solution while maintaining satisfactory electrical and optical properties.

However, the pure AZO film has lower carrier mobility and higher resistivity [61] and is more susceptible to water vapor corrosion. This results in a reported loss of conductivity [15]. AZO grows in a poly-crystalline structure that favors rapid penetration of water molecules into the crystal boundaries, leading to degradation of the electrical properties of the material [16]. Therefore, in order to improve the electrical properties of AZO and to enhance the damp-heat stability of the AZO film, different capping layers have

been introduced and investigated at the solar cell level. Such as aluminium oxide (Al_2O_3), silicon oxide (SiO_2), and silicon nitride (SiN_x). Adachi et al. reported that a SiO_2 capping layer on the ITO layer improved the damp-heat stability of SHJ solar cells [18]. Morales-Vilches et al. reported that the damp-heat stability of solar cells with AZO front TCO was improved when capped with SiO_2, SiO_2 capping layer hindered the moisture-induced degradation of AZO at the grain boundaries [17].

From the perspective of long-term outdoor operation, we believe that the stability of a PV product is at least as important as its efficiency.

2.2 Evolution of encapsulant materials

Chemically cross-linked ethylene-vinyl acetate (EVA) copolymer has been the dominant solar module encapsulant choice for decades since the 1980s, because of its advantages, such as high transmittance, good adhesion to glass, favorable mechanical properties, low cost, and field experience for more than 35 years. [62–64]. Although EVA is the most widely used encapsulant for solar modules, it has some drawbacks. To achieve thermal and thermo-mechanical stability, the material is equipped with curing agents (peroxides) that facilitate chemical crosslinking during the lamination process [65], forming a three-dimensional polymer network [66–70]. This time- and energy-consuming process of lamination also leaves reactive peroxides in the solar module, which can influence or accelerate certain modes of degradation [67, 71]. Another drawback of EVA is the production of corrosive acetic acid in the presence of moisture and other environmental stressors [62, 72], which can lead to several solar module failure mechanism, such as the corrosion of interconnection and solar cell metallization [21, 73–77] or potential induced degradation (PID), where acetic acid enhances sodium ion migration [77–79], resulting in decreased reliability of solar modules.

Over the past 20 years, a variety of materials have been developed to replace EVA [23], including ionomers [80, 81], thermoplastic silicone elastomers (TPSEs) [82], silicone elastomers [83, 84], polyethylene (PE), polyethylene copolymers, and polyvinyl butyral (PVB) [22, 85–87]. However, none of these early developments have been successful in reaching the market or have only been used in niche applications, such as ionic polymers for encapsulating double-glass copper-indium-gallium-selenide (CIGS) solar modules [88]. PVB have been found suitable for glass/glass solar module application, which provides a strong adhesion to the glass compared to EVA and is particularly suitable for building-integrated photovoltaics (BIPV) application. However, PVB has a very high water absorption rate and is prone to hydrolysis; therefore, the solar modules require an additional edge sealant [22, 89].

In recent years, different types of next-generation encapsulant foils have been introduced and have attracted increasing attention in the market, which includes polyolefin elastomer (POE) encapsulants, thermoplastic polyolefin (TPO) encapsulants [90, 91], and thermoplastic polyurethane (TPU). For POE and TPO, both of which consist of a polyethylene backbone with different side groups. The main advantage of these encapsulants is the replacement of the vinyl acetate side groups of EVA with acrylates, acrylic acids, or n-alkanes, without the formation of acid, consequently [92]. Similar to EVA, POE contains crosslinking agents (peroxide) and therefore has a similar lamination process as EVA. TPO is a thermoplastic elastomer that exploits thermo-reversible physical crosslinking, such as ion bonds, hydrogen bonds, or via crystallites [23], showing potential in the recycling of solar modules. The TPO foils have a high melting temperature of around 100 °C, resulting in low thermal expansion [23, 93]. This ensures thermo-mechanical stability during field operation [85, 87, 92] and allows lamination in less than 10 minutes [85, 94], as no time-consuming crosslinking process is required. This shows their potential for application in the encapsulation of perovskite and perovskite-incorporated tandem devices [95–97]. In addition, TPO is free of peroxides, which can corrode solar cells. Compared to EVA, it has a higher volume resistivity and a lower WVTR due to its specific low chemical polarity and high crystallinity [93], both of which significantly reduce the PID sensitivity of solar modules [85, 98–100]. However, high crystallinity makes the polymer brittle and rigid [85]. EPE (EVA/POE/EVA), which is a co-extruded of EVA and POE that combines the advantages of EVA with low cost and POE with better material properties. In general, these new types of encapsulants, such as TPO and POE, have lower WVTR than EVA and are suitable for moisture-sensitive advanced solar cell and module technologies [23, 93].

Although these types of materials have been on the market for several years, few studies have reported on the selection of encapsulant materials compatible with SHJ solar cell technology in lightweight solar module architecture and their long-term reliability [13, 101].

2.3 Challenges for lightweight SHJ solar modules

2.3.1 Lightweight c-Si-based solar modules

Conventional c-Si solar modules usually consist of a superstrate solar glass covering, several interconnected silicon solar cells, two layers of polymeric encapsulant (one on the front of the solar cells and another on the rear of the solar cells), a substrate polymeric back sheet or glass, an aluminum frame, a junction box, and other materials such as

ribbons [21, 63], as shown in Figure 2.2. This architecture was developed in the late 1970s and early 1980s within the Flat-Plate Solar Array Project [102]; it has remained largely unchanged since then. In a conventional solar module, the low-iron tempered glass accounts for 65% of the total weight. The glass/back sheet solar module normally has an area density in the range of 12 - 16 kg/m^2, and the glass/glass solar module has an area density in the range of 14 - 20 kg/m^2 [5–7], which poses limitations for application scenarios, such as roofs with low load tolerances and integrated applications. For these areas of application, properties such as lightweight and flexibility are becoming increasingly significant for the design of solar modules. Lightweight solar modules apply not only to the ground installations, but also to roofs with low load capacity and autonomous mobility scenarios, such as satellites [103], solar planes, cars, and boats [104–106].

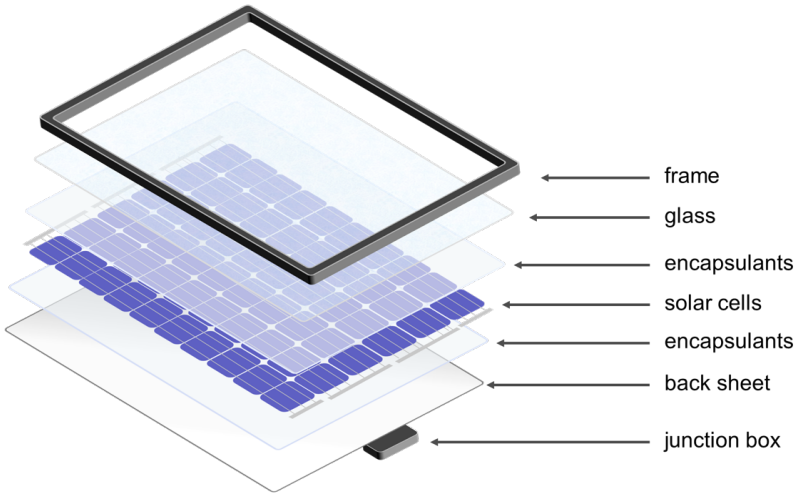


Figure 2.2: Schematic structure of a typical glass c-Si solar module.

In recent years, researchers have been working on the development of lightweight solar modules by substituting the cover glass with ultra-thin glass [8] or even lighter materials such as polymer sheets [5, 6, 9–13]. Figure 2.3(a) shows a schematic structure of a lightweight solar module, and (b) shows a prototype lightweight SHJ solar module developed in this work, with a low area density of around 2 kg/m^2. Since this sheet is placed on the front side, it must be transparent to sunlight and have a low refractive index. The long-term performance and reliability of lightweight solar modules are determined by the properties and compatibility of the materials used in their fabrication. The material used for the outer surface, which replaces conventional glass, must protect against moisture ingress, dust, and other contaminants. It must also provide excellent electrical insulation. Additionally, it must be mechanically robust to provide the solar module with impact resistance.

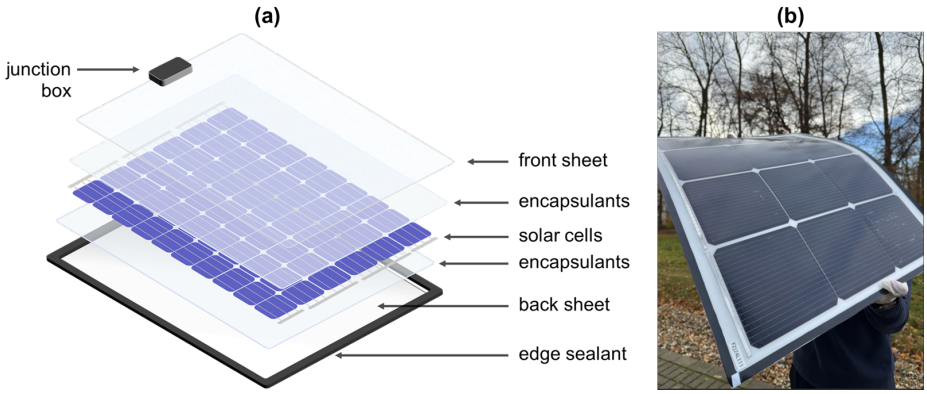


Figure 2.3: (a) Schematic structure of a lightweight c-Si solar module and (b) a prototype lightweight SHJ solar module developed in this work.

Lightweight c-Si solar modules have been developed using a glass fiber-reinforced polymer (GFRP) with a film on the front surface instead of low-iron tempered glass. A honeycomb sandwich structure provides mechanical strength on the back surface [7, 107]. Previous work demonstrated the possibility of producing a lightweight solar module weighing 5 kg/m^2, by replacing the typical front glass with an ethylene tetrafluoroethylene (ETFE) polymer sheet and the standard back sheet with a composite sandwich structure [7]. ETFE has been used as the front sheet owing to its high transparency and stability [5, 6]. It has been tested and found to have good scratch resistance under severe linear abrasion. It is also far more resilient than the porous silica antireflection coatings currently used on most solar modules. These results demonstrate the strong potential of ETFE for use as a front cover sheet for lightweight c-Si solar modules [13]. Martins et al. proposed a lightweight structure comprising an ETFE front sheet and a honeycomb back sheet, which improves the solar modules' hail impact resistance. It was found that the storage modulus and bending stiffness of the encapsulation materials significantly contribute to this resistance [5, 108]. Kutter et al. fabricated a lightweight c-Si solar module constructed with a layer of ETFE foil over a GFRP-hard-foam sandwich [109]. Govaerts et al. fabricated a lightweight solar module with a polyethylene terephthalate (PET) front sheet and a GFRP back sheet. Mechanical stability against hail impact was significantly improved by using four layers of front encapsulant and a thicker back sheet [110]. Budiman et al. successfully fabricated lightweight solar modules using polycarbonate (PC) for both the front and back sheets. However, they found that achieving good adhesion at the PC/EVA interface was the key fundamental challenge [111]. Kajisa et al. used a vacuum lamination process to fabricate a lightweight plastic solar module using an acrylic film as the front cover, which is 46% lighter than a standard glass-covered solar module [9]. At the same time, it meets the DH test requirements of the IEC standard

[112]. Luo et al. found that implementing a composite encapsulant integrated with a glass fiber and a carbon fiber-reinforced polypropylene (CFPP) back sheet with a low coefficient of thermal expansion (CTE) is beneficial to the thermo-mechanical reliability of lightweight solar modules [113]. They also found that increasing the thickness of both the reinforced back sheet and the front encapsulant layer benefits the impact resistance [101].

In conclusion, the selection of suitable materials is crucial for the fabrication of lightweight solar modules and their long-term stability.

2.3.2 Reliability and durability

The power output of solar modules is affected by various environmental factors, such as irradiation, UV radiation, temperature variations, moisture ingress, wind load, snow accumulation, and soiling during long-term field operation, as illustrated in Figure 2.4. These environmental factors would degrade the solar modules and reduce their power output over time [114–118].

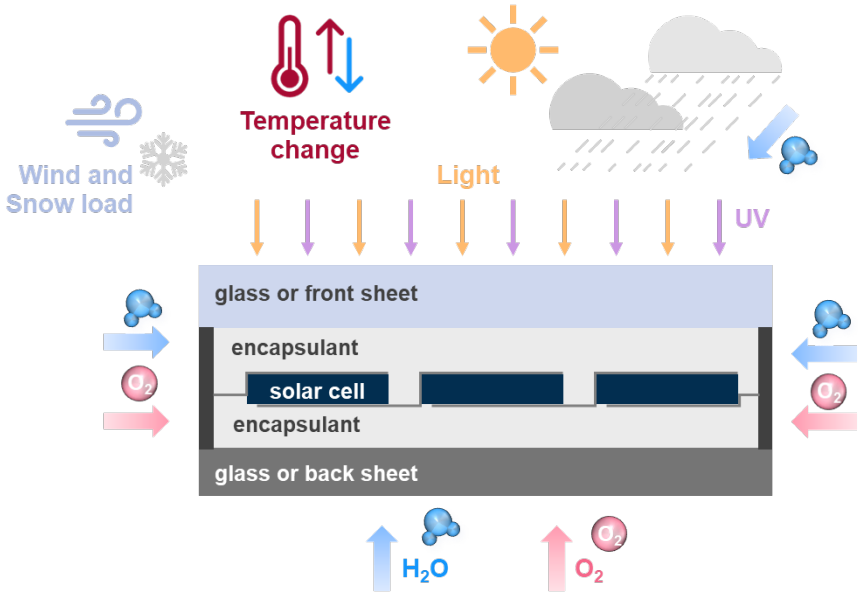


Figure 2.4: Key environmental stressors for solar modules during field operation.

Performance analyses have been conducted on bulk c-Si solar modules, which have been used to generate electricity as PV systems for over 30 years [118–135]. A review of numerous studies on the degradation rates of solar modules conducted worldwide over the past 40 years suggests that the average degradation rates of bulk c-Si and thin-film

technologies are 0.7% and 1.5% per year, respectively [116, 136, 137]. The polycrystalline silicon (poly-Si) solar modules were found to exhibit systematically smaller degradation rates than the monocrystalline silicon (mono-Si) solar modules and substantially lower rates than the amorphous silicon (a-Si) solar modules [136, 138–140].

SHJ solar modules typically degrade at a rate of less than 1% per year in solar farms [136, 141]. The degradation is mainly in V_{oc} rather than more typical changes in short-circuit current (I_{sc}), with some increase in series resistance (R_{s}), which can differ from other technologies [142, 143]. Arruti et al. reported that SHJ solar modules exhibit an average yearly degradation rate of 0.7% in the field, mainly related to failures caused by encapsulant discoloration, loss of passivation, moisture ingress, PID, and UV radiation [20].

Some studies have reported that an apparent V_{oc} loss, caused by loss of the surface passivation properties in the SHJ solar cells, is the main reason for degradation in SHJ solar modules. Luo et al. found a substantial loss in V_{oc} in SHJ solar modules installed in tropical Singapore [132], whereas Ishii et al. observed similar behavior in Kyushu, Japan [144]. Moreover, Schweiger et al. observed continuous V_{oc} degradation and performance loss in SHJ solar modules in several different climates [145]. Jordan et al. found that increased saturation currents at the solar module level, concluding that increased carrier recombination was the cause of the degradation. Further analysis confirmed that the passivation loss indicated by the reduction in V_{oc} could be caused by a reduction in the hydrogen content of the a-Si:H layers [142, 146]. Moreover, new failure modes can occur in field applications.

The correct choice of encapsulants would protect the solar modules from environmental factors and weathering degradation, which significantly affects the performance and stability of the solar modules [147]. In essence, this affects the cost and quality of the solar modules, and the appropriate combination of encapsulants and solar cell technology is critical to the longevity of the solar modules.

Regarding the lightweight solar modules, the front sheet/back sheet structure results in a different micro-environment as compared to traditional glass/back sheet solar modules. Lightweight encapsulation materials and reduced structural supports can compromise mechanical integrity, making solar modules more susceptible to damage from wind loads, hail impact, and snow accumulation. Additionally, ensuring long-term reliability is challenging as lightweight materials may be less resistant to environmental degradation factors such as UV radiation, moisture ingress, and temperature variations caused by changes in the time of day or season, which can lead to accelerated aging and reduced solar module lifetime. Therefore, there are higher requirements for the encap-

sulation materials of lightweight solar modules to ensure their long-term stability and reliability.

As we mentioned previously, SHJ solar cells are highly sensitive to moisture and UV radiation [24, 93, 148]; therefore, this thesis will primarily focus on the reliability of lightweight SHJ solar modules in terms of moisture ingress and UV radiation.

Moisture ingression

Moisture is an important stress factor for solar modules. During outdoor operations, moisture appears in various forms, including water vapor (or humidity), condensation (or dew), rain, snow, and ice. Elevated temperatures can correspondingly accelerate the water vapor penetration process, which can lead to various degradations such as corrosion, delamination, or discoloration [149–154]. This DHID is typically accompanied by severe reductions in solar module performance [155].

It was reported that PERC solar cells demonstrated less degradation after the damp-heat test in various lightweight structures (i.e., ETFE-GFRP, PET-honeycomb, and ETFE-honeycomb structures) [6, 156, 157]. In contrast, Tunnel Oxide Passivated Contact (TOPCon) and SHJ solar cells were found to degrade more easily during the damp-heat test. This poses a particular challenge for solar modules with lightweight structures [101, 110].

A reliable encapsulation solution is currently only available for glass/glass structures, and it is not yet ready for front sheet/back sheet structures. Naturally, the front-facing glass acts as the first protection line of the glass solar module. However, the lightweight solar module architecture faces the critical challenge of having a higher WVTR than conventional glass/back sheet or glass/glass encapsulated solar modules. Therefore, the lightweight solar module is literally more susceptible to DHID than the glass solar module. Consequently, a higher degree of protection is required for the front and back sheets, meaning a lower permeability of the components is required. These components, particularly the polymeric elements of solar modules, play a vital role in the durability and reliability of these devices [21, 22].

Encapsulation materials play an important role in solar module reliability because the most prominent solar module failure mechanisms are linked to the polymeric encapsulation materials used. Polymeric encapsulants and front or back sheets are important for solar modules because of their various functions [21, 62, 63]. However, these polymeric components are not perfectly air/water-tight and are prone to permeation of gases, including moisture, oxygen, and other gaseous species from ambient surroundings [73]. Moisture ingress usually occurs through polymeric materials, solar module edges, and

voids created by manufacturing, handling, and climatic stressors [158–162]. Once water penetrates the solar module, the accumulated moisture within the solar module in the presence of other climatic stressors can lead to all forms of degradation modes in the components of solar modules [163, 164]. Moisture ingress at elevated temperatures leads to the formation of acetic acid within the EVA encapsulant. Acetic acid accumulation in solar modules is a major precursor for interconnect corrosion, which usually occurs around solar cell interconnect ribbons and solar cell metallization in solar modules [21, 165–167]. According to Peshek et al. [167], the routes of corrosion are dominated by moisture ingress from the perimeter to the interior of the solar module. Discoloration can also result from moisture ingress in solar modules [159]. Particulate water trapped within the encapsulants acts as an optical barrier, increasing absorption losses, which has a significant effect on the quantum efficiency of the solar modules [167–169]. Additionally, moisture ingress induces adhesion loss and creates voids, which serve as a suitable reservoir for moisture and gas accumulation [170] in the encapsulants and back sheets, thereby predisposing all components of the solar module to corrosion [90, 91, 171, 172] and therefore may result in power loss [91, 155]. The loss of adhesion between solar cells, encapsulants, glass, and other active layers due to environmental, climatic, and/or artificial mechanical stressors results in delamination [64, 158]. Delamination and discoloration subsequently lead to degradation of optical performance [161, 173].

The selection of encapsulation materials that are compatible with the solar cell technology is critical to the longevity of the solar module. Therefore, before introducing new materials and material combinations, each new combination should be thoroughly tested [23].

UV radiation

UV radiation has been identified as another critical factor for solar module degradation and its lifetime by many research groups. UVB (280 - 315 nm) is the most damaging part of the UV light, in particular for polymeric materials in solar modules, despite its small power fraction (~ 1.5%) compared to UVA (315 - 400 nm; ~ 98.5%) according to the reference spectrum. UV radiation can trigger chemical reactions and degradation processes of polymers in solar modules, which changes the primary structure of the polymer, causing crosslinking or the breaking of the chains, and other chemical alterations [23, 63, 174–176]. Typical defects, such as encapsulant discoloration (e.g., EVA yellowing), are caused by photo-oxidation due to UV radiation, thereby decreasing its transmittance [26, 63, 83, 177]. Acetic acid and aldehyde can be formed due to UV radiation and temperature [63]. It has also been reported that encapsulants are susceptible to losing adhesion under UV irradiation [83, 178]. UV radiation will also lead to the degradation of the back sheet,

resulting in reliability issues such as powdering and embrittlement [23, 126].

In addition, from the perspective of SHJ solar cells, the silicon-hydrogen (Si-H) bond can be broken by high-energy UV photons, consequently leading to the deterioration of the chemical passivation properties of SHJ solar cells [24]. A study systematically examined the UVID phenomenon in SHJ solar cells alongside other advanced c-Si PV technologies. The findings revealed that SHJ solar cells were particularly sensitive to UV radiation, exhibiting substantial power losses of up to 11.8%, which was significantly higher than the conventional Al-BSF solar cells with power loss typically below 1% [24]. Furthermore, it was found that the efficiency degradation due to UV radiation was primarily a result of a decrease in V_{oc} and FF. Further research found that UVA photons, with a wavelength of 365 nm or lower, have the capacity to break Si-H bonds (bond dissociation energy of 3.4 eV corresponding to ~ 365 nm), increasing the dangling bond dissociation on the silicon surface, thus leading to a reduction in the chemical passivation of SHJ solar cells, resulting in increased surface recombination [179–181]. This process can significantly reduce the hydrogen content in both intrinsic (<i> a-Si:H) and doped a-Si:H films, thus leading to the degradation of the interface passivation layer, resulting in a decrease in V_{oc}. Sinha et al. [24] confirmed that the UVID of SHJ solar cells is ascribed to the loss of hydrogen (H) near the intrinsic hydrogenated amorphous silicon and crystalline silicon (<i> a-Si:H/c-Si) interface or in <i> a-Si:H layer, resulting in poor <i> a-Si:H/c-Si interface passivation.

Overall, the degradation of polymer encapsulation materials and SHJ solar cells due to UV radiation has a synergistic degradation effect on solar modules. This poses a serious concern when SHJ solar modules are operating in the field, particularly for lightweight solar module configurations, where flexible polymer-based front sheets may provide reduced shielding against UV radiation. The adoption of encapsulants with UV-blocking properties was used as one strategy to effectively mitigate the degradation of solar cells and materials induced by UV radiation, thereby ensuring the long-term stability of solar cells and modules.

In recent years, with the development of advanced c-Si solar cell technology, like SHJ and TOPCon solar cells [182, 183], the requirement for the maximum utilization of the short-wavelength response is increasing. Advanced solar cells have an optimized spectrum response in the short-wavelength range; however, they are typically more sensitive to UV radiation than Al-BSF and PERC solar cells [48]. Therefore, the implementation of UV-blocking encapsulants in SHJ and TOPCon solar modules is no longer the best option, as this will certainly diminish their advantages in short-wavelength response and come at the cost of a reduced short-circuit current. The other option is to use UV-transmitting encapsulants for advanced c-Si solar cell technology to better utilize the

photo-generated current in the short-wavelength range, thus improving the efficiency of the solar modules. However, these advanced c-Si solar cells are susceptible to UV radiation [25], as mentioned previously. To address these issues, it has been found that incorporating UV-downshifting encapsulants into solar modules is a more suitable solution [184–187]. UV-downshifting encapsulants, which are able to shift high-energy UV photons to visible light, offer promising benefits for both energy yield improvement and material protection. Firstly, the shifted photons can be used more effectively by the solar cell due to its higher external quantum efficiency (EQE) in the specific shifted wavelength range compared to its EQE in the UV wavelength range from which the photons were shifted, which improves the solar module efficiency. Secondly, most of the high-energy UV photons are shifted, preventing the UV photons from reaching the solar cells, thus diminishing the UVID. However, despite the promising potential of UV-downshifting encapsulants, the long-term reliability of SHJ solar modules incorporating UV-downshifting encapsulants remains insufficiently understood, particularly under prolonged UV exposure.

3 Experimental methods

This chapter begins by describing the design and fabrication process of lightweight SHJ solar modules. It then presents the accelerated aging tests used for reliability investigation in this study. Finally, the characterization methods for revealing the degradation mechanism employed in this study are presented.

3.1 Design and fabrication of the lightweight SHJ solar modules

3.1.1 Preliminary design

Figure 3.1 shows the schematic cross-section of the single-cell mini module with our preliminary design. The solar module has a stack-layer structure. The polymer front sheet, rather than glass, was used on the front side of the solar module. The SHJ solar cell is located between the front and rear encapsulants. The 0BB SHJ solar cell was connected using multi-wire interconnection technology consisting of 18 coated copper wires with polyethylene (PE) [188] as the carrier foil, namely interconnection foil (IF). Figure 3.2 illustrates the schematic of how the multi-wire is interconnected with the 0BB SHJ solar cell. A polyolefin-based foil with fluorine-free coating was used as the back sheet (hereafter referred to as Px-bs). The edges of the solar module were sealed with acrylic foam adhesive tape.

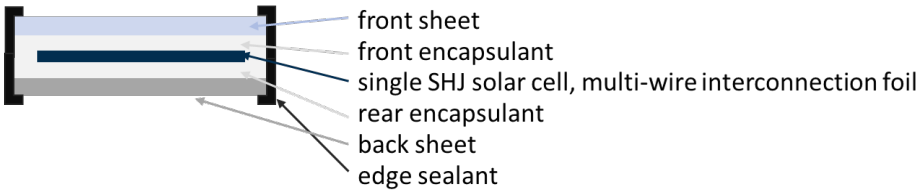


Figure 3.1: Schematic cross-section of the lightweight SHJ single-cell solar module (preliminary design).

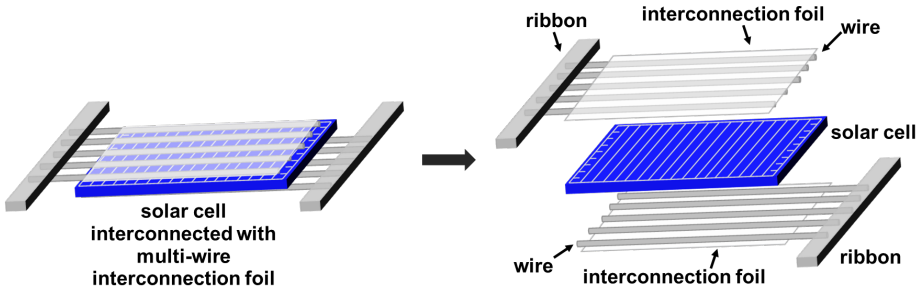


Figure 3.2: Schematic of a single 0BB SHJ solar cell interconnected with a multi-wire interconnection foil and its layer stack.

Figure 3.3 shows the top view of the lightweight solar module. The solar module has a dimension of 200 mm × 200 mm, with an M2 (156.75 mm × 156.75 mm) 0BB SHJ solar cell.

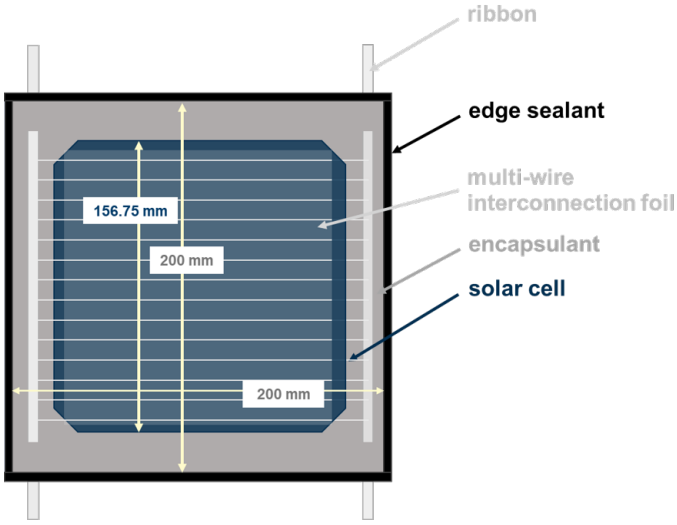


Figure 3.3: Top view of the lightweight SHJ single-cell solar module (preliminary design).

Figure 3.4 shows the fabrication process of the lightweight solar modules with preliminary design, as follows:

Step 1: Materials preparation. The front sheet, back sheet, and encapsulant foils are cut to size.

Step 2: One layer of encapsulant foil is placed on the back sheet.

Step 3: The rear interconnection foil is positioned, and the ribbon is routed through the back sheet. The wires are pre-soldered to the ribbon.

Step 4: The solar cell is placed on top of the rear interconnection foil.

Step 5: The front interconnection foil is positioned, and the ribbon is routed through the back sheet. The wires are pre-soldered to the ribbon.

Step 6: Another layer of encapsulant foil is placed on top of the solar cell.

Step 7: The front sheet is positioned on top.

Step 8: After stacking all foils, the sample is loaded into the laminator and processed under optimized parameters of temperature, pressure, and time. The solar modules are fabricated using a vacuum lamination process in a laminator from *SM Innotech*, which consists of a chamber and a membrane. The chamber includes a heating plate and movable pins that can regulate the heating rate, although the pin function was not used for the single-cell samples. A schematic diagram of this lamination process is shown in Figure 3.5. The temperature and pressure profiles of the lamination process used in the fabrication of the solar modules in this study are shown in Figure 3.6.

Step 9: Once cooled, an edge sealant is applied along the solar module perimeter, completing the fabrication process.

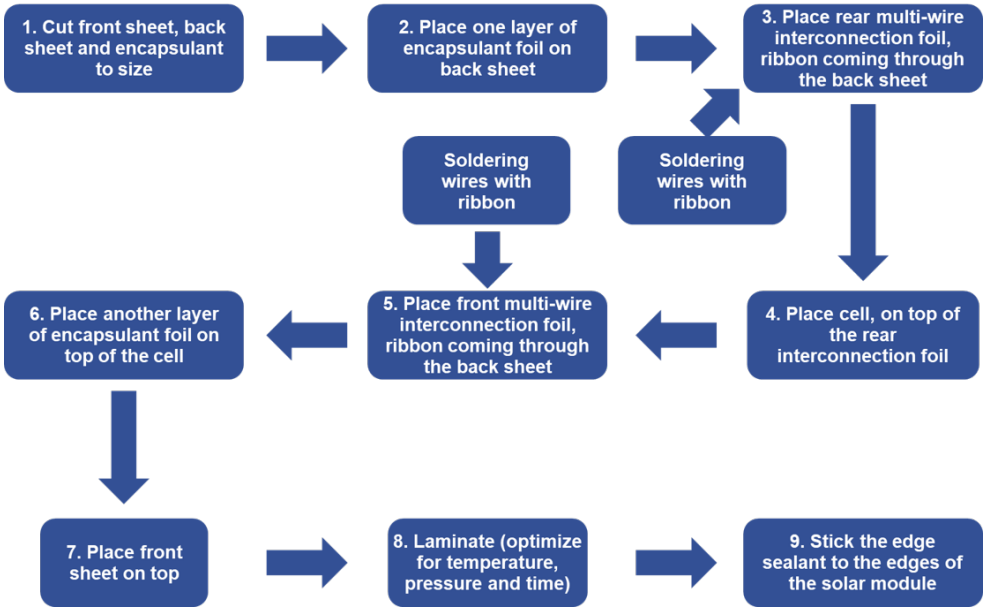


Figure 3.4: Fabrication process of lightweight SHJ single-cell solar modules (preliminary design).

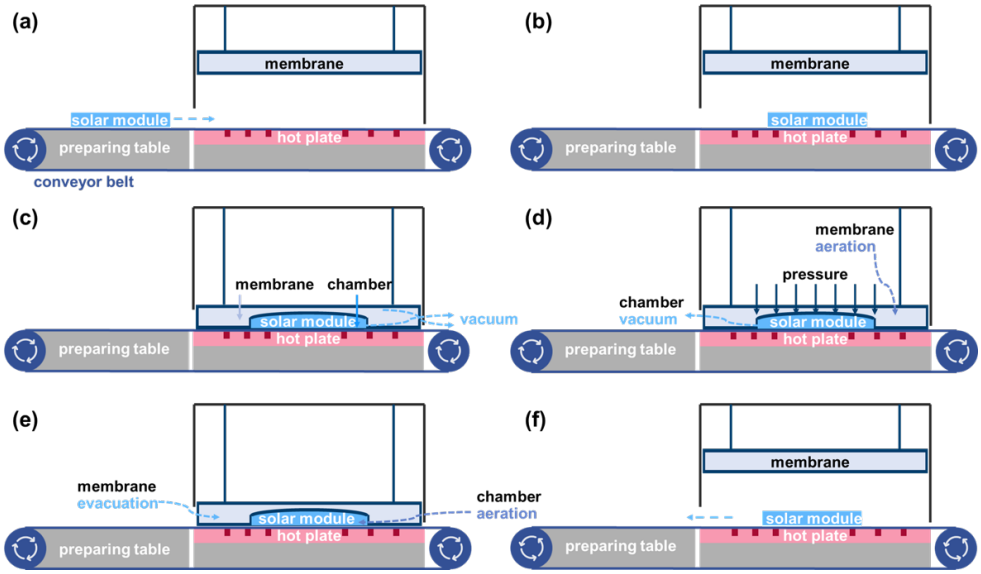


Figure 3.5: Schematic diagram of the lamination process: (a) Preparing the solar module on the preparing table; (b) Loading the solar module into the laminator; (c) The hot plate heats the solar module, the air in the membrane and chamber is evacuated to create a vacuum; (d) The chamber is evacuated and the membrane is aerated to apply pressure to the solar module. This pressure is maintained for a sufficient time to allow the encapsulant to crosslink; (e) The chamber is aerated, and the pressure in the membrane is gradually released; (f) The lamination process is complete; The solar module is then unloaded and allowed to cool naturally.

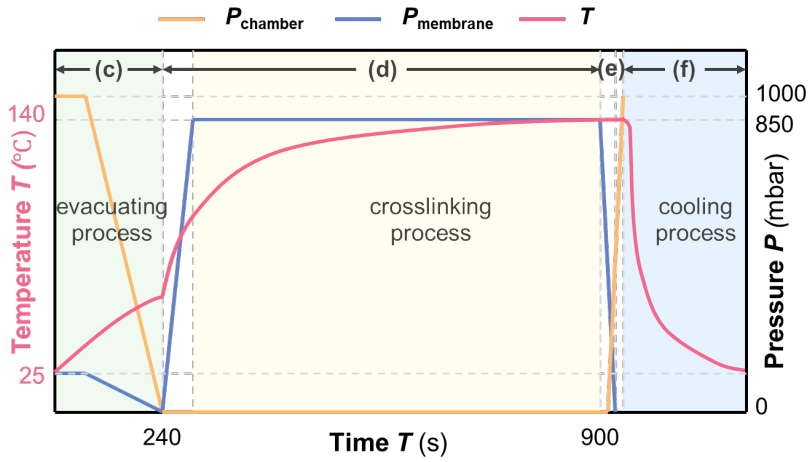


Figure 3.6: Temperature and pressure profiles of the lamination process used in the fabrication of the solar modules in this study. (c),(d),(e), and (f) refer to the steps shown in Figure 3.5.

3.1.2 Optimized design

Figure 3.7 shows the schematic cross-section of the single-cell mini module with our optimized design. Compared to the preliminary design, the major difference in the solar module structure is that a different edge sealant, polyisobutylene (PIB), was used, and the edge sealant has been inserted between the front sheet and the back sheet. The adhesion of the edge sealant to the front sheet and back sheet was formed during the lamination process. This structure was mainly applied to the fabrication of the solar modules in Chapter 5 and Chapter 6.

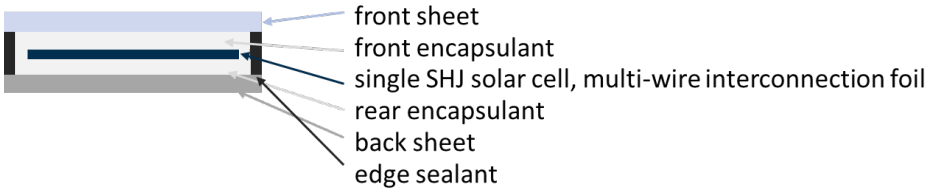


Figure 3.7: Schematic cross-section of the lightweight SHJ single-cell solar module (optimized design).

Figure 3.8(a) shows the cross-section and layer-stack of the lightweight solar module with optimized design, and (b) shows the top view of the solar module. The solar module has a dimension of 210 mm × 210 mm, with an M2 (156.75 mm × 156.75 mm) 0BB SHJ solar cell.

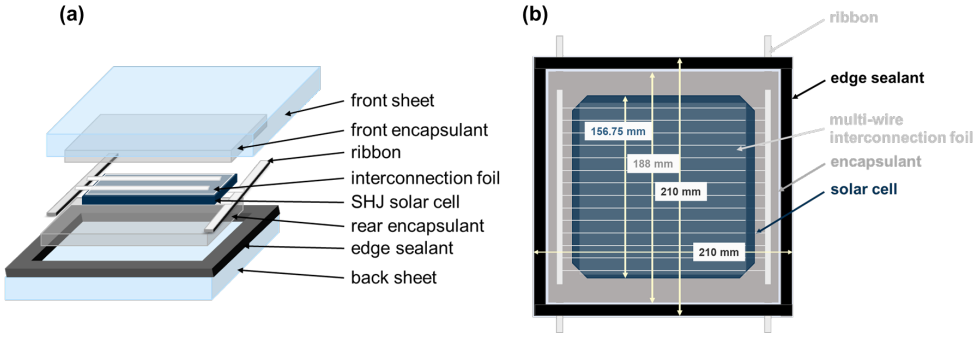


Figure 3.8: (a) Cross-section and layer-stack of the solar module and (b) top-view of the solar module, with optimized design.

Figure 3.9 shows the fabrication process of the lightweight solar modules with optimized design, as follows:

Step 1: Materials preparation. The front sheet, back sheet, and encapsulant foils are cut to size. The thickness of the edge sealant should match the combined thickness of

the front sheet, front encapsulant, solar cell, rear encapsulant, and back sheet in order to ensure proper sealing and improve the overall lamination quality.

Step 2: Stick down the edge sealant on the back sheet, with two intersecting edge sealants overlapping by approximately 50%.

Step 3: One layer of encapsulant foil is placed on the back sheet.

Step 4: The rear interconnection foil is positioned, and the ribbon is routed through the back sheet. The wires are pre-soldered to the ribbon.

Step 5: The solar cell is placed on top of the rear interconnection foil.

Step 6: The front interconnection foil is positioned, and the ribbon is routed through the back sheet. The wires are pre-soldered to the ribbon.

Step 7: Another layer of encapsulant foil is placed on top of the solar cell.

Step 8: The front sheet is positioned on top.

Step 9: After stacking all foils, the sample is loaded into the laminator and processed under optimized parameters of temperature, pressure, and time. The lamination process follows the same procedure illustrated in Figure 3.5.

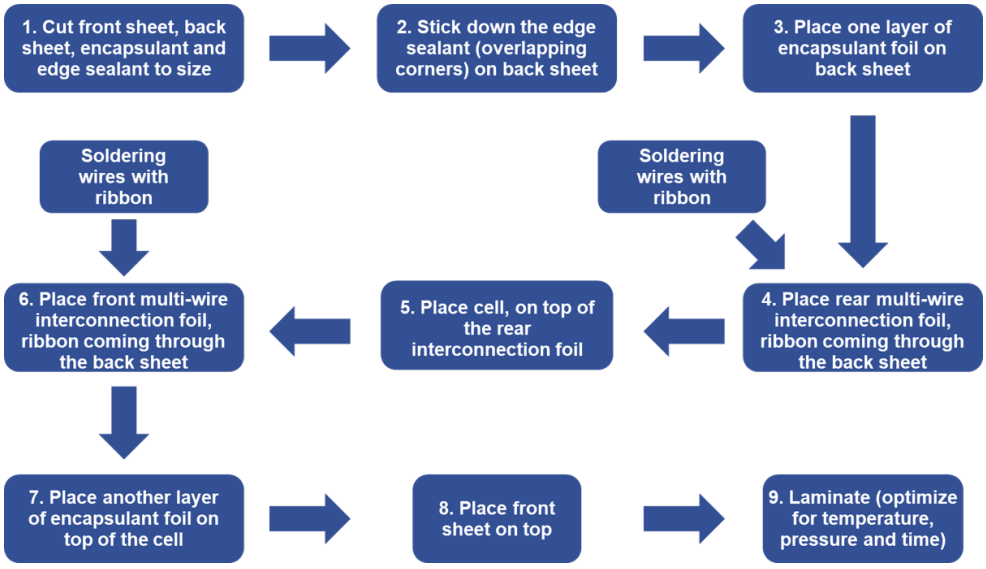


Figure 3.9: Fabrication process of lightweight SHJ single-cell solar modules (optimized design).

The above section is an overall description of the lightweight solar module's structure and fabrication process. The encapsulation material selection and lamination parameters

are critical for the fabrication of the lightweight solar modules. And the lamination parameters are highly dependent on the selected encapsulation materials. The material selection and lamination parameters are presented in the corresponding chapters.

3.2 Accelerated aging test

In order to rapidly identify vulnerabilities and predict the long-term performance of the solar module products, accelerated aging tests are performed before solar modules can be massively applied in the field. Accelerated aging tests are crucial for solar modules as they simulate long-term environmental stressors within a shortened time frame, allowing early detection of potential degradation mechanisms and failure modes. These tests replicate factors such as temperature fluctuations, humidity, UV radiation, and mechanical stress, et al., which collectively influence the lifespan and reliability of solar modules. Accelerated aging tests provide valuable data that informs material selection, manufacturing improvements, and reliability standards.

3.2.1 DH aging test



Figure 3.10: (a) Appearance of the climate chamber, and (b) solar module samples in the climate chamber.

Accelerated DH aging tests were performed at 85 °C and 85% RH in an *ESPEC* climate chamber for a total of 1000 h, following the IEC 61215 protocol [112]. The solar modules in open-circuit condition are exposed to an environment with elevated temperature and high humidity. They were placed vertically in a holder in a climate

chamber, as shown in Figure 3.10. During the accelerated DH aging test, a large amount of water vapor is generated on the surface of the solar module and drives it into the solar module. The primary goal of the DH test is to determine whether solar modules can withstand the penetration of moisture over extended periods. According to IEC 61215 [112], glass solar modules are considered to pass when they display a power loss of less than 5% of the initial output power after 1000 h of DH test.

3.2.2 UV aging test

UV exposure test was performed in a UV chamber supplied by *Opsytec Dr. Groebel GmbH*, Germany, equipped with mercury (Hg) light tubes manufactured by *Sankyo Denki Co., Ltd.* Figure 3.11(a) shows the solar module samples in the UV chamber, (b) shows the spectrum of the UVA lamp with a peak at a wavelength of 353 nm, along with the AM1.5G [189, 190] solar spectrum in the UV-related range. The accumulated UV intensity is approximately 56 W/m^2 integrated from 300 to 400 nm. The cumulative UV radiation dose is 120 kWh/m^2. After each 15 kWh/m^2, the solar module samples will be taken out of the chamber for characterization. The temperature of the plate was not controlled, but was monitored by a type K Class 1 thermocouple, which was around 25 °C during the UV exposure. All the solar module samples were in an open-circuit condition during the UV exposure.

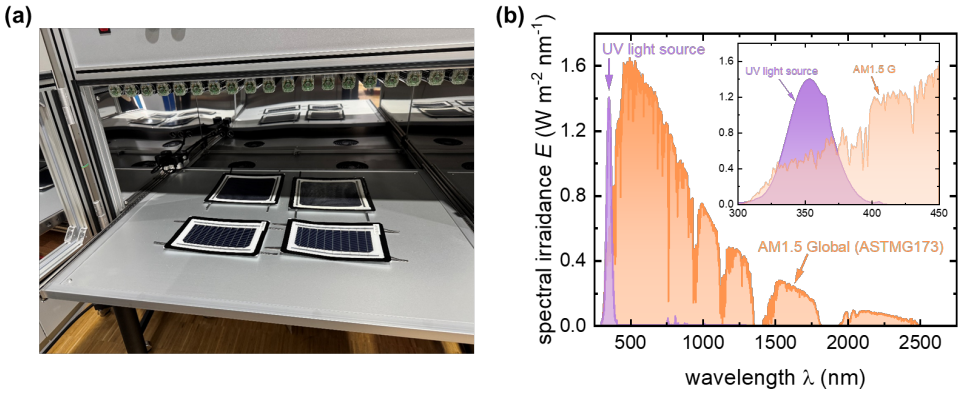


Figure 3.11: (a) Solar module samples in the UV chamber; (b) Spectrum of UV light source and sun spectrum at AM1.5G.

According to data from the Deutsche Wetterdienst (DWD) [191], the annual global irradiation in Aachen, Germany, was approximately 1050 kWh/m^2, (1991-2020). In general, an average UV fraction of 4 - 5% of the global irradiation is considered a reasonable assumption for locations without direct UV monitoring [183]. While the local climate

tends to be relatively stable from year to year, significant differences can occur between regions or climatic zones. Based on this value, the corresponding annual UV radiation dose in the Jülich area, located about 27 km from Aachen, can be estimated at roughly 47.25 kWh/m². In our UV exposure test, the total UV radiation dose was 120 kWh/m², which corresponds to approximately 30 months of field exposure.

3.3 Characterization

This section introduces the characterization methods used for solar cells, solar modules, and polymer encapsulation materials.

3.3.1 Optical properties

Spectrophotometry The total spectral transmittance (T) and reflectance (R) of encapsulation foils were measured from 300 nm to 1200 nm in 5 nm steps using a calibrated Ultraviolet-Visible-Near infrared spectroscopy (UV-Vis-NIR)(*Perkin Elmer, LAMBDA 950*). The system is equipped with a dual light source comprising both deuterium and halogen, as well as a 150 mm-diameter integrating sphere with a 0°/8° port configuration to include scattered light. The two detectors of the system, a photomultiplier tube and an InGaAs detector, enable measurements in the wavelength range of 250 - 2500 nm. The samples are always oriented with the film side facing the incident probing light. For the transmittance measurement, the sample is positioned at the optical entrance of the sphere. For the reflectance measurement, it is positioned on the opposite side of the optical entrance. The total absorptance (A) is calculated by

$$A = 1 - T - R. \tag{3.1}$$

However, the UV-Vis-NIR spectrometer used in this study cannot directly detect the downshifting effect, as it operates with a monochromator and a wavelength-selective intensity sensor. This limitation can lead to inaccurate results due to the varying sensitivities of the sensor across different wavelengths.

Adapted optical setup To evaluate the downshifting effect of the encapsulant, an in-house-built adapted setup was developed. Unlike conventional UV/Vis spectrometers, which use a monochromator to scan through individual wavelengths, this setup employs a broadband light source to illuminate the sample with a continuous spectrum spanning the UV and visible ranges. Although this broadband source extends through the UV–visible

range, its emitted spectral intensity is not perfectly flat. To address this, we record a reference spectrum both before and after the sample measurement. By comparing the measured spectrum against these reference spectra, we can correct for any source-intensity fluctuations and thus obtain a more accurate transmission spectrum.

As shown in Figure 3.12, a broadband light source is shaped by an aperture and a focusing lens to form a small, well-defined spot with appropriate intensity. A fold mirror redirects the conditioned beam onto the sample, minimizing path length and easing alignment. The light then interacts with the encapsulant sample, where the visible light is transmitted, and part of the UV light is shifted to longer wavelengths due to downshifting effects. Both the transmitted and emitted light from the sample are collected and directly into a spectrally resolved spectrometer. This allows the entire spectrum to be recorded simultaneously, enabling both the transmittance and the downshifted emission to be captured in a single measurement.

This approach provides a fast and comprehensive characterization of the sample's optical properties, particularly its ability to shift UV light into visible light.

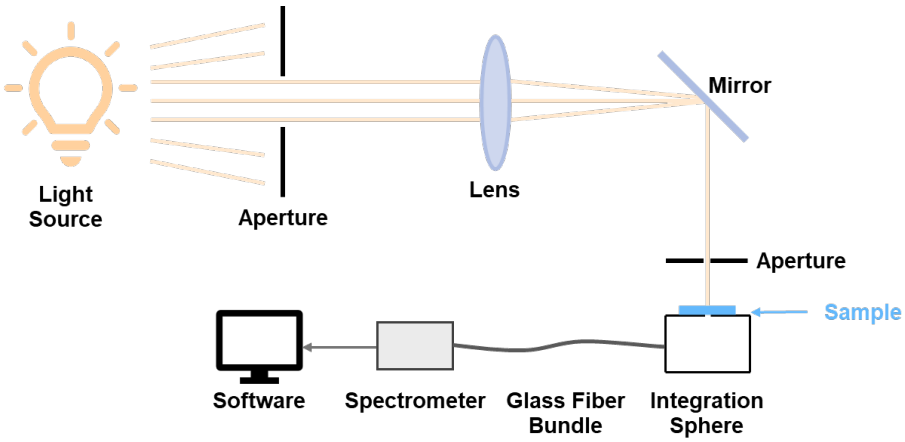


Figure 3.12: Schematic mechanism of the adapted optical measurement setup.

Sample preparation To characterize the optical properties of the unweathered polymer encapsulant foils, foil samples were prepared by placing the encapsulant foil between two sheets of non-stick Teflon® foil and then laminating it in a laminator using the same parameters as those for corresponding solar module fabrication. Teflon foils were removed after lamination as shown in Figure 3.13. Then, the laminated plain foil was used to measure transmittance and reflectance.



Figure 3.13: (a) Encapsulant foil laminated with two Teflon foils; (b) Remove the Teflon foils after lamination.

3.3.2 Electrical properties

Hall effect measurement Hall effect measurements play an important role in the characterization of semiconductor materials [192–194]. By analyzing both the Hall voltage and the resistivity, essential electrical properties such as the conductivity type, carrier concentration, and carrier mobility can be determined. These parameters are vital for understanding and optimizing the performance of semiconductor devices. The Hall effect is fundamentally based on the Lorentz force, which arises from the combined action of electric and magnetic forces on charge carriers. A more detailed explanation of the Hall effect can be found in references [192, 194]. To extract key electrical properties of the semiconductor, including resistivity (ρ), carrier mobility (μ), and carrier concentration (n), the van der Pauw technique is employed [195]. This technique combines resistivity and Hall measurements conducted at room temperature. The glass substrates with thin semiconductor films were cut into squares measuring 1.2 × 1.2 cm^2. Electrical contacts were made by placing sharp metal needles at the four edges of each sample. A detailed, step-by-step description of the measurement procedure is provided in references [192–194].

3.3.3 Optoelectronic properties

Current density-Voltage (*J-V*) characteristics The J-V characteristics of the solar cells/modules were measured at standard test conditions (AM1.5G, 1000 W/m^2, 25 °C) using a LOANA solar cell analysis system from *PV-Tools GmbH* equipped with Wavelabs Sinus 220 light sources. To describe a solar cell's J-V behavior, a two-diode model [196–198] is introduced, and the equivalent circuit is shown in Figure 3.14(b). The model treats the superposition of the collected photocurrent and the injected junction current at a voltage as a constant current source in parallel with two ideal diodes. The first diode captures the 'ideal' Shockley diffusion current and is characterized by the saturation current density J_{01} and an ideality factor n_1, which reflects recombination in the base, emitter, and as well as their surfaces [197, 199]. The second, 'recombination' diode accounts for recombination in the depletion region, device edges, or localized high-defect areas; it is described by a saturation current density J_{02} and an ideality factor n_2 [196,

198, 200–203]. A shunt resistance R_{sh} represents parasitic leakage currents proportional to voltage, while a series resistance R_s lumps ohmic (Joule) losses. The resulting current density J is given by

$$J(V) = J_{ph} - J_{01} \cdot [\exp(\frac{q(V + JR_s)}{n_1 kT}) - 1] - J_{02} \cdot [\exp(\frac{q(V + JR_s)}{n_2 kT}) - 1] - \frac{V + JR_s}{R_{sh}}. \quad (3.2)$$

Where n_1 and n_2 are the ideality factors of diodes 1 and 2, J_0 denotes the corresponding recombination current densities, k is the Boltzmann constant, T is the temperature in Kelvin, q is the elementary charge, and J_{ph} is the photo-current density.

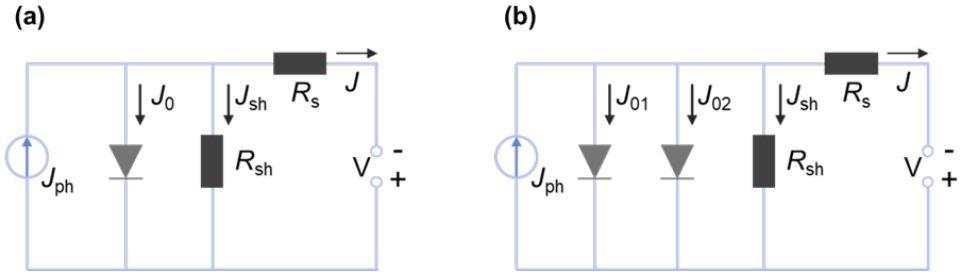


Figure 3.14: The equivalent circuit diagram of the (a) one-diode model, and (b) two-diode model, including the series resistance (R_s) and the shunt resistance (R_{sh}).

The setup performs three kinds of J-V measurements, including JV-dark, JV-light, and JV-$J_{sc}V_{oc}$. The breakthrough behavior in reverse mode and the shunt resistance in dark conditions can be determined by JV-dark measurements. The JV-light is a JV sweep under the illumination of 1 sun, from which we can obtain the V_{oc} at V (J = 0 mA/cm^2), the J_{sc} at J ($V = 0$ V), and the V_{mpp} as well as the J_{mpp}. The η of the solar cell/module is defined by

$$\eta = \frac{P_{mpp}}{P_{sun}} = \frac{J_{mpp}V_{mpp}}{P_{sun}} = \frac{J_{sc}V_{oc}FF}{P_{sun}}. \quad (3.3)$$

Where the P_{mpp} is the power density at maximum power point, the P_{sun} is the input power density of the sun simulator (100 mW/cm^2), and the FF is the fill factor defined by

$$FF = \frac{J_{mpp}V_{mpp}}{J_{sc}V_{oc}}. \quad (3.4)$$

The JV-$J_{sc}V_{oc}$ characteristics are determined under various illumination intensities using two separate sweeps, one at short-circuit and the other at open-circuit conditions. The first measure just measures the J_{sc} as a function of intensity, which is varied. The second

sweep also measures V_{oc} based on intensity. As the R_s has a negligible effect on both V_{oc} and J_{sc} when $R_s < 10\ \Omega/cm^2$, an almost R_s-free JV-sweep can be obtained by combining the intensity-dependent data from both sweeps, allowing for the extraction of the pseudo fill factor (pFF). For simplicity, the extraction of pFF is modeled using a one-diode model (Figure 3.14(a)).

In the one-diode model with R_s and R_{sh}, as shown in

$$J = J_{ph} - J_0 \cdot [\exp(\frac{q(V + JR_s)}{nkT}) - 1] - \frac{V + JR_s}{R_{sh}}. \tag{3.5}$$

Under open-circuit conditions: $J = 0$

thus,

$$0 = J_{ph} - J_0 \cdot [\exp(\frac{q\,V_{oc}}{nkT}) - 1] - \frac{V_{oc}}{R_{sh}}. \tag{3.6}$$

Multiple sets of (V_{oc}, J_{ph}) are obtained at different light intensities (different J_{ph}).

When R_{sh} is sufficiently large,

$$V_{oc} \approx \frac{nkT}{q} \ln(\frac{J_{ph}}{J_0} + 1). \tag{3.7}$$

The n and J_0 is obtained from Equation 3.7

The pseudo J-V curve is obtained using

$$J_{pseudo}(V) = J_{ph} - J_0[\exp(\frac{qV}{nkT}) - 1] - \frac{V}{R_{sh}}. \tag{3.8}$$

The R_s is not included in Equation 3.8. Therefore, the resulting FF does not contain series resistance losses, and this FF is defined as pFF. A detailed description of the underlying principle and experimental setup can be found in Ref.[204].

The detremination of R_s from JV-light and JV-$J_{sc}\,V_{oc}$ is defined by

$$Rs_{FF\text{-}pFF} = (1 - \frac{FF}{pFF}) \cdot \frac{V_{oc}}{J_{sc}}. \tag{3.9}$$

Dark J-V measurements were conducted to gain insights into the diode characteristics, shunt resistance R_{sh}, and potential breakdown mechanisms. The dark J-V curve eliminates any influence from the photogenerated current.

Moreover, light J-V measurements were performed at multiple illumination intensities (1-sun, 0.6-sun, 0.8-sun, and 1.2-sun) to evaluate the R_{s} of the solar module [205]. This R_{s} was employed as an indicator for evaluating series resistive losses in solar modules in this study.

Table 3.1 summarizes the main characteristic values of the solar cell/module by each J-V measurement.

Table 3.1: The main characteristic values of the solar cell/module measured by each J-V measurement.

Measurements	**Characteristic values**
JV-dark	Break through behavior, R_{sh}
JV-light	Efficiency, J_{sc}, V_{oc}, FF, J_{mpp}, V_{mpp}
JV-$J_{\mathrm{sc}}V_{\mathrm{oc}}$	pFF, R_{s}, R_{sh}
JV-multiple light	R_{s}

Electroluminescence (EL) imaging EL imaging is a valuable tool for fast and spatial characterization of c-Si solar cells and modules [206–217]. The technique can be used to survey entire solar modules, but also to visualize microscopic defects on the micrometer scale. The emission of light by application of an electrical bias is just the complementary reciprocal action of the photovoltaic effect taking place in solar cells/modules. Therefore, all important physical processes that influence the photovoltaic performance of a solar cell - such as recombination, resistive, and optical losses - are, in a complementary way, reflected in the EL of the same device.

According to the reciprocity theorem, the EL intensity ϕ_{em} of a p-n junction solar cell emitted at any position $\mathbf{r}$ = (x,y) of the solar-cell surface is given by

$$\begin{aligned}\phi_{\mathrm{em}}(E,\mathbf{r}) &= [1-R(E,\mathbf{r})]\,Q_{\mathrm{i}}(E,\mathbf{r})\phi_{\mathrm{bb}}(E)\exp(\frac{qV(\mathbf{r})}{kT}) \\ &= Q_{\mathrm{e}}(E,\mathbf{r})\phi_{\mathrm{bb}}(E)\exp(\frac{qV(\mathbf{r})}{kT}).\end{aligned} \tag{3.10}$$

Where kT/q is the thermal voltage, V($\mathbf{r}$) is the internal junction voltage, E is the photon energy, and $Q_{\mathrm{e}}(\mathbf{r})$ = [1 - $R(\mathbf{r})$]$Q_{\mathrm{i}}(\mathbf{r})$ is the local external quantum efficiency (QE) determiined by the front surface reflectance $R(\mathbf{r})$ and the internal QE $Q_{\mathrm{i}}(\mathbf{r})$. The spectral photon density ϕ_{bb} of a black body is given by

$$\phi_{\mathrm{bb}}(E) = \frac{2\pi E^2/(h^3c^2)}{\exp(E/kT) - 1}. \tag{3.11}$$

ϕ_{bb} depends on Plank's constant h and the vacuum speed c of light. The EL emission of a solar cell is recorded with a charge-coupled device (CCD) camera; the EL signal $S_{\mathrm{cam}}(E, \mathbf{r})$ in each camera pixel is given by

$$S_{\mathrm{cam}}(\mathbf{r}) = \int Q_{\mathrm{cam}}(E) Q_{\mathrm{e}}(E, \mathbf{r}) \phi_{\mathrm{bb}}(E) dE \ \exp(\frac{qV(\mathbf{r})}{kT}). \tag{3.12}$$

Where Q_{cam} is the energy-dependent sensitivity of the detecting camera. Since in Equation 3.12, $\phi_{\mathrm{bb}}(E)$ and $Q_{\mathrm{cam}}(E)$ depend on energy but not on the surface position $\mathbf{r}$, lateral variations in the detected EL intensity emitted from different surface positions originate only from the lateral variations of the external QE Q_{e} and of the internal voltage V. Therefore, Equation 3.10 and Equation 3.12 consider all losses occurring in solar cells: the external QE Q_{e} expresses the recombination and optical losses, while the internal voltage V reflects the resistive losses. In some cases, the exponential voltage-dependent term dominates the image, making EL analysis a tool that is especially suitable for analyzing resistive losses.

In this work, the EL imaging was performed under two current injection conditions: low and high injection. Three types of solar cells with different dimensions, M2, M2+, and half-cut M2+, were used in this work. The current injection conditions are summarized in Table 3.2 and Table 3.3. Under conditions of forward bias, minority carriers are electrically injected into the solar cell, where they subsequently recombine radiatively with majority carriers, emitting photons within the near-infrared wavelength range (typically 900 - 1400 nm). A silicon charge-coupled device (Si-CCD) camera is utilized to capture this emitted radiation, with the resulting intensity distribution reflecting local variations in carrier concentration, voltage, and recombination rates. The recombination rate is proportional to the pn product, which is largely dependent on the excess minority carrier concentration in the bulk of the solar cell [206]. This, in turn, depends on the local voltage, as well as on the rate of recombination due to defects in the bulk and at the surface. Consequently, EL imaging can reveal various defects, including solar cell cracks, corrosion, and contact failures. Additionally, by comparing EL images taken at different current injection conditions, the R_{s} of the device can be extracted and scaled to absolute values; the method is shown in Ref.[218]. However, it should be noted that the interpretation of EL images alone has the potential to conflate issues of material quality and electrical connectivity.

Table 3.2: Current injection conditions for EL imaging of solar modules using M2 or M2+ solar cells.

Current injection condition	Current	Exposure time	Current density M2 (244.32 cm²)	Current density M2+ (246.21 cm²)
High injection	8 A	5 s	32.74 mA/cm²	32.49 mA/cm²
Low injection	0.5 A	0.1 s	2.05 mA/cm²	2.03 mA/cm²

Table 3.3: Current injection conditions for EL imaging of solar modules using M2+ half-cut solar cells.

Current injection condition	Current	Exposure time	Current density M2+ half-cut (123.1 cm²)
High injection	4 A	5 s	32.49 mA/cm²
Low injection	0.25 A	0.1 s	2.03 mA/cm²

Apart from the methods using EL imaging, a large number of methods have been developed for photoluminescence (PL) as well, which allow similar investigations on solar cells and solar modules [219–222].

Photoluminescence (PL) imaging PL imaging [219–222] is demonstrated to be an extremely fast spatially resolved and non-destructive diagnostic technique to evaluate the quality of the material and detect defects in c-Si solar cells and solar modules. The spatial variation of the effective minority carrier lifetime is measured without being affected by minority carrier trapping in all practical cases [223], or by excess carriers in space charge regions, effects that lead to experimental artifacts in other techniques, such as quasi-steady-state photoconductance [224].

In this work, the PL imaging was performed using an in-house-built setup. Solar modules are illuminated using a 90 W near-infrared laser at 808 nm, which is widened with a beam homogenizer. The laser excites electron-hole pairs within the silicon substrate. The subsequent radiative recombination of these charge carriers results in the emission of photons, which are captured using a near-infrared (NIR) InGaAs camera. Laser light reflected from the sample surface is blocked by a 1050 ± 30 nm band-pass filter located between the sample and the camera, preventing incident laser light from contributing to the measured PL intensity. The key advantage of PL imaging over EL imaging is that it is contactless. It can therefore be applied to silicon wafers at any processing stage, enabling the impact of individual steps on local material properties to be monitored [219]. As it is not dependent on electrical injection, it is also unaffected by series resistance. This

makes it a particularly useful technique for distinguishing between material-related and electrical defects.

By combining qualitative PL and EL imaging methods, a comprehensive understanding of solar cell/module characteristics, degradation mechanisms, and electrical quality can be achieved.

Quantum efficiency (QE) and reflectance (*R*) The spectrally resolved quantum efficiency provides a detailed insight into the optical absorption and the carrier extraction in solar cells/modules as a function of the light wavelength. The *EQE* is defined as the fraction of charge carriers collected by the solar cell per incident photon ϕ_{in}, according to

$$EQE = \frac{J_{\text{sc}}}{q\phi_{\text{in}}}. \tag{3.13}$$

And the *EQE* is determined by measuring the short-circuit current response to illumination with monochromatic light. Assuming a conformal response of the solar cell, the short-circuit current density evaluated from the *EQE* ($J_{\text{sc},EQE}$) is expressed by

$$J_{\text{sc},EQE} = q \int EQE(\lambda)\phi_{\text{AM1.5G}}(\lambda)d\lambda. \tag{3.14}$$

Where $\phi_{\text{AM1.5G}}$ is the photon flux of the AM1.5G spectrum [189, 190]. An integrating sphere with highly reflective and diffuse internal coating was used to measure the reflectance of the solar cell/module. The *IQE* is the ratio between absorbed photons and collected electrons, as shown by

$$IQE = EQE/(1 - R). \tag{3.15}$$

IQE excluding optical loss arising from solar cell/module reflectance. The analysis of the *IQE* provides information about the emitter quality, the diffusion length, and the independent observation of losses within the solar cell. In this work, the LOANA system from *PV-Tools GmbH* was used for the *EQE* and reflectance measurement in a wavelength range of 280 - 1200 nm in steps of 10 nm. The probing spot for both measurements is usually at the size of 12 × 12 mm^2.

3.3.4 Microstructural properties

Scanning electron microscopy (SEM) Scanning electron microscopy (SEM) [225, 226] was employed to investigate the microstructural features of the TCO layers used in the

solar cells before and after the accelerated DH aging test. Surface morphologies were examined using a field-emission scanning electron microscope (*Zeiss Supra 1550 VP*). The instrument was operated at an accelerating voltage of 5 kV with a working distance of 5 - 8 mm to obtain high-resolution secondary electron images of the TCO grain structure, surface roughness, and film continuity.

X-ray computed tomography (XCT) XCT [113, 227] is a non-destructive imaging technique increasingly utilized in the analysis of solar modules to assess internal structures and detect manufacturing defects or degradation phenomena. By reconstructing cross-sectional and three-dimensional images from X-ray projections, XCT allows for high-resolution visualization of internal layers, interfaces, and components within the solar module. This technique is particularly valuable for identifying voids, delamination, cracks, corrosion, and solder joint failures within solar modules that may not be visible through conventional optical inspection. XCT also facilitates the evaluation of the adhesion property of the encapsulant, mechanical integrity changes resulting from environmental stress testing. Unlike destructive cross-sectioning, XCT preserves the sample while providing detailed insights into its internal morphology, making it an essential tool in both quality assurance and failure analysis of solar modules. In this work, XCT images were taken using a *Zeiss Xradia Versa 620*, voxel size is 740 nm, X-ray tube voltage is 100 kV.

3.3.5 Physical properties

Water vapor transmission rate (WVTR) The WVTR is a critical parameter in evaluating the moisture barrier performance of polymer encapsulation materials used in solar modules [73, 228]. Encapsulant foils and other polymeric materials are designed not only to provide mechanical and optical protection but also to limit the ingress of moisture, which can lead to corrosion of metallic contacts, delamination, and degradation of the active layers. WVTR testing quantifies the rate at which water vapor permeates through a material under controlled temperature and humidity conditions, typically expressed in grams per square meter per day ($g/m^2 \cdot day$). Accurate measurement of WVTR is essential for assessing the long-term durability and reliability of encapsulants. Instruments based on gravimetric, coulometric, or infrared sensor methods are commonly used, with test conditions often aligned with industry standards such as ASTM F1249 [229] or ISO 15106 [230]. A low WVTR value is generally desirable, indicating strong moisture resistance and improved potential for long service life of the solar module.

In this work, the WVTR of polymer encapsulation foils used for the encapsulation of solar modules was measured at 38 °C and 90% RH conditions by a *Labthink C301H* device based on infrared sensor methods. It can measure the WVTR down to 0.005 g/m²·day, with a resolution of 0.0001 g/m²·day.

3.3.6 Chemical properties

X-ray photoelectron spectroscopy (XPS) XPS [231, 232] was used to analyze the chemical composition and oxygen-related species (O^{2-} and OH^-) in the TCO layers before and after DH aging. Measurements were carried out on a PHI 5000 VersaProbe II system (*ULVAC-PHI Inc.*, USA) equipped with a monochromatic Al K-α X-ray source ($h\upsilon$ = 1486.6 eV). The X-ray power was set to 50 W at 15 kV with a 200 μm beam spot. Wide-range survey spectra and high-resolution spectra of O 1s and relevant cation core levels (e.g., Sn 3d, In 3d, Zn 2p) were recorded under ultra-high vacuum conditions. The binding-energy scale was calibrated by setting the adventitious carbon C 1s peak to 284.8 eV. High-resolution O 1s spectra were deconvoluted into components corresponding to lattice oxygen (O^{2-}) and surface hydroxyl/chemisorbed species (OH^-/H_2O) using a Shirley background and mixed Gaussian-Lorentzian peak shapes.

Differential scanning calorimetry (DSC) DSC [233] is employed to characterize the thermal behavior of the encapsulant materials used in the solar modules. In this technique, the sample and an inert reference are subjected to an identical, controlled heating program while the instrument records the difference in heat flow between them. Our measurements were carried out using a *NETZSCH DSC 204 F1 PHOENIX*. The heat flow versus temperature curves were measured in a temperature range of -40 °C to 220 °C with a heating rate of 10 K/min, under nitrogen flow with a rate of 40 mL/min to minimize oxidative effects, followed by cooling to room temperature and, when required, a second heating cycle. The encapsulant film samples were prepared using a 5-mm punch with sample masses of 6 - 8 mg, weighed with a *METTLER TOLEDO XS205DU* (resolution of 0.01 mg and repeatability of 0.02 mg). The measurements were performed in 25-μL aluminum crucibles, with an empty crucible used as the reference. The resulting thermograms provided quantitative information on transition temperatures and enthalpic changes, enabling the identification of glass transition, melting, and curing-related exothermic events. These parameters are crucial for evaluating thermal stability, crystallinity, degree of crosslinking, and processing windows, thereby assessing the suitability of the encapsulant for solar module lamination and long-term performance.

Raman spectroscopy Raman spectroscopy [234] is a fast and non-destructive measurement. Raman spectroscopy is a vibrational spectroscopic technique based on the Raman effect, which was first reported by Raman in 1928 [235]. If the incident photon imparts energy to the lattice in the form of a phonon (phonon emission), it emerges as a lower-energy photon. This down-converted frequency shift is known as Stokes-shifted scattering. Raman spectroscopy is based on inelastic scattering of monochromatic light (usually from a laser). When this light interacts with molecular vibrations or phonons in a material, a small fraction of the light shifts in energy. This Raman shift reveals a molecular 'fingerprint' unique to each substance. During Raman spectroscopy measurements, the sample is illuminated by an intense monochromatic light source. The weak scattered light or signal is passed through a double monochromator, and the Raman-shifted wavelengths are detected by a photodetector. Raman spectroscopy is reported as a powerful tool for analyzing the degradation behavior of polymer encapsulants in solar modules [236].

In this work, the encapsulants extracted from aged solar modules after DH or UV weathering, as well as the encapsulants extracted from non-aged reference solar modules, were analyzed by Raman spectroscopy. Raman spectra of the polymer encapsulant foils were performed from 0 - 4000 cm^{-1} using an *inVia confocal Raman* microscope with 10 mW power, 50X magnification, 532 nm excitation laser source, and 10 s of exposure time.

Fourier-transform infrared spectroscopy (FTIR) FTIR [69] is a widely employed analytical technique for characterizing the chemical structure and composition of materials, making it particularly valuable in the study of solar module encapsulants. FTIR spectroscopy enables the identification of key functional groups within these polymers and provides insight into chemical changes due to aging, degradation, or crosslinking reactions. By analyzing the infrared absorption spectra, it is possible to monitor oxidation (e.g., formation of carbonyl groups), hydrolysis, or additive loss over time. This makes FTIR an essential tool in evaluating the long-term reliability and durability of encapsulant materials under accelerated aging or real-world exposure conditions. Its non-destructive nature, rapid measurement, and sensitivity to polar functional groups make FTIR particularly well-suited for quality control and degradation studies in solar module encapsulation research [23, 69].

In this work, changes in the chemical structure of the encapsulants in both aged solar modules exposed to DH or UV weathering, as well as in non-aged reference solar modules, were characterized by FTIR spectroscopy (*Thermo Fisher Scientific*) in attenuated total reflectance (ATR) mode (FTIR-ATR), with a spectral resolution of 4 cm^{-1} and 16 accumulated scans.

Pyrolysis-Gas Chromatography-Mass spectrometry (PY-GC-MS) PY-GC-MS is a powerful analytical technique used to characterize complex organic materials by breaking them down into smaller, volatile components through thermal decomposition [237, 238]. In this method, a sample is rapidly heated in the absence of oxygen, causing it to undergo pyrolysis, which fragments the material into simpler molecules. These pyrolysis products are then introduced into a gas chromatograph, where they are separated based on their volatility and interaction with the chromatographic column. Subsequently, the separated compounds are identified and quantified using mass spectrometry, which provides detailed information on their molecular structure and composition. PY-GC-MS is especially valuable for analyzing polymers, coatings, composites, and other materials where direct chemical characterization is challenging due to their high molecular weight or insolubility. The technique enables a detailed understanding of material composition, thermal stability, and degradation pathways, making it widely applicable in materials science, forensic analysis, environmental studies, and polymer research [239].

The analysis was conducted using a coupled EGA/Py-3030D pyrolysis furnace equipped with an AS-1020E autosampler (*Frontier Laboratories Ltd.*), integrated with a Trace 1300 gas chromatograph (*Frontier Laboratories Ltd.*) and an ISQ 7000 mass spectrometer (*Thermo Scientific*). In line with the operational principle of PY-GC-MS, the procedure consisted of sequential thermal desorption steps to release volatile and semi-volatile components, followed by gas chromatographic separation and mass spectrometric identification.

A two-step thermal desorption was performed before pyrolysis, employing helium (He) as the carrier gas at a constant flow rate. In the first step, samples were held at 100 °C for 3 min to remove the most volatile species, and the resulting products were analyzed via GC-MS. In the second step, the temperature was ramped from 100 °C at 30 °C/min to 300 °C to release less volatile compounds. The subsequent pyrolysis step, set at 600 °C for 0.2 min, was applied primarily to flush the column and remove residual materials. For each desorption stage, the interface temperature between the pyrolyzer and the GC inlet was maintained 100 °C above the corresponding desorption temperature to ensure complete transfer of analytes.

To prevent contamination of the GC column by undesired decomposition fragments, a selective sampler (SS-1010E, *Frontier Laboratories Ltd.*) was used. Furthermore, a cryotrap MJT-1035E can be used, allowing a more precise separation of volatile components in the column.

Following desorption, the extracted compounds were separated in the gas chromatograph according to molecular mass and polarity (column interaction). A cold trap (liquid nitrogen) can initially enable a simultaneous flow of molecules. The desorbed molecules

then reach the mass spectrometer sequentially. Here, the eluted components are analyzed according to their mass/charge (m/z) ratio to enable molecular identification.

The separated analytes were introduced into the GC system fitted with an Ultra Alloy Capillary Column (30 m length, 0.25 mm internal diameter, 25 μm film thickness; *Frontier Laboratories Ltd.*), with helium as the carrier gas. Multiple thermal desorption (TD) steps were applied to determine the eluted components. For the first desorption step, the GC inlet was maintained at 280 °C, the column flow at 1.2 mL/min, purge flow at 5 mL/min, and split flow at 25 mL/min. The oven temperature was programmed from 40 °C (1 min hold) at 10 °C/min to 325 °C with a subsequent plateau time of 20 min. In the second desorption step, the GC inlet was maintained at 280 °C, the column flow at 1.2 mL/min, purge flow at 5 mL/min, and split flow at 25 mL/min. The oven temperature was programmed from 40 °C (1 min hold) at 10 °C/min to 325 °C with a subsequent plateau time of 20 min. For the pyrolysis step, the GC inlet was maintained at 280 °C, the column flow at 1.2 mL/min, purge flow at 3 mL/min, and split flow at 50 mL/min. The oven temperature was programmed from 40 °C (2 min hold) at 20 °C/min to 320 °C with a subsequent plateau time of 14 min.

Mass spectrometric (MS) detection was carried out using an ISQ 7000 system operating in electron ionization mode (70 eV), with an initial detector gain of 3×10^5, scanning an m/z range from 29 to 800. FC43 ($C_{12}F_{27}N$) was used as the internal tuning substance, with the $m/z = 219$ peak adjusted to an intensity of 2×10^7 for normalization. The detector gain during measurements ranged between 1.8×10^5 and 2.8×10^5, depending on ion source conditions. The MS transfer line temperature and ion source temperature were set at 320 °C and 300 °C, respectively. Compound identification was performed by matching acquired spectra against the National Institute of Standards and Technology (NIST) mass spectral library.

4 Insights into DHID of lightweight SHJ solar modules with different TCOs

TCOs are a critical component for SHJ solar cells; however, they are typically vulnerable to degradation caused by moisture ingress, necessitating improved encapsulation techniques to ensure the long-term stability of SHJ solar modules. In this chapter, we investigate the DH stability of lightweight SHJ solar modules incorporating different TCOs, including ITO and AZO, and compare their performance with that of conventional glass-glass solar modules (see Section 4.1). Subsequently, the underlying mechanism of DHID in SHJ cells with various TCOs is examined in detail in Section 4.2. To enhance the DH resistance of AZO-incorporated SHJ solar cells and lightweight solar modules, a capping layer strategy is proposed. The effectiveness of this capping layer in mitigating DHID is discussed in Section 4.3. Furthermore, the influence of interconnection foils on DHID behavior in lightweight solar modules with different TCOs is analyzed in Section 4.4.

4.1 DH stability of lightweight and glass SHJ solar modules with different TCOs

4.1.1 Preparation of tested solar module samples

The solar cells used for the fabrication of solar modules

Figure 4.1 illustrates the structures of the SHJ cells incorporating different TCO layers, ITO, and AZO, which were used for subsequent solar module fabrication. In the first configuration, 70 nm of ITO was applied as both the front and rear TCO layers, while the second configuration employed 70 nm of AZO as both the front and rear TCO layers. The fabrication of these solar cells was carried out based on our established SHJ solar cell baseline process [47]. The parameter optimization of the films and devices regarding

the counterbalance between optical and electrical properties was already reported in our previous work [61].

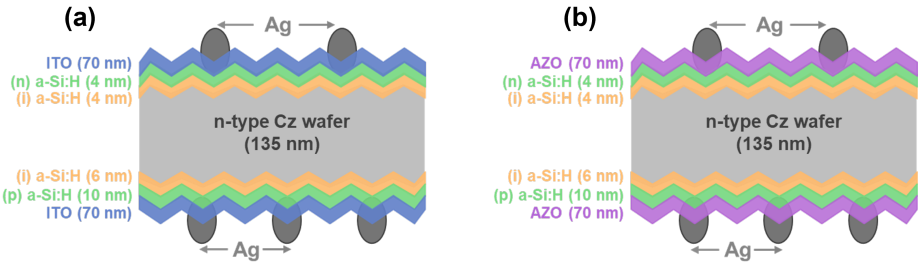


Figure 4.1: Schematic cross-section of SHJ solar cells with different TCO layers: (a) ITO at the front and rear sides and (b) AZO at the front and rear sides.

Fabrication of solar modules

All solar modules were prepared as 200 mm × 200 mm single-cell mini-module samples using M2+ (246.21 cm^2) bifacial monocrystalline busbar-free n-type rear-junction SHJ solar cells with two types of TCO layers (ITO and AZO), as shown in Figure 4.1.

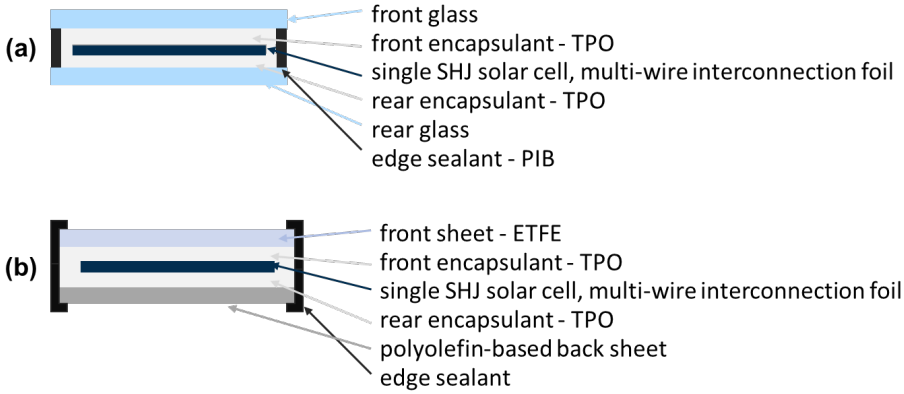


Figure 4.2: Schematic cross-section of the (a) glass/glass SHJ single-cell solar module, (b) front sheet/back sheet SHJ single-cell solar module.

Figure 4.2 shows the schematic cross-section of the single-cell mini modules with two different structures: (a) a glass/glass solar module configuration and (b) a front sheet/back sheet solar module configuration. In terms of solar module encapsulation, 3.2 mm white glass was used as the front cover material for the glass/glass solar module, and ETFE was used as the front cover material for the front sheet/back sheet lightweight solar module. The solar cell is embedded between the front and rear encapsulant (TPO). The solar cells

were connected using multi-wire interconnection technology consisting of 18 coated copper wires with polyolefin as the carrier foil (interconnection foil - first version, denoted as IF1 in the following). Sn-Pb-coated copper ribbons (5 mm wide, 0.2 mm thick) were used as connectors. 3.2 mm glass was also used as the back sheet for the glass/glass solar module. A polyolefin-based foil with a fluorine-free coating was used as the back sheet (hereafter referred to as Px-bs) for the front sheet/back sheet lightweight solar module. The solar module fabrication process is illustrated in Figure 3.4 for the front sheet/back sheet solar module and in Figure 3.9 for the glass/glass solar module, while Table 4.1 summarizes the configurations of SHJ single-cell solar modules with different module structures.

Table 4.1: Configurations of SHJ single-cell solar modules with different solar module structures.

Module No.	Front sheet	Encapsulant (front/rear)	TCO	Interconnection	Back sheet
4.1	ETFE	TPO	ITO	IF1	Px-bs
4.2	ETFE	TPO	AZO	IF1	Px-bs
4.3	Glass	TPO	ITO	IF1	Glass
4.4	Glass	TPO	AZO	IF1	Glass

After solar module fabrication, the optoelectronic properties of the solar modules are characterized, including I-V characteristics and EL imaging. The solar modules are then subjected to an accelerated DH aging test in a climate chamber. Performance assessments are conducted at regular intervals, every 200 h, and at the final stage after 1000 h of DH exposure.

4.1.2 DH test results

Figure 4.3 shows the time evolution of the degradation of the I-V characteristics of the SHJ solar modules with different TCO films in different solar module configurations at fixed time intervals during the DH test. Each value was normalized to its initial value (before the DH test). Both ITO- and AZO-incorporated glass/glass solar modules exhibit stable performance after 1000 h of DH test, with less than 5% relative efficiency degradation. Among them, the ITO-incorporated glass/glass solar module demonstrates superior stability, showing almost no decline in efficiency. In contrast, the front sheet/back sheet lightweight solar modules display reduced stability under DH conditions compared to their glass/glass counterparts. Notably, the AZO-incorporated front sheet/back sheet solar module experiences significant degradation, with a 58.57%$_{\mathrm{rel}}$ reduction in efficiency after 1000 h of DH exposure. This deterioration is primarily attributed to losses in FF,

which decreased by 44.24%$_{rel}$, and J_{sc}, which declined by 23.47%$_{rel}$. The reduction in *FF* is mainly caused by a pronounced increase in R_s [142]. Noteably, the ITO-incorporated front sheet/back sheet solar module also shows some degradation in efficiency after 1000 h of DH test. However, the extent of degradation is much lower than that of the AZO-incorporated counterpart. This loss is mainly attributed to the *FF* due to the increase in R_s.

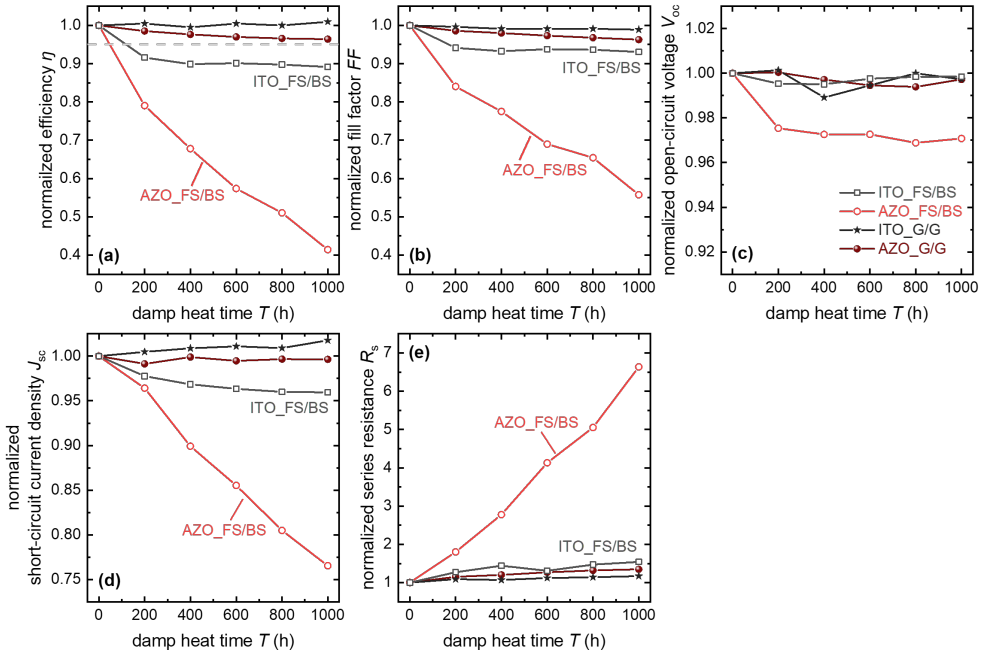


Figure 4.3: Normalized values of (a) efficiency (η), (b) fill factor (*FF*), (c) open-circuit voltage (V_{oc}), (d) short-circuit current density (J_{sc}), and (e) series resistance (R_s) as a function of damp-heat exposure time for ITO- and AZO-incorporated SHJ solar modules in front sheet/back sheet (FS/BS) or glass/glass (G/G) configurations.

As shown in the EL images in Figure 4.4, a pronounced defect appeared in the AZO-incorporated front sheet/back sheet solar module after 1000 h of the DH test. The defect observed in the AZO-incorporated lightweight solar module is most likely attributable to moisture penetration, which leads to corrosion of the AZO films. In contrast, no such defect was found in the AZO-incorporated glass/glass solar module, indicating that the glass/glass configuration provides superior protection against moisture ingress compared to the front sheet/back sheet configuration. Importantly, such defects were not observed in any of the ITO-incorporated solar modules, including those with a front sheet/back sheet structure, suggesting that ITO exhibits greater resistance to moisture than AZO. A more detailed analysis of this phenomenon is presented in Subsection 4.3.2.

Based on the above analyses, it can be concluded that AZO-incorporated SHJ solar

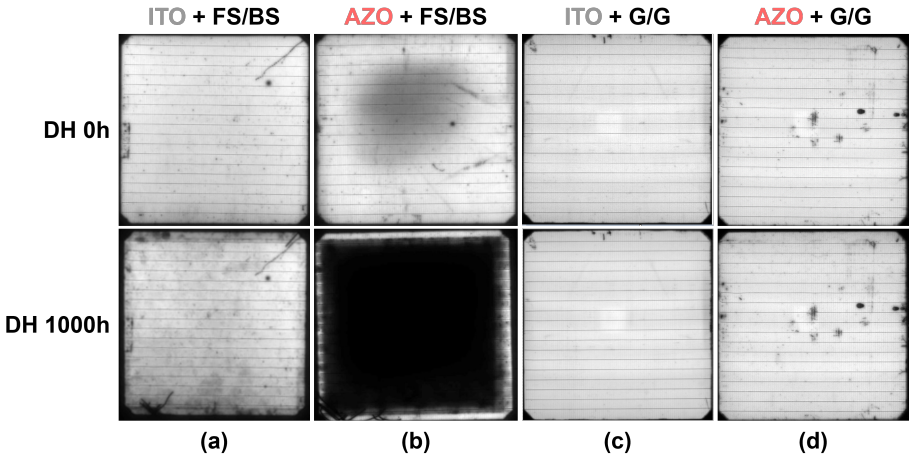


Figure 4.4: EL images under low current injection ($J = 2.03$ mA/cm^2) of SHJ solar modules with ITO and AZO layer in different configurations: (a) ITO-incorporated SHJ solar module with front sheet/back sheet (FS/BS), (b) AZO-incorporated SHJ solar module with front sheet/back sheet (FS/BS), (c) ITO-incorporated SHJ solar module with glass/glass (G/G), and (d) AZO-incorporated SHJ solar module with glass/glass (G/G), taken before and after 1000 h of the DH test.

modules are more susceptible to DHID compared to their ITO-incorporated counterparts. Therefore, in the following section, we will conduct an in-depth investigation into the degradation mechanisms affecting AZO-incorporated SHJ solar cells under damp heat conditions.

4.2 DHID mechanism of SHJ solar cells with different TCOs

4.2.1 Optoelectronic properties of SHJ solar cells

To know the DH stability of non-encapsulated SHJ solar cells, independent of the influence of encapsulants. The bare SHJ solar cells were exposed to the same DH conditions as the solar modules. Figure 4.5 shows the time evolution of the normalized I-V characteristic of SHJ cells incorporating different TCO films, measured at fixed intervals of 200 h during the DH test. Each parameter was normalized to its initial value (before the DH test). After 1000 h of DH test, the bare AZO-incorporated SHJ solar cell exhibited a 16.38%$_{\text{rel}}$ decrease in efficiency, primarily due to a 9.84%$_{\text{rel}}$ loss in FF. This FF degradation is mainly attributed to a substantial increase in R_{s}. In contrast, the ITO-incorporated SHJ solar

cell showed only a $2.80\%_{\mathrm{rel}}$ reduction in efficiency over the same period. A pronounced increase in R_{s} for AZO-incorporated SHJ solar cell is evident in the I-V curve shown in Figure 4.6. This increase in R_{s} has been previously reported to result from a rise in the resistivity (ρ) of the AZO electrode, which is attributed to moisture-induced corrosion [17]. A microstructure analysis of solar cells' surface will be presented in the following sections.

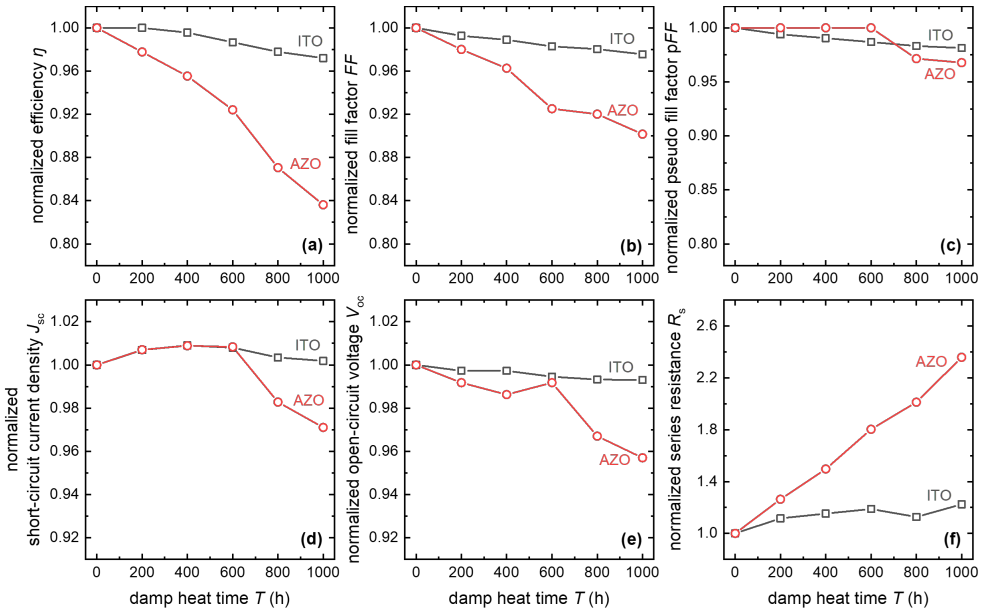


Figure 4.5: Normalized values of (a) efficiency (η), (b) fill factor (FF), (c) open-circuit voltage (V_{oc}), (d) short-circuit current density (J_{sc}), and (e) series resistance (R_{s}) as a function of damp-heat time for SHJ solar cells with different TCOs.

Figure 4.7 shows the evolution of EL images for SHJ solar cells with ITO and AZO TCO layers during the DH test. Pronounced EL defects were observed in the AZO-incorporated SHJ solar cell. The defect outlined with a white dashed line is presumed to result from sputter-induced damage during the AZO deposition process [61]. In addition, the overall reduction in EL intensity is likely attributed to an increase in the resistivity of the AZO films [17]. In the following section, the changes in the electrical properties of the standalone TCO films will be systematically investigated.

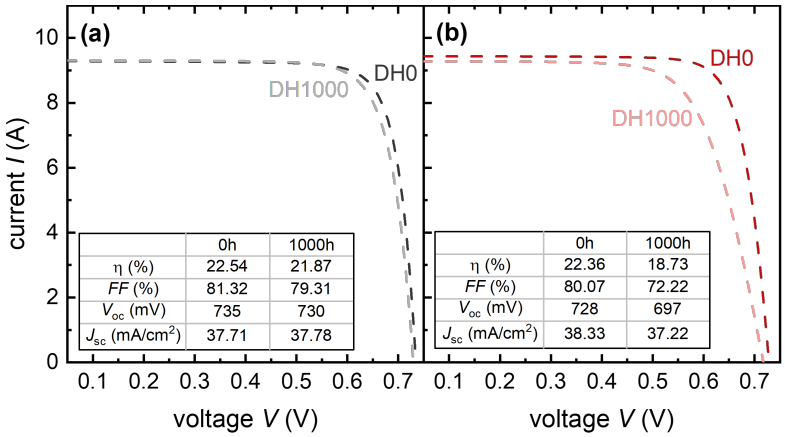


Figure 4.6: *I-V* curves of each solar cell sample: (a) ITO, (b) AZO, before and after 1000 h of the DH test.

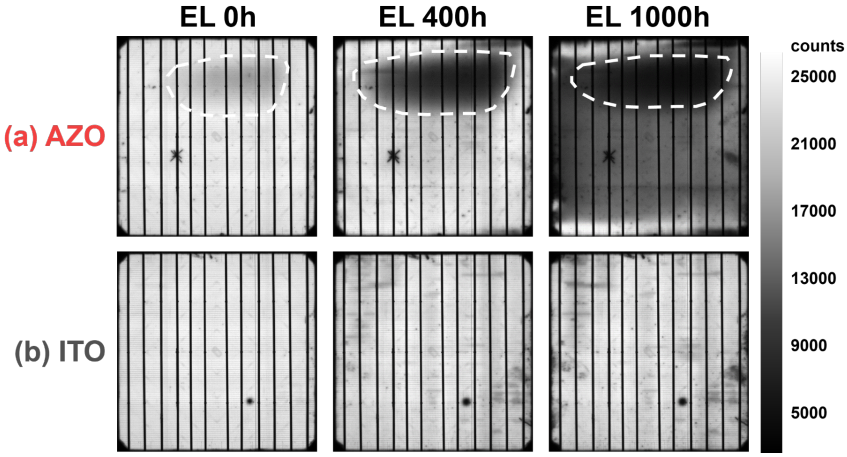


Figure 4.7: EL images under high current injection ($J = 32.49$ mA/cm^2) of the SHJ solar cells with (a) AZO and (b) ITO layers, taken before, after 400 h, and after 1000 h of the DH test.

Figure 4.8 shows SEM images of AZO- and ITO-incorporated SHJ solar cells before and after 1000 h of DH test. Before the DH test, both AZO and ITO films exhibited uniform and dense coverage on the textured pyramidal silicon surface. However, after 1000 h of DH exposure, the AZO film developed visible grooves on its surface, indicating surface degradation. In contrast, the ITO film maintained a uniform and dense structure even after prolonged exposure to DH. Previous studies have reported significant changes in the surface morphology of AZO films following DH exposure, suggesting that water molecules can diffuse into and penetrate the AZO layer [19, 240]. Dhakal et al. [241]

observed surface corrosion on AZO films under high-humidity conditions, where large and small spots appeared across the surface. Elemental analysis of these spots revealed the presence of contaminants such as Ca, Mg, and Si, indicating that these may be water stains formed by moisture condensation during DH exposure. Similarly, the formation of surface dots containing Ca, C has also been reported in [242], potentially originating from distilled water in the climate chamber.

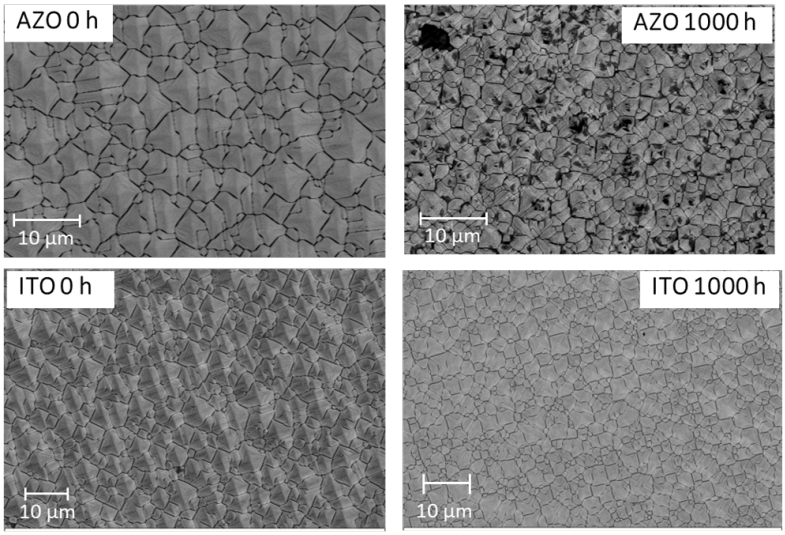


Figure 4.8: SEM images of AZO- and ITO-incorporated SHJ solar cells before and after 1000 h of the DH test.

4.2.2 Electrical properties of TCO films

To better understand the performance degradation observed in SHJ solar cells under damp heat conditions, the electrical properties of standalone TCO films, specifically ITO and AZO, were investigated. Key parameters such as carrier density (n), carrier mobility (μ), and resistivity (ρ) were evaluated before and after DH exposure to assess their stability. Both types of films were deposited on Corning glass substrates using the same sputtering processes employed during solar cell fabrication. These samples were then subjected to the DH test in a climate chamber under identical conditions and duration as the tested solar cells.

Figure 4.9 illustrates the evolution of key electrical parameters - carrier density, mobility, and resistivity - for both AZO and ITO films throughout the DH test. A significant increase in resistivity, along with a marked decrease in both charge carrier density and carrier mobility, was observed in the AZO films after 1000 h of DH exposure.

Water vapor is known to be adsorbed at grain boundaries, which leads to enhanced scattering of carriers and trapping of free carriers, thus reducing carrier concentration and mobility [243]. Adsorbed water could further lead to the capture of free electrons and contribute to grain boundary scattering in carrier transport. In contrast, the ITO films exhibited no notable changes in these parameters, demonstrating excellent stability and moisture resistance. These findings confirm that the combined effects of humidity and elevated temperature directly cause the dramatic rise in the resistivity of the AZO films. This behavior is consistent with previous observations reported by Greiner et al. [15, 16].

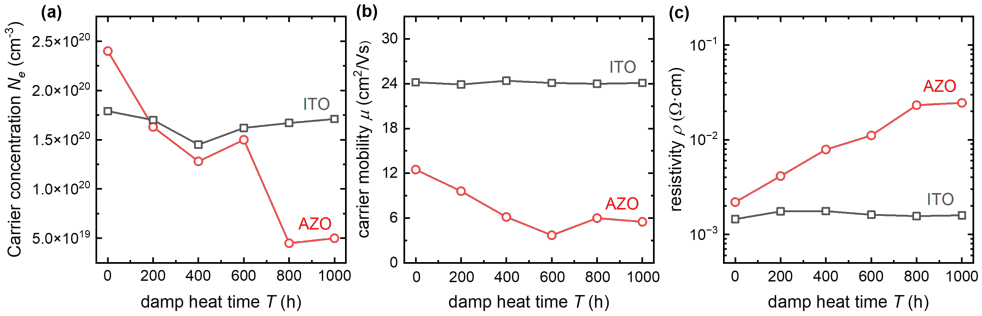


Figure 4.9: Evolution of (a) carrier (electron) density (n_e), (b) carrier (electron) mobility (μ_e), and (c) resistivity (ρ) of 60-nm-thick AZO and 70-nm-thick ITO films deposited on Corning glass substrates during the DH test, measured using Hall-effect characterization.

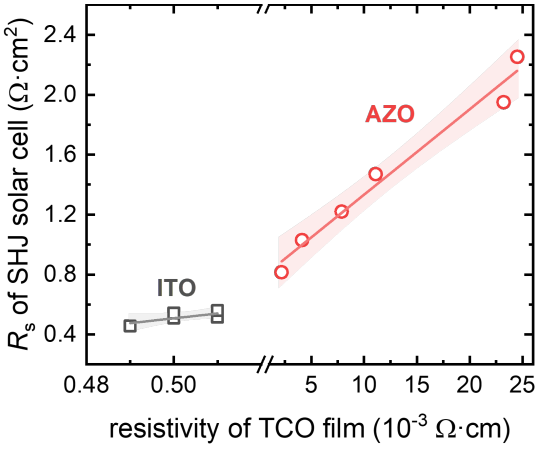


Figure 4.10: Relationship between the series resistance (R_s) of ITO- and AZO-incorporated SHJ solar cells and the resistivity (ρ) of the corresponding TCO films.

Figure 4.10 shows the direct proportional relationship between the series resistance of ITO- and AZO-incorporated SHJ solar cells and the resistivity of the corresponding TCO

films. The data clearly show that the series resistance of the AZO solar cells increases with the resistivity of the AZO films. In AZO-incorporated SHJ solar cells, the rise in R_s is therefore strongly governed by the increase in AZO film resistivity. This correlation confirms that the increase in resistivity observed in AZO films, induced by moisture ingress and elevated temperature during the DH test, leads to a corresponding increase in series resistance of AZO-incorporated SHJ solar cells. Consequently, this increase in series resistance is a key factor contributing to the degradation in solar cell efficiency. However, the resistivity of the ITO film and the series resistance of the corresponding ITO solar cell only increased slightly after 1000 h of DH exposure. This confirms that the ITO film is less susceptible to damp heat corrosion.

In addition, besides the electrical properties analysis, the elemental composition of AZO and ITO films before and after 1000 h of the DH test was analyzed using XPS. The detailed oxygen chemical states are analyzed by analyzing O 1s peaks of TCOs from XPS analysis, this is done to identify the chemisorbed of the hydroxyl (OH^-) group. The peak at 530.8 eV, which corresponds to O^{2-} anions binding with Zn^{2+} or Al^{3+} cations. The component peak at 532 eV is associated with chemisorbed O species or OH^- group [244], as shown in Figure 4.11. A notable increase in the intensity of the OH^- peak was observed in the AZO film after DH exposure compared to its initial state. This indicates that moisture had penetrated the AZO layer. Previous studies have reported that the relatively open grain boundary structure and imperfect intergranular bonding in AZO films facilitate the diffusion of OH^- species, making them susceptible to physical adsorption or chemical reactions [15, 240]. In contrast, no significant increase in the OH^- peak intensity was observed in the ITO films, suggesting that ITO exhibits superior resistance to moisture ingress compared to AZO.

Based on the above analyses of surface morphology, elemental composition, and electrical properties, it is confirmed that the AZO film is more vulnerable to moisture-induced corrosion compared to the ITO film. This susceptibility leads to the degradation of AZO-incorporated SHJ solar cells and lightweight solar modules under damp heat conditions. To address this issue, the next section explores a capping layer strategy aimed at enhancing the moisture resistance of AZO films.

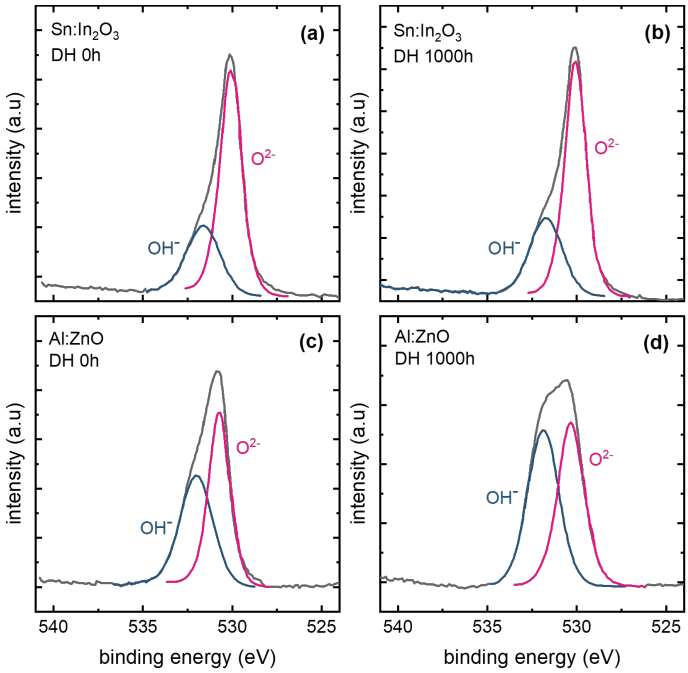


Figure 4.11: XPS analysis of AZO and ITO films before and after the 1000 h of the DH test: (a) ITO before DH, (b) ITO after DH, (c) AZO before DH, and (d) AZO after DH.

4.3 Improved DH resistance: the role of the capping layer

As demonstrated in the previous sections, AZO-incorporated SHJ solar cells and lightweight solar modules are particularly susceptible to DHID, primarily due to moisture corrosion of the AZO films. To address this issue, this section explores the implementation of a capping layer strategy aimed at enhancing the moisture resistance of AZO films and thereby improving the overall durability of the solar cells and solar modules under damp heat conditions.

4.3.1 AZO-incorporated SHJ solar cell with a capping layer

Figure 4.12 illustrates the structures of SHJ cells incorporating different TCO layers: (a) an ITO-incorporated SHJ solar cell, (b) an AZO-incorporated SHJ solar cell, and (c) a triple-layer TCO structure consisting of an ITO (10 nm)/AZO (50 nm)/ITO (10 nm) stack as the front TCO layer, with a 70 nm AZO layer used on the rear side. In this

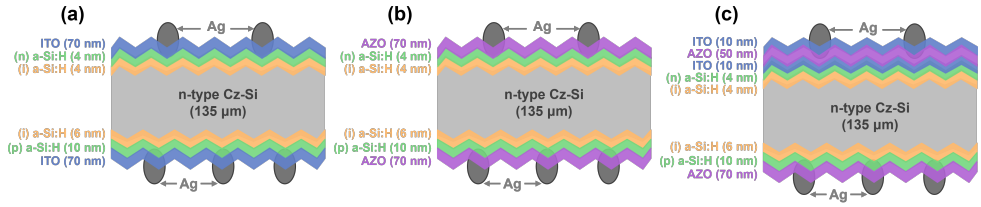


Figure 4.12: Schematic cross-section of SHJ solar cells with different TCO layers: (a) ITO layers at both the front and rear sides, (b) AZO layers at both the front and rear sides, and (c) a triple-layer front TCO stack of ITO/AZO/ITO and an AZO layer at the rear side.

configuration, the top ITO layer functions as a capping layer, while the bottom ITO layer serves as a seed layer. All solar cells were fabricated using our established SHJ baseline process [57]. The optimization of film and device parameters, focusing on balancing optical and electrical performance, has been detailed in our previous work [61]. These solar cells were subsequently used for the fabrication of lightweight SHJ solar modules.

4.3.2 DH stability of AZO-incorporated lightweight SHJ solar modules featuring a capping layer

Configuration of the lightweight solar modules

All of the solar modules were prepared as 200 mm × 200 mm single-cell mini-module samples using M2+ (246.21 cm^2) bifacial monocrystalline busbar-free n-type rear-junction SHJ solar cells with three types of TCO configurations as shown in Figure 4.12. Figure 4.13 shows the schematic cross-section of a lightweight SHJ single-cell solar module with front sheet/back sheet structure. In terms of solar module encapsulation, ETFE was used as the front cover material. The solar cell is embedded between the front and rear encapsulant (TPO). The solar cells were connected using multi-wire interconnection technology consisting of 18 coated copper wires with polyolefin as the carrier foil (interconnection foil - first version, IF1). Sn-Pb-coated copper ribbons (5 mm wide, 0.2 mm thick) were used as connectors. A polyolefin-based foil with a fluorine-free coating was used as the back sheet (hereafter referred to as Px-bs) for the front sheet/back sheet lightweight solar module. The solar module fabrication process is illustrated in Figure 3.4, while Table 4.2 summarizes the configurations of SHJ single-cell solar modules with different module structures.

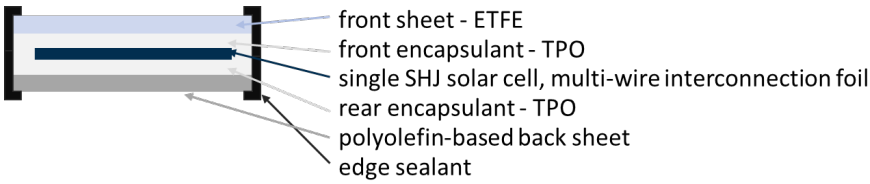


Figure 4.13: Schematic cross-section of a lightweight SHJ single-cell solar module with front sheet/back sheet (FS/BS) structure.

Table 4.2: Configurations of lightweight SHJ single-cell solar cells with different TCO layers.

Module No.	Front sheet	Encapsulant (front/rear)	TCO	IF	Back sheet
4.1	ETFE	TPO	ITO	IF1	Px-bs
4.2	ETFE	TPO	AZO	IF1	Px-bs
4.5	ETFE	TPO	ITO/AZO/ITO	IF1	Px-bs

CTM loss analysis

To evaluate the impact of solar module integration on device performance, a cell-to-module (CTM) analysis was conducted. This analysis compares the electrical performance of SHJ solar cells before and after encapsulation into lightweight solar modules. The variations in key electrical parameters from cell to module are shown in Figure 4.14. An absolute efficiency loss of approximately 2% was observed after solar module integration. This reduction is primarily attributed to losses in both *FF* and J_{sc}. The *FF* loss is mainly caused by an increase in R_s introduced during the solar cell interconnection process. Meanwhile, the reduction in J_{sc} is largely due to optical losses, including reflection at the front surface and absorption by the front sheet and encapsulant materials.

The optical properties of the solar modules were evaluated using *EQE* measurements. Figure 4.15 presents the *EQE* spectra of solar modules incorporating three different TCO configurations. Among them, the ITO-incorporated solar module exhibits a slightly higher *EQE* across the spectrum compared to the AZO and ITO/AZO/ITO-incorporated solar modules. The marginally lower *EQE* observed in the AZO-incorporated solar module is primarily attributed to the higher optical absorption of the AZO layer, as previously reported in [61].

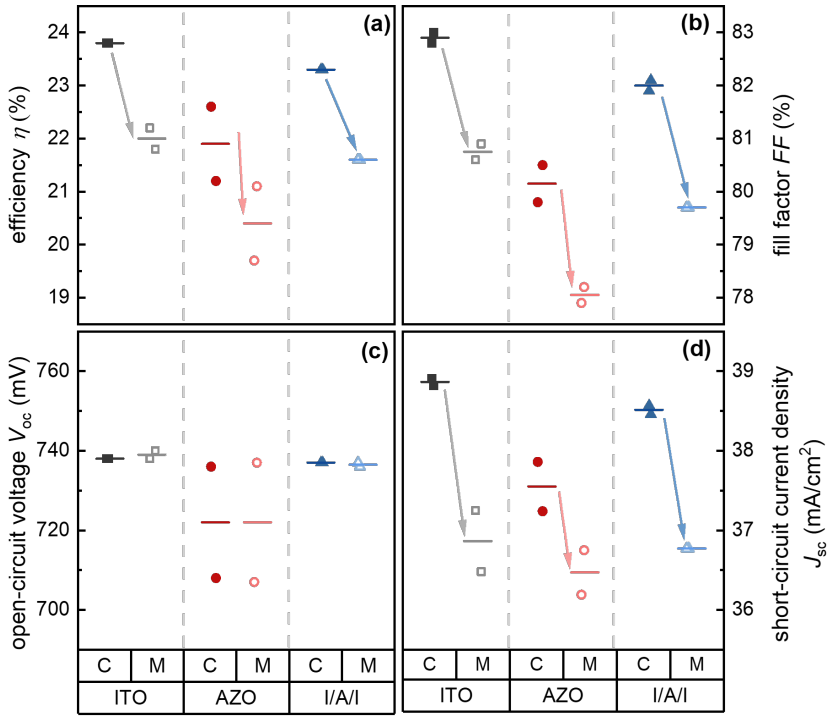


Figure 4.14: CTM analysis of (a) efficiency (η), (b) fill factor (FF), (c) open-circuit voltage (V_{oc}), and (d) short-circuit current density (J_{sc}). 'C' denotes the solar cell, 'M' denotes the solar module, and 'I/A/I' denotes the ITO/AZO/ITO.

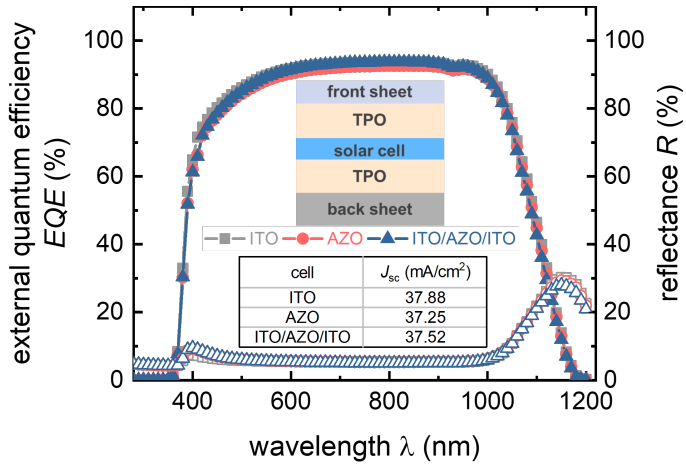


Figure 4.15: *EQE* (solid symbols) and reflectance (hollow symbols) spectra of the solar modules with three types of TCO layers. A schematic of the single-cell solar module sample is shown in the inset.

Enhanced DH stability with a capping layer

Figure 4.16 shows the evolution of electrical performance degradation in lightweight SHJ solar modules incorporating different TCO films at fixed time intervals during the DH test. All measured values were normalized to their respective initial values (before DH exposure) to enable direct comparison of stability over time. The corresponding raw data and I-V curves are presented in Figure 4.17.

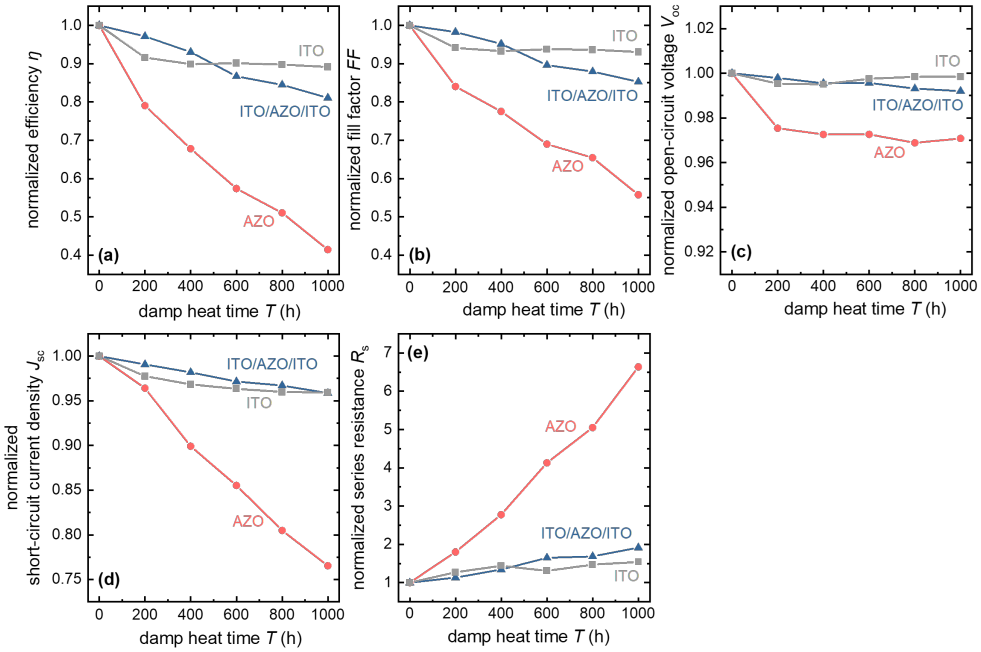


Figure 4.16: Normalized values of (a) efficiency (η), (b) fill factor (FF), (c) open-circuit voltage (V_{oc}), (d) short-circuit current density (J_{sc}), and (e) series resistance (R_{s}) as a function of damp-heat exposure time for lightweight SHJ solar modules with different TCO layers.

The AZO-incorporated lightweight solar module exhibited a 58.57%$_{\mathrm{rel}}$ efficiency degradation after 1000 h of DH test, primarily resulting from losses in FF (44.24%$_{\mathrm{rel}}$) and J_{sc} (23.47%$_{\mathrm{rel}}$). The degradation in FF is mainly attributed to a pronounced increase in R_{s}. This increase in R_{s} is related to an increase in resistivity of the AZO front electrode, as discussed in Subsection 4.2.2, or by deterioration at the AZO/a-Si interface. The observed degradation is believed to result from the influence of humidity on the AZO film, which leads to reduced conductivity under DH conditions. This is consistent with previous findings by Greiner et al. [15, 16], who reported that the crystalline structure of AZO facilitates rapid moisture penetration along grain boundaries, thereby compromising its electrical performance. Furthermore, Greiner et al. observed that non-encapsulated cells subjected to DH exposure showed a significant increase in series resistance, primarily due

to increased lateral sheet resistance of the transparent AZO front contact [16]. For the ITO/AZO/ITO solar module samples, a small decrease in *FF* was observed compared to the AZO-incorporated solar modules, indicating the effectiveness of the ITO layer as a protective capping layer in suppressing moisture-induced degradation.

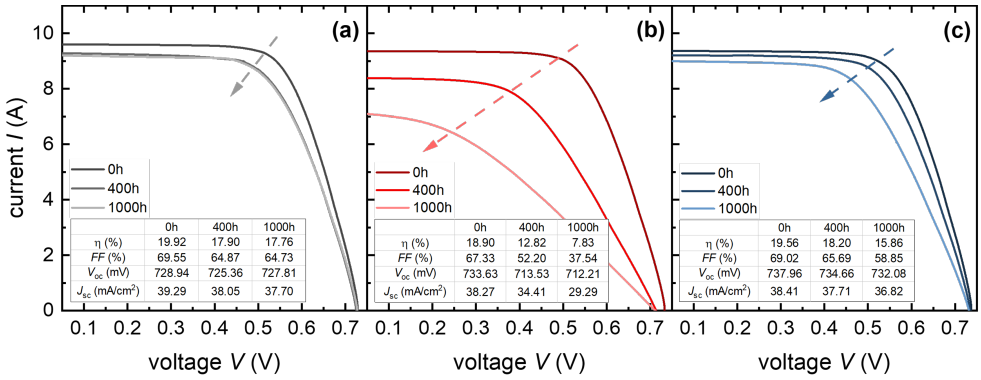


Figure 4.17: *I-V* curves of (a) ITO-, (b) AZO-, and (c) ITO/AZO/ITO-incorporated SHJ solar modules, measured before (0 h), after 400 h, and after 1000 h of DH exposure.

From EL images shown in Figure 4.18(b), two distinct types of defects can be clearly identified. The circular dark area outlined by the white dashed line, located at the center of the AZO-incorporated solar module even before DH exposure, originates from sputter-induced damage to the a-Si:H layer caused by ion bombardment during the AZO deposition process [245], as reported in our previous study [61]. However, sputter-induced damage was not observed when a 10 nm ITO seed layer was introduced between the AZO layer and the n-type a-Si:H, as previously reported in [61]. As the DH test progresses, this circular region becomes noticeably darker, indicating a continued decrease in EL intensity. Furthermore, this dark circular region is visible in the PL image after 1000 h of DH exposure, suggesting increased passivation damage and enhanced carrier recombination. This degradation likely contributed to the observed reduction in V_{oc} of the solar module. The results imply that moisture ingress through the AZO layer gradually worsened the passivation quality of the underlying a-Si:H layer over time. As discussed in Subsection 4.2.2, SEM analysis of bare AZO cells after 1000 h of DH test revealed a clear change in surface morphology, becoming more porous and forming grooves. These structural changes facilitate the diffusion and percolation of water vapor molecules through the AZO film, further accelerating the degradation of solar cell performance.

In contrast, rectangular dark-area defects (highlighted by red dashed lines) that developed during the DH test were attributed to moisture-induced degradation of the AZO layer. This failure mode was further verified through PL measurements under open-circuit conditions. Notably, the rectangular defect appeared only in the EL image, but not in the

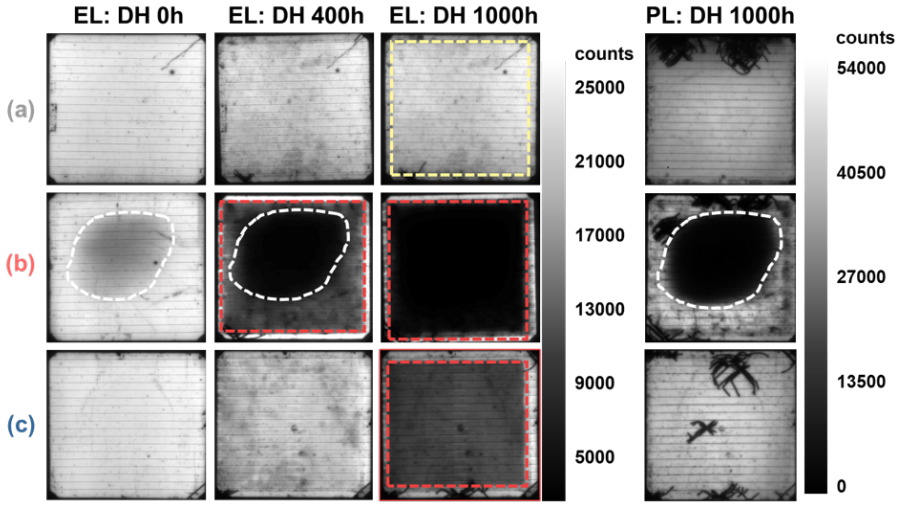


Figure 4.18: EL images under low current injection (J = 2.03 mA/cm^2) of (a) ITO-, (b) AZO-, and (c) ITO/AZO/ITO-incorporated SHJ solar modules before, after 400 h, and after 1000 h of DH test. The severe cracking observed in the PL image after 1000 h of DH test resulted from mechanical damage during transport after the I-V and EL measurements.

PL image, suggesting that this defect was due to electrical degradation of the AZO film rather than passivation degradation. Additionally, cracks observed in the PL images were not related to the DH test but were instead caused by the transport of the solar modules after EL measurements. The contrast between PL and EL patterns is indicative of a localized increase in R_s due to prolonged environmental exposure [246]. While reduced EL intensity results from drops in local junction voltage caused by increased R_s, the PL signal under open-circuit conditions reflects the intrinsic semiconductor quality and local defect states, and is not influenced by contact issues [143]. Therefore, the appearance of rectangular dark areas in the EL image indicates that carrier transport is hindered due to electrical degradation of the AZO film. This confirms that the electrical properties of the AZO layer deteriorated after 1000 h of DH exposure, leading to a significant increase in film resistivity, a dramatic rise in R_s, and a corresponding decline in FF. These findings are consistent with the results obtained from plain AZO films and bare AZO cells, as discussed in Section 4.2.

One hypothesis for the origin of the rectangular dark-area defect is that the adhesion between the AZO layer and the interconnection foil is weaker than that of ITO. During the DH exposure, moisture ingress may have caused the interconnection foil to delaminate from the AZO layer, mechanically damaging the AZO layer. Visual inspection of the solar modules, as shown in Figure 4.19, revealed severe delamination along the interconnection

wires in the AZO-incorporated solar modules. Voids were clearly visible in these regions, suggesting that the failure was more likely due to foil delamination from the AZO layer, rather than AZO detaching from the wafer surface. In contrast, such delamination defects were minimal in the ITO-incorporated solar module samples, indicating better interfacial adhesion.

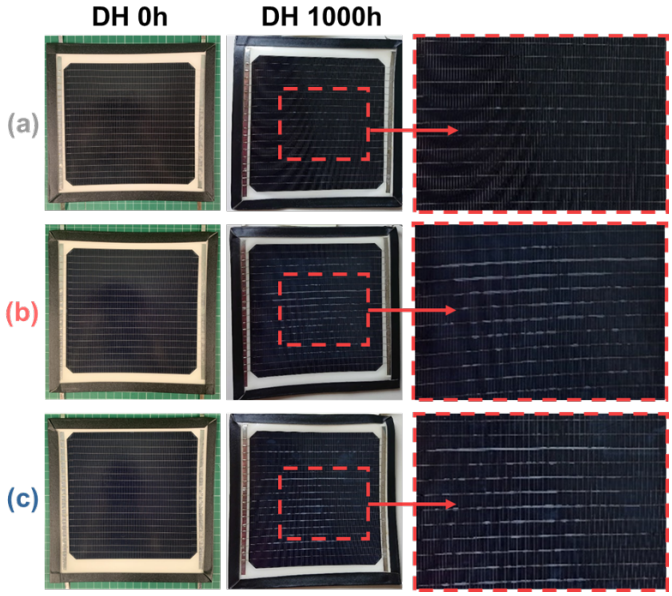


Figure 4.19: Visual inspection images of the lightweight SHJ solar modules with different TCOs: (a) ITO, (b) AZO, and (c) ITO/AZO/ITO before and after 1000 h of DH test. Delamination along the interconnection wires is clearly visible in (b) AZO and (c) ITO/AZO/ITO samples, indicating severe adhesion failure. The slight yellow tint in the images taken before the DH test is due to differences in lighting conditions during photography.

A second hypothesis is that chemical degradation of the AZO layer occurred due to interaction with substances released from the interconnection foil, which may have reacted with water molecules during DH exposure. Both proposed degradation mechanisms, mechanical delamination and chemical corrosion, appear to be closely associated with the interconnection foil - AZO interface, highlighting it as a critical reliability concern in AZO-incorporated lightweight solar module design.

To validate the proposed hypotheses regarding the origin of the rectangular dark-area defects, an additional experiment was conducted. Specifically, half of the interconnection foil was manually removed, leaving only the wires in that region, while the other half of the solar module remained fully intact. Standard interconnection and lamination processes were then applied. The corresponding visual and EL images after 1000 h of DH test are

shown in Figure 4.20.

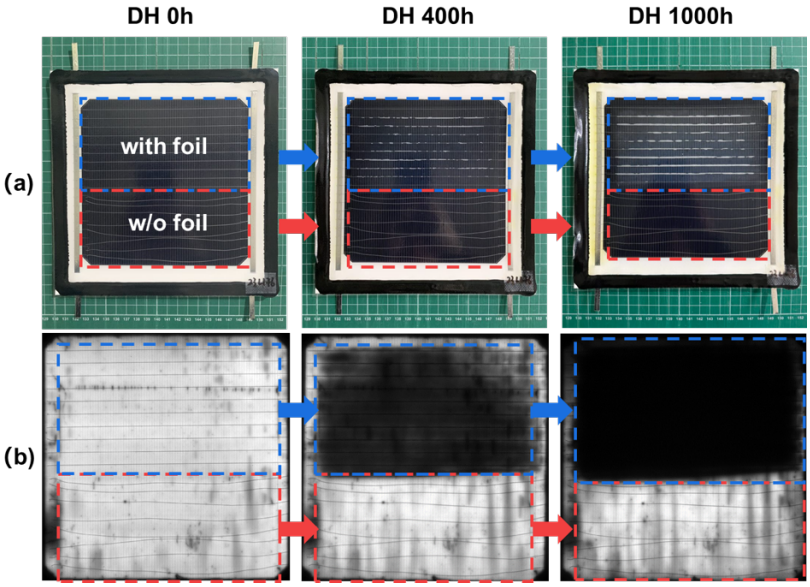


Figure 4.20: AZO-incorporated SHJ solar module with interconnection foil (wires and interconnection foil, blue dashed line) and without interconnection foil (only wires, red dashed line). (a) Visual images before, after 400 h, and after 1000 h of the DH test; (b) EL images at low current injection (J = 2.03 mA/cm^2) taken before, after 400 h, and after 1000 h of the DH test.

The EL images taken after 1000 h of the DH test clearly show that the rectangular dark-area defect is absent in the region where the interconnection foil was removed, confirming that the defect is linked to the presence of the interconnection foil. As shown in Figure 4.20(a), delamination along the wires is prominently visible in the area where the interconnection foil remains, accompanied by a noticeable color change in the AZO layer. These visual indicators correlate with the rectangular dark areas observed in the EL image in Figure 4.20(b), further substantiating the degradation. These results clearly demonstrate that the interconnection foil has a detrimental effect on the performance and stability of AZO-incorporated lightweight solar modules under damp-heat conditions, likely due to either poor adhesion or chemical interaction with moisture.

In contrast, the rectangular dark area in the solar module with ITO/AZO/ITO as the front TCO layer is noticeably less pronounced than that in the solar module employing pure AZO as the front TCO layer, as shown in Figure 4.18. The efficiency loss of the ITO/AZO/ITO module after DH exposure is significantly lower than that of the AZO module, indicating that the DH stability of the AZO film is improved by capping it with an ITO protective layer. However, while the 10 nm ITO capping layer enhances DH

resistance, it does not provide sufficient adhesion to the interconnection foil. As a result, delamination defects were still observed in the ITO/AZO/ITO module, though they were less severe compared to those in the AZO module, as evidenced by the visual inspection in Figure 4.19.

The ITO solar module exhibited a phenomenon opposite to that of the AZO solar module. As shown in Figure 4.18(a), the EL images of the ITO solar module show a higher intensity in the rectangular area where the interconnection foil is located (as indicated by the yellow dashed line), compared to the solar module edges. This contrast appears to be an edge effect, rather than an indication of degradation in the central region. Furthermore, almost no delamination was observed in the ITO solar module, indicating that the interconnection foil adheres more effectively to the ITO layer than to the AZO layer. This suggests that, in the case of ITO, the interconnection foil may act as an additional encapsulation barrier, offering localized protection against moisture ingress. As a result, the solar module edges, which are not covered by the interconnection foil, become more vulnerable to humidity exposure. This spatial difference in degradation is reflected in the EL images: the central region of the ITO solar module, covered by the interconnection foil, displays higher EL intensity, while the edges show lower intensity, consistent with increased moisture-induced degradation in the unprotected areas.

Interpretation of degradation mechanisms

Based on the above analyses, the degradation mechanisms of the AZO-incorporated lightweight solar module can be interpreted as illustrated in Figure 4.21, which presents a schematic diagram of moisture ingress and the associated degradation pathways.

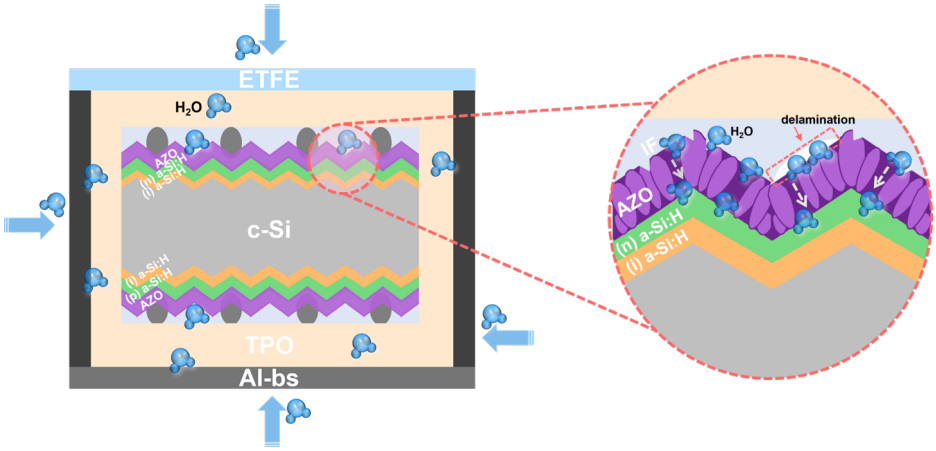


Figure 4.21: Schematic diagram of moisture ingress and degradation mechanisms in lightweight AZO-incorporated SHJ solar modules.

1. The delamination of the interconnection foil from the AZO film is attributed to moisture ingress and inherently poor adhesion between the AZO layer and the interconnection foil.

2. This delamination facilitates further moisture penetration into the AZO film. The combined effects of delamination and moisture ingress cause structural damage in the AZO layer, resulting in the formation of vacancies that significantly reduce its electrical conductivity. As a result, the R_s of the AZO solar modules increases dramatically, leading to a substantial decrease in FF. The dramatic increase in R_s leads to a decrease in carrier collection efficiency, resulting in a significant reduction in J_{sc}.

3. Consequently, the compromised AZO layer allows moisture to percolate into the a-Si:H passivation layer, causing passivation degradation, which leads to an increase in recombination, resulting in a decrease in V_{oc} of the AZO solar modules. These degradation phenomena were most prominent in the central region of the solar module, where the interconnection foil was located. This observation also explains the significant reduction in EQE intensity at the solar module center, rather than at the edges, after 1000 h of DH test, as shown in Figure 4.22(b).

The EQE and reflectance measurements were conducted at different positions of the solar modules. Figure 4.22(d) shows the light spot positions (1-center and 2-edge) when

measuring the *EQE* and reflectance of the solar modules. The center indicates that the light spot is in the middle of the solar cell, and the edge indicates that the light spot is close to the edge of the solar cell. The dashed line indicates the location of the interconnection foil. Position 1 is almost at the center of the solar cell. Therefore, the light illuminates the interconnection foil. Position 2 is located near the edge of the solar cell. The light partly illuminates the interconnection foil.

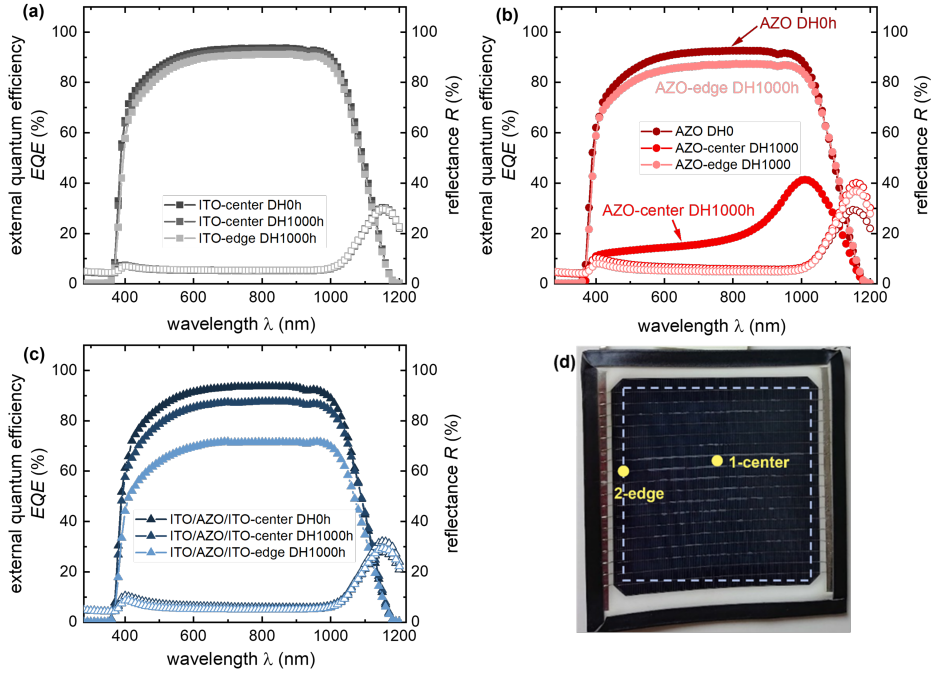


Figure 4.22: *EQE* (solid symbols) and reflectance (hollow symbols) of (a) ITO-, (b) AZO-, (c) ITO/AZO/ITO-incorporated SHJ lightweight solar modules before and after 1000 h of the DH test. (d) The light spot positions, 1-center and 2-edge.

Although it remains challenging to quantitatively assess the extent of moisture penetration through the encapsulation foil into the TCO and passivation layers, this study provides valuable insights into the degradation mechanisms of AZO-incorporated lightweight SHJ solar modules. The results highlight the critical role of the ITO capping layer in mitigating moisture diffusion and enhancing the DH stability of AZO-incorporated SHJ solar cells and modules.

Furthermore, the interconnection foil was identified as a key contributor to performance degradation, particularly due to its poor adhesion to the AZO layer and its facilitation of moisture ingress. In the following section, the use of an alternative interconnection foil will be investigated to further improve the durability and reliability of AZO-incorporated lightweight SHJ solar modules under damp-heat conditions.

4.4 Improved DH resistance: the role of the interconnection foil

In the previous section, it was shown that AZO-incorporated lightweight solar modules incorporating the first-version interconnection foil (IF1) exhibited significant performance degradation after 1000 h of DH test. This deterioration was attributed to delamination of IF1 and subsequent moisture percolation into the underlying AZO and passivation layers. To address this issue, the present section investigates the use of a second-version interconnection foil (denoted as IF2) for solar module fabrication. The performance and stability of solar modules using IF2 are systematically compared with those of solar modules using IF1 to assess improvements in DH reliability.

4.4.1 CTM loss analysis of lightweight SHJ solar modules using two different interconnection foils

Configurations of the solar modules

A modified lightweight solar module design was employed in this section. Figure 4.23 illustrates the schematic cross-section of the redesigned lightweight SHJ single-cell solar module. ETFE was used as the front cover material. The solar cell is embedded between the front and rear encapsulant (TPO). The solar cells were connected using multi-wire interconnection technology. Sn-Pb-coated copper ribbons (5 mm wide, 0.2 mm thick) were used as connectors. A polyolefin-based foil with aluminum as the interlayer was used as the back sheet, which is denoted as Al-bs in the following. The edges of the solar modules were sealed using PIB tape with a width of 10 nm and a thickness of 1 nm. The solar module fabrication process is illustrated in Figure 3.9.

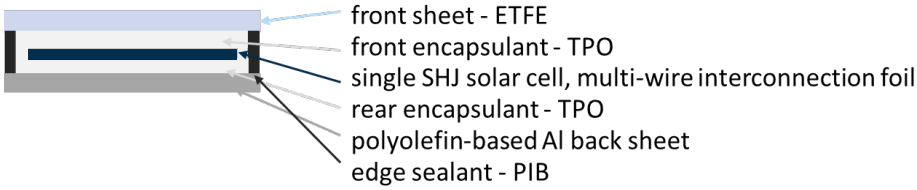


Figure 4.23: Schematic cross-section of the lightweight SHJ single-cell solar module.

Table 4.3 summarizes the configurations of the lightweight SHJ solar modules incorporating two different interconnection foils: IF1 and IF2. Full-size single cells were used in combination with IF1, which is composed of 18 coated copper wires, while half-cut

cells were used with IF2, which is composed of 16 coated copper wires. Apart from the dimension of the solar cell and interconnection foil types, all other aspects of the solar module structure were kept consistent across both designs.

Table 4.3: Configurations of lightweight SHJ solar modules with different interconnection foils.

Module No.	Front sheet	Encapsulant (front/rear)	Solar cell type	TCO	IF	Back sheet
4.6	ETFE	TPO	full cell	ITO	IF1	Al-bs
4.7	ETFE	TPO	full cell	AZO	IF1	Al-bs
4.8	ETFE	TPO	half-cut cell	ITO	IF2	Al-bs
4.9	ETFE	TPO	half-cut cell	AZO	IF2	Al-bs

CTM loss analysis

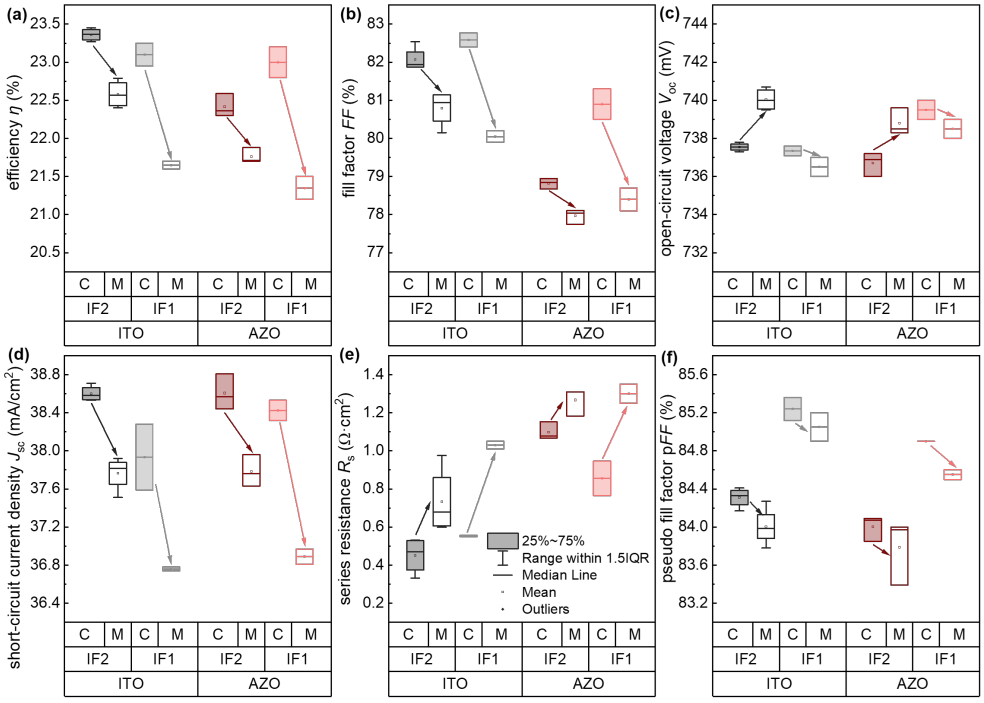


Figure 4.24: CTM analysis of (a) efficiency (η), (b) fill factor (FF), (c) open-circuit voltage (V_{oc}), (d) short-circuit current density (J_{sc}), (e) series resistance (R_s), and (f) pseudo fill factor (pFF). 'C' denotes the solar cell, and 'M' denotes the solar module.

The variations in electrical parameters from cell-to-module (CTM) are shown in Figure 4.24. Solar modules using IF2 exhibit a lower CTM efficiency loss compared to those using IF1. This improvement is primarily attributed to the reduced FF, which results from a smaller increase in R_{s} from cell to module. Additionally, the ITO-incorporated solar modules demonstrate superior performance compared to the AZO-incorporated ones, largely due to the inherently lower R_{s} of the ITO front contact.

4.4.2 DH stability of AZO-incorporated lightweight SHJ solar modules with different interconnection foils

Figure 4.25 shows the time evolution of the degradation in electrical properties of AZO- and ITO-incorporated lightweight SHJ solar modules incorporating two different interconnection foils (IF1 and IF2) at fixed time intervals during the DH test. All values are normalized to their initial values before the DH test. The AZO-incorporated solar module with IF2 exhibited significantly improved stability compared to the one with IF1. Specifically, the efficiency of the AZO-incorporated solar module decreased by $52.36\%_{\mathrm{rel}}$ with IF1, while the solar module with IF2 showed a considerably smaller decrease of $17.65\%_{\mathrm{rel}}$ after 1000 h of DH exposure. This improvement is primarily due to the mitigated loss in FF, which results from a smaller increase in R_{s}. Furthermore, reductions in V_{oc} and pFF were also less pronounced, indicating that passivation damage due to heat-assisted moisture ingress was effectively suppressed. A smaller decrease in J_{sc} was also observed. As discussed in Subsection 4.3.2, the optoelectronic properties of the AZO film degrade after prolonged DH exposure, contributing to the reduction in J_{sc}. In contrast, ITO-incorporated lightweight solar modules exhibited stable performance during the DH test with both IF1 and IF2. However, the ITO-incorporated solar modules with IF2 performed slightly better than those with IF1, suggesting that the improved interconnection design also benefits solar modules with inherently more stable TCOs.

Figure 4.26 shows the visual images of the ITO- and AZO-incorporated lightweight SHJ solar modules combined with two different interconnection foils (IF1 and IF2), before and after 1000 h of the DH test. For the AZO-incorporated solar modules combined with IF1, delamination of the interconnection foil and a visible color change of the solar cell, highlighted by the white dashed rectangle, were clearly observed after DH exposure. In contrast, these degradation features were not observed in the AZO-incorporated solar modules using IF2, indicating improved adhesion and DH stability. For ITO-incorporated lightweight solar modules, no delamination or color change was observed with either IF1 or IF2, demonstrating the inherently better adhesion and stability of the ITO layer under DH conditions.

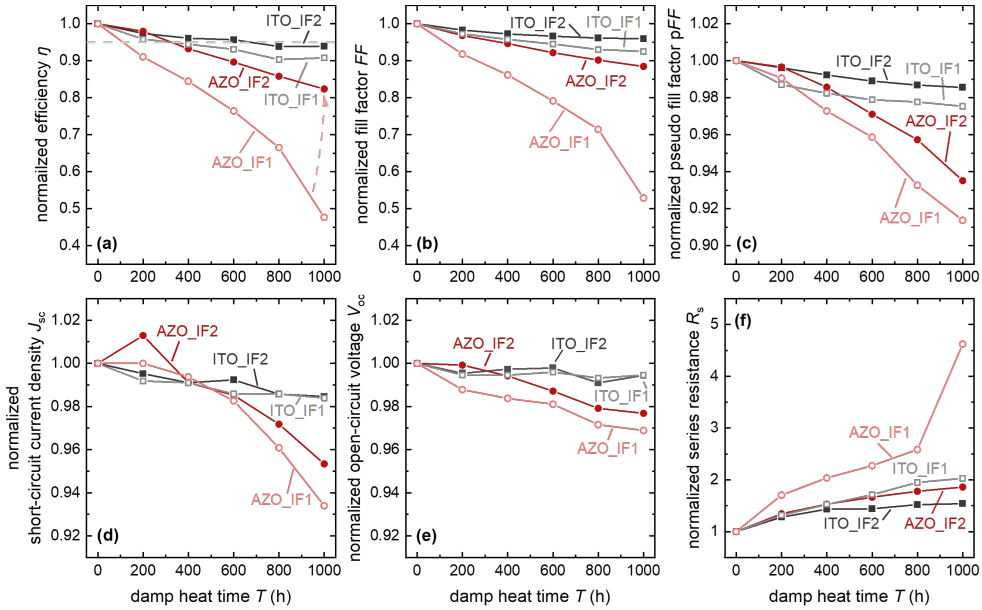


Figure 4.25: Normalized values of (a) efficiency (η), (b) fill factor (FF), (c) pseudo fill factor (pFF), (d) short-circuit current density (J_{sc}), (e) open-circuit voltage (V_{oc}), and (f) series resistance (R_s) as a function of damp-heat time for solar modules in combination with two different interconnection foils.

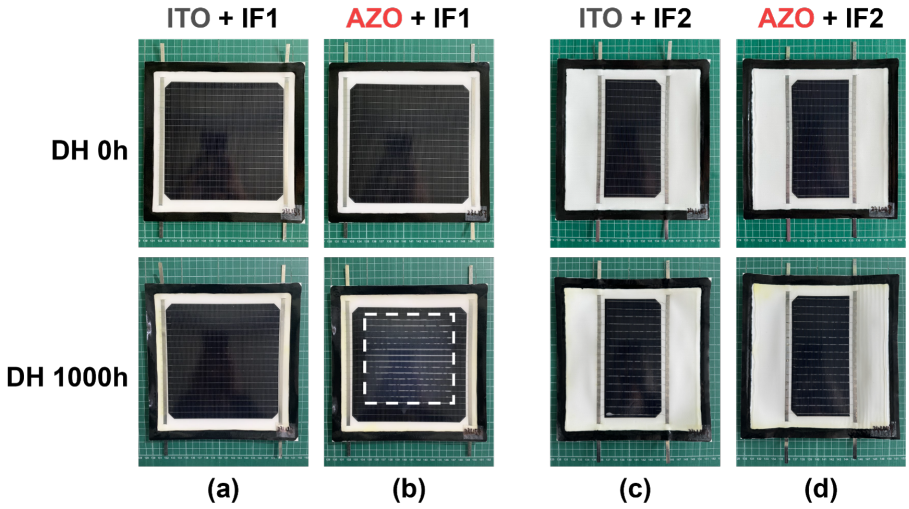


Figure 4.26: Visual images of ITO- and AZO-incorporated FS/BS solar modules in combination with two different interconnection foils (IF1 and IF2), before and after 1000 h of the DH test. (a) ITO + IF1, (b) AZO + IF1, (c) ITO + IF2, and (d) AZO + IF2.

These visual findings are further supported by the corresponding EL and PL images shown in Figure 4.27 and Figure 4.28, respectively. In the AZO-incorporated solar modules with IF2, the EL and PL images reveal significantly fewer defects, confirming that the moisture-related degradation caused by the combined effects of interconnection foil delamination and moisture ingress was substantially mitigated by using the improved interconnection foil (IF2).

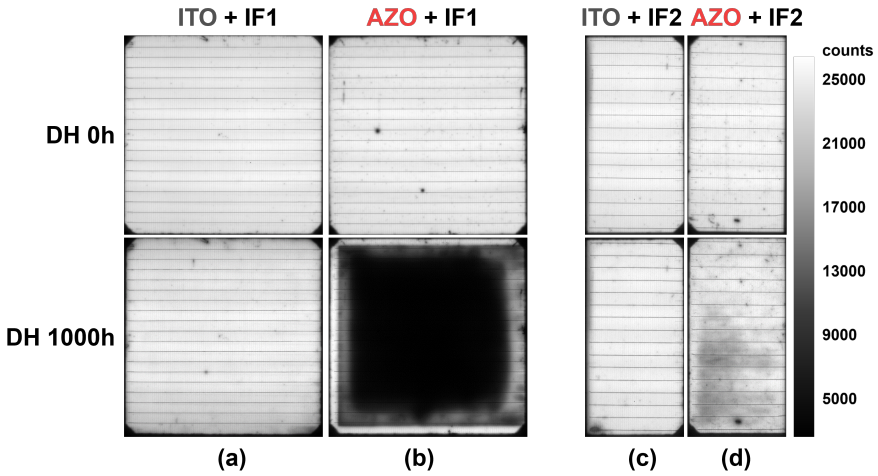


Figure 4.27: EL images under low current injection (J = 2.03 mA/cm^2) of ITO- and AZO-incorporated FS/BS solar modules in combination with two different interconnection foils (IF1 and IF2), before and after 1000 h of DH. (a) ITO + IF1, (b) AZO + IF1, (c) ITO + IF2, and (d) AZO + IF2.

Figure 4.29 shows the *EQE* and reflectance of the ITO- and AZO-incorporated lightweight SHJ solar modules combined with two different interconnection foils (IF1 and IF2), before and after 1000 h of the DH test. As shown in Figure 4.29(b), a substantial decrease in *EQE* was observed in the AZO module with IF1, indicating significant performance degradation. In contrast, the *EQE* reduction was significantly mitigated in the AZO module with IF2, confirming the improved stability provided by the alternative interconnection foil. The observed *EQE* decline can be attributed to two key factors: (1) reduced carrier collection efficiency due to degradation of the AZO film, and (2) increased carrier recombination caused by deterioration of the passivation layer. These effects together contribute to the observed optoelectronic performance loss. Importantly, the *EQE* trends are consistent with the findings from previous structural, electrical, and imaging analyses discussed earlier in this work.

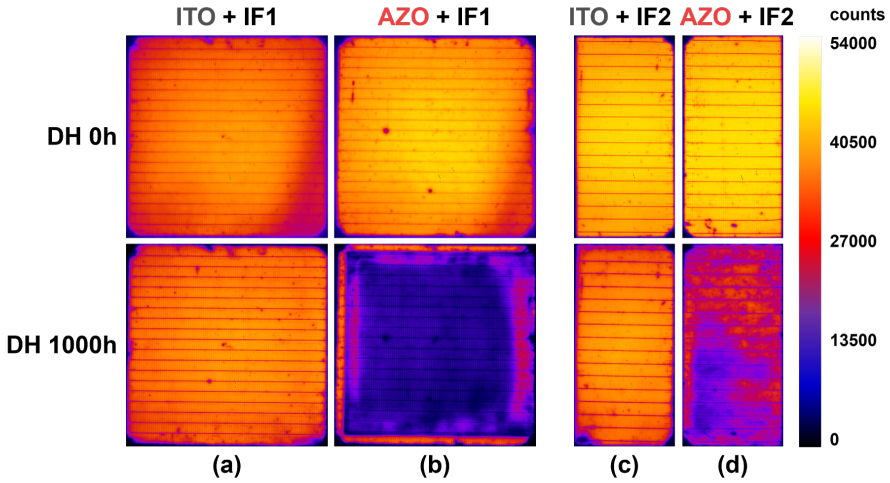


Figure 4.28: PL images of ITO- and AZO-incorporated FS/BS solar modules in combination with two different interconnection foils (IF1 and IF2), before and after 1000 h of DH. (a) ITO + IF1, (b) AZO + IF1, (c) ITO + IF2, and (d) AZO + IF2.

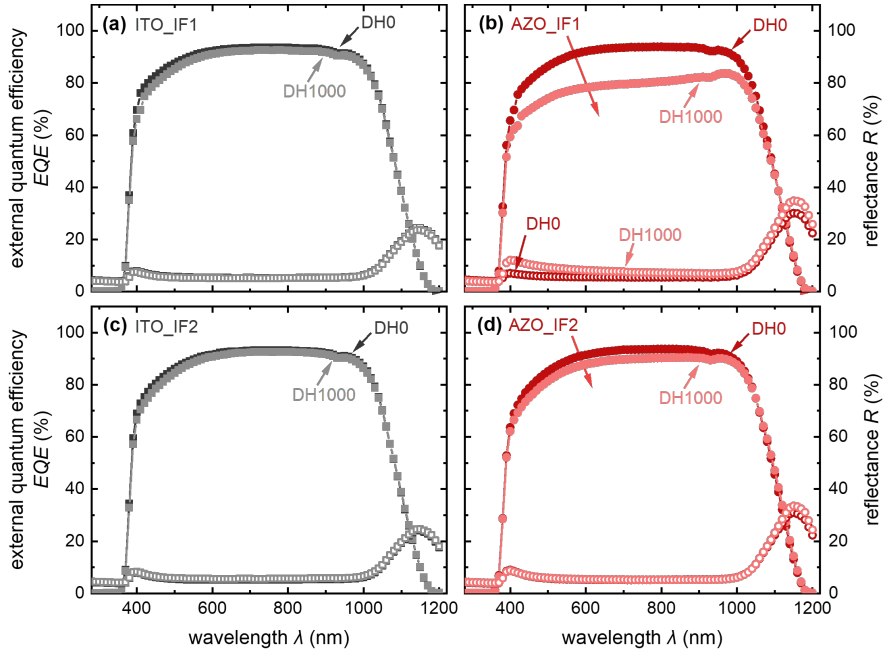


Figure 4.29: *EQE* (solid symbols) and reflectance (hollow symbols) of ITO- and AZO-incorporated FS/BS solar modules in combination with two different interconnection foils (IF1 and IF2), before and after 1000 h of DH. (a) ITO + IF1, (b) AZO + IF1, (c) ITO + IF2, and (d) AZO + IF2.

5 Influence of encapsulation materials on the DH stability of lightweight SHJ solar modules

In the previous chapter, it was identified that AZO-incorporated lightweight SHJ solar modules are susceptible to DHID than ITO-based lightweight SHJ solar modules. The AZO film was damaged by the synergistic effects of moisture ingress and delamination of the interconnection foil, resulting in a decrease in the conductivity of the AZO film, leading to a dramatic increase in R_s and a decrease in FF of the solar modules. In particular, after capping the AZO film with an ITO film, the efficiency loss of the ITO/AZO/ITO solar module was significantly reduced, suggesting that the ITO film is a promising protective capping layer for the AZO-incorporated solar cells.

In this chapter, the influence of encapsulation materials on the DH stability of lightweight SHJ solar modules is comprehensively investigated. It is worth noting that ITO-incorporated SHJ solar cells were used for solar module fabrication in this chapter, since ITO is more stable than AZO in DH conditions. The investigation on the effect of encapsulants on the DH stability of lightweight SHJ solar modules is presented in Section 5.1. The degradation mechanisms specific to each solar module have also been revealed. The DH-stable lightweight SHJ solar modules were developed with different front sheet materials, as presented in Section 5.2. Accordingly, a discussion about the equivalence between the accelerated DH aging test and outdoor test is presented in Section 5.3.

5.1 Effect of encapsulants on the DH stability of lightweight SHJ solar modules

5.1.1 Physical properties of different encapsulants

Table A.1 in the appendix shows the specifications of the encapsulants from different suppliers that were used to fabricate the lightweight solar module in this section, including thermoplastic polyolefin (TPO), thermoplastic polyurethane (TPU), ethylene-vinyl acetate (EVA), another thermoplastic polyolefin named PO [PO-S: PO with a UV-transmitting property and PO-UV: PO with a UV-blocking property], EVA/POE/EVA (EPE), UV-downshifting EVA (DS-EVA), and UV-downshifting EPE (DS-EPE). Figure A.1 in the appendix shows the structural formula of typical polymer encapsulants.

Optical properties of the different encapsulants

These polymer encapsulants are categorized into three groups based on their light transmission to ultraviolet (UV) light (280 - 400 nm). TPO, TPU, and PO-UV are UV-blocking encapsulants. EPE, PO-S, and EVA are UV-transmitting encapsulants. DS-EVA and DS-EPE are UV-downshifting encapsulants that can convert UV light to blue light. Figure 5.1 shows the total transmittance and reflectance of different encapsulants.

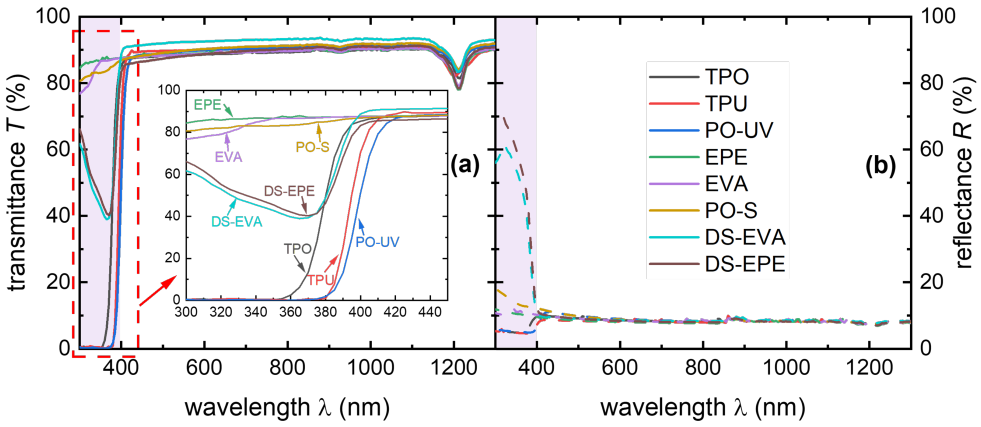


Figure 5.1: Optical properties of different encapsulants, (a) transmittance (T) and (b) reflectance (R). The inset graph shows the transmittance in the wavelength range from 300 - 450 nm.

WVTR of different encapsulants

Figure 5.2 shows the WVTR of different encapsulants measured in different foil forms. One is in a plain laminated foil. The other is combined with ETFE foil to better correlate with the solar module structure. WVTR tests were performed at 38 °C, 90% RH conditions. This is an important parameter for indicating the water vapor transmission properties of polymer foils [247]. TPU laminated foil has the highest WVTR of 45.68 g/m^2 × day, while TPO laminated foil has the lowest WVTR of 3.34 g/m^2 × day. The WVTR exhibits significant variations from one encapsulant to another. However, using a combination of ETFE and encapsulant foils significantly reduces the WVTR. A combination of ETFE and TPU has a WVTR of 0.1291 g/m^2 × day, while a combination of ETFE and TPO has a WVTR of 0.167 g/m^2 × day. Variations in WVTR are also significantly reduced among encapsulants. Except for TPU, the combination of ETFE and other encapsulants has a WVTR below 0.025 g/m^2 × day.

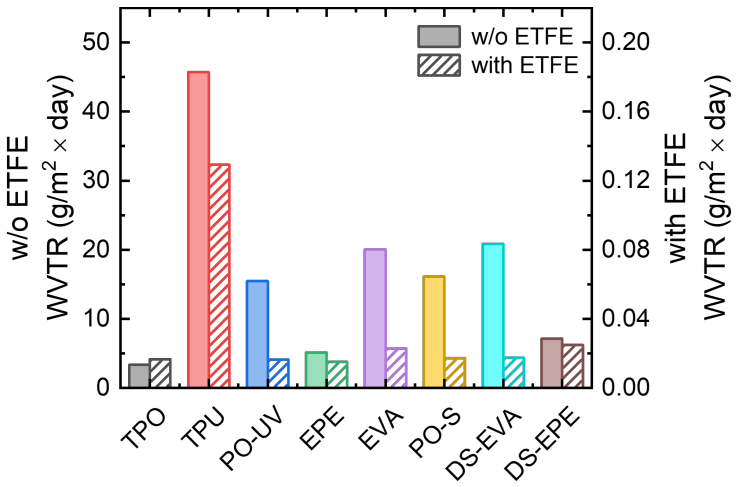


Figure 5.2: WVTR of different encapsulants in plain laminated foil form and in combination with ETFE foil.

Thermal behavior of the encapsulant materials

Figure 5.3 presents the thermal properties of the pristine encapsulant (as received, before any treatment) films measured by DSC. All films exhibit distinguishable melting behavior. TPO shows a melting peak (T_{mp}) at approximately 54 °C, while TPU exhibits a peak at around 80 °C. For the rest of the encapsulants, two melting peaks were observed, corresponding to two distinct crystalline populations. The lower temperature

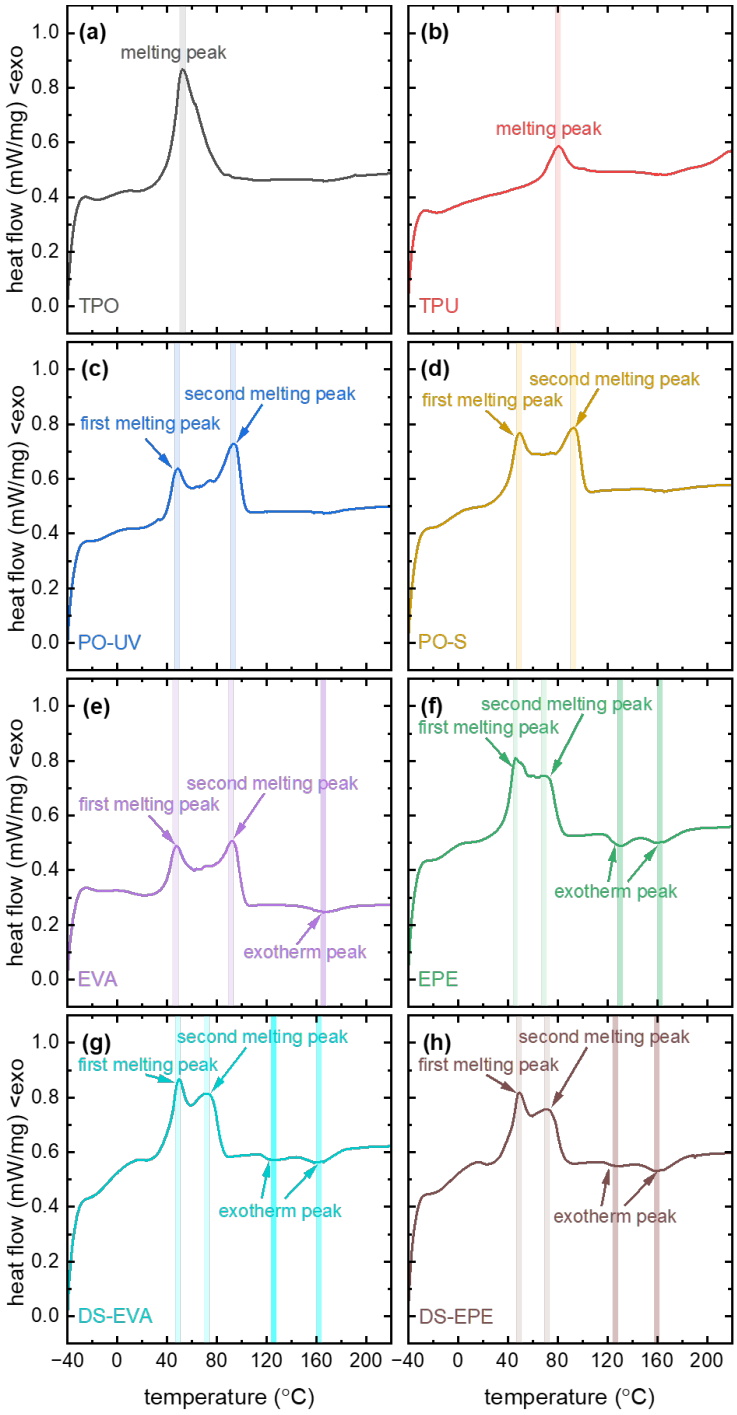


Figure 5.3: Differential scanning calorimetry (DSC) thermograms (first heating run) of the different pristine encapsulants.

endothermic peak is associated with the melting of less stable crystallites, whereas the higher temperature peak corresponds to the melting of more ordered crystalline populations [248]. PO-UV and PO-S display similar melting characteristics, each with two melting peaks located near 50 °C and 90 °C. EVA exhibits a broader melting region with two peaks at about 46 °C and 93 °C. The lower-temperature peak (46 °C) corresponds to less ordered crystals, whereas the higher-temperature peak (93 °C) originates from more highly organized polyethylene chain crystals. Similarly, EPE exhibits melting peaks at 45 °C and 70 °C, DS-EVA at 48 °C and 72 °C, and DS-EPE at 48 °C and 72 °C. Besides, for EVA, EPE, DS-EVA, and DS-EPE, exotherm peaks due to the decomposition of the crosslinking agent, usually the peroxide, can be seen for these pristine encapsulants [66, 67]. The DSC curve of EVA shows an exotherm peak at around 165.5 °C. EPE shows two exotherm peaks at approximately 130 °C and 158.6 °C. DS-EVA shows two exotherm peaks at approximately 125 °C and 158.6 °C. And DS-EPE shows two exotherm peaks at approximately 127 °C and 158.4 °C.

From the DSC curves, the onset temperature (T_{onset}), which indicates the start of the exothermal reaction, the peak temperature (T_{peak}), and the exothermal reaction enthalpy (ΔH_{r}) can be extracted. As shown in Figure 5.4(a), T_{onset} and T_{peak} characterize the crosslinking process, while Figure 5.4(b) presents the corresponding exothermal reaction enthalpies. The physical crosslinking encapsulants, TPO and TPU, show no measurable ΔH_{r}, reflecting their high thermal stability. In contrast, EPE exhibits the highest ΔH_{r}, indicating poor thermal stability. DS-EVA and DS-EPE also display relatively high ΔH_{r}, suggesting that their thermal resistance is lower compared to other encapsulants.

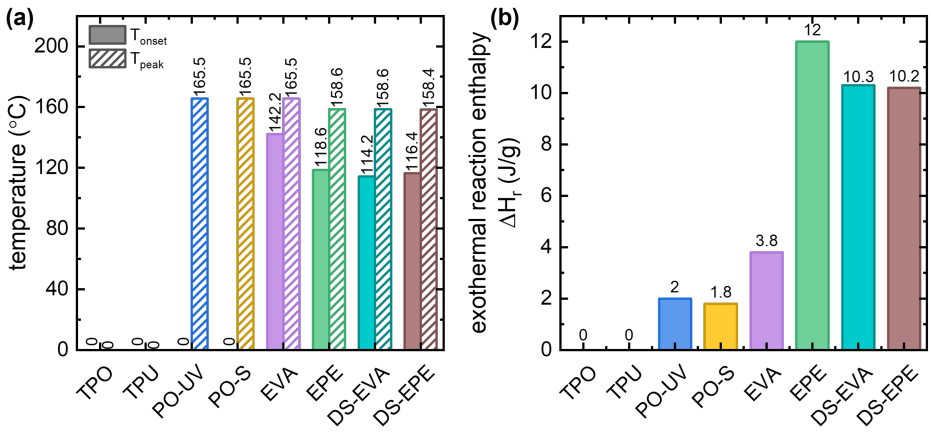


Figure 5.4: Differential scanning calorimetry (DSC), (a) T_{onset} (temperature at which chemical crosslinking commences) and T_{peak} (chemical crosslinking peak temperature); (b) Exothermal reaction enthalpy of different encapsulants.

5.1.2 Configurations of solar modules with different encapsulants

Design and fabrication of the solar modules

Figure 5.5 shows the schematic cross-section of the lightweight SHJ solar module. Single-cell mini-module samples measuring 210 mm × 210 mm were prepared using M2 (156.75 mm × 156.75 mm) size, bifacial, monocrystalline, busbar-free, n-type rear-junction SHJ solar cells. The solar cells are connected using mult-iwire interconnection (IF1) technology, which consists of 18 coated copper wires with polyethylene (PE) as the carrier foil. This foil is in direct contact with the solar cell and sits between the solar cell and the encapsulant. Sn-Pb-coated Cu-ribbons were used as connectors. For the fabrication of the solar modules, ETFE was used as the front sheet material. The specifications of the front sheets are listed in Table A.2. The different encapsulants were used as shown in the above section. A polyolefin-based foil with aluminum as the interlayer was used as the back sheet, which is denoted as Al-bs in the following. The specifications of the back sheet are listed in Table A.2. The edges of the solar modules were sealed using polyisobutylene (PIB) tape with a width of 10 mm and a thickness of 1 mm. The overall thickness of the solar modules was less than 2 mm.

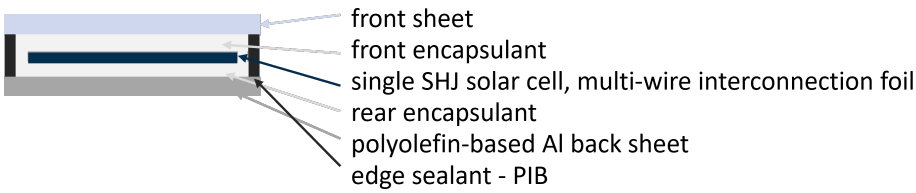


Figure 5.5: Schematic cross-section of the lightweight SHJ single-cell solar module.

Table 5.1 lists the configurations of the test solar modules with different encapsulants. The solar modules were fabricated by a vacuum lamination process. The solar module fabrication process is shown in Figure 3.9. The parameters of the lamination process for each sample type are listed in Table Table A.3. Two identical solar modules were fabricated for each configuration. The maximum deviation in efficiency of all SHJ solar cells used for solar module fabrication is less than 1.50%$_{\mathrm{rel}}$.

Table 5.1: Configurations of the test solar modules with different encapsulants.

Module No.	Front sheet	Encapsulant (front/rear)	Interconnection	Back sheet
5.1	ETFE	TPO	IF1	Al-bs
5.2	ETFE	TPU	IF1	Al-bs
5.3	ETFE	PO-UV	IF1	Al-bs
5.4	ETFE	EPE	IF1	Al-bs
5.5	ETFE	EVA	IF1	Al-bs
5.6	ETFE	PO-S	IF1	Al-bs
5.7	ETFE	DS-EVA	IF1	Al-bs
5.8	ETFE	DS-EPE	IF1	Al-bs

CTM loss analysis

The variations in the electrical parameters from cell to module (CTM) of lightweight solar modules with different encapsulants are shown in Figure 5.6. The efficiency loss from the solar cell to the solar module is mainly attributed to the loss of *FF* and J_{sc}. The *FF* loss is mainly due to the increase in R_s after solar cell interconnection. The J_{sc} loss is mainly due to the light reflection from the front surface and light absorption by encapsulant materials. The TPO module shows the least CTM efficiency loss, mainly due to its lower increase in *FF* loss. The EVA module shows the largest CTM efficiency loss, mainly due to its higher increase in *FF* loss. The PO-UV module shows the largest loss in J_{sc}, which is attributed to its higher UV blocking properties, as indicated in Figure 5.1. The solar modules with different encapsulants show variations in initial performance, which is highly related to the properties of the encapsulants. The difference in these properties also has a different influence on the long-term stability and durability of solar modules.

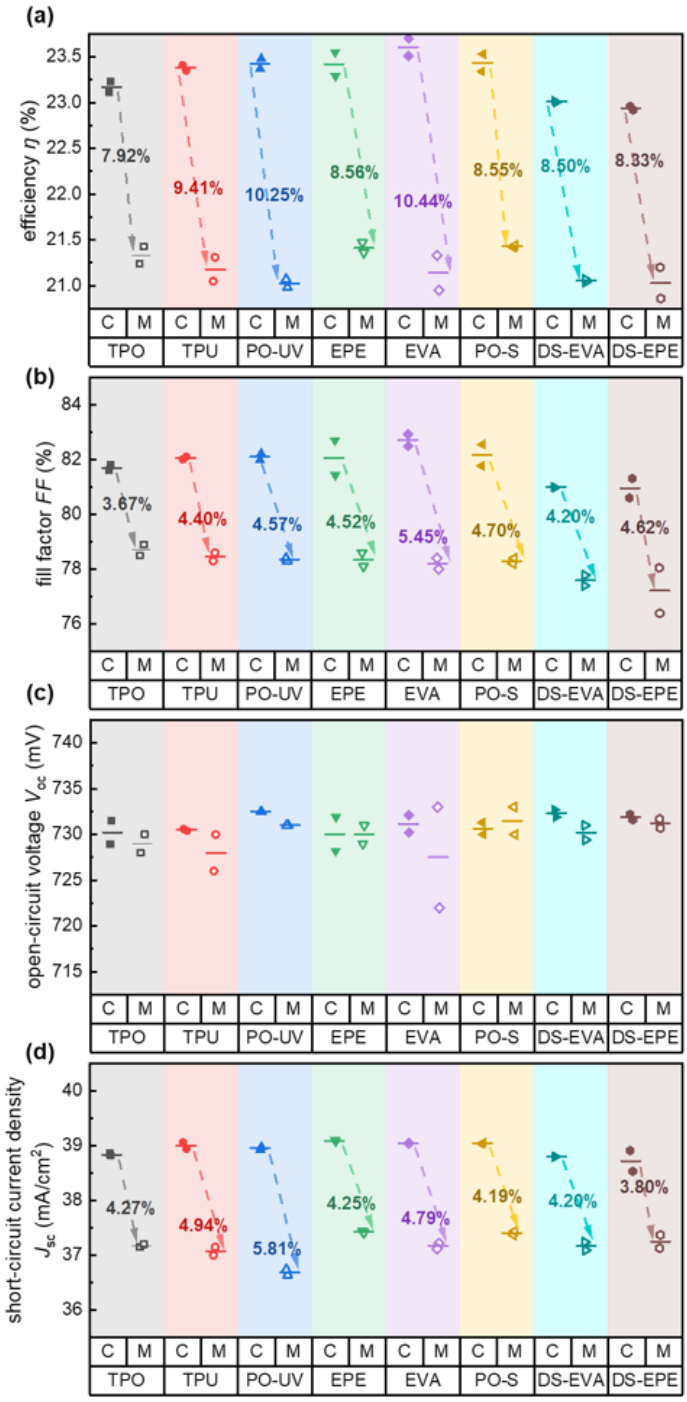


Figure 5.6: CTM loss of (a) efficiency (η), (b) fill factor (FF), (c) open-circuit voltage (V_{oc}) and (d) short-circuit current density (J_{sc}) of solar modules with different encapsulants. 'C' denotes the solar cell, and 'M' denotes the solar module.

5.1.3 DH stability of lightweight SHJ solar modules with different encapsulants

I-V characteristics of solar modules

Figure 5.7 shows the development of the electrical properties of the solar modules encapsulated with different encapsulants over a regular time interval (200 h) during the DH test. It was found that after 1000 h of DH test, the solar module encapsulated with EPE had the largest efficiency degradation of 54.06%$_{\mathrm{rel}}$, whereas the solar module encapsulated with TPO had the lowest efficiency degradation of 3.22%$_{\mathrm{rel}}$. The relative efficiency degradation ($D_\eta{}^{\mathrm{rel}}$) was defined and calculated by

$$D_\eta{}^{\mathrm{rel}}(\%) = (1 - \frac{\eta_{\mathrm{DH1000h}}}{\eta_{\mathrm{DH0h}}}) \times 100. \tag{5.1}$$

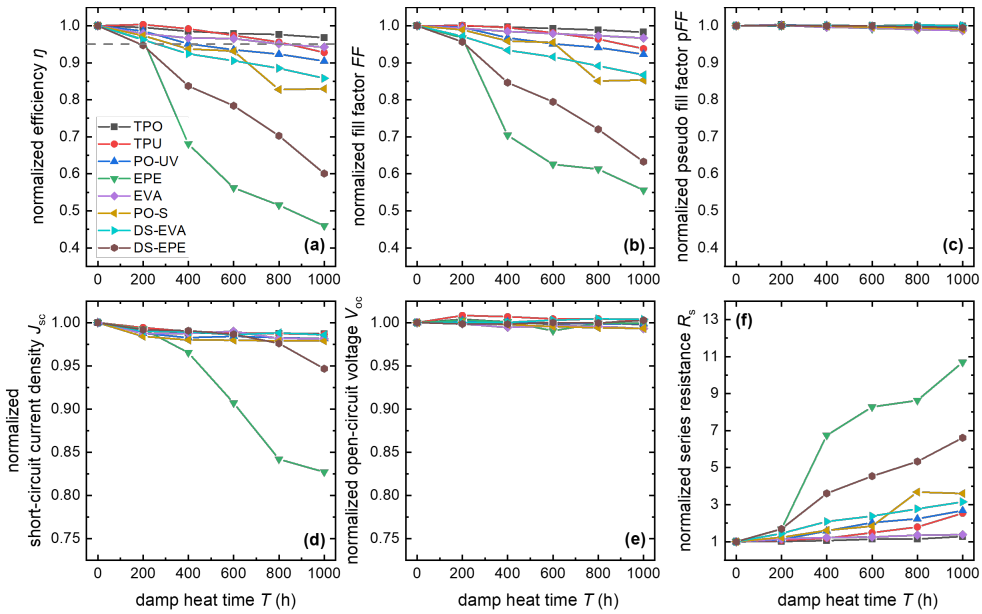


Figure 5.7: Normalized values of (a) efficiency (η), (b) fill factor (FF), (c) pseudo fill factor (pFF), (d) short-circuit current density (J_{sc}), (e) open-circuit voltage (V_{oc}), and (f) series resistance (R_{s}) as a function of damp-heat time for solar modules encapsulated with different encapsulants.

An efficiency/power loss of less than 5%$_{\mathrm{rel}}$ is required for c-Si solar modules by IEC 61215 [112]. However, there is no specific norm for lightweight glass-free modules. It is easy to see that the efficiency degradation of solar modules is mainly due to the decrease in FF. The FF loss was mainly attributed to the increase in R_{s}, as the pFF was almost

constant during DH. Among all the solar modules, the EPE module demonstrates a dramatic increase in R_s, which was assumed to be attributed to the electrical contact problems that probably arise from two parts: the contact between the fingers and wires, and the contact between the wires and ribbons [249]. Additionally, a very large increase in R_s (typical values are from 0.8 - 10 Ω/cm^2) would lead to a decrease in J_{sc} [205, 250], which was also observed in the EPE module. In addition, the DS-EPE module also demonstrated a significant increase in R_s.

The TPO-encapsulated solar module exhibited the most stable performance with slower degradation kinetics during DH aging compared to the other investigated encapsulants. From the perspective of material properties, TPO exhibits the highest degree of crystallinity compared to POE and EVA, as reported by Oreski et al. [23, 93]. In terms of thermo-mechanical stability, TPO exhibits the most stable behavior due to its high melting temperature, resulting in low thermal expansion [23, 93]. Studies also show that crystallinity has a dominant effect on the thermo-mechanical behavior of encapsulants [23], which explains why TPO exhibits better thermo-mechanical stability. In addition, TPO encapsulants have good hydrolytic stability due to their specific low chemical polarity and high crystallinity [93]. The TPO and ETFE laminated film exhibits low WVTR, as shown in Figure 5.2, and thus could provide better resistance to moisture ingress compared with other investigated encapsulants.

Moisture ingress can trigger DH-induced defects. However, from the WVTR results shown in Figure 5.2, there is no direct relationship between the WVTR of encapsulation materials and the solar module efficiency degradation. The degradation of the lightweight silicon heterojunction solar modules is the consequence of the synergistic effect of moisture ingress and the properties of the polymer material. These properties depend not only on hydrolytic properties, but also on factors such as chemical composition and thermo-mechanical properties.

EL imaging of solar modules

Figure 5.8 shows the EL images taken at low current injection conditions with an exposure time of 3 s for all solar modules before and after 1000 h of DH test. EPE and DS-EPE solar modules showed significant defects in the EL images, while the EPE module showed very specific defects in the EL images. Looking at the EL images of the EPE module shown in Figure 5.8(d), a dark band, which is marked by a red rectangular shape, was found on the top of the EPE module after 1000 h of the DH test, probably caused by the contact failure between the wires and ribbons. This defect was also observed in the DS-EPE module, as shown in Figure 5.8(h).

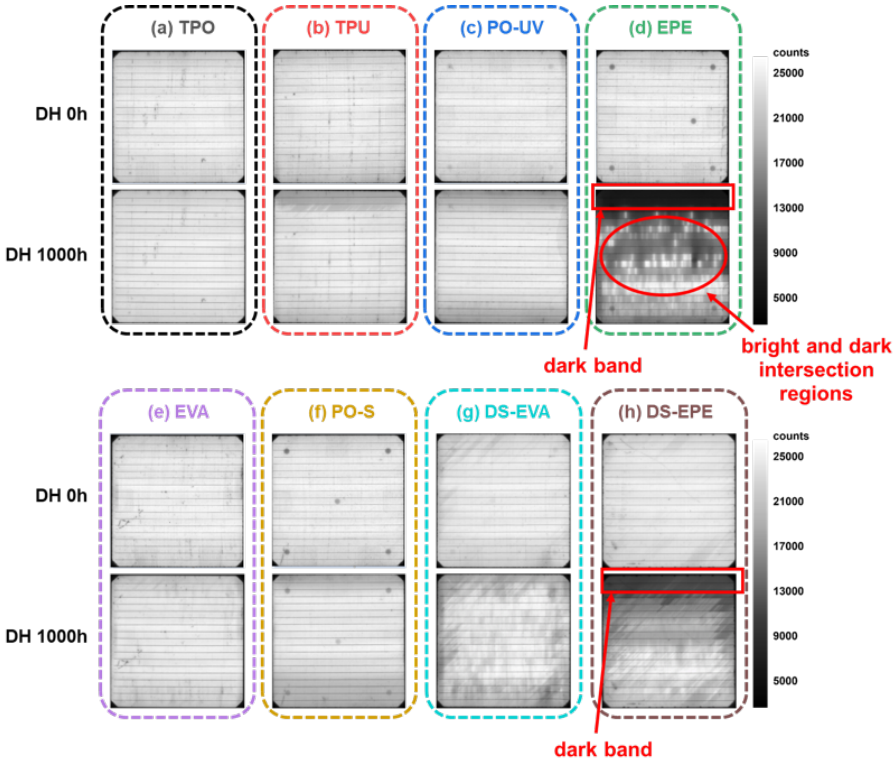
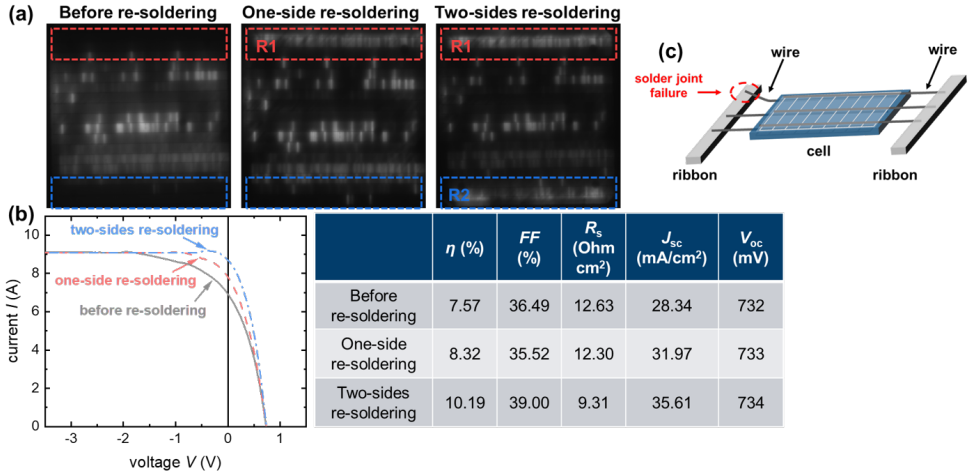


Figure 5.8: EL images (low current injection, $J = 2.05$ mA/cm^2) of the solar modules with different encapsulants before and after 1000 h of the DH test.

To investigate this issue further, a re-soldering process was performed on another EPE module with the same configuration, which underwent the same DH test batch and showed identical defects to those observed in the EPE module shown here. The EL images and I-V characteristics were measured again after each re-soldering process, as shown in Figure 5.9. The efficiency of the EPE module was increased to 10% after the wires were resoldered with ribbons. The R_s was reduced, and J_{sc} also improved. Additionally, examining the light I-V curves shown in Figure 5.9(b), the current in the reverse-bias voltage can reach saturation, indicating that the decrease in J_{sc} is due to the increase in R_s rather than being influenced by optical degradation. The significant increase in R_s affected the transport of the carriers, resulting in a decrease in J_{sc}. Moreover, the dark band in the EL was eliminated. This indicates that the dark band in the EL of the EPE and DS-EPE solar modules was caused by the detachment of the contacts between the wires and ribbons due to the solder joint failure, resulting in a significant increase in R_s. Figure 5.9(c) shows a schematic of the solder joint failure between wire and ribbon. A slight bending of the solar module edges was observed because of the elevated temperature during the DH process, as the lightweight solar module was not as rigid as the glass solar

module. The solar modules were placed vertically in a holder within the climate chamber, and the edges in contact with the holder were easily softened by the high temperature. This increases the risk of solder joint deterioration, resulting in wire detachment from the ribbon.



	η (%)	FF (%)	R_s (Ohm cm^2)	J_{sc} (mA/cm^2)	V_{oc} (mV)
Before re-soldering	7.57	36.49	12.63	28.34	732
One-side re-soldering	8.32	35.52	12.30	31.97	733
Two-sides re-soldering	10.19	39.00	9.31	35.61	734

Figure 5.9: (a) EL images of the EPE solar module before and after two re-solderings. The dark band defects are marked by red and blue dashed rectangles. R1 stands for the first re-soldering. R2 stands for the second re-soldering, which means that the two sides were re-soldered. (b) Light I-V curves of the EPE solar module before and after two re-solderings and the corresponding I-V characteristics. (c) Schematic of the solder joint failure between wire and ribbon.

In addition to this dark band defect, we also observed another defect in the EL of the EPE solar module. Some bright and dark intersection regions can be seen in the EL image of the EPE solar module, as shown in Figure 5.9(d). In general, contact failure could be induced by chemical corrosion, such as acetic acid formation, or thermal stress [176]. We suspected that this defect was probably caused by contact failure between the fingers and wires due to thermal stress, rather than corrosion of the metallization. Corrosion of metal contacts is mostly prominent when using EVA encapsulants, which form acetic acid [23]. Acetic acid formation can also occur with EPE encapsulants. However, there is no indication of increased acetic acid in the EPE module after 1000 h of the DH test from Raman Spectroscopy analysis. The solar cell is additionally protected by a polyethylene interconnection foil, which is in direct contact with the solar cell and sits between the solar cell and the encapsulant. The moisture/acetic acid would degrade the surface of the solar cell (e.g., ITO) earlier than corrode contacts [19]. The defect is supposed to expand due to the diffusion of moisture/acetic acid. However, the expansion of such defects was not observed in the evolution of the EL images at 200-hour intervals, as shown in Figure 5.10. It is identified that the defect occurred between 200 and 400 h, and that the defect was

exacerbated by prolonging the DH aging time. Meanwhile, the efficiency degradation shows a significant drop between 200 and 400 h. Therefore, we can temporarily conclude that this bright and dark intersection defect was primarily caused by contact failure due to thermal stress. A detailed microscopic analysis of this defect was carried out using XCT as described in Subsection 5.1.3.

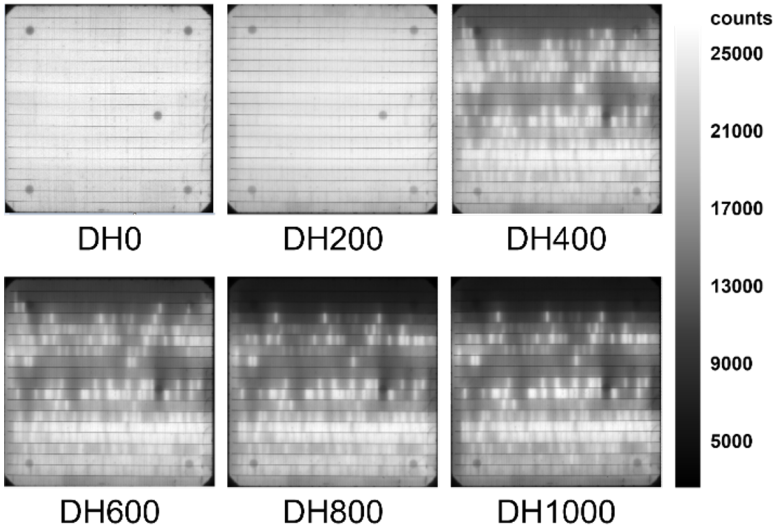


Figure 5.10: Evolution of EL images (low current injection, $J = 2.05$ mA/cm^2) of the EPE solar module in every 200 hours during DH aging.

In the DS-EVA module, defects in the EL image are also likely to be caused by the interconnection issue between the fingers and interconnection wires. Additionally, an edge defect [228] due to the moisture ingress from the solar module edges was also observed in the DS-EVA module. The bands with lower luminescence were also found in EL images in TPU, PO-UV, and PO-S modules, and are also likely to be caused by the degradation of the contact between the wires and ribbons. For the rest of the solar modules, we did not observe any obvious defects in the EL images.

X-ray computed tomography

To have a deep understanding of the bright and dark intersection region defect in the EL of the EPE module. XCT was used for an in-depth investigation. A strip of the degraded EPE module was selected and cut out for X-ray scanning. The area selected for X-ray scanning is marked by a blue rectangle in Figure 5.11(a) and is divided into eight regions of interest (ROI) from ROI1 to ROI8. Two areas (ROI1-ROI2 and ROI7-ROI8), which contained two distinct EL intensities, were selected for further XCT scanning analysis.

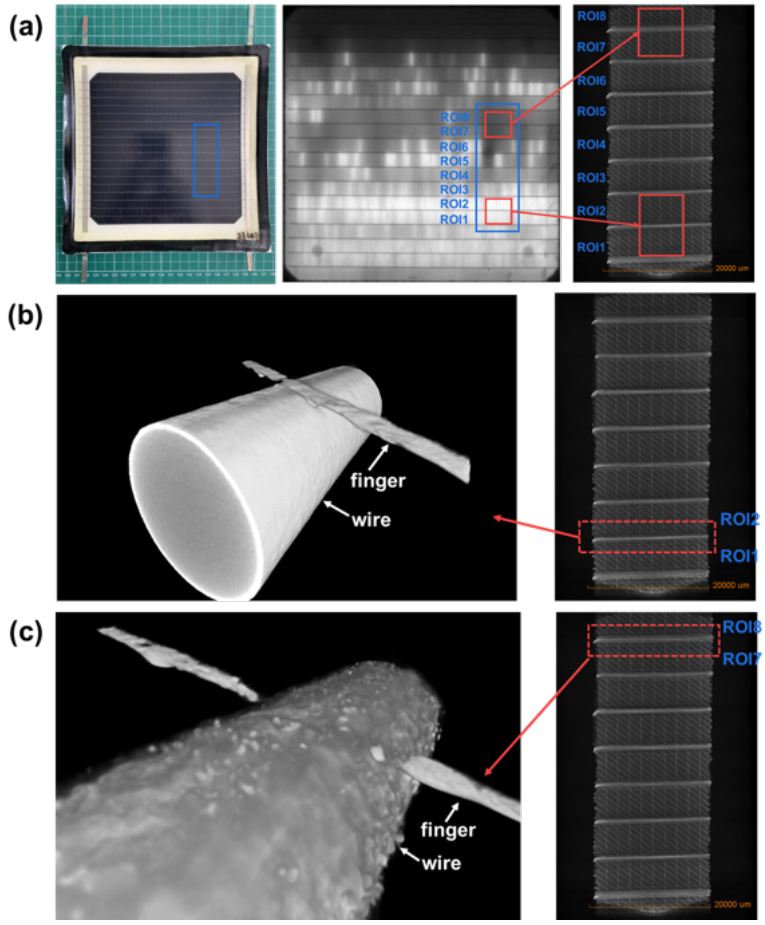


Figure 5.11: X-ray computed tomography (XCT) of the degraded EPE solar module: (a) X-ray scanning of two areas, ROI1-ROI2 and ROI7-ROI8, which contain two distinct EL intensities. (b) Reconstructed image showing intact interaction of the finger with the wire in the ROI1-ROI2 area. (c) Reconstructed image showing finger breakage in the ROI7-ROI8 area. The XCT images were taken by Zeiss Xradia Versa 620, voxel size is 740 nm, X-ray tube voltage is 100 kV, exposure time per projection is 15 s, and the number of projections is 1200.

From the reconstructed images in Figure 5.11(b), we can clearly see the intact interaction of the finger and wire in the ROI1-ROI2 area. However, we found the finger breakage in the ROI7-ROI8 area, as shown in Figure 5.11(c), which was caused by the detachment of the wires, resulting in contact failure between the fingers and wires. It is reported that the thermal loading creates deformation in copper wires, and this deformation is stored in the copper wires as strain energy. As the strain energy accumulates with increased thermal loading, this eventually results in fatigue failure [251, 252]. As discussed in the EL imaging analysis. We believed that the decrease in conductivity between the wires and

fingers was caused by the wires detaching from the fingers due to thermal stress during the DH process. This was confirmed by the results of the XCT analysis. In a solar module, each layer has a different coefficient of thermal expansion (CTE), and these differences can create thermal stresses during temperature changes [251]. Differential expansion and contraction of materials with varying CTE can lead to cracking, solder joint fatigue, and interface delamination, thus affecting the long-term reliability of the solar module. However, the investigation of the degradation mechanism of the thermo-mechanical properties of the solar module is beyond the scope of this work.

The above analyses from EL imaging and XCT confirm that the increase in R_s in the EPE module is primarily caused by solder joint failures between the wires and ribbons, and interconnection failures between the fingers and wires.

Visual inspection of solar modules and optical properties analyses of encapsulants

In addition to analyzing the electrical properties of the solar modules before and after the DH test, a visual inspection of the solar modules was carried out to identify defects such as cracks, discoloration, delamination, and soldering defects. Visual images of all types of solar modules before and after the DH test are shown in Figure 5.12.

From the visual inspection of the solar module, a slight bending at the edges of the solar module was observed. Because the solar modules were placed vertically in a holder in the climate chamber, the edges softened owing to the elevated temperature. Additionally, an obvious yellowing effect was observed in the EVA module, particularly at the edges of the solar module (over the white back sheet), as shown in Figure 5.13(a). Several investigations have shown that EVA discoloration (yellowing or browning) results primarily from the formation of polyconjugated C=C bonds (polyenes) by multistep deacetylation and the presence of 1,3-unsaturated carbonyl groups due to thermal oxidation, and is enhanced by increased UV radiation [62, 63, 253]. Another source for discoloration is the production of chromophores and luminophores from additives in encapsulant and not from the encapsulant itself [63]. In our case, a single DH process without UV radiation resulted in a light yellowing effect.

To identify the changes in the optical properties of the encapsulants, the solar modules were dismantled to obtain aged encapsulants. The transmittance and reflectance spectra of the aged encapsulants were measured and compared with those of unaged encapsulants. The EVA encapsulant exhibited a minor reduction in transmittance in the 300 - 400 nm wavelength range, whereas the reflectance remained constant before and after DH, as shown in Figure 5.13(b). This indicates that the optical loss from the encapsulant was mainly due to the increased light absorption. Therefore, we observed only a $0.93\%_{\mathrm{rel}}$

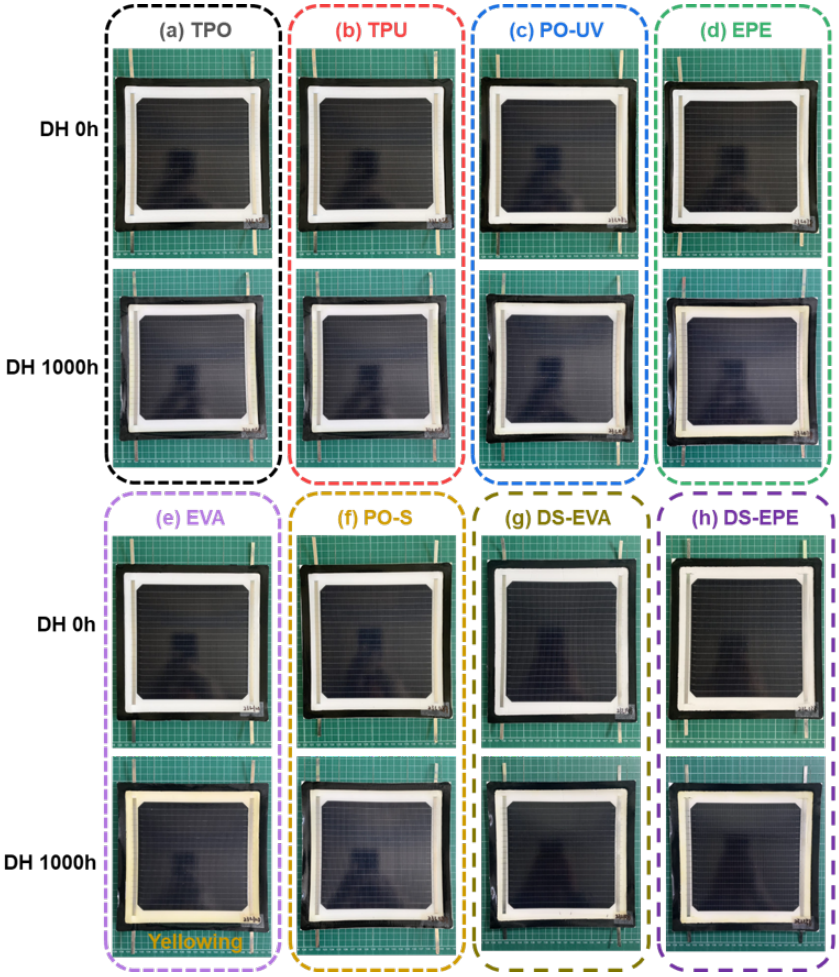


Figure 5.12: Visual images of modules encapsulated with different encapsulants (a) TPO, (b) TPU, (c) PO-UV, (d) EPE, (e) EVA, (f) PO-S, (g) DS-EVA, and (h) DS-EPE before and after 1000 h of the DH test.

reduction in the photocurrent for the EVA module according to the integrated current calculated from the *EQE* measurements, as shown in Figure 5.18(e). This indicates that the negligible reduction in photocurrent was caused by the yellowing effect of the EVA modules. As for the rest of the solar modules, we did not observe any obvious discoloration or other defects.

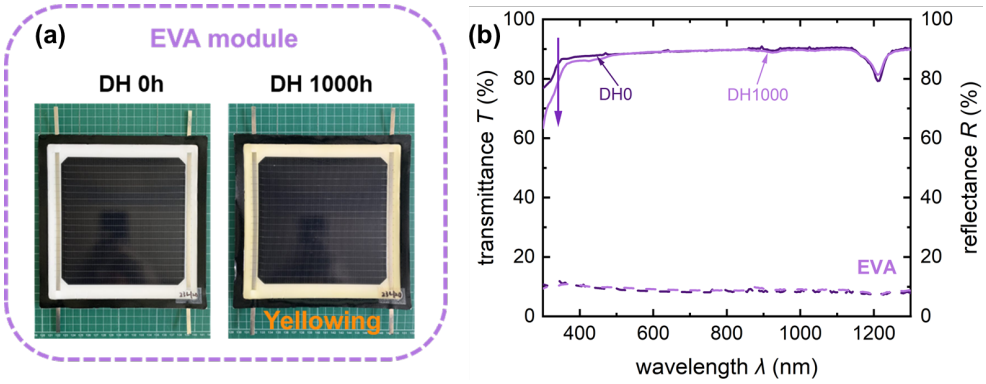


Figure 5.13: (a) Visual images of EVA-encapsulated solar modules before and after 1000 h of the DH test. (b) Transmittance (solid line) and reflectance (dashed line) of EVA encapsulant foil before and after 1000 h of the DH test.

Raman Spectroscopy analysis of encapsulants

Raman Spectroscopy analyses were performed on the encapsulant samples before and after 1000 h of the DH test to further check the polymer encapsulants degradation process. The aged encapsulant samples were obtained from the dismantled solar modules after 1000 h of the DH aging test. The encapsulant sample was positioned at the center and above the solar cell.

Figure 5.14 shows the Raman raw spectra of the different encapsulants before and after 1000 h of the DH tests. This is mainly an investigation of the fluorescence background [234, 236]. A significant increase in the fluorescence background was observed in the DS-EPE module. TPU showed the least increase in the fluorescence background, as shown in Figure 5.14(c). The intensity of the fluorescence background, which is related to the formation of chromophore groups (containing polyconjugated C=C bonds), is an indicator of polymer aging. The chromophore groups can exhibit strong fluorescence and are one reason for the yellowing of the encapsulant [236].

In addition, the raw Raman spectra of the EVA encapsulants at different locations in the EVA module after 1000 h of DH test were analyzed, as shown in Figure 5.15. We obtained EVA-encapsulant samples from three typical positions in the solar module. Two samples were located on the left edge of the solar module, over the white back sheet. Two samples were located on the top edge of the solar module, over the white back sheet. Two samples were located at the center of the solar module over the solar cell. Strong fluorescence background in raw Raman spectra (Figure 5.15) is observed at the left and top edges of the solar module. This indicates that the chromophore groups were mainly generated at the edges of the solar module, resulting in yellowing of the EVA module.

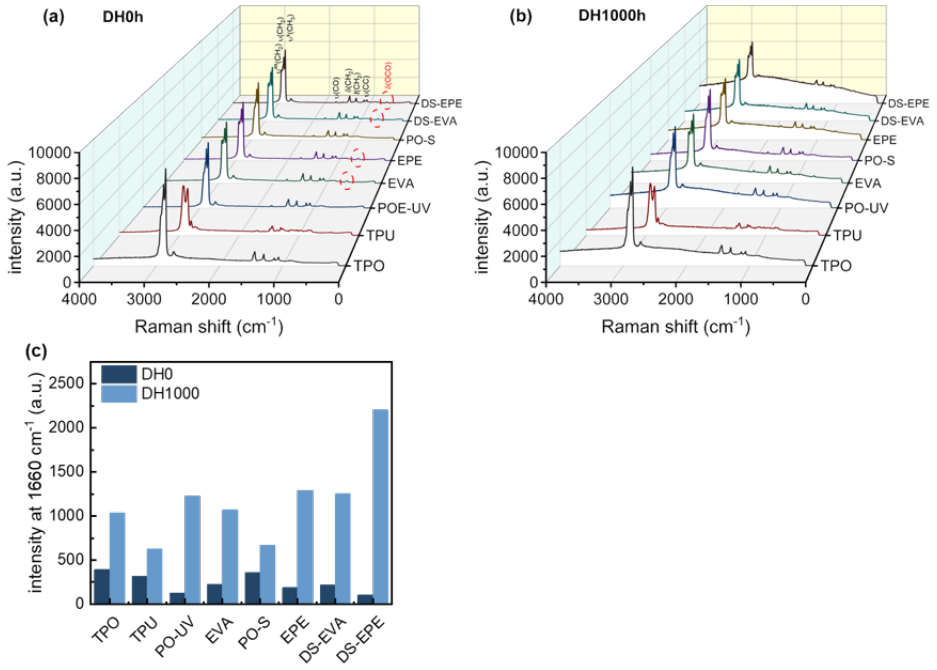


Figure 5.14: Raw Raman spectra of encapsulant samples (a) before and (b) after 1000 h of the DH test. (c) Fluorescence background intensity of the solar modules at 1660 cm^{-1} before and after 1000 h of the DH test.

These findings confirmed that moisture ingress as the driver of discoloration is more severe at the solar module edges than at the center of the solar module.

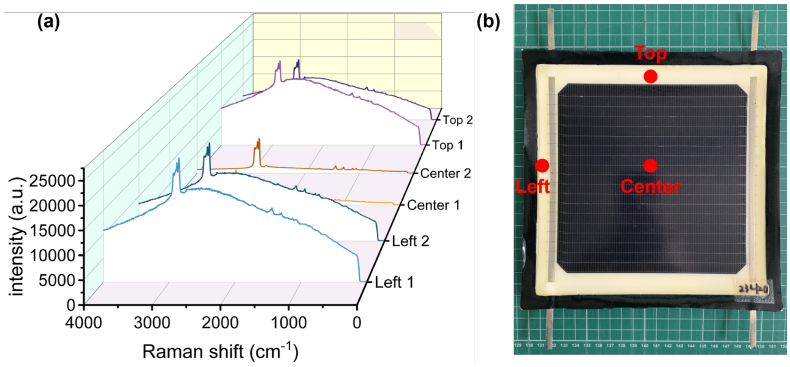


Figure 5.15: (a) Raw Raman spectra of EVA encapsulants at different locations (left, center, and top) in the EVA module after 1000 h of the DH test. (b) Indicating the left, center, and top positions in the solar module.

The normalized Raman spectra are shown in Figure 5.16. We did not observe any obvious decrease in the Raman peaks of encapsulants. The EVA encapsulant is most

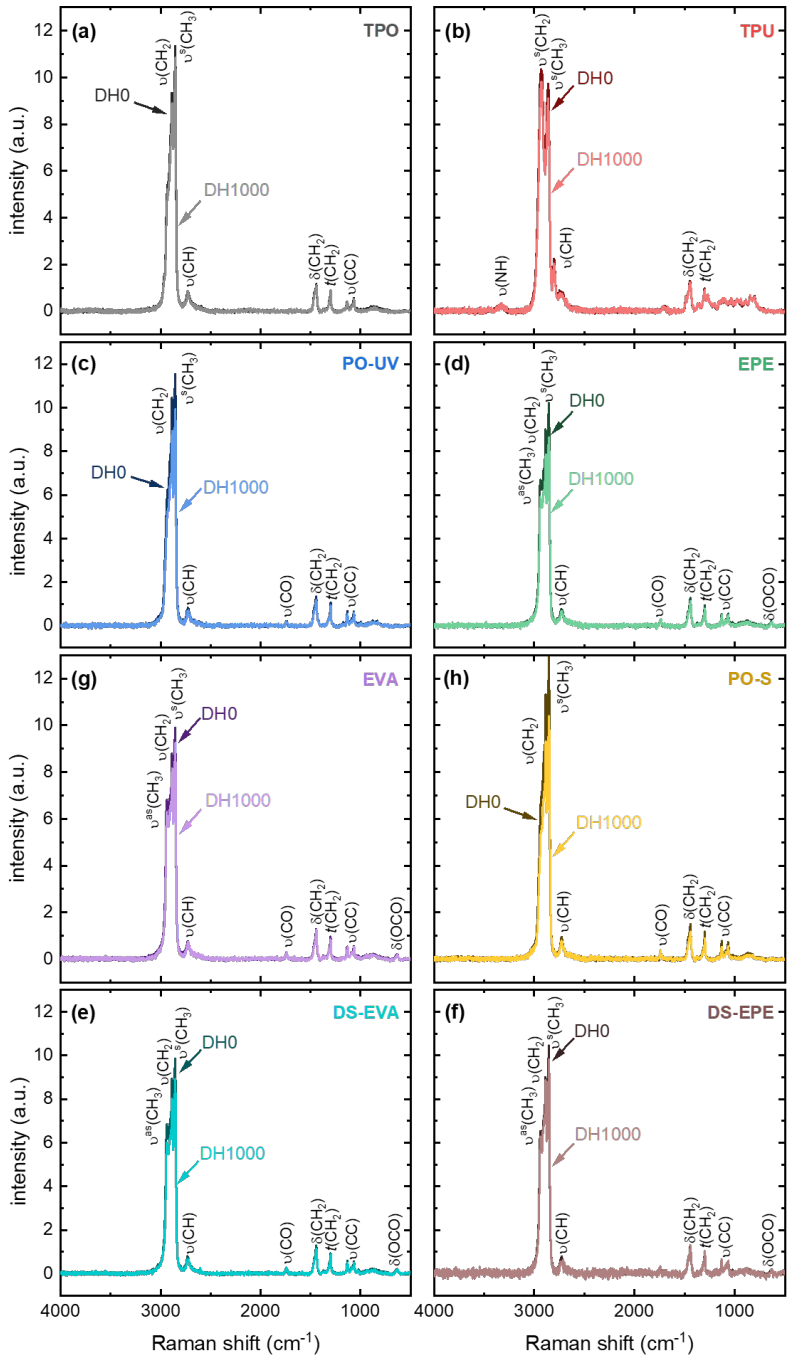


Figure 5.16: Normalized Raman spectra of encapsulant samples (a) TPO, (b) TPU, (c) PO-UV, (d) EPE, (e) EVA, (f) PO-S, (g) DS-EVA, and (h) DS-EPE before and after 1000 h of the DH test.

likely to release acetic acid in the presence of moisture, which can lead to the corrosion of metal grids and other components of solar modules, resulting in an increased R_s. However, the normalized Raman spectra show no sign of an increase in the acetate group (OCO, 629 cm^{-1}). And no typical corrosion defects were observed in the EL imaging. This indicates that there is no formation of acetic acid after DH. The increase in R_s is as low as that of the TPO module, which is free of acid formation. Therefore, we conclude that acid corrosion is not the major degradation mechanism for the EVA module in our case. In addition, for other EVA-containing encapsulants (EPE, DS-EVA, and DS-EPE), the intensity of the acetate group shows no changes before and after 1000 hours of DH, as shown in Figure 5.16. This confirms that failure due to acid corrosion is not the primary degradation mechanism in this work.

FTIR analysis of encapsulants

Figure 5.17 shows the normalized FTIR spectra of the different encapsulants before and after 1000 h of the DH tests. The aged encapsulant samples were obtained from the dismantled solar modules after 1000 h of the DH aging test. The results indicate that most materials undergo oxidative degradation during aging, as evidenced by the appearance or intensification of carbonyl (C=O) absorption bands and other functional group changes. The FTIR spectra of TPO remain largely unchanged after DH exposure, suggesting good structural retention and moderate resistance to thermo-oxidative stress. And the TPO was identified as polyethylene. For TPU, minor changes are observed, including a modest increase in the C=O stretching vibration near 1700 cm^{-1} and a slight enhancement in the N–H stretching region (3300 - 3400 cm^{-1}). These changes suggest degradation of urethane linkages, likely due to chain scission or hydrogen bond rearrangement, highlighting TPU's limited stability under DH conditions. PO-UV and PO-S show a C=O stretching vibration at 1733 cm^{-1} and a corresponding C-O stretching vibration at 1164 cm^{-1}, which can be attributed to a butyl acrylate side group. Moreover, PO-UV and PO-S exhibit excellent DH stability, as their FTIR spectra show virtually no changes after aging. The characteristic C–H stretching bands at 2915 and 2850 cm^{-1}, along with CH_2 bending at 1465 cm^{-1}, remain stable. Notably, no new or intensified carbonyl peaks are observed, indicating strong resistance to oxidation and structural degradation.

For EVA and EVA-containing encapsulants (EPE, DS-EVA, and DS-EPE), an absorption was observed at 1380 cm^{-1} and was attributed to the bending vibration of the methylene (CH_3) group. The bands at 1738 cm^{-1} (C=O stretching), 1240 cm^{-1} (CO(=O) stretching), and 1020 cm^{-1} (C-O-C stretching) are caused by vibrations of the acetate group. EVA displays clear signs of oxidative degradation after DH aging, as evidenced

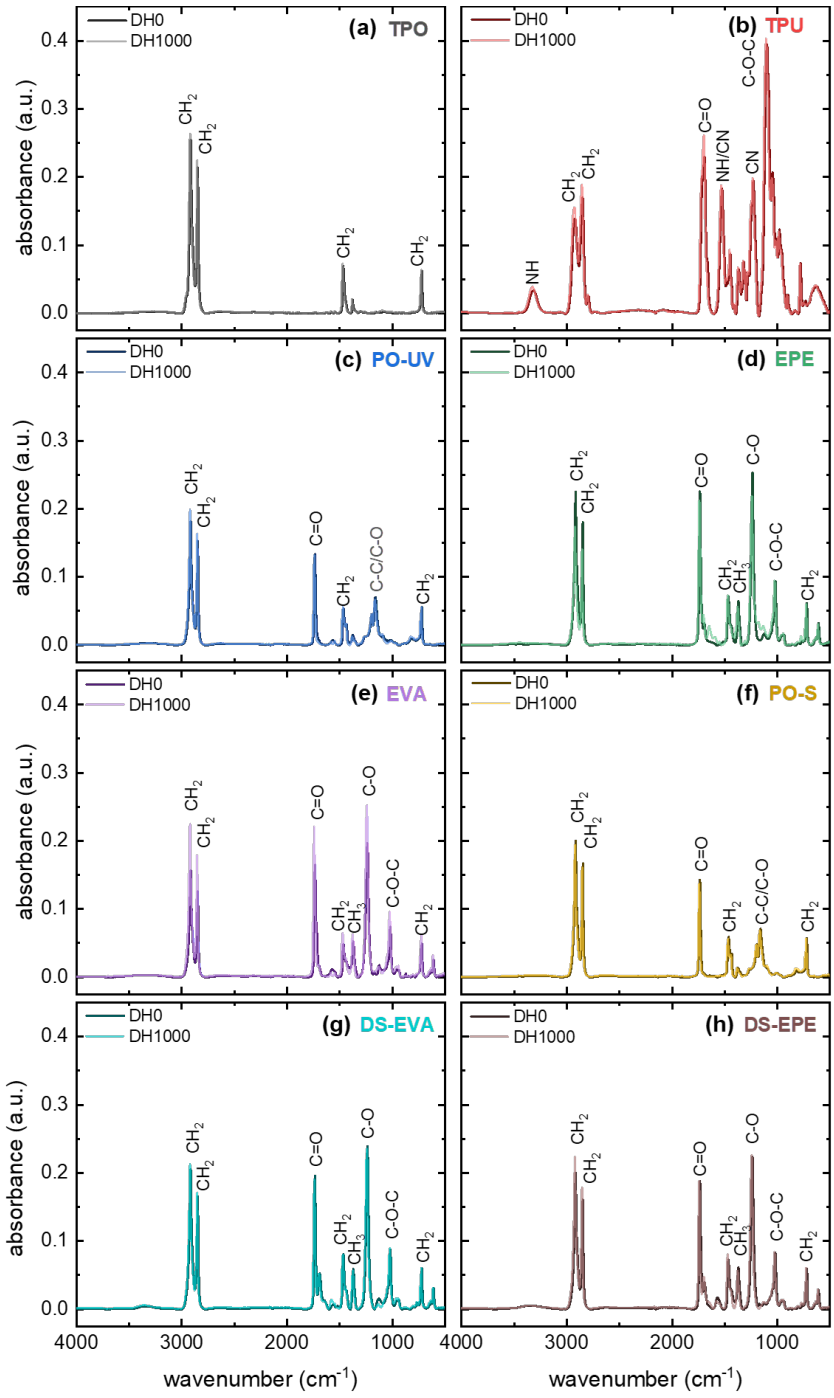


Figure 5.17: Normalized FTIR spectra of encapsulant samples (a) TPO, (b) TPU, (c) PO-UV, (d) EPE, (e) EVA, (f) PO-S, (g) DS-EVA, and (h) DS-EPE before and after 1000 h of the DH test.

by a pronounced increase in the carbonyl absorption around 1735 cm^{-1}. This suggests hydrolysis or oxidation of the vinyl acetate (VA) units, potentially resulting in carbonyl-containing degradation products such as acetic acid. However, since this peak overlaps with those of other carbonyl-containing species (e.g., esters, aldehydes, ketones), it is not conclusive. Additionally, no distinct hydroxyl (O-H) absorption was observed in the 3200 – 3500 cm^{-1} region, which would typically indicate the formation of hydroxyl-containing degradation products like alcohols or carboxylic acids. While a reduction in ester-related C–O peaks near 1240 cm^{-1} would support the occurrence of hydrolysis, an increase in this region was actually observed. Therefore, no direct spectral evidence confirms the formation of acetic acid in EVA following DH aging.

For EPE, a slight decrease in the C–H stretching bands suggests potential chain scission and polymer backbone degradation. However, similar to EVA, no direct FTIR evidence of acetic acid generation was observed. DS-EVA and DS-EPE exhibit relatively minor changes in the C=O region after DH aging, and the other characteristic absorption bands (C–H, C–O) remain largely stable. These results imply good resistance to DH-induced degradation.

EQE analysis of solar modules

In addition, *EQE* and reflectance analyses were conducted on the solar modules before and after 1000 h of the DH test. A general minor decrease in the spectral response of EQE from 400 - 1200 nm was observed for the modules encapsulated with DS-EVA and DS-EPE, as shown in Figure 5.18(g) and (h). This was due to a slight increase in light absorption ($A = 1 - T - R$) of the encapsulants after the DH test, as shown in Figure 5.19. Moreover, an apparent decrease in *EQE* and a slight decrease in reflectance in the short-wavelength range (280 - 400 nm) were also observed for these two types of modules, which is attributed to a deterioration in the UV-downshifting effect and/or an increase in the light absorption. Overall, the photocurrent losses due to the changes in optical properties of the encapsulants were $1.72\%_{rel}$ for the DS-EVA module and $1.98\%_{rel}$ for the DS-EPE module. The downshifting encapsulants shed light on protecting advanced cell technologies from UV degradation while simultaneously utilizing UV light. However, more attention should be paid not only to the UV stability but also to the DH stability of such new encapsulants when combined with unconventional module structures, such as lightweight solar module structures. Further investigation into its DH and UV stability is presented in.

A slight reduction in *EQE* from 280 - 500 nm was observed in the EVA module, as shown in Figure 5.18(e). This reduction was attributed to the increased parasitic absorption of the EVA encapsulant after 1000 h DH, as discussed in the *Visual inspection*

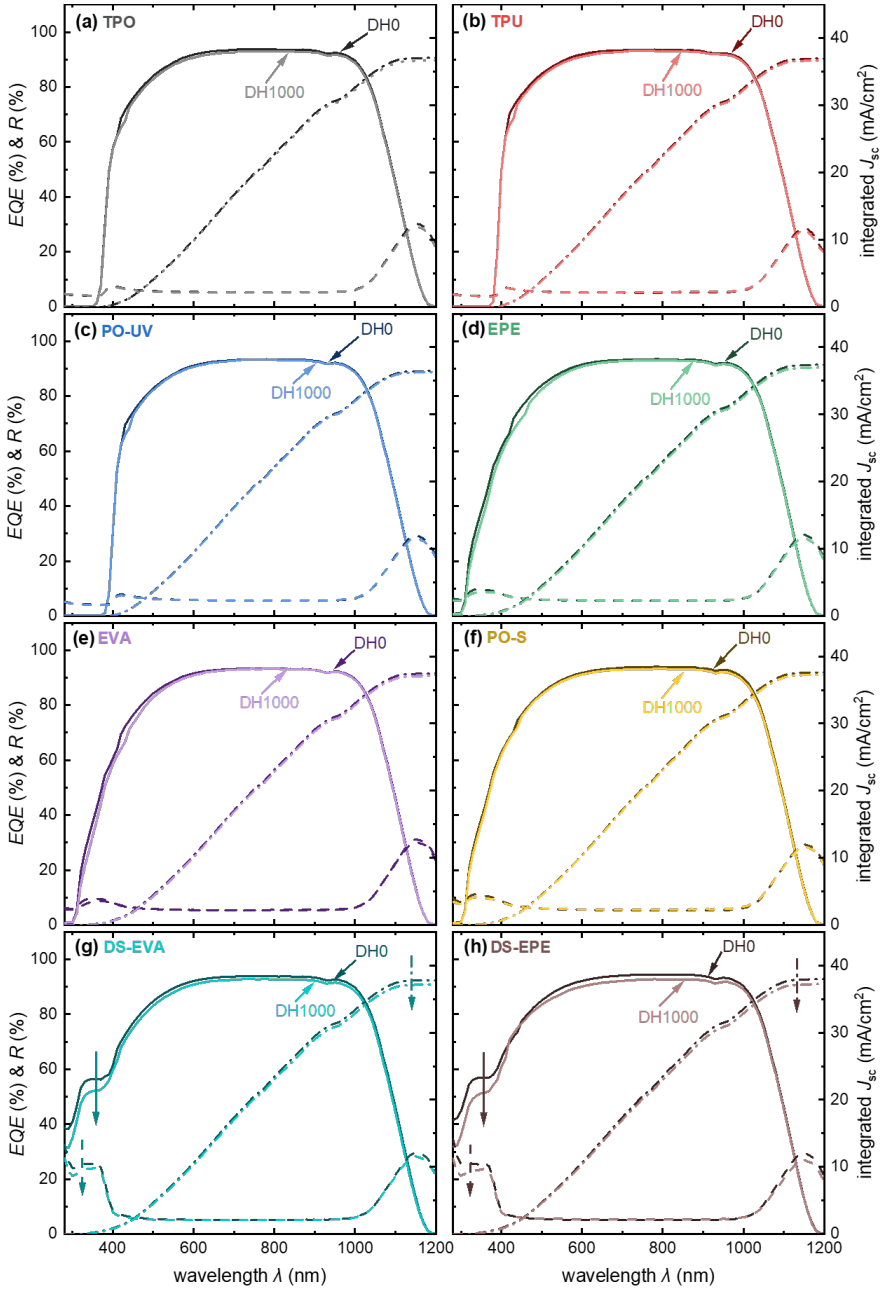


Figure 5.18: *EQE* (solid line), reflectance (dashed line), and integrated short-circuit current density (J_{sc}) (dashed dot line) of the modules encapsulated with different encapsulants: (a) TPO, (b) TPU, (c) PO-UV, (d) EPE, (e) EVA, (f) PO-S, (g) DS-EVA, and (h) DS-EPE before and after 1000 h of the DH test.

and optical properties analyses. For the remaining solar modules, we observed no obvious change in *EQE* and reflectance before and after DH, as shown in Figure 5.18.

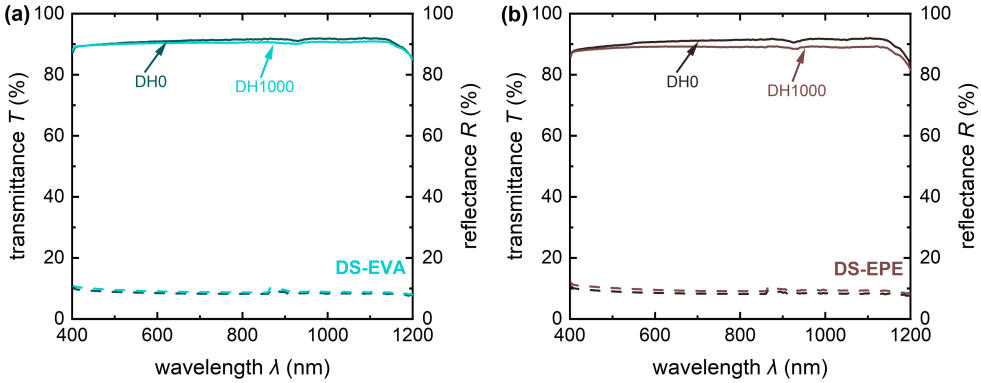


Figure 5.19: Transmittance T (solid line) and reflectance R (dashed line) of (a) DS-EVA encapsulant foil and (b) DS-EPE encapsulant foil before and after 1000 h of the DH test.

5.2 Optimized DH stability of lightweight solar modules with different front sheets

The optimum combination of different encapsulants with SHJ solar cells within a lightweight module structure was determined in Section 5.1. The lightweight module with TPO as the encapsulant, ETFE as the front sheet, and polyolefin-based foil with an aluminum interlayer as the back sheet showed the most damp-heat-stable performance, with only $3.22\%_{\text{rel}}$ efficiency degradation after 1000 h of the DH test compared with modules using other encapsulants. The efficiency degradation of such lightweight modules is even lower than the $5\%_{\text{rel}}$ required by IEC 61215 [112] for glass modules. To further enhance the damp-heat stability of the lightweight modules, this section investigated various front sheet materials, including ETFE, PVF (polyvinyl fluoride), and PET/PVF laminated foil (denoted as PET1), as well as PET (PET2 and PET3 from different suppliers).

5.2.1 Configurations of solar modules with different front sheets

Design and fabrication of solar modules

Table 5.2 lists the configurations of the test solar modules with different front sheets. The optical properties of the different front sheets were characterized by UV/vis spectroscopy.

Figure 5.20 shows the transmittance and reflectance of different front sheets. The ETFE has the highest transmittance and is also transparent to UV light. While PVF, PET1, PET2, and PET3 block UV light. The specifications of the front sheets are listed in Table A.2. Figure A.1 shows the structural formula of typical polymer encapsulants. All the solar modules used TPO as encapsulants. A polyolefin-based foil with an aluminum interlayer was used as the back sheet. The glass/glass and glass/back sheet solar modules were used as references for comparison. The solar modules were fabricated by a vacuum lamination process. The solar module fabrication process is shown in Figure 3.9. The parameters of the lamination process for each sample type are listed in Table Table A.3. Two identical solar modules were fabricated for each configuration. The maximum deviation in efficiency of all SHJ solar cells used for solar module fabrication is less than $1.50\%_{\mathrm{rel}}$.

Table 5.2: Configurations of the test solar modules with different front sheets.

Module No.	Front sheet	Encapsulants (front/rear)	Interconnection	Back sheet
5.1	ETFE	TPO	IF1	Al-bs
5.9	PVF	TPO	IF1	Al-bs
5.10	PET1	TPO	IF1	Al-bs
5.11	PET2	TPO	IF1	Al-bs
5.12	PET3	TPO	IF1	Al-bs
5.13	Glass	TPO	IF1	Al-bs
5.14	Glass	TPO	IF1	Glass

Figure 5.21 shows the power-to-weight ratio (solar module output power divided by solar module weight) and area density (solar module weight divided by solar module area) of the solar modules for each configuration. Lightweight solar modules have a lower area density while keeping a higher power-to-weight ratio compared to conventional glass/glass and glass/back sheet solar modules, demonstrating their great potential for integrated PV applications.

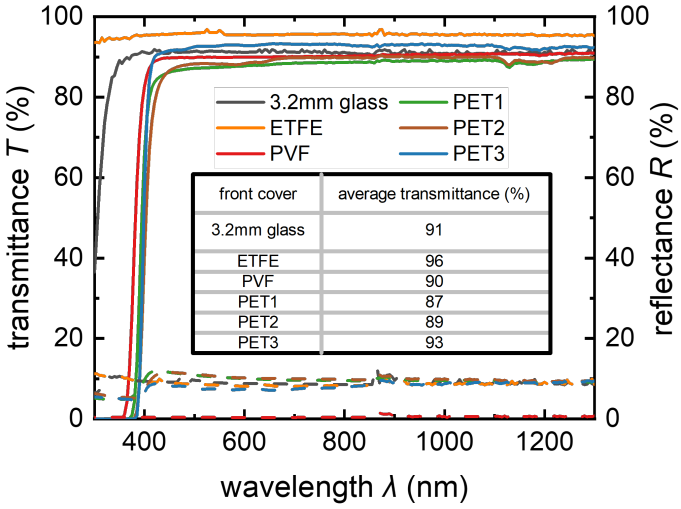


Figure 5.20: The transmittance (T, solid line) and reflectance (R, dashed line) of different front sheet materials.

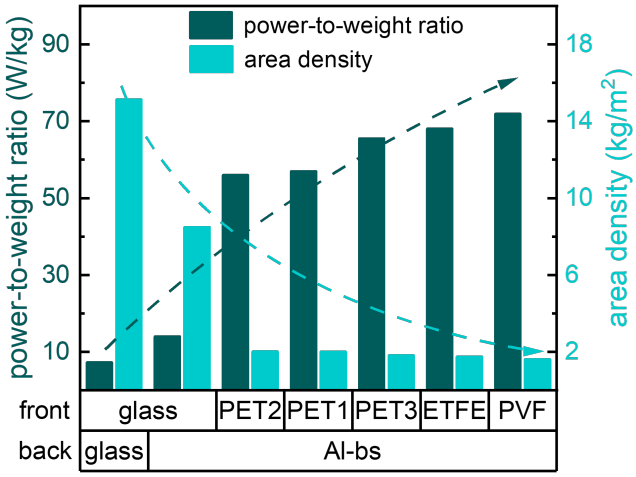


Figure 5.21: Power-to-weight ratio and area density of solar modules with different configurations.

CTM loss analysis

Figure 5.22 shows the electrical performance loss from cell-to-module (CTM) for solar modules with different configurations. The CTM efficiency loss was calculated by

$$CTM(\%) = (1 - \frac{\eta_{\text{module}}}{\eta_{\text{cell}}}) \times 100. \tag{5.2}$$

In general, the CTM efficiency loss is mainly attributed to the decrease in J_{sc} and the increase in R_s, as shown in Figure 5.22. The CTM J_{sc} loss is related to the different optical properties of the different front sheets, as shown Figure 5.20, and the light absorption by the front side TPO encapsulant. The PET3 module had the lowest CTM efficiency due to its low J_{sc} loss and the small increase in R_s. However, the glass/glass solar module had the highest CTM J_{sc} loss. This is because the glass is also used as a back cover, which does not have the benefit of reflecting light from the rear side, compared to other solar modules that use a white back sheet.

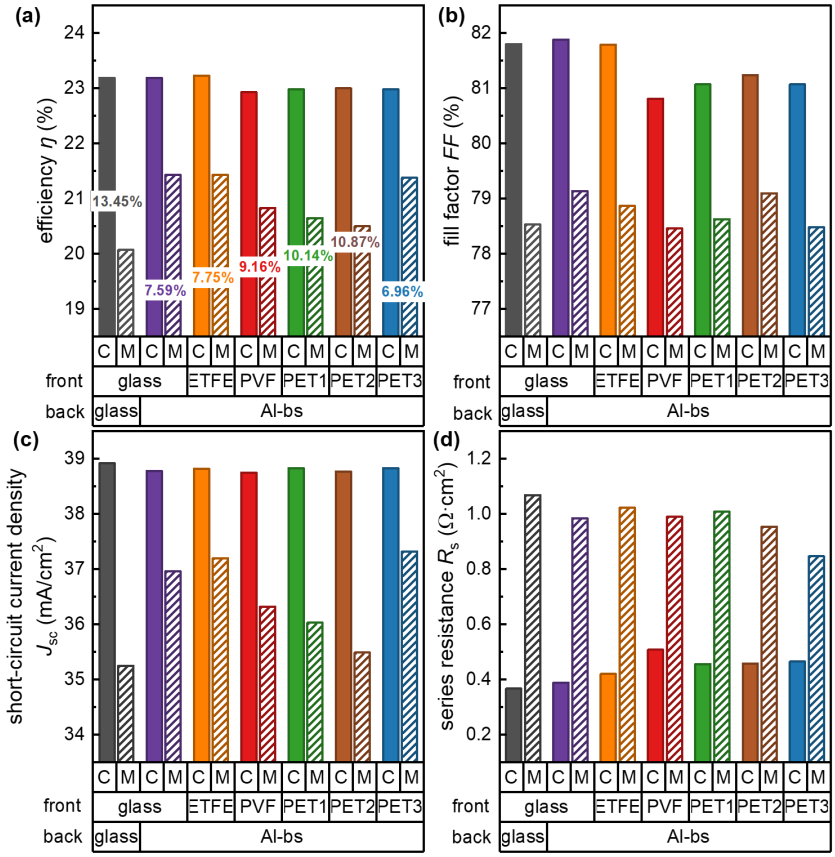


Figure 5.22: CTM loss from (a) efficiency (η), (b) fill factor (FF), (c) short-circuit current density (J_{sc}), and (d) series resistance (R_s) of solar modules with different configurations. 'C' denotes solar cell, and 'M' denotes solar module. The numbers in the graph indicate the CTM efficiency loss.

5.2.2 DH stability of lightweight SHJ solar modules with different front sheets

Figure 5.23 shows the development of the electrical properties of the solar modules with different front sheets after 1000 h of DH test. It was found that replacing the ETFE with a PET3 front sheet reduced the solar module efficiency degradation from $3.22\%_{\mathrm{rel}}$ to $0.47\%_{\mathrm{rel}}$ after 1000 h of DH test. Its damp-heat stability is the same as that of a traditional glass/back sheet solar module. We did not find any obvious defects in these solar modules after 1000 h of DH by visual inspection, as shown in Figure 5.24 and the EL images, as shown in Figure 5.25. The increase in R_{s} due to the damp-heat effect was still the major cause of solar module efficiency degradation after 1000 h of DH test.

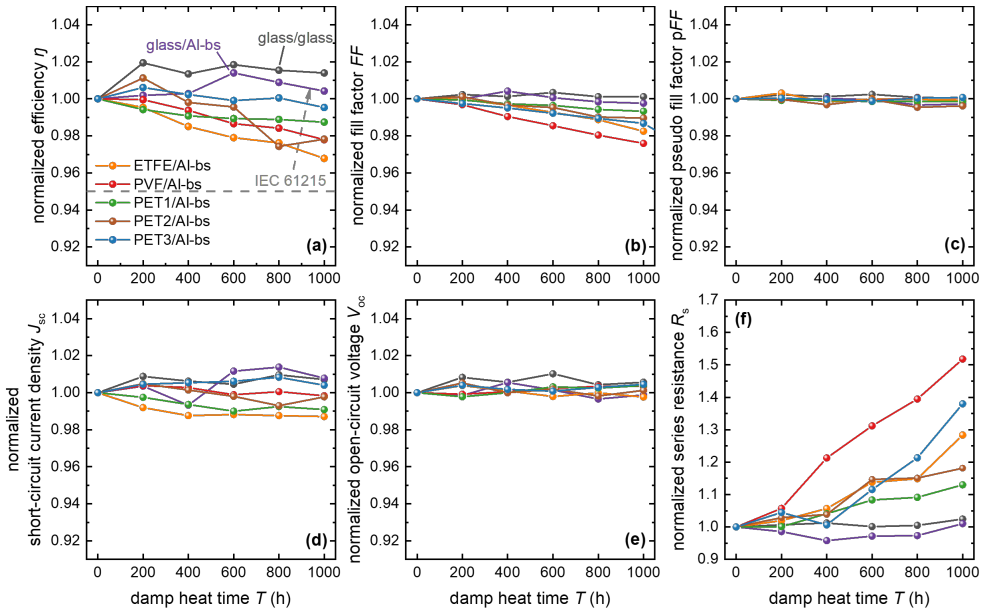


Figure 5.23: Normalized values of (a) efficiency (η), (b) fill factor (FF), (c) pseudo fill factor (pFF), (d) short-circuit current density (J_{sc}), (e) open-circuit voltage (V_{oc}), and (f) series resistance (R_{s}) as a function of damp-heat time for solar modules encapsulated with different front sheets.

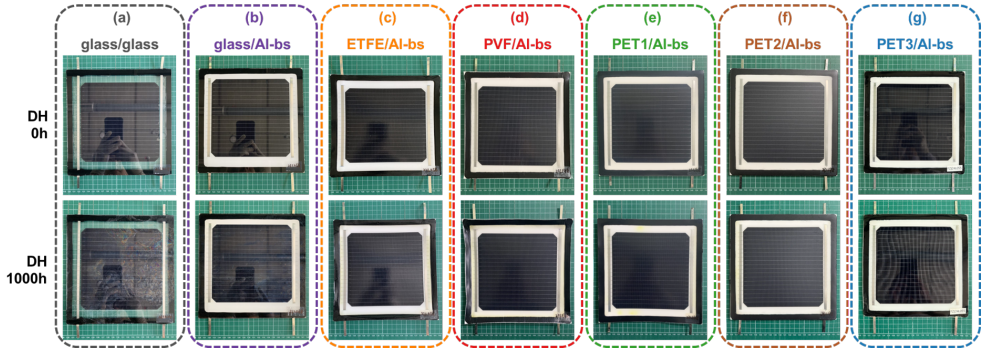


Figure 5.24: Visual images of solar modules encapsulated with different configurations (a) glass/glass, (b) glass/Al-bs, (c) ETFE/Al-bs, (d) PVF/Al-bs, (e) PET1/Al-bs, (f) PET2/Al-bs, and (g) PET3/Al-bs before and after 1000 h of the DH test.

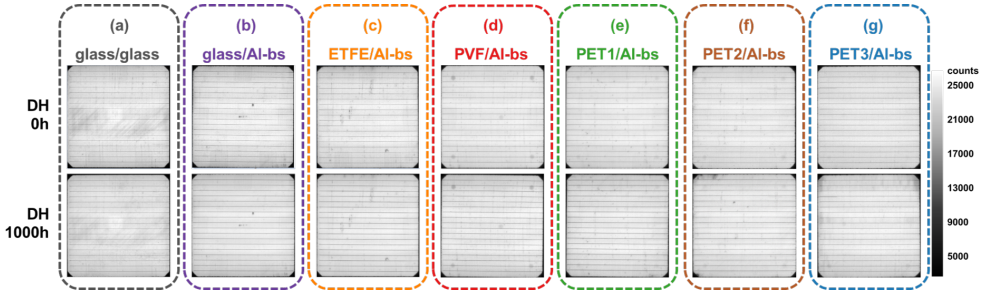


Figure 5.25: EL images (low current injection, $J = 2.05$ mA/cm^2) of the solar modules with different front sheets before (0 h) and after 1000 h of the DH test.

5.3 Equivalence between accelerated DH aging and field conditions

The optimized lightweight SHJ solar modules exhibited promising performance and stability in accelerated DH aging tests, showing results comparable to those of conventional glass/backsheet solar modules. Nevertheless, concerns remain regarding their long-term reliability and performance under actual field conditions. Field testing is essential to accurately assess the lifetime and reliability of solar modules in real-world scenarios. However, since field tests typically require significant time to yield measurable degradation, accelerated aging tests are commonly employed as a time-saving alternative. Although field-testing the reliability and performance of lightweight SHJ solar modules lies beyond the scope of this work, an acceleration factor (AF) model has been proposed [254–257] to bridge accelerated test conditions with real-world field performance.

5.3.1 Accelerated degradation model

The extent of solar module degradation under damp-heat conditions primarily depends on temperature and humidity. The individual or combined effects of these microclimatic factors on solar module degradation can be modeled using various approaches, including the Arrhenius equation, the modified Arrhenius equation, and the modified Peck's equation [254]. Among these, the Arrhenius model is the most commonly used [254], as it describes the degradation rate explicitly as a function of temperature according to

$$f(T) = A \cdot e^{\left(-\frac{E_a}{k_B T}\right)}. \tag{5.3}$$

In Equation 5.3:

- f(T) is the DH aging rate of the solar modules, which depends on temperature.
- k_B is the Boltzmann constant.
- E_a is the activation energy.
- A is a pre-exponential constant specific to the Arrhenius model.

Although the pristine Arrhenius model is widely used for temperature-dominated reactions, it is insufficient to describe module degradation involving hydrolysis, as temperature alone cannot trigger DHID. Relative humidity is also a critical factor contributing to degradation. To address this limitation, a modified version of the Arrhenius equation, known as the Peck model, was proposed [180, 254, 258], as illustrated by

$$f(T, RH) = A \cdot e^{\left(-\frac{E_a}{k_B T}\right)} \cdot (RH)^n. \tag{5.4}$$

The AF between the accelerated aging tests and field conditions can then be calculated using

$$AF = \exp\left[-\frac{E_a}{k_B}\left(\frac{1}{T_{test}} - \frac{1}{T_{field}}\right)\right] \cdot \left(\frac{RH_{test}}{RH_{field}}\right)^n. \tag{5.5}$$

In Equation 5.5:

- T_field is the solar module temperature in field conditions, typically ranging from 25 to 75 °C depending on the geographic location and weather [259].
- T_test is the temperature during the DH test, typically set at 85 °C.

• RH_{field} is the relative humidity under field conditions, which varies by location and weather.

• RH_{test} is the relative humidity during the DH test, commonly set at 85%.

• n is a model parameter that quantifies the influence of relative humidity on solar module degradation.

The determination of E_{a} is critical for accurate modeling, as it is influenced not only by temperature but also by the encapsulation material and the overall solar module configuration. And it is also influenced by the failure criterion chosen. Solar modules utilizing different encapsulants exhibit varying degradation behaviors under DH conditions. To obtain a reliable estimate of E_{a}, experimental data from at least three different temperature settings and corresponding linear degradation processes are required. Consequently, DH tests must be conducted at three distinct temperatures to ensure robust modeling. Therefore, in addition to the standard 85°C, 85% RH DH test, supplementary tests were performed on the solar modules, including 1200 h at 55°C, 85% RH and 600 h at 95°C, 85% RH.

5.3.2 Determination of acceleration factors

The ETFE/Al-bs lightweight solar module was selected as a representative case for calculating the AF, as it exhibited more pronounced degradation compared to other solar module configurations after 1000 h of DH exposure.

Figure 5.26 illustrates the evolution of the electrical parameters of the ETFE/Al-bs solar module during the DH tests conducted under three different conditions. DHID is highly dependent on temperature. The solar module efficiency shows a rapid decline under 95 °C, 85% RH conditions, primarily attributed to the decrease in FF, which is consistent with our previous discussion. The increase in R_{s} under damp-heat conditions is identified as the main cause of the FF reduction. V_{oc} remains almost unchanged throughout the DH tests, and the observed fluctuations in J_{sc} fall within the measurement error range. Since FF serves as a direct indicator of degradation induced by temperature-assisted moisture ingression, it was chosen as the decisive parameter for deriving the E_{a}. Figure 5.27(b) presents the linear fitting of FF degradation under different temperature conditions during DH testing. As described in Equation 5.3, $f(T)$ represents the DH aging rate of the solar module, defined here as the ratio of the FF of the aged solar module to the FF of the initial solar modules. To determine the pre-exponential factor A and the E_{a} in Equation 5.3, the equation can be expressed in logarithmic form, resulting in a straight-line relationship as given by

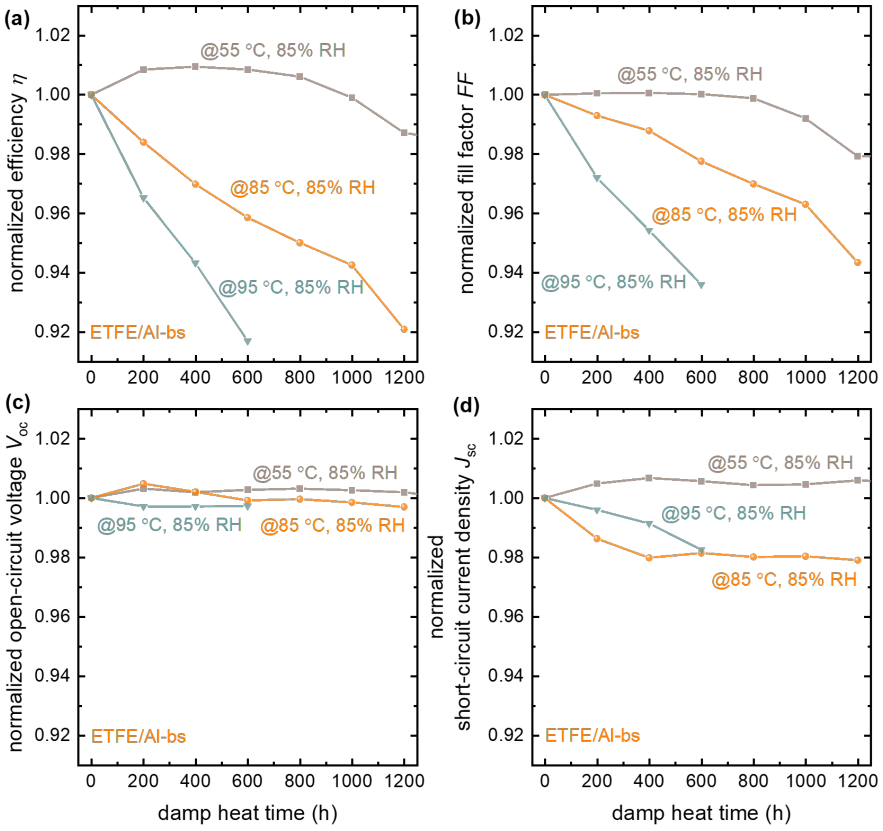


Figure 5.26: Normalized values of (a) efficiency (η), (b) fill factor (FF), (c) open-circuit voltage (V_{oc}), and (d) short-circuit current density (J_{sc}) as a function of damp-heat exposure time for the ETFE/Al-bs solar module under DH test conditions of 85°C, 85% RH, 55°C, 85% RH, and 95°C, 85% RH.

$$ln(f(T)) = E_a \cdot \frac{1}{k_B T} + ln(A). \tag{5.6}$$

In this study, the failure criterion was defined at 0.99 FF, corresponding to the degradation threshold observed after 1200 h of DH testing under 55 °C, 85% RH conditions. Therefore, when the FF ratio drops below 99%, $f(T)$ is determined and plotted in the Arrhenius diagram, as shown in Figure 5.27(c). The plot of ln(f(T)) versus 1/kT yields a linear Arrhenius relationship, where the slope corresponds to E_a and the intercept represents ln(A). The E_a was calculated using experimental data obtained under three DH test conditions: 55°C, 85% RH; 85°C, 85% RH; and 95°C, 85% RH. Based on Equation 5.6, the estimated E_a of the ETFE/Al-bs lightweight SHJ solar module was found to be 0.63 eV, which is significantly higher than the E_a reported for glass/glass SHJ solar modules by Ren et al. [180]. A higher E_a indicates a lower degradation rate. The methodology

presented here can be broadly applied to evaluate and compare the activation energies associated with time-to-failure across different solar module configurations.

The AF modeling plays a crucial role in predicting the performance degradation rate and estimating the operational lifetime of solar modules under real outdoor conditions. Typically, AF is derived from time-to-failure models based on solar module output power. However, in this study, we focus specifically on FF loss as the primary indicator of resistance degradation caused by temperature-assisted moisture ingression. Accordingly, we propose a methodology to determine AF for a specific degradation mechanism (moisture ingression) in a particular solar module configuration (front sheet/back sheet) subjected to well-defined climatic conditions.

The AF between the accelerated DH aging tests and actual field conditions can be calculated using Equation 5.5. In this calculation, the average module temperature in the field is assumed to be approximately 50 °C [145], while the average relative humidity is estimated to be around 80% RH in Jülich, Germany, according to the data from [260]. The parameter n, which quantifies the influence of relative humidity on module degradation, is taken as 1.042 based on the findings reported in [180].

The calculated AF under each DH condition are plotted in Figure 5.27(d), with values of 1.54 at 55°C, 85% RH; 9.95 at 85°C, 85% RH; and 17.34 at 95°C, 85% RH. The data points are interpolated using an exponential fitting curve. This AF modeling enables the extrapolation of module time-to-failure under arbitrary temperatures.

The predicted equivalent field lifetime to the accelerated DH aging at 85°C, 85% RH can be calculated by

$$t_{field} = AF \cdot t_{DH}. \tag{5.7}$$

Where t_{field} represents the equivalent solar module lifetime under field conditions, and t_{DH} denotes the DH aging duration at 85°C, 85% RH.

According to Equation 5.5 and Equation 5.7, for the ETFE/Al-bs lightweight SHJ solar module, a 1000-hour DH test at 85°C, 85% RH corresponds to approximately 1.1 years of operation under field conditions in the German region of Jülich (50°C, 80% RH), during which about $5\%_{\text{rel}}$ efficiency degradation was observed.

It should be noted that this result is specific to the tested solar module, as it depends on the particular materials, solar module structure, and the selected failure criterion. To achieve a more accurate estimation of E_{a}, a larger dataset covering a broader range of conditions would be required. Furthermore, additional research is needed to develop a

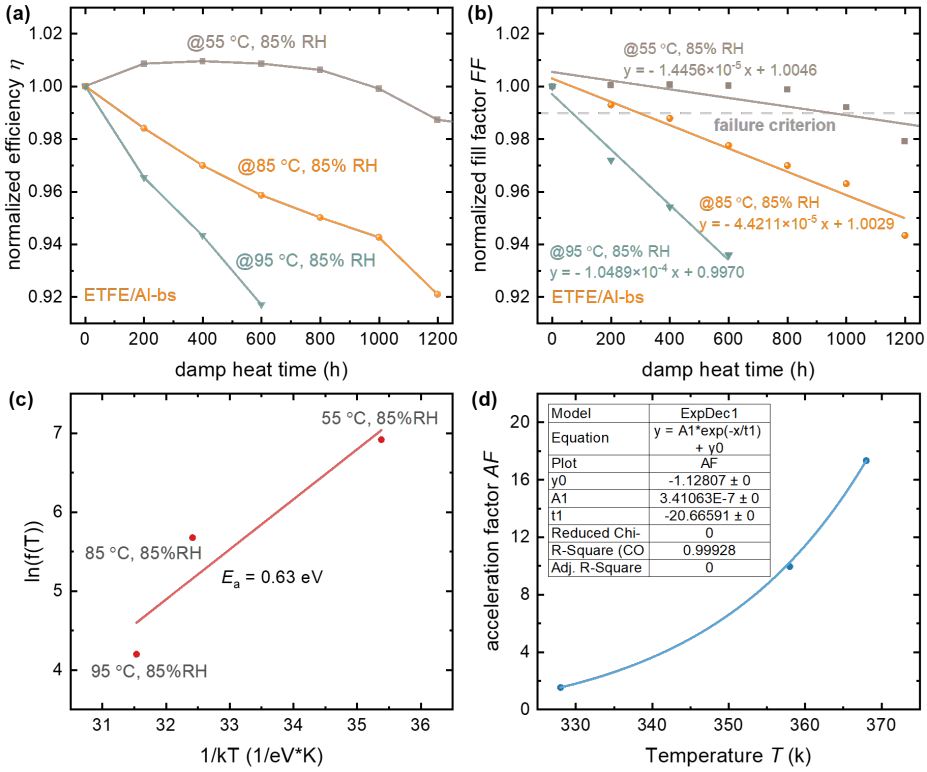


Figure 5.27: (a) Evolution of normalized efficiency (η) during DH test under different temperature conditions. (b) Linear fitting of FF degradation during DH test at various temperatures. (c) Lifetime variation of the ETFE/Al-bs solar module under different DH conditions, with E_a calculated based on the Arrhenius equation. (d) Exponential fitting of AF derived from different DH conditions.

comprehensive mechanistic model, which is expected to enhance the precision of degradation curve fitting and improve the prediction of solar module lifetimes.

6 Insights into UVID in lightweight SHJ solar modules with different encapsulants

In the previous chapter, the DH effect on lightweight SHJ solar modules incorporated with different encapsulants was comprehensively investigated. Selecting the appropriate encapsulation material is crucial for the DH stability and durability of lightweight solar modules. UV radiation is another critical concern for SHJ solar modules, which will degrade the encapsulation materials and solar cells, particularly lightweight solar module configurations, where flexible polymer-based front sheets may provide reduced shielding against UV radiation.

Therefore, in this chapter, the UV stability of encapsulation materials is investigated as presented in Section 6.1. The UV-induced degradation behavior of lightweight SHJ solar modules utilizing encapsulants with different UV transmittance is investigated and presented in Section 6.2. Section 6.3 reveals the underlying degradation mechanism of the downshifting effect in lightweight SHJ solar modules utilizing downshifting encapsulants. A strategy for enhancing the performance and UV stability of lightweight SHJ solar modules is proposed in Section 6.4.

6.1 UV stability of encapsulation materials

The long-term reliability of lightweight SHJ modules is closely linked to the UV stability of their encapsulation materials, as UV radiation can induce optical degradation, yellowing, or chemical changes that directly affect solar module performance. In this section, the optical properties of various encapsulation materials, comprising different front sheets and encapsulants, were systematically assessed before and after a 120 kWh/m^2 of UV exposure test. This evaluation enables a comparative understanding of material-specific resistance to UV-induced degradation, which is essential for optimizing encapsulation design. The detailed test conditions and procedures are described in Subsection 3.2.2.

6.1.1 UV stability of front sheet materials

Front sheets serve as the first barrier against UV radiation and play a critical role in determining the amount of UV light that reaches the encapsulant and the solar cell layers. Their optical properties, particularly UV transmittance, directly influence the rate of UV-induced degradation within the solar module. In this study, four front sheet materials - namely ETFE, PVF, PET1, and glass - were evaluated for their optical performance before and after UV exposure.

As shown in Figure 5.20, ETFE exhibits the highest overall transmittance among the materials investigated. The front sheets also differ substantially in their UV-light transmission characteristics: ETFE and glass allow UV radiation to pass through, whereas PVF and PET1 effectively block it.

Figure 6.1 presents the transmittance and reflectance spectra of the front sheet materials before and after UV exposure with a total dose of 120 kWh/m^2. The optical properties of all front sheet materials remained essentially unchanged throughout the exposure, indicating excellent UV stability.

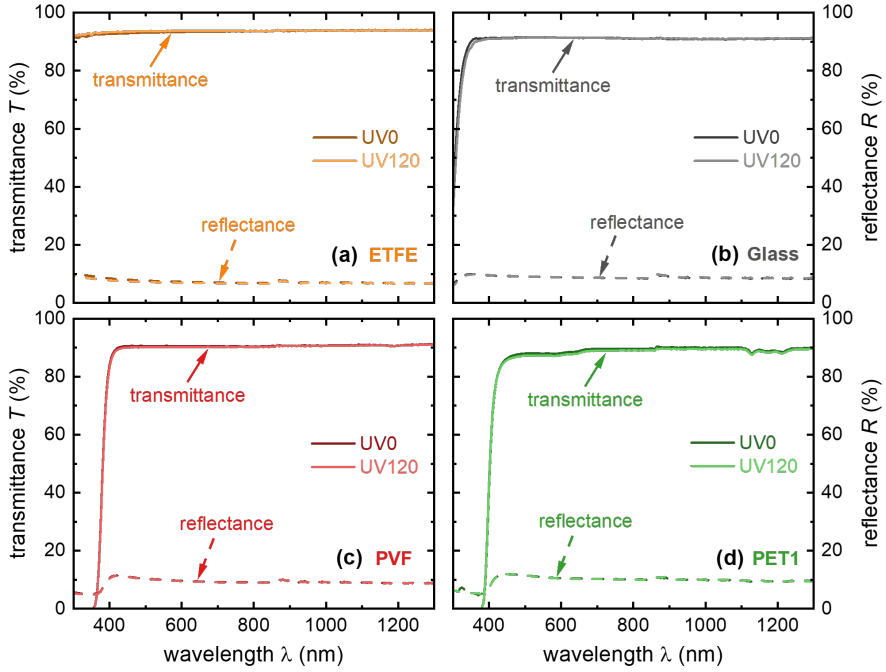


Figure 6.1: Transmittance (T, solid line) and reflectance (R, dashed line) spectra of different front sheet materials: (a) ETFE, (b) glass, (c) PVF, and (d) PET1, before and after 120 kWh/m^2 of UV exposure.

Based on its combination of high UV transparency and superior UV stability, ETFE was selected as the front sheet material for fabricating the lightweight SHJ solar module samples in this chapter.

6.1.2 UV stability of encapsulants

Encapsulants provide mechanical bonding between the front sheet, solar cells, and backsheet while also serving as a barrier against environmental stress factors. Their optical stability under UV radiation is crucial, as yellowing or chemical degradation can reduce light transmission and impair module performance. In this section, several encapsulant types, including TPO, PO-UV, EVA, and DS-EVA, were evaluated for their optical properties before and after UV exposure.

Optical properties before UV exposure

The encapsulants differ in both their initial optical transmittance and their ability to filter UV light. As shown in Figure 6.2(a), the laminated encapsulants can be classified into three categories based on their UV-light transmission in the 280 - 400 nm range, which was measured by UV-Vis-NIR. TPO and PO-UV are UV-blocking encapsulants with distinct cut-off wavelengths: TPO blocks UV radiation below 350 nm, hereafter referred to as UV-B_{350}, whereas PO-UV blocks UV radiation below 375 nm (UV-B_{375}). EVA is a UV-transmitting encapsulant (UV-T), while DS-EVA is a UV-downshifting encapsulant (UV-DS) that shifts UV light into blue light. The excitation and emission spectra of the UV-DS encapsulant are presented in Figure 6.2(b).

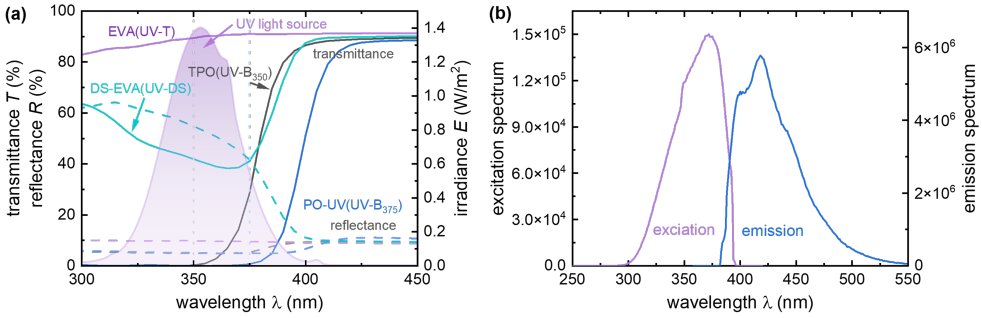


Figure 6.2: (a) Transmittance (solid line, T) and reflectance (dashed line, R) spectra of encapsulants with different UV-transmission properties in the range of 300 - 450 nm. The shaded curve shows the spectrum of the UV light source. (b) Excitation and emission spectra of the downshifting encapsulant foil (Source: from Cybrid).

Optical properties after UV exposure

Figure 6.3 presents the transmittance and reflectance spectra of the encapsulants before and after UV exposure with a total dose of 120 kWh/m^2. All encapsulants maintained stable optical properties in the visible range, indicating good overall UV stability. However, the UV-transmitting encapsulant EVA exhibited a slight increase in transmittance and no measurable change in reflectance for wavelengths below 400 nm, as shown in Figure 6.3(c). This behavior indicates a reduction in light absorption. Previous studies have attributed such increases in UV transmittance to the loss of additives or changes in polymer crystallinity during UV exposure [261].

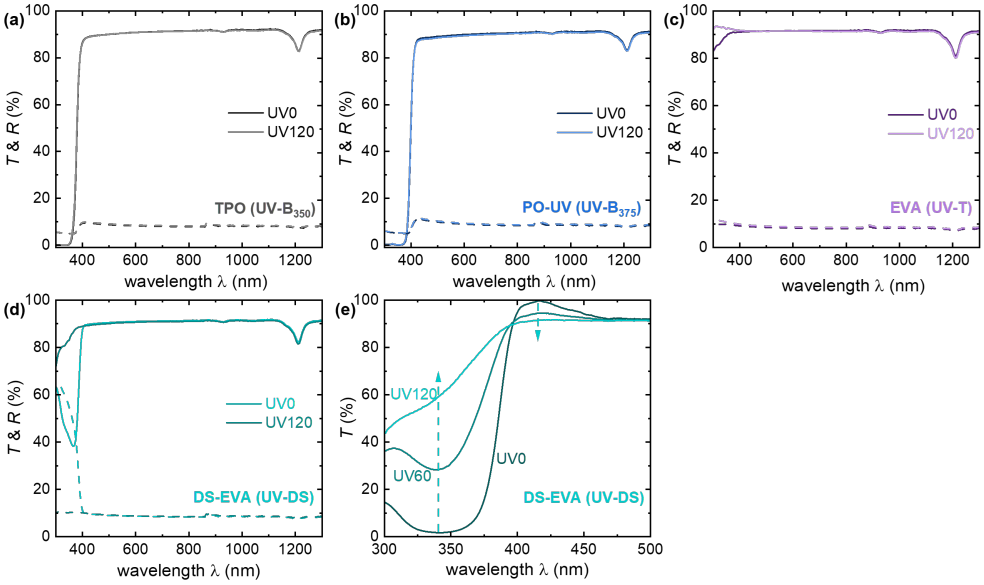


Figure 6.3: Transmittance (T) (solid line) and reflectance (R) (dashed line) spectra of different encapsulants: (a) TPO, (b) PO-UV, (c) EVA, (d) DS-EVA, and (e) DS-EVA, measured using an in-house-built setup, before and after UV exposure with a total dose of 120 kWh/m^2. (f) DS-EVA encapsulant is covered with ETFE foil on both the front and rear sides.

For the UV-downshifting encapsulant DS-EVA, an increase in transmittance and a decrease in reflectance were observed for wavelengths below 400 nm after UV exposure, as shown in Figure 6.3(e). This behavior suggests either a reduction in light absorption or a diminished downshifting (DS) effect. However, the UV/Vis spectrometer used in this study cannot directly detect the downshifting effect, as it operates with a monochromator and a wavelength-selective intensity sensor. This limitation can lead to inaccurate results due to the varying sensitivities of the sensor across different wavelengths. To address this issue, a modified, in-house-built optical setup (see Subsection 3.3.1) was developed to accurately measure the DS effect. Furthermore, to better simulate the operating conditions

of a practical solar module and minimize the influence of external environmental factors, the transmittance of the DS-EVA foil was measured after encapsulation with a double ETFE layer, as shown in Figure 6.3(f).

The transmittance spectra of the laminated DS-EVA foil encapsulated with a double ETFE layer were measured over the wavelength range of 300 - 500 nm before UV exposure and after cumulative doses of 60 and 120 kWh/m^2, as shown in Figure 6.3(e). The results confirm that the DS-EVA foil is capable of downshifting UV light from a peak near 340 nm to visible light with a peak around 420 nm, and this wavelength shift remained unchanged during UV exposure. However, as the UV radiation dose increased from 0 to 120 kWh/m^2, transmittance in the 300 - 400 nm range increased, while transmittance in the 400 - 500 nm range decreased. This behavior suggests that the DS effect of the DS-EVA foil deteriorates even when encapsulated with a double ETFE layer.

Degradation of the downshifting effect: mechanism interpretation

A reduction in the downshifting effect was observed in the downshifting encapsulants after DH and UV exposure, respectively, as presented in Subsection 5.1.3 and Subsection 6.1.2, respectively. To gain a deeper understanding of the mechanism underlying this reduction, qualitative and quantitative analyses of the formulations of the downshifting encapsulants were conducted. A combination of three-step thermal desorption in the pyrolysis chamber, gas chromatography, and mass spectrometry was employed, which is PY-GC-MS as detailed in Subsection 3.3.6.

The analysis revealed that the polymer films contain crosslinking additives (peroxide and accelerator), various types of adhesion promoters, antioxidants, plasticizers, hindered amine light stabilizers (HALS) along with their degradation fragments, and one additive not identified in the NIST library, which is presumed to be an organic UV downshifting agent. No UV absorbers were detected, suggesting that the observed reduction in absorbance measured by UV-Vis-NIR spectroscopy, as presented in Figure 6.3(d), can be entirely attributed to the degradation of the UV downshifting agent.

Figure 6.4 presents the intensities of selected additives that are particularly relevant to long-term stability under DH and UV exposure, namely antioxidants, HALS, and their degradation fragments, and the presumed UV downshifting agent (DS agent). The intensities were measured for both pristine and aged samples and normalized to the sample mass, enabling direct comparison and tracking of relative changes. The antioxidant content in DS-EVA decreased more significantly during UV weathering than during DH weathering. A similar trend was observed for HALS, which was completely depleted after 120 kWh/m^2 of UV exposure.

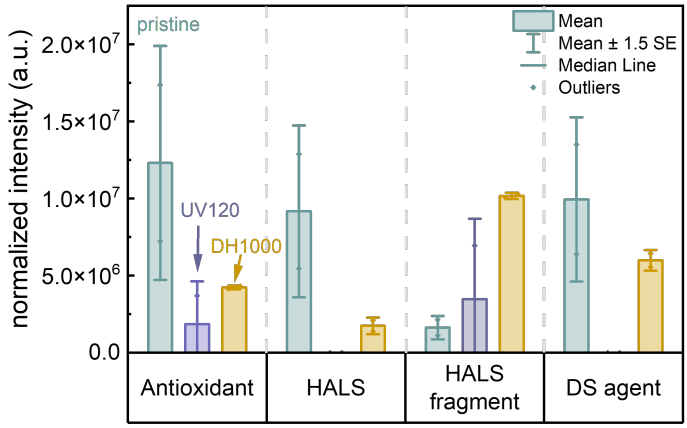


Figure 6.4: Normalized intensity of the additives before and after 120 kWh/m² UV or 1000 h DH exposure, quantified by Pyrolysis-Gas chromatography-Mass spectrometry (PY-GC-MS).

As reported in [262], HALS can degrade under both UV and DH conditions. During aging, large HALS molecules fragment into smaller species, which remain active and continue to protect the polymer. The presumed organic UV downshifting agent exhibited only a slight decrease in concentration after DH exposure but was completely depleted after UV exposure. This observation supports the hypothesis that the additive functions as a UV downshifting agent. Nevertheless, its exact chemical nature remains to be elucidated, for example, through detailed mass spectrometric analysis. Organic UV downshifting agents are generally known to be susceptible to photo-oxidation (UV + O_2) [263]. Therefore, the depletion of antioxidants and HALS could negatively affect the stability of the UV downshifting agent.

6.2 UVID behavior of lightweight SHJ solar modules with different encapsulants

In the previous section, the UV stability of various encapsulation materials was evaluated. In this section, the UV stability of lightweight SHJ solar modules fabricated using these encapsulation materials is assessed.

6.2.1 Configurations of solar modules with different encapsulants

Design and fabrication of solar modules

Figure 6.5 shows the schematic cross-section of the single-cell lightweight SHJ solar module. Two types of bifacial monocrystalline n-type rear-junction ITO-incorporated SHJ solar cells were used for solar module fabrication: M2 0-busbar (0BB) and M2-half-cut (156.75 mm × 78.37 mm) 9-busbar (9BB) solar cells. The solar cells were interconnected using IF1, while an electrically conductive adhesive tape (ECT) was employed as an alternative for comparison, as described in Subsection 6.2.2. Sn-Pb-coated Cu-ribbons (5 mm wide, 0.2 mm thick) served as connectors. For solar module encapsulation, ETFE was used as the front cover material. The encapsulants foils, including TPO, PO-UV, EVA, and DS-EVA, which were evaluated in the previous section, were incorporated. An Al-bs was used as the back sheet. Glass/glass and glass/back sheet solar modules were fabricated as references for comparison. 3.2 mm-thick glass was used. The solar module edges were sealed with PIB tape.

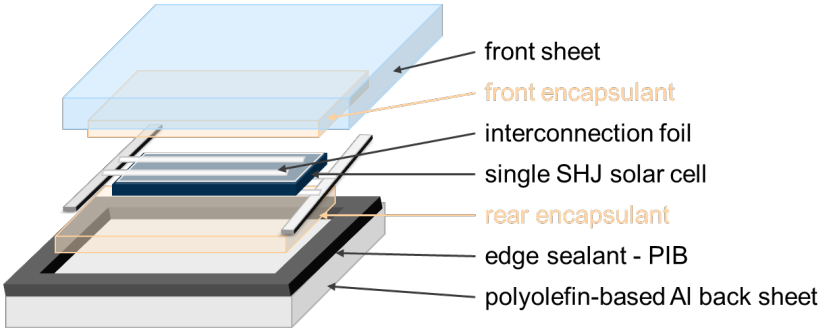


Figure 6.5: Schematic of the lightweight SHJ single-cell solar module.

Table 6.1 lists the configurations of the test solar modules incorporating different encapsulants. All solar modules were fabricated using a vacuum lamination process, as illustrated in Figure 3.9. The specific lamination parameters for each sample type are provided in Table A.3.

Table 6.1: Configurations of the test solar modules.

Module No.	Front sheet	Encapsulant (front/rear)	Solar cell	IF	Back sheet
6.1	ETFE	TPO	M2 0BB	IF1	Al-bs
6.2	ETFE	PO-UV	M2 0BB	IF1	Al-bs
6.3	ETFE	EVA	M2 0BB	IF1	Al-bs
6.4	ETFE	DS-EVA	M2 0BB	IF1	Al-bs
6.5	Glass	DS-EVA	M2 0BB	IF1	Al-bs
6.6	Glass	DS-EVA	M2 0BB	IF1	Glass
6.7	ETFE	EVA	M2-half-cut 9BB	ECT	Al-bs

CTM loss analysis

Figure 6.6 shows the CTM loss of lightweight SHJ solar modules with different encapsulants. The results indicate that the CTM efficiency loss is primarily caused by a reduction in J_{sc} and an increase in R_s, the latter leading to a decrease in FF. The solar module with the UV-DS encapsulant exhibits the smallest J_{sc} loss from cell to module, benefiting from the UV-downshifting effect, in which UV photons are shifted into visible light that can be utilized more efficiently by SHJ solar cells. In contrast, the solar module with the UV-B_{375} encapsulant shows the largest J_{sc} loss, as most UV photons are absorbed by the encapsulant. For all types of solar modules, the V_{oc} remains almost unchanged from the cell to the module.

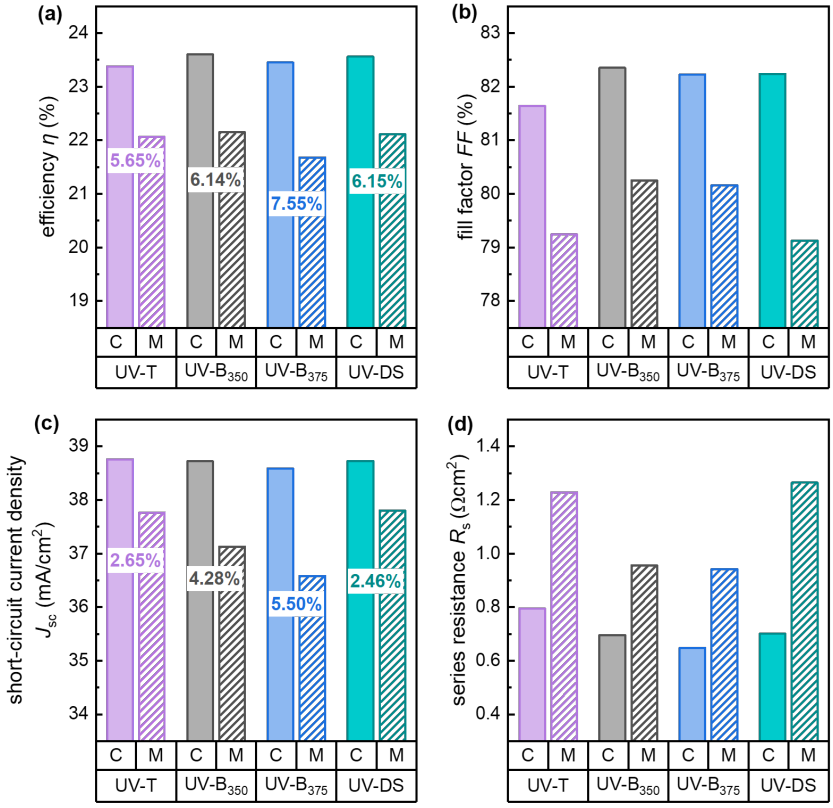


Figure 6.6: CTM loss from (a) efficiency (η), (b) fill factor (FF), (c) short-circuit current density (J_{sc}), and (d) series resistance (R_s) of lightweight SHJ solar modules incorporating encapsulants with different UV-transmission properties. 'C' denotes solar cell, and 'M' denotes solar module.

6.2.2 UVID mechanism of lightweight SHJ solar modules with different encapsulants

Following solar module fabrication and initial measurements, an indoor UV exposure test with a total dose of 120 kWh/m^2 was conducted in a UV chamber. The specifications of the UV chamber and the detailed test procedures are provided in Subsection 3.2.2.

I-V characteristics of solar modules

Figure 6.7 shows the evolution of the electrical parameters of lightweight SHJ solar modules with different encapsulants during UV exposure. The UV-T module exhibited the largest relative efficiency degradation, amounting to 9.25%$_{rel}$ after 120 kWh/m^2 of UV exposure, which corresponds to approximately 30 months of outdoor exposure in Jülich, Germany, as extimated in Subsection 3.2.2.

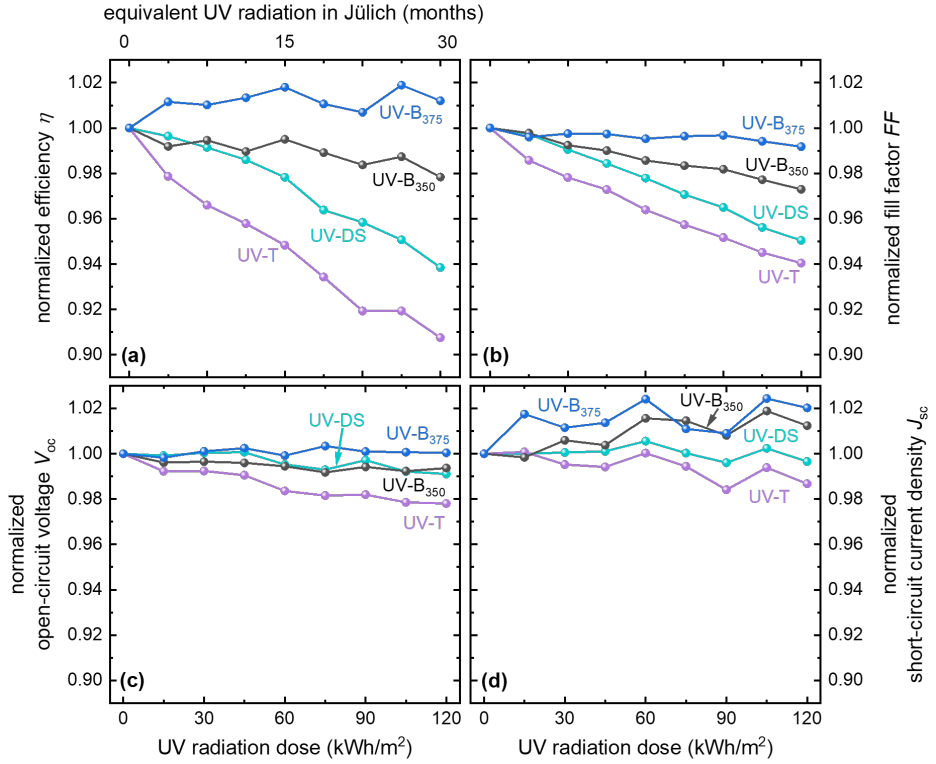


Figure 6.7: Normalized values of (a) efficiency (η), (b) fill factor (FF), (c) open-circuit voltage (V_{oc}), and (d) short-circuit current density (J_{sc}) as a function of UV radiation dose for lightweight SHJ solar modules incorporating encapsulants with different UV-transmission properties.

The efficiency loss is mainly attributed to the decrease in FF and V_{oc}. Previous studies have shown that reductions in V_{oc} and FF in SHJ solar cells are mainly caused by the deterioration of the surface passivation. High-energy UV photons can break the Si-H bonds used for chemical passivation [24, 179, 264], leading to the formation of additional dangling bonds on the silicon surface and, consequently, an increase in surface recombination.

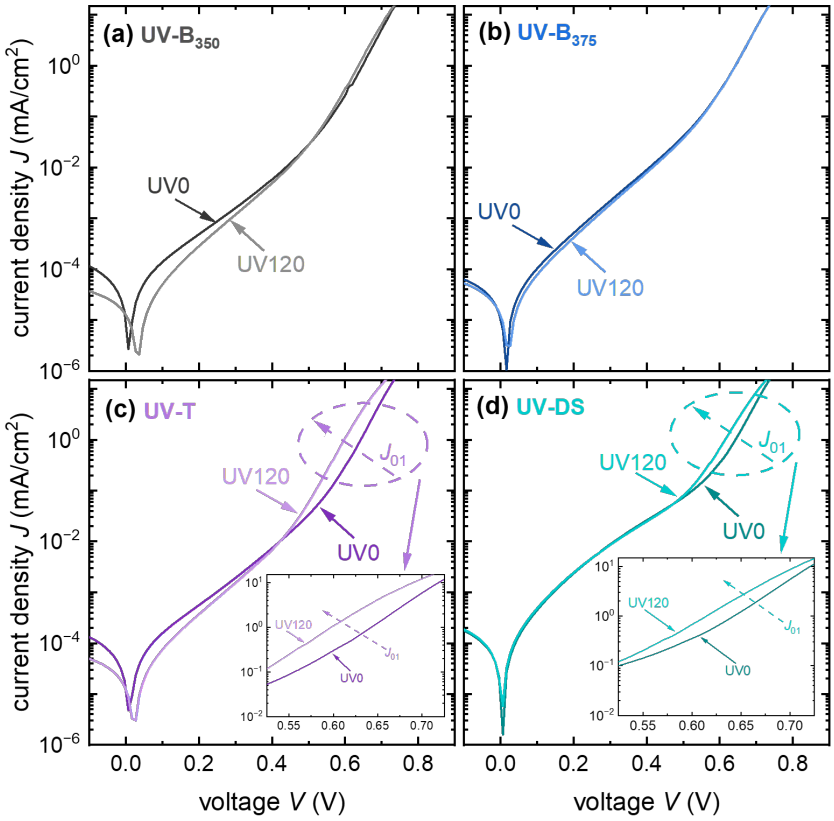


Figure 6.8: Dark J-V curves of the lightweight SHJ solar modules incorporating encapsulants with different UV-transmission properties: (a) UV-B_{350}, (b) UV-B_{375}, (c) UV-T, and (d) UV-DS, before and after 120 kWh/m² of UV exposure.

From the dark J-V curves of the solar modules, as shown in Figure 6.8, a pronounced increase in J_{01} was observed for the UV-T module, along with a slight increase for the UV-DS module. The increase in J_{01}, which is associated with recombination processes occurring at the surface and within the bulk of the solar cell [250, 265], is most evident in the medium- and high-voltage regions of the dark J-V curve. This behavior is consistent with our observations and suggests that the surface passivation of the SHJ solar cells in the UV-T and UV-DS modules degraded as a result of UV radiation. The reduction in V_{oc} can be explained by the increase in J_{01}, according to the relationship between V_{oc}

and J_{01} [266], as expressed by

$$V_{oc} = \frac{k_B T}{q} ln(\frac{J_{sc}}{J_{01}} + 1). \tag{6.1}$$

The drop in the V_{oc} after 120 kWh/m² of UV exposure was calculated from the light I-V and J_{01}, respectively, and is summarized in Table 6.2.

Table 6.2: V_{oc} drop after 120 kWh/m² of UV exposure, calculated from the J_{01} and light I-V.

Module type	$\boldsymbol{J_{01}}$ (fA/cm²) at UV0	$\boldsymbol{J_{01}}$ (fA/cm²) at UV120	ΔV_{oc} (mV) from J_{01}	ΔV_{oc} (mV) from light I-V
UV-B_{350}	10.35	11.87	-3.2	-4.7
UV-B_{375}	10.73	10.84	0.3	0.3
UV-T	11.26	26.37	-22.5	-16.2
UV-DS	10.69	14.1	-7.3	-6.6

Among the encapsulants tested, the UV-blocking types exhibited the highest V_{oc} retention after UV exposure, whereas the UV-T encapsulant showed the most severe V_{oc} degradation, highlighting the strong dependence of V_{oc} stability on the encapsulant's UV-transmission characteristics.

The solar module with the UV-B_{375} encapsulant, which absorbs most UV photons, exhibited the most stable performance with the least efficiency degradation. The UV-B_{350} module showed only a slight efficiency loss. As the UV-B_{350} encapsulant cannot completely block UV light, the residual UV photons that are not absorbed can still reach the solar cell and cause surface passivation damage. Interestingly, the UV-DS module demonstrated improved UV stability compared to the UV-T module; however, it still exhibited a relative efficiency degradation of $6.15\%_{rel}$ compared to the module with the UV-B encapsulant. This can be explained by two factors. First, the UV-DS encapsulant cannot fully shift all incident UV photons into blue light; unshifted UV photons can still reach the solar cell and degrade the surface passivation. Second, the downshifting effect itself may deteriorate during UV exposure, leading to an increased fraction of UV photons that are no longer shifted to blue light. This deterioration of the DS effect was confirmed in plain DS-EVA foils after 120 kWh/m² of UV exposure through both optical and PY-GC-MS analyses, as presented in Subsection 6.1.2.

PL imaging of solar modules

To provide a direct visualization of the recombination behavior, PL imaging was performed. Figure 6.9 presents the PL images of lightweight SHJ solar modules with different encapsulants before and after 120 kWh/m^2 of UV exposure. The UV-T module exhibited a pronounced reduction in PL intensity, as a large fraction of UV photons penetrated the encapsulant and reached the solar cell. The high-energy UV photons broke the Si-H bonds, leading to deterioration of the surface passivation and thus increased charge-carrier recombination, which in turn reduced the PL intensity. The UV-DS module showed moderate degradation because part of the UV photons was shifted into visible light, thereby reducing the number of UV photons reaching the solar cell and mitigating recombination losses. However, as the DS effect cannot fully convert all UV photons, and may itself degrade under prolonged UV exposure, some unshifted UV photons could still reach the solar cell, causing partial passivation loss. In contrast, the solar modules with either UV-B_{350} or UV-B_{375} encapsulants exhibited negligible changes in PL intensity. This is because a large fraction of UV photons was absorbed by the UV-blocking encapsulant, effectively preventing harmful UV photons from reaching the solar cell. Consequently, the passivation properties of these solar cells remained stable.

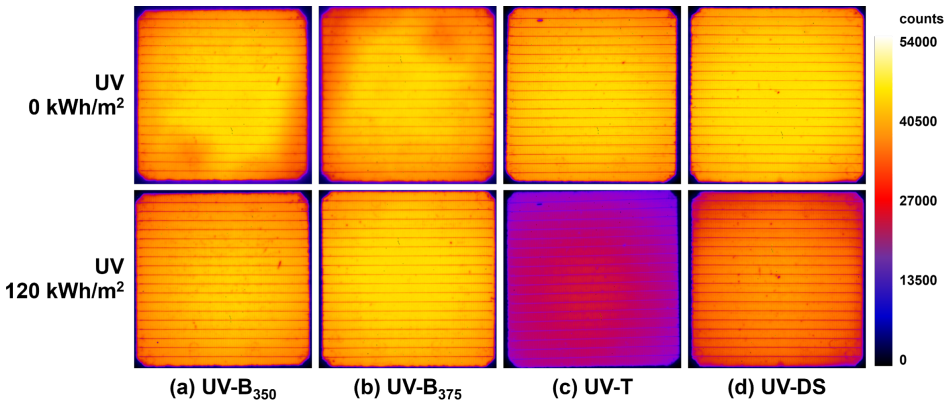


Figure 6.9: PL images of the lightweight SHJ solar modules incorporating encapsulants with different UV-transmission properties: (a) UV-B_{350}, (b) UV-B_{375}, (c) UV-T, and (d) UV-DS, before and after 120 kWh/m^2 of UV exposure.

Overall, both PL intensity and V_{oc} serve as indicators of surface passivation quality, and the observed V_{oc} degradation trends are consistent with the PL imaging results, as described by

$$V_{oc} = {V_{oc}}^{ref} + \frac{k_B T}{q} ln(\frac{I_{PL}}{{I_{PL}}^{ref}}). \tag{6.2}$$

The drop in the V_{oc} after 120 kWh/m^2 of UV exposure was calculated from the light I-V and PL intensities, and is summarized in Table 6.3. The comparison of changes in V_{oc} calculated by three methods is shown in Figure 6.10.

Table 6.3: V_{oc} drop after 120 kWh/m^2 of UV exposure, calculated from the PL intensities and light$I$-V.

Module type	**PL intensity** at UV0	**PL intensity** at UV120	ΔV_{oc} (mV) from PL	ΔV_{oc} (mV) from light I-V
UV-B$_{350}$	42169	38750	-2.2	-4.7
UV-B$_{375}$	41710	42059	0.2	0.3
UV-T	42093	22398	-16.4	-16.2
UV-DS	42442	32718	-6.8	-6.6

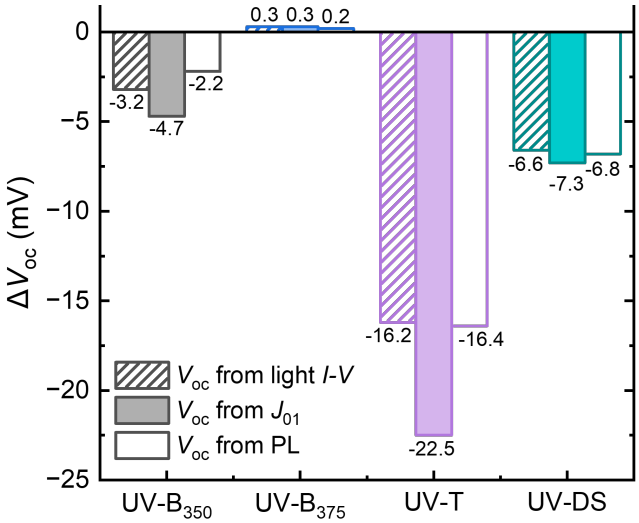


Figure 6.10: V_{oc} changes calculated from light I-V, J_{01}, and PL intensity for solar modules with: (a) UV-B$_{350}$, (b) UV-B$_{375}$, (c) UV-T, and (d) UV-DS, before and after 120 kWh/m^2 of UV exposure.

In addition to the efficiency loss associated with the decrease in V_{oc}, a decrease in FF is another major contributor to UV-induced efficiency degradation. It should be noted that FF losses are influenced not only by carrier recombination, but also by factors such as R_s and R_{sh}. A detailed discussion of FF losses will be presented in the following section.

EQE analysis of solar modules

As shown in Figure 6.11, the *EQE* and reflectance of the lightweight SHJ solar modules with different UV-transmission encapsulants were measured before and after 120 kWh/m^2 of UV exposure. A notable decline in *EQE*, ranging from 400 to 1000 nm, was observed in the UV-T module after UV exposure. Since the transmittance and reflectance above 400 nm of both the front sheet and the UV-T encapsulant remained stable after UV exposure, as shown in Figure 6.3(c) and Figure 6.1(a), the *EQE* loss can be attributed to increased carrier recombination caused by passivation deterioration, rather than enhanced parasitic absorption in the encapsulation materials. This interpretation is consistent with the *I*-*V* and PL imaging results, where increased carrier recombination led to reductions in V_{oc}, PL intensity, and *EQE* in the 400–1000 nm range. In contrast, solar modules with UV-blocking encapsulant exhibited no measurable change in *EQE* after UV exposure.

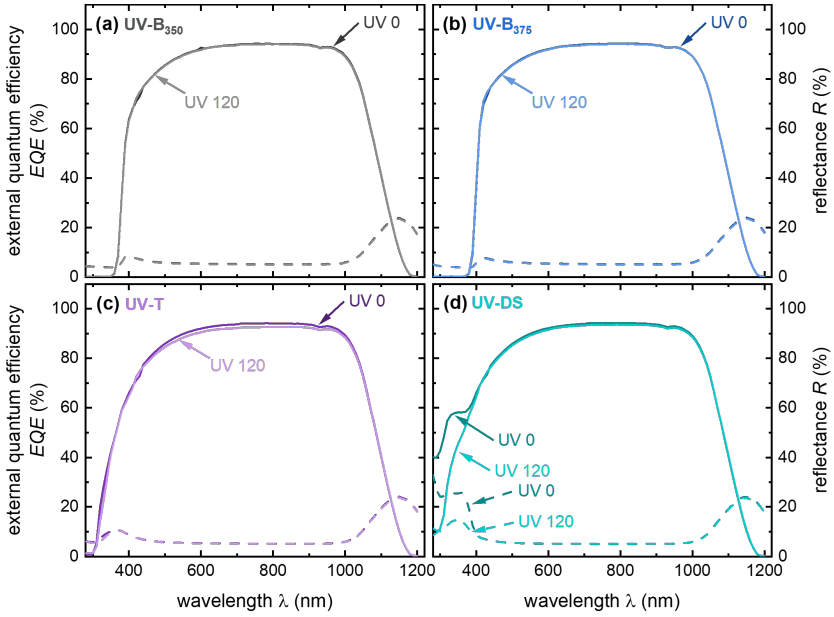


Figure 6.11: *EQE* (solid line) and reflectance (dashed line) of lightweight SHJ solar modules incorporating encapsulants with different UV-transmission properties: (a) UV-B_{350}, (b) UV-B_{375}, (c) UV-T, and (d) UV-DS, measured before and after 120 kWh/m^2 of UV exposure.

However, the solar module with UV-DS encapsulant exhibited a pronounced reduction in both *EQE* and reflectance at wavelengths below 400 nm. The *EQE* decrease in this range may result from increased absorption within the UV-DS encapsulant or degradation of its DS effect. As evidenced in Figure 6.3(e), the transmittance spectra of the UV-DS encapsulant after 120 kWh/m^2 of UV exposure showed a decrease in blue-light output accompanied by an increase in transmitted UV light, providing direct proof of DS

effect deterioration. This degradation reduces the conversion of UV photons into visible photons, allowing a greater fraction of harmful UV light to reach the solar cell. Consequently, the increased UV photons at the solar cell accelerate passivation loss, thereby lowering the overall solar module efficiency.

FF losses analysis of solar modules

To further elucidate the mechanisms underlying *FF* degradation, the p*FF* of the lightweight SHJ solar modules was analyzed. The p*FF* quantifies the *FF* excluding resistive losses and therefore serves as a general indicator of carrier recombination in solar modules.

Figure 6.12 presents the absolute changes in p*FF* and *FF* for lightweight SHJ solar modules with encapsulants possessing different UV-transmission properties during UV exposure. As shown in Figure 6.12(c) and (d), *FF* losses after 120 kWh/m² of UV exposure were primarily attributed to p*FF* losses for the UV-T and UV-DS modules, indicating that carrier recombination was the dominant factor. Specifically, the UV-T module exhibited decreases of 4.72%$_{\text{abs}}$ in *FF* and 3.72%$_{\text{abs}}$ in p*FF*, while the UV-DS module showed corresponding reductions of 3.92%$_{\text{abs}}$ and 2.68%$_{\text{abs}}$. As shown in Figure 6.12(c), the module with UV-T encapsulant exhibited the fastest and most significant degradation in p*FF*, which correlates with its highest UV transmittance.

In contrast, the UV-B$_{375}$ module displayed almost no p*FF* decrease, as shown in Figure 6.12(b), suggesting that UV photons were effectively blocked by the encapsulant and caused no measurable harm to the surface passivation of the solar cell. The small *FF* loss in this module was mainly due to increased R_{s}-related *FF* losses. Compared to the UV-B$_{375}$ module, the UV-B$_{350}$ module exhibited larger *FF* and p*FF* reductions, 2.17%$_{\text{abs}}$ and 1.07%$_{\text{abs}}$, respectively, with p*FF* losses and R_{s}-related losses contributing almost equally to the total *FF* degradation.

After 120 kWh/m², the R_{s}-related *FF* losses were similar across the solar modules with different encapsulants, with values of 1.10%$_{\text{abs}}$, 0.67%$_{\text{abs}}$, 1.00%$_{\text{abs}}$, and 1.24%$_{\text{abs}}$ for the UV-B$_{350}$, UV-B$_{375}$, UV-T, and UV-DS modules, respectively. A previous study [264] attributed a noticeable increase in R_{s}-related *FF* losses in SHJ solar cells under UV exposure to elevated interface contact resistivity, rather than deterioration of the Ag electrodes or ITO thin films. In the present case, however, the similar increases observed for all solar modules suggest that the rise in R_{s}-related *FF* losses is not directly linked to UV transmission characteristics. A more detailed analysis of this phenomenon will be provided in the following section.

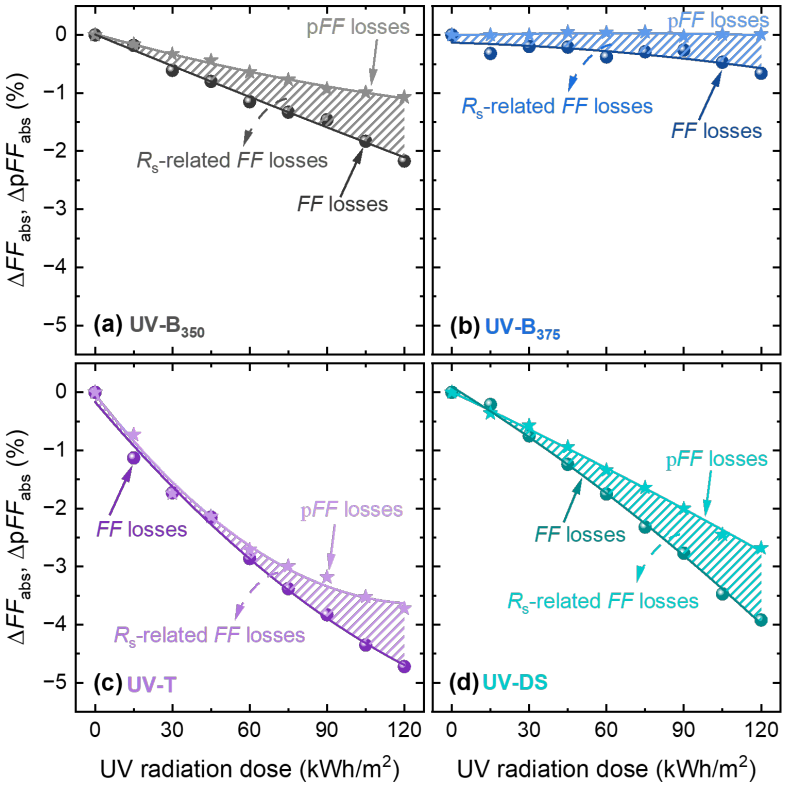


Figure 6.12: Changes in pseudo fill factor (p*FF*) and fill factor (*FF*) of lightweight SHJ solar modules incorporating encapsulants with different UV-transmission properties: (a) UV-B_{350}, (b) UV-B_{375}, (c) UV-T, and (d) UV-DS, as a function of UV radiation dose. ΔpFF_{abs} and ΔFF_{abs} denote the absolute changes in p*FF* and *FF*, respectively.

Root causes of the increase in R_s-related *FF* losses

As discussed in the "*FF losses analysis*", R_s-related *FF* losses were similar across all encapsulant types after 120 kWh/m^2 of UV exposure, suggesting that the increase in R_s is not primarily driven by UV-induced effects but is more likely linked to other factors. One plausible explanation is that the rise in R_s originates from the interconnection method rather than from encapsulant degradation. To investigate this hypothesis, additional solar modules using the UV-T encapsulant were fabricated with electrically conductive adhesive tape (ECT) in place of interconnection foil (IF1), as shown for solar module No. 6.9 in Table 6.1, and subsequently subjected to the same UV exposure protocol.

Figure 6.13 compares the changes in p*FF* and *FF* for solar modules encapsulated with the UV-T encapsulant and interconnected using either IF or ECT. Both configurations exhibited similar overall p*FF* degradation rates. For the ECT-interconnected solar module, *FF* losses were almost entirely attributable to p*FF* losses, with minimal increase

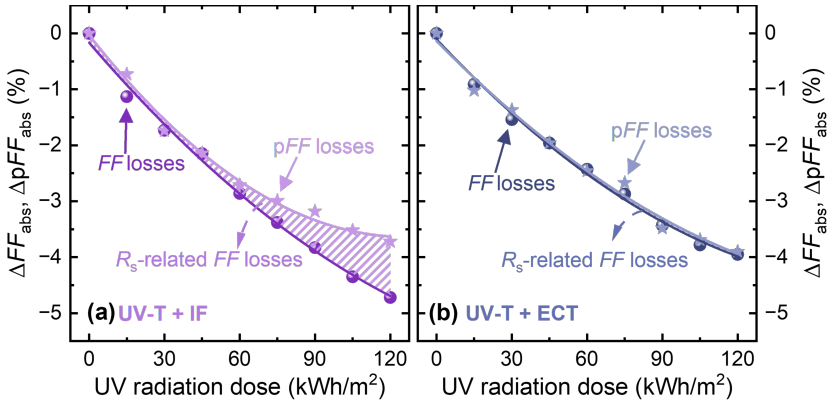


Figure 6.13: Changes in pseudo fill factor (pFF) and fill factor (FF) of the UV-T lightweight SHJ solar modules with different interconnection methods: (a) interconnection foil (IF1) and (b) electrically conductive adhesive tape (ECT), as a function of UV radiation dose. $\Delta \mathrm{p}FF_{\mathrm{abs}}$ and ΔFF_{abs} denote the absolute changes in pFF and FF, respectively.

in R_{s}-related FF losses. In contrast, the IF-interconnected solar module showed a clear increase in R_{s}-related FF losses. This suggests that the increase in R_{s}-related FF losses in lightweight SHJ solar modules stems from the interconnection foil rather than direct UV effects on the solar cells. Previous studies have reported that interconnection foils in lightweight SHJ solar modules degrade under damp-heat conditions [12]. We therefore suspect that moisture ingress into the solar module may be responsible for the observed R_{s} increase. Further discussion is provided in Subsection 6.3.2.

6.3 UVID of SHJ solar modules with downshifting encapsulants

Building on the results in Section 6.2, where the UV stability of lightweight SHJ solar modules with different encapsulants was investigated, this section focuses on solar modules incorporating UV-DS encapsulants. In particular, we examine how the solar module structure, specifically glass/glass versus lightweight configurations, affects the UVID behavior. The optoelectronic properties of these solar modules were monitored before and after controlled UV exposure to elucidate the combined influence of encapsulant type and solar module architecture on performance stability.

6.3.1 Interpretation of the UVID mechanism of lightweight SHJ solar modules with downshifting encapsulants

In the previous section, the UV-DS module exhibited only moderate degradation compared with the UV-T module, as part of the UV photons were shifted into visible light, thereby reducing the number of UV photons reaching the solar cell and mitigating recombination losses. However, since the DS effect cannot fully shift all incident UV photons, a decline in the DS effect was observed in lightweight solar modules with downshifting encapsulants, driven by the synergistic action of UV photons and oxidants. Organic UV downshifting agents are inherently susceptible to photo-oxidation, which diminishes their ability to shift UV photons into visible photons. Consequently, a greater fraction of harmful UV light penetrates the encapsulant and reaches the solar cell. These high-energy UV photons can break the Si-H bonds, deteriorating the surface passivation and increasing charge-carrier recombination, ultimately lowering the overall solar module efficiency. Figure 6.14 illustrates the degradation mechanism of the DS effect.

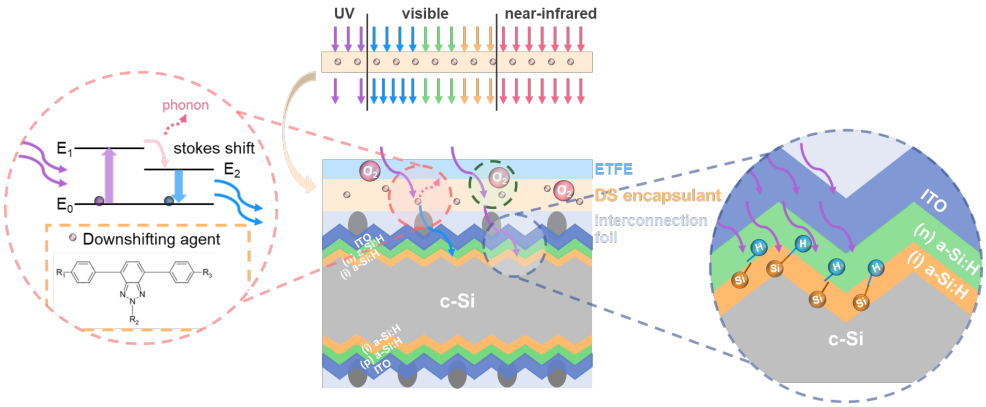


Figure 6.14: Schematic diagram of the working principle of UV-downshifting effect (marked by red circle), degradation mechanism of the downshifting (DS) effect (marked by green circle), and UVID mechanism in SHJ solar cells (marked by blue circle).

6.3.2 UVID of SHJ solar modules with downshifting encapsulants: influence of solar module structure

I-V characteristics of solar modules

Figure 6.15 presents the evolution of normalized electrical parameters for SHJ solar modules with UV-DS encapsulant in different solar module structures under increasing UV radiation dose. After 120 kWh/m^2 of UV exposure, the G/G and G/BS solar modules

exhibited relatively low efficiency degradations of 2.18%$_{rel}$ and 1.62%$_{rel}$, respectively, compared to 6.15%$_{rel}$ for the FS/BS solar module. In the glass/glass solar module, efficiency loss was dominated by a J_{sc} reduction of 1.32%$_{rel}$, with minimal changes in FF and V_{oc}. The G/BS solar module showed a similar degradation profile to the G/G solar module. By contrast, the FS/BS solar module suffered the largest efficiency loss, primarily driven by declines in FF and V_{oc}. As shown in Figure 5.20, the ETFE front sheet exhibits higher UV transmittance than glass, allowing more high-energy UV photons to reach the solar cells and accelerate passivation deterioration.

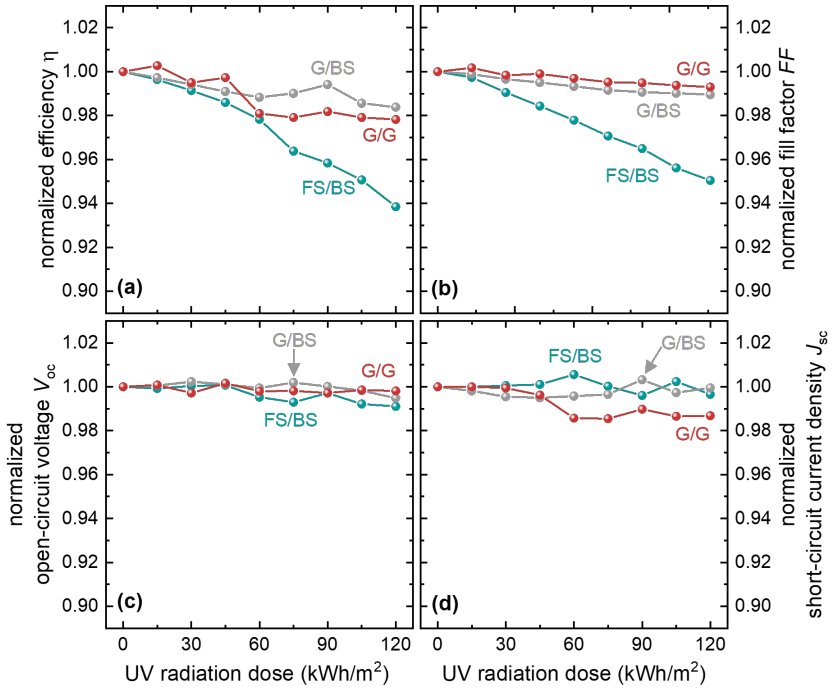


Figure 6.15: Normalized values of (a) efficiency (η), (b) fill factor (FF), (c) open-circuit voltage (V_{oc}) and (d) short-circuit current density (J_{sc}) as a function of UV radiation dose for solar modules with UV-DS encapsulant in different solar module structures: front sheet/back sheet (FS/BS), glass/back sheet (G/BS) and glass/glass (G/G) solar modules.

FF losses analysis of solar modules

Figure 6.16 illustrates the evolution of pFF and FF for SHJ solar modules with UV-DS encapsulant in different solar module structures under increasing UV radiation dose. After 120 kWh/m^2 of exposure, the G/BS and G/G solar modules exhibited markedly smaller pFF reductions than the FS/BS solar module. As established in earlier analyses, pFF loss is closely linked to UV-induced degradation. In the FS/BS solar modules,

deterioration of the DS effect allowed more UV photons to reach the solar cell, thereby increasing pFF loss. In contrast, the G/G and G/BS configurations effectively suppressed DS degradation, resulting in significantly lower pFF losses.

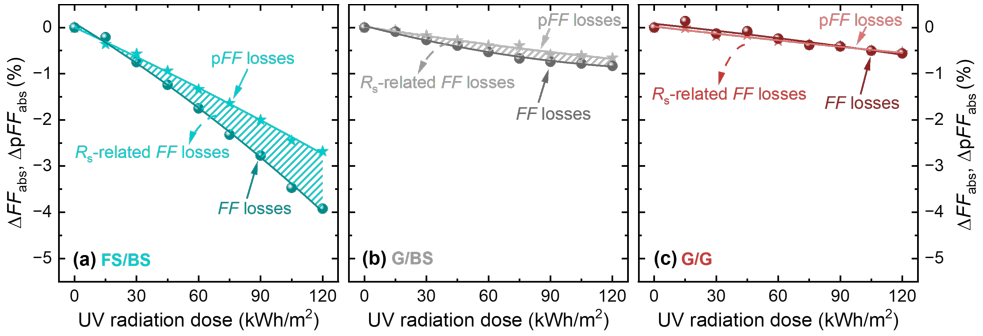


Figure 6.16: Changes in pseudo fill factor (pFF) and fill factor (FF) of solar modules with UV-DS encapsulant in different solar module structures: (a) front sheet/back sheet (FS/BS), (b) glass/back sheet (G/BS), and (c) glass/glass (G/G), as a function of UV radiation dose. ΔpFF_{abs} and ΔFF_{abs} denote the absolute changes in pFF and FF, respectively.

Furthermore, R_s-related FF losses were negligible in the G/G solar module and only slightly increased in the G/BS solar module. As discussed earlier, such losses in lightweight solar modules originate from the interconnection foil (IF1). Due to the higher water-vapor transmission rates of polymer front and back sheets, lightweight designs allow for greater moisture ingress than conventional glass solar modules. The penetrated moisture can degrade solar cell interconnections employing interconnection foil, thereby increasing R_s-related FF losses [12]. We therefore speculate that the increase in R_s-related FF losses is due to degradation of the interconnection foil caused by moisture ingress.

EQE analysis of solar modules

Figure 6.17 compares the EQE and reflectance of UV-DS modules with different solar module structures before and after 120 kWh/m² of UV exposure. In the FS/BS solar module, both EQE and reflectance dropped markedly at wavelengths below 400 nm, whereas the G/G and G/BS solar modules showed no observable changes. These results confirm that the DS effect degraded in the FS/BS configuration but remained stable in G/G and G/BS solar modules. Previous studies have shown that the synergistic action of UV photons and oxygen can trigger photo-oxidation, leading to polymer encapsulant degradation [23, 177, 267]. It is therefore reasonable to attribute the deterioration of the downshifting agent in FS/BS solar modules to photo-oxidation. Compared with a glass front cover, the polymer front sheet in FS/BS solar modules provides less protection against oxidants such as ozone and oxygen, facilitating their ingress and subsequent

degradation of the downshifting agent. The detailed chemical mechanism underlying this degradation has already been discussed in Subsection 6.1.2.

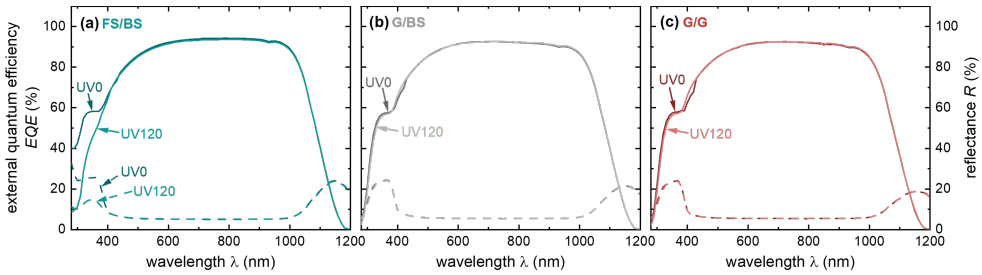


Figure 6.17: *EQE* (solid line) and reflectance (dashed line) of solar modules using UV-DS encapsulants in different solar module structures: (a) front sheet/back sheet (FS/BS), (b) glass/back sheet (G/BS) and (c) glass/glass (G/G), measured before and after 120 kWh/m^2 of UV exposure.

Currently, G/G and G/BS configurations dominate the PV market. This study demonstrates that pairing downshifting encapsulants with these configurations yields high UV stability. In contrast, integrating downshifting encapsulants into lightweight solar module designs significantly reduces UV stability, highlighting the need for more reliable encapsulation strategies tailored to lightweight solar modules or more stable UV downshifting materials.

6.4 A strategy for enhancing the performance and UV stability of lightweight SHJ solar modules

6.4.1 Dual-layer encapsulation approach

From the above analysis, the UV-DS encapsulant has been shown to shift UV photons into the visible range. However, residual UV photons that are not shifted can still penetrate the encapsulant, inducing UVID in the solar cells. Furthermore, degradation of the DS effect was observed in lightweight solar modules with UV-DS encapsulants during UV exposure. As the DS effect deteriorates, an increasing fraction of UV photons remains unshifted, leading to greater passivation degradation and, consequently, higher efficiency losses.

To address this issue, a novel dual-layer encapsulant design was proposed, combining a UV-DS layer with a UV-blocking layer as the front encapsulant in lightweight solar modules. The solar module structure is illustrated in Figure 6.18. In this design, UV

photons not effectively shifted by the UV-DS layer are subsequently blocked by the additional UV-blocking layer, thereby protecting the solar cells from UV-induced damage. A 120 kWh/m² UV exposure test was conducted to assess the UV stability of this configuration and to compare it with a solar module using a single-layer UV-DS encapsulant. The configurations of the test solar modules are listed in Table 6.4, the fabrication process is shown in Figure 3.9, and the lamination parameters for each sample type are provided in Table A.3.

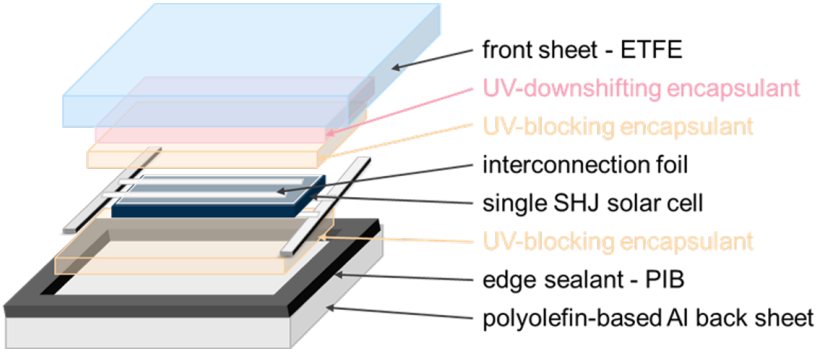


Figure 6.18: Schematic of the lightweight SHJ single-cell solar module with a dual-layer front encapsulant.

Table 6.4: Configurations of the test solar modules.

Module No.	Front sheet	Encapsulant (front/rear)	Solar cell	IF	Back sheet
6.4	ETFE	DS-EVA	M2 0BB	IF1	Al-bs
6.8	ETFE	DS-EVA+TPO/ TPO	M2 0BB	IF1	Al-bs
6.9	ETFE	DS-EVA+PO-UV/ PO-UV	M2 0BB	IF1	Al-bs

6.4.2 Performance and stability of solar modules with dual-layer encapsulation design

To evaluate the effectiveness of the dual-layer encapsulation design in improving the UV stability of lightweight SHJ modules, the optoelectronic properties of the fabricated test solar modules were monitored during UV exposure. In particular, solar modules with the proposed dual-layer front encapsulant (UV-DS + UV-blocking) were compared against reference solar modules using a single-layer UV-DS encapsulant.

I-V characteristics of solar modules

Figure 6.19 presents the evolution of normalized electrical parameters during UV exposure for lightweight SHJ solar modules with the proposed dual-layer encapsulant design, compared with the single-layer UV-DS encapsulant design. Two dual-layer configurations were investigated: (i) UV-DS combined with UV-B_{375} encapsulant and (ii) UV-DS combined with UV-B_{350} encapsulant. The results show that both dual-layer designs exhibit lower efficiency degradation than the single-layer UV-DS module. Notably, the UV-DS + UV-B_{375} module maintained η, FF, V_{oc}, and J_{sc} nearly unchanged after 120 kWh/m^2 of UV exposure, indicating excellent UV stability. In contrast, the UV-DS + UV-B_{350} module displayed a slight efficiency reduction, primarily due to a decline in FF. This observation is consistent with the earlier discussion that even a minimal number of UV photons in the 350 - 375 nm wavelength range can induce UVID in SHJ solar cells.

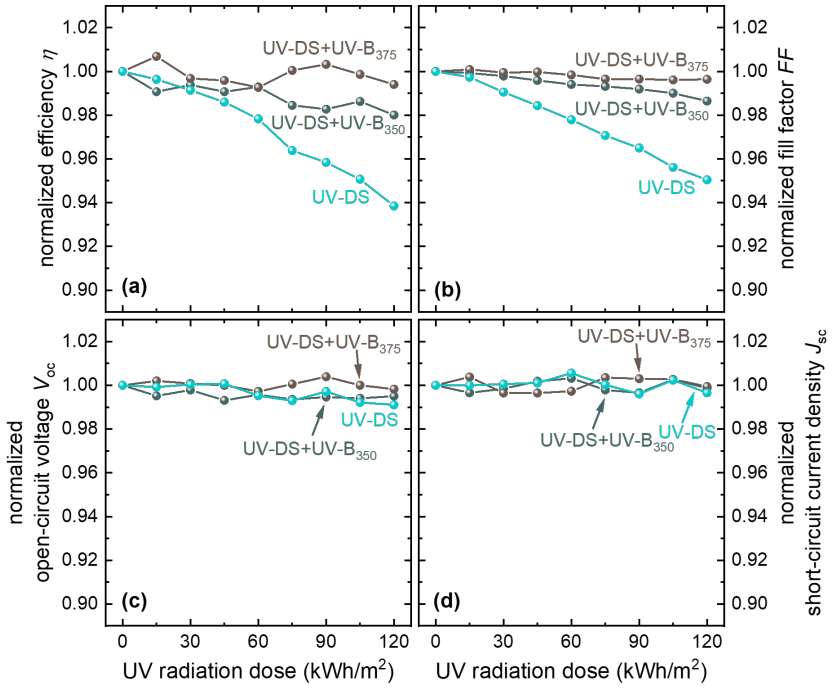


Figure 6.19: Normalized values of (a) efficiency (η), (b) fill factor (FF), (c) open-circuit voltage (V_{oc}) and (d) short-circuit current density (J_{sc}) as a function of UV radiation dose for lightweight SHJ solar modules with UV-DS, UV-DS+UV-B_{350}, and UV-DS+UV-B_{375} as the front encapsulant.

PL imaging of solar modules

A comparison of PL imaging among the three solar module types is shown in Figure 6.20. The PL intensity of the UV-DS + UV-B encapsulant solar modules remained virtually unchanged after UV exposure, indicating stable passivation of the SHJ solar cells. In contrast, the UV-DS module exhibited a noticeable reduction in PL intensity, attributable to passivation degradation.

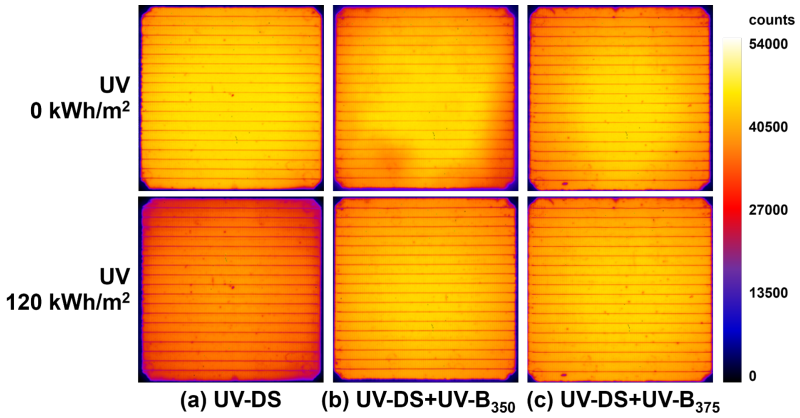


Figure 6.20: PL images of lightweight SHJ solar modules with (a) UV-DS, (b) UV-DS+UV-B_{350}, and (c) UV-DS+UV-B_{375} before and after 120 kWh/m^2 of UV exposure.

FF losses analysis of solar modules

As previously discussed, *FF* losses are the primary cause of efficiency degradation in lightweight SHJ solar modules during UV exposure. Figure 6.21 presents the absolute changes in p*FF* and *FF* for solar modules with dual-layer and single-layer encapsulants. The dual-layer design (UV-DS + UV-B) exhibited smaller p*FF* and R_s-related *FF* losses than the single-layer (UV-DS) design. Notably, the p*FF* of the UV-DS + UV-B_{375} module remained stable, whereas the UV-DS + UV-B_{350} module showed a slight p*FF* reduction. This minor decrease is attributed to the insufficient UV cut-off wavelength of the UV-B_{350} encapsulant, as discussed earlier.

Furthermore, the R_s-related *FF* losses were markedly reduced in the UV-DS + UV-B module, demonstrating that the novel dual-layer encapsulation design can effectively suppress R_s-related *FF* losses. As discussed in Section 6.3, the increase in R_s in lightweight solar modules is likely induced by moisture ingress, which deteriorates solar cell interconnections. The improved stability observed here can be attributed to the enhanced barrier

properties of the dual-layer encapsulant, which more effectively hinders the ingress of moisture and oxidants (e.g., ozone, oxygen) compared with the single-layer design.

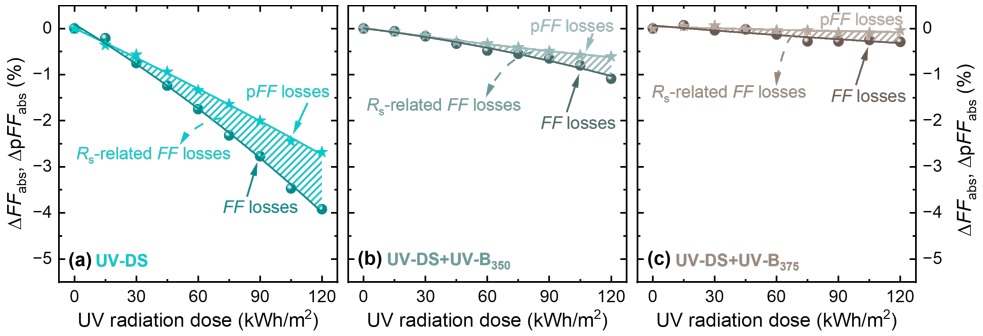


Figure 6.21: Changes in pseudo fill factor (p*FF*) and fill factor (*FF*) of lightweight SHJ solar modules with (a) UV-DS, (b) UV-DS+UV-B_{350} and (c) UV-DS+UV-B_{375}, as a function of UV radiation dose. ΔpFF_{abs} and ΔFF_{abs} denote the absolute changes in p*FF* and *FF*, respectively.

EQE analysis of solar modules

Figure 6.22 presents the *EQE* and reflectance of lightweight SHJ solar modules with the dual-layer encapsulant design, in comparison with those using a single-layer encapsulant, measured before and after 120 kWh/m² of UV exposure. *EQE* and reflectance of the lightweight solar modules exhibited a pronounced reduction in the short-wavelength range (280-400 nm). The overall photocurrent loss, derived from the *EQE* data, was $0.90\%_{rel}$ for the UV-DS module, $0.85\%_{rel}$ for the UV-DS+UV-B_{350} module, and only $0.32\%_{rel}$ for the UV-DS and UV-B_{375} module. The latter effectively blocked most UV photons from reaching the solar cells, resulting in negligible p*FF* degradation and stable passivation properties, as indicated in Figure 6.21. Consequently, the observed *EQE* reduction in the UV-DS+UV-B_{375} module is attributed primarily to degradation of the DS effect, with the associated current loss limited to $0.32\%_{rel}$. Furthermore, the DS utilization efficiency, estimated from the *EQE* spectra, decreased from approximately 34% to 21% after 120 kWh/m² of UV exposure.

Although the DS effect degraded in all lightweight solar modules with DS encapsulants, the resulting photocurrent loss was limited to only $0.32\%_{rel}$. Incorporating a UV-B encapsulant in a dual-layer configuration with UV-DS significantly enhanced UV stability by reducing carrier recombination losses compared to a single-layer UV-DS design. As shown in Figure 6.23, the dual-layer solar module retained over 98% of its initial efficiency after 120 kWh/m² of UV exposure, representing an $8.92\%_{rel}$ higher post-exposure efficiency than the solar module with a UV-T encapsulant. This design not only delivers

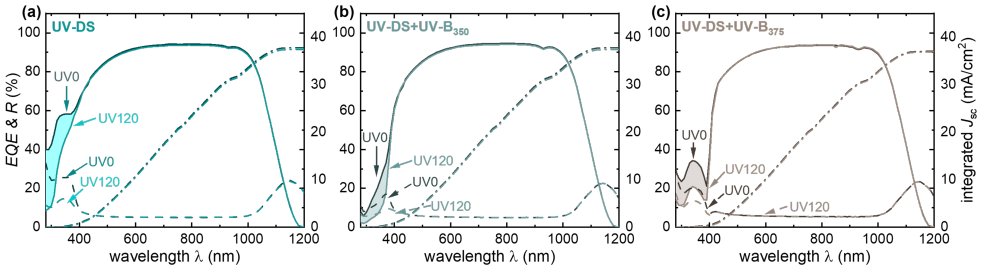


Figure 6.22: *EQE* (solid line) and reflectance (R) (dashed line) and integrated short-circuit current density (J_{sc}) (dashed dot line) of lightweight SHJ solar modules with (a) UV-DS, (b) UV-DS+UV-B_{350}, and (c) UV-DS+UV-B_{375}, measured before and after 120 kWh/m^2 of UV exposure.

a higher initial power output but also maintains superior performance after UV exposure, indicating strong potential for improved long-term energy yield.

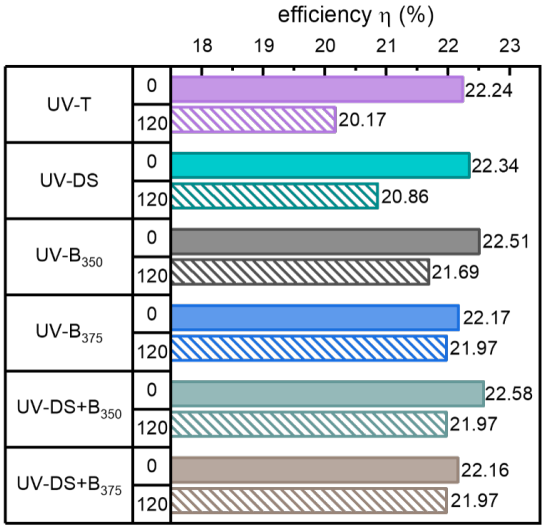


Figure 6.23: Solar module efficiencies before and after 120 kWh/m^2 of UV exposure, with currents for efficiency calculation derived from *EQE* measurements.

To more accurately compare the absolute efficiency loss of modules with different encapsulants before and after UV radiation, we calculated efficiency using the *EQE* integral current for the following two reasons. Firstly, The SunSimulator used for *I-V* testing does not have an UV part which is very close to AM1.5, but it complies with the standard. However, the spectrum for *EQE* measurements does. Secondly, compared to modules using UV-blocking encapsulants, modules using UV-downshifting encapsulants exhibit a current gain of approximately 2%$_{rel}$. However, we observed fluctuations in the J_{sc} measured via *I-V* testing (approximately 2%$_{rel}$), as shown in Figure 6.7(d).

7 Summary and outlook

This study aims to develop a high-performance, lightweight SHJ solar module with low area density and high power-to-weight ratio by employing encapsulation materials that are most compatible with SHJ technology, with particular focus on its DH and UV stability. The findings contribute to the advancement of lightweight SHJ solar modules with high stability suitable for industrialized mass production.

A complementary and in-depth understanding of DHID in lightweight SHJ solar modules was established, focusing on two critical design variables: TCO layers and encapsulation materials. The comparative analyses and comprehensive investigation provide key insights into the DHID behavior of lightweight SHJ solar modules incorporating different encapsulants, elucidating degradation mechanisms specific to individual material types and thereby offering practical guidelines for lightweight solar module design and material selection. A rough estimation of the equivalence between accelerated DH aging and real field conditions was derived using Arrhenius-based modeling.

In parallel, a comprehensive investigation of the degradation mechanisms under UV exposure, using encapsulants with different UV-transmission properties, revealed the vulnerabilities and performance trade-offs of these materials. The results further suggest a practical encapsulation strategy to improve durability and ensure long-term performance in lightweight SHJ solar modules.

Overall, this chapter summarizes the main findings of the study and outlines the remaining challenges and critical issues related to the performance and reliability of lightweight SHJ solar modules, setting a foundation for future improvements in materials engineering and structural design.

7.1 Summary

7.1.1 Damp-heat stability of lightweight SHJ solar modules

Role of TCOs In Chapter 4, lightweight SHJ solar modules employing ITO, AZO, and a hybrid ITO/AZO/ITO front TCO were exposed to 85 °C/85% RH for 1000 h. The AZO-based modules suffered the most severe performance loss ($58.57\%_{\mathrm{rel}}$), primarily due to the synergistic effect of moisture-induced delamination of the interconnection foil and penetration of water molecules into the AZO grain boundaries, leading to a sharp rise in sheet resistance of the AZO layer, resulting in a decrease in the conductivity of the AZO layer, leading to a dramatic increase in R_{s} and a corresponding decrease in the FF of the AZO modules. The dramatic increase in R_{s} leads to a decrease in carrier collection efficiency, resulting in a significant decrease in J_{sc}. In addition, moisture penetrates through the damaged AZO layer into the a-Si:H passivation layer, causing passivation degradation, which leads to an increase in recombination, resulting in a decrease in V_{oc} of the AZO modules. By contrast, capping AZO with a thin ITO layer significantly reduced efficiency loss to $18.92\%_{\mathrm{rel}}$, demonstrating that even a minimal ITO top layer can serve as an effective moisture barrier and improve long-term stability.

Although it remains challenging to quantitatively determine the extent of moisture penetration through the encapsulation foil into the TCO and passivation layers, this study offers valuable insights into the degradation mechanisms of AZO-based lightweight SHJ solar modules. The findings underscore the critical role of the ITO capping layer in suppressing moisture diffusion and enhancing the DH stability of AZO-based SHJ solar cells and modules.

Role of interconnection foil Interconnection foil was identified as a key contributor to performance degradation, primarily due to its poor adhesion to the AZO layer, which facilitates moisture ingress. AZO-based lightweight solar modules incorporating the first-version interconnection foil (IF1) exhibited substantial performance losses after 1000 h of DH exposure. This deterioration was attributed to delamination of IF1 and subsequent moisture percolation into the underlying AZO and passivation layers.

To address this issue, the performance and stability of solar modules using a second-version interconnection foil (IF2) for solar module fabrication were systematically compared with those of IF1-incorporated solar modules to evaluate potential improvements in DH reliability. Results clearly show that the AZO-incorporated solar module with IF2 exhibited markedly enhanced stability, with efficiency decreasing by only $17.65\%_{\mathrm{rel}}$

after 1000 h of DH exposure, compared to a 52.36%$_{\text{rel}}$ loss for the IF1-incorporated solar module. This improvement is largely attributed to the reduced loss in FF, driven by a smaller increase in R_{s}. Furthermore, the reductions in V_{oc} and pFF were less pronounced, indicating that passivation degradation from heat-assisted moisture ingress was effectively suppressed. Visual inspection, together with EL and PL imaging, confirmed that the moisture-related degradation caused by the combined effects of foil delamination and moisture ingress was substantially mitigated through the use of the improved interconnection foil (IF2).

Role of encapsulation materials Chapter 5 demonstrates the feasibility of fabricating lightweight SHJ solar modules with a low area density (approximately 2 kg/m^2) while maintaining a high power-to-weight ratio (around 70 W/kg) and excellent damp-heat stability, even in single-cell configurations. For larger solar modules, the power-to-weight ratio is expected to increase further owing to the reduced proportion of interconnection and edge sealant materials per unit area. In this work, the compatibility of various encapsulation materials, incorporating TPO, TPU, PO-UV, PO-S, EVA, EPE, DS-EVA, and DS-EPE, with SHJ solar cells in lightweight solar module architectures was systematically evaluated under DH conditions. A comprehensive degradation analysis was conducted, focusing on the optoelectronic performance of the solar modules as well as the chemical properties of the polymer encapsulants.

The results show that efficiency losses after 1000 h of DH exposure varied widely, from 3.22%$_{\text{rel}}$ to 54.06%$_{\text{rel}}$, depending strongly on the encapsulant type. In most cases, the dominant degradation mechanism was an increase in R_{s}. Solar modules encapsulated with EPE exhibited the largest efficiency loss, primarily due to a substantial R_{s} increase caused by two factors: (i) wires detachment from ribbons due to solder-joint failure, and (ii) interconnection failure from wires detachment at the solar cell fingers. XCT confirmed finger breakage resulting from wire detachment, consistent with EL observations. EL imaging and Raman spectroscopy further indicated that metal corrosion was not the primary degradation pathway. While the EVA-encapsulated solar module showed noticeable yellowing after 1000 h of DH exposure, its impact on performance was negligible. In contrast, the TPO-encapsulated solar module exhibited the lowest degradation, only 3.22%$_{\text{rel}}$, attributed to TPO's low water permeability, high crystallinity, low chemical polarity, and high thermal stability, making it a highly promising encapsulant for moisture-sensitive solar cells. Based on Arrhenius-based modeling, 1000 h of DH testing at 85 °C, 85% RH is estimated to correspond to approximately 1.1 years of exposure under typical field conditions for the ETFE/Al-bs lightweight SHJ solar module with TPO encapsulants, during which about 5%$_{\text{rel}}$ efficiency degradation was observed.

Building on these findings, an optimized DH-stable lightweight solar module was developed using PET3 as the front sheet, a polyolefin-based aluminum back sheet, and TPO as the encapsulant. This configuration achieved an exceptionally low efficiency loss of just $0.47\%_{\mathrm{rel}}$ after 1000 h of DH exposure, comparable to that of conventional glass/back sheet solar modules, demonstrating that lightweight designs can match the long-term stability of traditional solar module architectures.

7.1.2 UV stability of lightweight SHJ solar modules

Role of encapsulation materials Chapter 6 presents a comprehensive investigation of UVID in lightweight SHJ solar modules employing UV-blocking, UV-transmitting, and UV-downshifting encapsulants. After 120 kWh/m^2 of indoor UV exposure, equivalent to approximately 30 months of outdoor exposure in Jülich, Germany, these solar modules exhibited relative efficiency losses of 2.17%, 9.25%, and 6.15%, respectively. The efficiency decline was primarily driven by reductions in V_{oc} and FF, accompanied by a decrease in pFF. The loss in pFF was identified as the dominant contributor to the FF reduction, arising from the deterioration of solar cell passivation under UV radiation. High-energy UV photons can break Si-H bonds used for chemical passivation, increasing the density of dangling bonds at the silicon surface and thereby increasing surface recombination. In addition, a comparison of UV-transmitting encapsulated solar modules interconnected with either IF or ECT revealed that the R_{s}-related FF loss was predominantly caused by degradation of the interconnection foil rather than by UV radiation itself.

Degradation of downshifting effect Lightweight SHJ solar modules with UV-downshifting encapsulants exhibited lower degradation than those with UV-transmitting encapsulants, yet higher degradation than those with UV-blocking encapsulants. This indicates that UV-downshifting encapsulants can effectively mitigate UVID, though they cannot fully shift all incident UV photons. EQE measurements showed a reduction in downshifting utilization efficiency from approximately 34% to 21% after 120 kWh/m^2 of UV exposure, reflecting a loss in the ability to shift UV photons to visible light. As the DS effect degraded, an increasing fraction of UV photons penetrated the encapsulants and reached the solar cell, accelerating passivation loss and efficiency decline. PY-GC-MS analysis revealed that the presumed organic UV downshifting agent exhibited only a slight decrease in concentration after DH exposure but was completely depleted after UV exposure. Organic UV downshifting agents are generally susceptible to photo-oxidation; thus, depletion of antioxidants and HALS in the encapsulant matrix can further compromise the stability. Furthermore, comparison with glass-covered solar modules confirmed that the polymer

front sheet in lightweight designs provides less protection against oxidants, such as ozone and oxygen, than a glass front cover. The ingress of these oxidants, in combination with UV photons, can accelerate the degradation of the downshifting agent.

A strategy for enhancing performance and UV stability of lightweight SHJ solar modules To address these limitations, a novel dual-layer encapsulation architecture was developed, combining a UV-downshifting layer with an additional UV-blocking layer. In this configuration, UV-photons that cannot be effectively shifted are blocked before reaching the solar cell, while the barrier properties of the dual-layer structure also reduce the ingress of moisture and oxidants. This approach not only mitigates R_s-related *FF* losses by protecting interconnections but also preserves solar cell passivation. This design maintained over 98% of the initial solar module performance after UV exposure and delivered an efficiency $8.92\%_{rel}$ higher than that of the UV-transmitting solar module. The dual-layer configuration not only provided higher initial power output but also retained it over time, offering a significant energy-yield advantage.

7.2 Outlook

7.2.1 Pathways toward durable, lightweight SHJ solar modules

Looking forward, the route toward commercially viable lightweight SHJ solar modules lies in an integrated materials-and-design approach to mitigate moisture- and temperature-driven degradation. On the TCO side, hybrid structures such as a capping layer strategy of ITO/AZO/ITO offer a promising balance between reduced indium consumption and improved damp-heat stability. Nevertheless, their long-term adhesion to interconnection foils must be enhanced, which could be achieved through interface engineering, surface treatments, or alternative interconnection strategies. For encapsulation, peroxide-free, low-WVTR polymers with high crystallinity, such as TPO, should be prioritized due to their demonstrated compatibility with SHJ solar cells and their ability to suppress DHID. The thermoplastic elastomer that exploits thermo-reversible physical crosslinking, such as ion bonds, hydrogen bonds, or via crystallites, shows potential in the recycling of solar modules. Edge sealing should be further improved to reduce ingress pathways.

Mechanical reliability is another major challenge. Solder joint fatigue and thermo-mechanical stresses arising from mismatched CTE remain critical concerns. Kutter et al. [268] reported that the conventional soldered ribbon-based interconnections combined with polymer-based cover materials induce unfavorable stresses during thermal cycling

(TC), and similar defects were observed in our DH tests. Moisture ingress exacerbates these effects by reducing mechanical integrity through corrosion, delamination, or hydrolysis. When thermal cycling or temperature gradients occur simultaneously, the differential expansion of materials can accelerate cracking, solder joint fatigue, and interface delamination. Compared with glass, polymeric top covers lack the sufficient rigidity to counteract ribbon compression-induced forces. In particular, ETFE exhibits a high CTE of 9.4×10^{-5}/K, which is nearly two orders of magnitude higher than that of glass, leading to intensified finger breakage and ribbon disconnection [268].

The absence of a rigid glass front cover also reduces solar module stiffness, rendering lightweight solar modules more susceptible to solar cell cracking and mechanical damage under external stress, as highlighted in a recent study [269]. Optimizing solar module materials to reduce cracking propensity is therefore of great interest. Composite substrates have shown significant promise in this regard. Martins et al. [6] developed a polymer-front-sheet solar module with a composite sandwich back sheet incorporating an aluminum honeycomb core and a polyolefin adhesive layer, which demonstrated excellent resistance to both TC and DH tests. In another study, Martins et al. [5] emphasized the importance of balancing front sheet rigidity and back sheet stiffness to maximize hail resistance and mechanical rigidity while minimizing the solar module's weight. The front sheet with a high storage modulus can mitigate hail-induced damage. In addition, the high rigidity of the front sheet helps to dissipate the impact energy generated by hailstones on the solar module surface. On the contrary, the stiffness of the composite back sheet has a significant impact on hail resistance, and low-stiffness back sheets can reduce damage caused by hailstones. This effect is attributed to a global energy dissipation of the hail impacts through the entire structure [269]. The use of a composite encapsulant can reduce the CTE differences in the material stack and establish a favorable coupling between solar cell strings and the back sheet due to a dramatically increased stiffness of the back encapsulant [113]. Among all factors, the Young's modulus of the back sheet was identified as a dominant determinant of impact and thermo-mechanical reliability, surpassing the influence of the encapsulant modulus [270]. Finite element modeling (FEM) of stress distributions during thermal cycling and bending is a powerful tool for guiding such design optimizations.

In addition to thermo-mechanical stability, optical and chemical durability must be addressed. Our results highlight the potential of UV-downshifting encapsulants to enhance the optoelectronic performance of lightweight SHJ solar modules, but also their vulnerability to UV-induced degradation, particularly in polymer front sheet structures. The synergistic action of UV photons and oxidants was identified as a key driver of downshifting agent depletion, leading to a reduction in downshifting efficiency. Future efforts should focus on the development of UV- and photo-oxidation-resistant downshift-

ing materials, particularly inorganic or hybrid downshifting agents, and the refinement of encapsulant formulations to enhance long-term outdoor stability. The dual-layer encapsulation concept proposed in this work, combining UV-downshifting and UV-blocking layers, exhibited excellent UV resilience and should be further explored for scale-up and commercialization. In parallel, advanced spectral management strategies, such as downshifting agents capable of shifting UV photons into lower-energy visible bands (e.g., green light), or even downconversion materials [271] that can split a single UV photon into two lower-energy photons, represent exciting opportunities to further improve photon utilization efficiency.

Finally, future reliability assessments should move beyond single-stress testing to consider accelerated combined-stress and sequence-aging protocols, including damp-heat, UV, thermal cycling, and mechanical stress. Such holistic testing will better capture real-world degradation pathways and inform robust design standards.

By integrating moisture-resistant TCO stacks, chemically stable encapsulants, and mechanically optimized solar module architectures, lightweight SHJ solar modules could achieve durability comparable to that of conventional glass-based systems while delivering unprecedented power-to-weight ratios - paving the way for widespread adoption in integrated- and portable- PV applications.

7.2.2 Perovskite/SHJ tandem lightweight solar modules

Perovskite/SHJ tandem architectures represent one of the most promising pathways to push lightweight solar modules beyond the single-junction efficiency limits while maintaining the stability and flexibility required for emerging applications. The highest certified efficiency for perovskite/SHJ tandem solar cells has been achieved by LONGi [272], who recently reached 34.85%, certified by the National Renewable Energy Laboratory (NREL). This sets a new world record for perovskite/crystalline silicon tandem solar cells. The high open-circuit voltage and excellent low-temperature processing compatibility of SHJ solar cells make them ideal bottom solar cells for perovskite integration, while the tunable bandgap of perovskites enables optimal current matching and enhanced spectral utilization. In lightweight configurations, such tandems could deliver exceptional power-to-weight ratios, making them particularly attractive for integrated PV, aerospace, and portable power applications. However, realizing this potential will require overcoming several challenges: ensuring long-term perovskite stability under moisture, heat, and UV exposure; developing encapsulation strategies that simultaneously protect both the perovskite top cell and the SHJ bottom cell; and managing mechanical reliability in flexible or polymer-based solar module stacks. Additionally, optical and interconnection

designs must be optimized to minimize parasitic absorption and resistive losses without compromising mechanical integrity. Advances in barrier films, UV-filtering or downshifting layers, and thermally stable interconnection foils, many of which are already being explored for SHJ solar modules, can be leveraged for tandem designs. If these materials and engineering challenges are addressed in parallel with scalable manufacturing solutions, perovskite/SHJ lightweight tandem solar modules have the potential to achieve efficiencies exceeding 35% with lifetimes approaching those of conventional glass-based solar modules, enabling a new generation of ultra-high-performance, application-adaptable solar modules.

A Appendix

Table A.1: Specifications of the polymer encapsulants.

Encapsulant	**Material composition**	**Color**	**Thickness (μm)**	**Crosslinking type**
TPO	Thermoplastic polyolefin	Transparent	450	Physical
TPU	Thermoplastic polyurethane	Transparent	600	Physical
PO-UV	Thermoplastic polyolefin	Transparent	450	Physical
EPE	EVA/POE/EVA	Transparent	600	Chemical
EVA	Ethylene-vinyl acetate	Transparent	600	Chemical
PO-S	Thermoplastic polyolefin	Transparent	450	Physical
DS-EVA	UV-downshifting EVA	Transparent	420	Chemical
DS-EPE	UV-downshifting EPE	Transparent	420	Chemical

Table A.2: Specifications of front sheets and back sheets.

Type	Material	Material Composition	Thickness (μm)
front sheet	ETFE	Ethylene tetrafluoroethylene	100
	PVF	Polyvinyl fluoride	150
	PET1	PET/PVF laminated foil	300
	PET2	Polyethylene terephthalate	370
	PET3	Polyethylene terephthalate	203
back sheet	Px-bs	Polyolefin-based foil	175
	Al-bs	A polyolefin-based foil with aluminum as interlayer	202

Table A.3: The parameters of the lamination process for each type of solar module sample.

Module No.	Temperature (°C)	Evacuation time (s)	Lamination time (s)	Pressure (mbar)
4.1	125	240	600	750
4.2	125	240	600	750
4.3	125	240	600	700
4.4	140	400	600	750
4.5	125	240	600	750
4.6	125	300	600	750
4.7	125	300	600	800
4.8	125	300	600	750
4.9	125	300	600	750
5.1	120	300	600	750
5.2	135	300	600	800
5.3	125	240	600	700
5.4	140	400	600	750
5.5	140	300	600	750
5.6	125	240	600	700
5.7	145	360	660	700
5.8	145	240	960	750
5.9	120	240	600	750
5.10	125	320	600	750
5.11	125	300	600	750
5.12	125	300	600	750
5.13	120	240	600	750
5.14	150	360	600	800
6.1	120	300	600	750
6.2	125	240	600	700
6.3	140	300	600	750
6.4	140	420	780	750
6.5	140	390	660	750
6.6	140	420	660	750
6.7	140	360	600	750
6.8	140	420	780	750
6.9	140	420	780	750

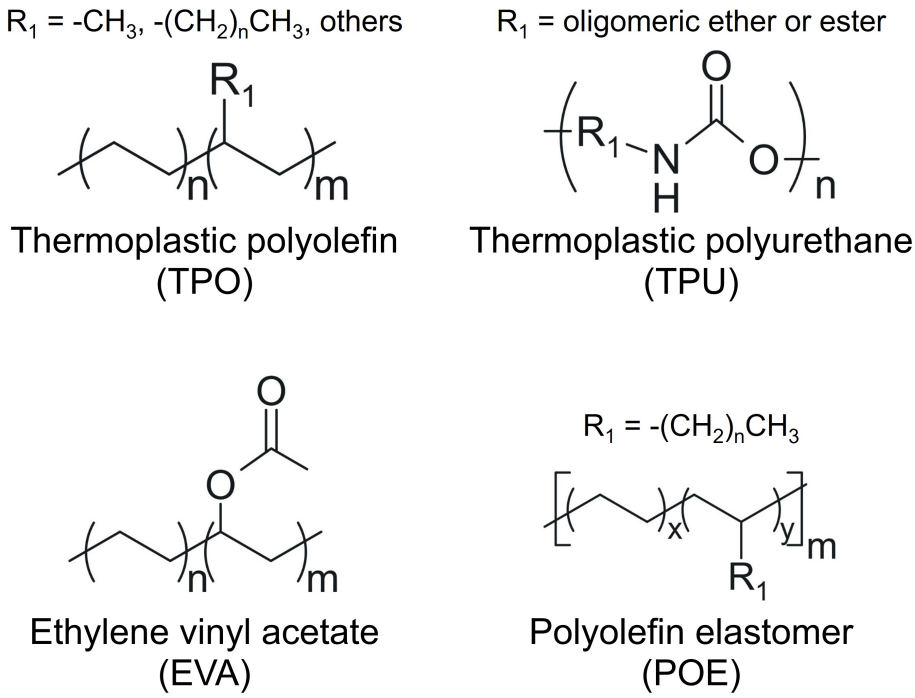


Figure A.1: Structural formula of typical polymer encapsulants.

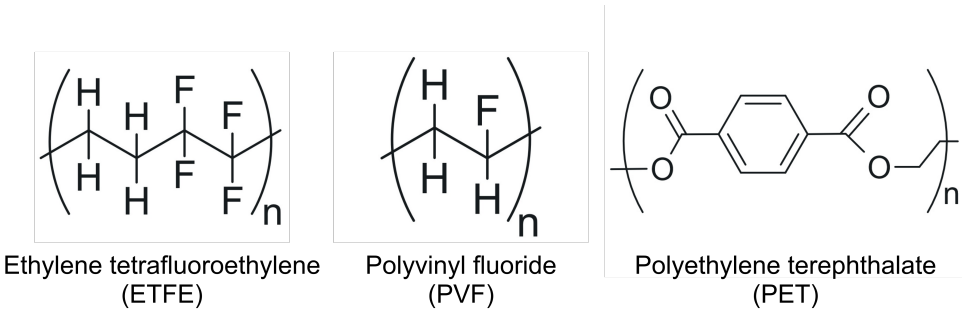


Figure A.2: Structural formula of typical front sheet materials.

B Symbols and abbreviations

Variables and physical constants

ΔFF_{abs}	absolute change in FF
ΔH_{r}	exothermal reaction enthalpy
$\Delta \mathrm{p}FF_{\mathrm{abs}}$	absolute change in pFF
η	power conversion efficiency
μ	charge carrier mobility
μ_{e}	electron mobility
$\phi_{\mathrm{AM1.5G}}$	incident photon at AM1.5G
ϕ_{bb}	spectral photon density of a black body
ϕ_{em}	EL intensity
ϕ_{in}	incident photon
π	Archimedes' constant
ρ	resistivity
c	vacuum speed of light
h	Plank's constant
n	ideality factor
n_1	ideality factor 1
n_2	ideality factor 2
AF	acceleration factor
A	absorptance

EQE	external quantum efficiency
E	photon energy
E_{a}	activation energy
FF	fill factor
IQE	internal quantum efficiency
I_{sc}	short-circuit current
J	current density
J_{01}	saturation current density of the first diode
J_{02}	saturation current density of the second diode
J_0	saturation current density
J_{mpp}	current densities at the maximum power point
J_{ph}	photo-generated current density
$J_{\mathrm{sc},EQE}$	short-circuit current density evaluated from the EQE
J_{sc}	short-circuit current density
P_{mpp}	power density at the maximum power point
P_{sun}	input power density
Q_{cam}	energy-dependent sensitivity of the detecting camera
Q_{e}	external QE
Q_{i}	internal QE
R	reflectance
R_{sh}	shunt resistance
R_{s}	series resistance
$Rs_{FF\text{-}\mathrm{p}FF}$	series resistance from JV-light and JV-$J_{\mathrm{sc}}\,V_{\mathrm{oc}}$
S_{cam}	EL signal
T	transmittance
T_{mp}	melting peak temperature
T_{onset}	onset temperature

T_{peak}	peak temperature
V	voltage
V_{mpp}	voltage at the maximum power point
V_{oc}	open-circuit voltage
k_{B}	Boltzmann's constant
n	carrier density/concentration
n_{e}	electron density/concentration
q	elementary charge
pFF	pseudo fill factor
QE	quantum efficiency

Materials and elements

a-Si	amorphous silicon
a-Si:H	hydrogenated amorphous silicon
Al_2O_3	aluminium oxide
AZO	Al-doped zinc oxide
C	carbon
c-Si	crystalline silicon
Ca	calcium
CIGS	copper-indium-gallium-selenide
CO_2	carbon dioxide
ECT	electrically conductive adhesive tape
EPE	EVA/POE/EVA
ETFE	ethylene tetrafluoroethylene
EVA	ethylene-vinyl acetate

H_2O	water
HALS	hindered amine light stabilizers
He	helium
Hg	mercury
In	indium
InGaAs	indium gallium arsenide
ITO	indium tin oxide
Mg	magnesium
mono-Si	monocrystalline silicon
O_2	oxygen
Pb	lead
PC	polycarbonate
PE	polyethylene
PET	polyethylene terephthalate
PIB	polyisobutylene
POE	polyolefin elastomer
poly-Si	polycrystalline silicon
PVB	polyvinyl butyral
PVF	polyvinyl fluoride
Si	silicon
Si-H	silicon-hydrogen
SiN_x	silicon nitride
SiO_2	silicon oxide
Sn	tin
TCO	transparent conductive oxide
TCOs	transparent conductive oxides
TPO	thermoplastic polyolefin

TPU	thermoplastic polyurethane
VA	vinyl acetate

Abbreviations

I-V	current-voltage
J-V	current density-voltage
0BB	0-busbar
9BB	9-busbar
Al-bs	polyolefin-based aluminum back sheet
Al-BSF	aluminum back surface field
ATR	attenuated total reflectance
BIPV	building-integrated PV
BSF	back surface field
CFPP	carbon fibre-reinforced polypropylene
CTE	coefficient of thermal expansion
CTM	cell-to-module
DH	damp-heat
DHID	damp-heat-induced degradation
DS	downshifting
DS agent	downshifting agent
DS-EPE	UV-downshifting EPE
DS-EVA	UV-downshifting EVA
DSC	differential scanning calorimetry
DWD	Deutscher Wetterdienst
EL	electroluminescence
FEM	finite element modeling
FS/BS	front sheet/back sheet
FTIR	Fourier-transform infrared spectroscopy

FTIR-ATR	Fourier-transform infrared spectroscopy - attenuated total reflectance
FZJ	Forschungszentrum Jülich GmbH
G/G	glass/glass
GFRP	glass fiber-reinforced polymer
GHGs	greenhouse gases
HBC	heterojunction back contact
HIT	heterojunction with intrinsic thin-layer
IBC	interdigitated back contact
IEA	International Energy Agency
IEC	International Electrotechnical Commission
IF	interconnection foil
MS	mass spectrometric
NIR	near-infrared
NIST	National Institute of Standards and Technology
NREL	National Renewable Energy Laboratory
PECVD	plasma-enhanced chemical vapor deposition
PERC	passivated emitter and rear cell
PID	potential-induced degradation
PL	photoluminescence
PV	photovoltaic
PVD	physical vapor deposition
Px-bs	A polyolefin-based back sheet
PY-GC-MS	Pyrolysis-Gas chromatography-Mass spectrometry
Raman	Raman spectroscopy
RH	relative humidity
ROI	regions of interest
SEM	Scanning electron microscopy
SHJ	silicon heterojunction
Si-CCD	silicon charge-coupled device
TC	thermal cycling
TD	thermal desorption

TOPCon	tunnel oxide passivated contact
TPSEs	thermoplastic silicone elastomers
UV	ultraviolet
UV-B	UV-blocking
UV-B_{350}	block the UV light under 350 nm
UV-B_{375}	block the UV light under 375 nm
UV-DS	UV-downshifting
UV-T	UV-transmitting
UV-Vis-NIR	Ultraviolet-Visible-Near infrared spectroscopy
UVID	UV-induced degradation
VIPV	vehicle-integrated PV
WVTR	water-vapor transmission rate
XCT	X-ray computed tomography
XPS	X-ray photoelectron spectroscopy

C List of publications

Journal publications

1. **K. Zhang**, R. Zhang, A. Lambertz, K. Bittkau, H. Gattermann, U. Rau, K. Ding. *Mitigation of UV-induced degradation in lightweight SHJ solar modules via a UV-downshifting encapsulation strategy*, Prog Photovolt Res Appl, **34**(6), 771-785 (2026).

2. **K. Zhang**, A. Lambertz, K. Dzięcioł, K. Bittkau, R. Zhang, Y. Liu, A. Gerber, H. Gattermann, R.A. Eichel, U. Rau, C.J. Brabec, K. Ding. *Towards integrated photovoltaic applications: Lightweight silicon heterojunction solar modules with different encapsulation materials and their damp heat stability*, Applied Energy, **400**, 126570 (2025).

3. **K. Zhang**, O. Mashkov, M.A. Yaqin, B. Doll, A. Lambertz, K. Bittkau, W. Duan, I.M. Peters, C.J. Brabec, U. Rau, K. Ding. *Damp-heat-induced degradation of lightweight silicon heterojunction solar modules with different transparent conductive oxide layers*, Prog Photovolt Res Appl, **33**(4), 541-550 (2025).

4. B. Xu, K. Bittkau, A. Eberst, **K. Zhang**, Y. Liu, J. Yang, W. Duan, M.A. Yaqin, V. Smirnov, C. Zhou, W. Wang, X. Xu, A. Lambertz, U. Rau, K. Ding. *Downshifting Encapsulant: Optical Simulation Evaluation of the Solution to Ultraviolet-Induced Degradation in Silicon Heterojunction Solar Cells*, Advanced Energy and Sustainability Research, 2400227 (2024).

5. W. Duan, G. Mains, H.T. Gebrewold, K. Bittkau, A. Lambertz, B. Xu, V. Lauterbach, A. Eberst, N. Nicholson, L. Korte, M.A. Yaqin, **K. Zhang**, Q. Yang, U. Rau, K. Ding. *Enhancing the Selectivity and Transparency of the Electron Contact in Silicon Heterojunction Solar Cells by Phosphorus Catalytic Doping*, Adv. Funct. Mater., **34**, 2310552 (2024).

6. Q. Tang, W. Duan, A. Lambertz, K. Bittkau, M.A. Yaqin, Y. Zhao, **K. Zhang**, Q. Yang, D. Qiu, F. Gunkel, Mo. Weber, U. Rau, K. Ding. *> 85% indium reduction*

for high-efficiency silicon heterojunction solar cells with aluminum-doped zinc oxide contacts, Sol Energy Mater Sol Cells, **251**, 112120 (2023).

Conferences

1. **K. Zhang**, R. Zhang, A. Lambertz, B. Xu, A. Eberst, K. Bittkau, X. Li, H. Gattermann, U. Rau, K. Ding. *UV stability of lightweight silicon heterojunction solar modules with downshifting encapsulation materials*, 42nd European Photovoltaic Solar Energy Conference and Exhibition (EUPVSEC), Sept. 2025, Bilbao, Spain. (**poster award**)

2. **K. Zhang**, A. Lambertz, Y. Liu, K. Bittkau, U. Rau, K. Ding. *Damp heat stability of lightweight silicon heterojunction solar modules with various encapsulation materials and architectures*, 41st European Photovoltaic Solar Energy Conference and Exhibition (EUPVSEC), Sept. 2024, Vienna, Austria. (oral presentation)

3. **K. Zhang**, A. Lambertz, Y. Liu, K. Bittkau, K. Ding, U. Rau. *Analysis of the damp heat stability of lightweight silicon heterojunction solar modules with various encapsulation materials*, IEEE 52nd Photovoltaic Specialist Conference (PVSC), Jun. 2024, Seattle, USA. (poster presentation)

4. **K. Zhang**, O. Mashkov, M.A. Yaqin, B. Doll, A. Lambertz, K. Bittkau, W. Duan, I.M. Peters, U. Rau, C.J. Brabec, K. Ding. *Damp heat stability of light weight silicon heterojunction solar modules*, 40th European Photovoltaic Solar Energy Conference and Exhibition (EUPVSEC), Sept. 2023, Lisbon, Portugal. (oral presentation)

5. **K. Zhang**, M.A. Yaqin, O. Mashkov, A. Lambertz, Y. Liu, W. Duan, K. Ding, B. Doll, O. Stroyuk, I.M. Peters, U. Rau. *Impact of damp-heat on flexible and lightweight silicon heterojunction solar modules*, 33rd Photovoltaic Science and Engineering Conference (PVSEC), Nov. 2022, Nagoya, Japan. (oral presentation)

D Curriculum vitae

Personal information

Name	Kai Zhang
Date of birth	Sept. 26th, 1991
Place of birth	Gansu, China
Citizenship	Chinese

Education

2021 - 2025	PhD student at the Forschungszentrum Jülich GmbH, IMD-3, Photovoltaics
2015 - 2017	Master in Material Engineering School of Material Science and Technology Sun Yat-Sen University, Guangzhou, China
2010 - 2014	Bachelor in Chemical engineering and technology School of Chemical and Biological Engineering Lanzhou Jiaotong University, Lanzhou, China
2007 - 2010	Lanzhou No.2 Secondary School, Lanzhou, China
2004 - 2007	Lanzhou No.10 Middle School, Lanzhou, China
1998 - 2004	An Le Cun Primary School, Lanzhou, China

References

[1] "Global Electricity Review 2025," EMBER, Report, 2025.

[2] "Snapshot of Global PV Markets 2025," IEA PVPS, Report, 2025.

[3] IEA. Is there enough global wind and solar pv manufacturing to meet net zero targets in 2030? Accessed: Jun. 2023. https://www.iea.org/reports/renewable-energy-market-update-june-2023/is-there-enough-global-wind-and-solar-pv-manufacturing-to-meet-net-zero-targets-in-2030?utm_source=chatgpt.com.

[4] PVTECH. Global solar module manufacturing capacity to reach 1.8tw in 2025 – report, Accessed: Mar. 2025. https://www.pv-tech.org/global-solar-module-manufacturing-capacity-to-reach-1-8tw-in-2025-report/?utm_source=chatgpt.com.

[5] A. C. Martins, V. Chapuis, A. Virtuani, and C. Ballif, IEEE Journal of Photovoltaics **9**, 1, 2019.

[6] A. C. Martins, V. Chapuis, A. Virtuani, H.-Y. Li, L.-E. Perret-Aebi, and C. Ballif, Solar Energy Materials and Solar Cells **187**, 2018.

[7] A. C. Martins, V. Chapuis, F. Sculati-Meillaud, A. Virtuani, and C. Ballif, Progress in Photovoltaics: Research and Applications **26**, 9, 2018.

[8] J. Gaume, in *33rd Eur. Photovolt. Sol. Energy Conf. Exhib.*, 2017.

[9] T. Kajisa, H. Miyauchi, K. Mizuhara, K. Hayashi, T. Tokimitsu, M. Inoue, K. Hara, and A. Masuda, Japanese Journal of Applied Physics **53**, 9, 2014.

[10] A. Boulanger, J. Gaume, F. Quesnel, P. Ruols, and F. Rouby, in *33rd Eur. Photovolt. Sol. Energy Conf. Exhib.*, 2017.

[11] G. Oreski, A. Halm, V. Schenk, W. Krumlacher, and H. Nussbaumer, in *33rd Eur. Photovolt. Sol. Energy Conf. Exhib.*, 2017.

[12] K. Zhang et al., Progress in Photovoltaics: Research and Applications, 2025.

[13] F. Lisco, F. Bukhari, L. O. Jones, A. M. Law, J. M. Walls, and C. Ballif, IEEE Journal of Photovoltaics **13**, 3, 2023.

[14] Trinasolar. Trinasolar sets new n-type solar cell efficiency world record of 27.08%, Accessed: Dec. 20, 2024. https://static.trinasolar.com/us/resources/newsroom/Trinasolar-Sets-n-type-Efficiency-World-Record.

[15] J. Hüpkes, J. I. Owen, M. Wimmer, F. Ruske, D. Greiner, R. Klenk, U. Zastrow, and J. Hotovy, Thin Solid Films **555**, 2014.

[16] D. Greiner, S. E. Gledhill, C. Köble, J. Krammer, and R. Klenk, Thin Solid Films **520**, 4, 2011.

[17] A. B. Morales-Vilches, A. Cruz, S. Pingel, S. Neubert, L. Mazzarella, D. Meza, L. Korte, R. Schlatmann, and B. Stannowski, IEEE Journal of Photovoltaics **9**, 1, 2019.

[18] D. Adachi, T. Terashita, T. Uto, J. L. Hernández, and K. Yamamoto, Solar Energy Materials and Solar Cells **163**, 2017.

[19] J. Yu et al., eScience **4**, 3, 2024.

[20] O. Arriaga Arruti, A. Virtuani, and C. Ballif, Progress in Photovoltaics: Research and Applications **31**, 7, 2023.

[21] A. Omazic, G. Oreski, M. Halwachs, G. C. Eder, C. Hirschl, L. Neumaier, G. Pinter, and M. Erceg, Solar Energy Materials and Solar Cells **192**, 2019.

[22] C. Peike, I. Hädrich, K.-A. Weiß, and I. Dürr, Photovoltaics International **19**, 2013.

[23] G. Oreski, A. Omazic, G. C. Eder, Y. Voronko, L. Neumaier, W. Mühleisen, C. Hirschl, G. Ujvari, R. Ebner, and M. Edler, Progress in Photovoltaics: Research and Applications **28**, 12, 2020.

[24] A. Sinha, J. Qian, S. L. Moffitt, K. Hurst, K. Terwilliger, D. C. Miller, L. T. Schelhas, and P. Hacke, Progress in Photovoltaics: Research and Applications **31**, 1, 2022.

[25] F. T. Thome, P. Meßmer, S. Mack, E. Schnabel, F. Schindler, W. Kwapil, and M. C. Schubert, Solar RRL **8**, 23, 2024.

[26] R. Witteck, B. Veith-Wolf, H. Schulte-Huxel, A. Morlier, M. R. Vogt, M. Köntges, and R. Brendel, Progress in Photovoltaics: Research and Applications **25**, 6, 2017.

[27] C. Ballif, S. De Wolf, A. Descoeudres, and Z. C. Holman, "Chapter two - amorphous silicon/crystalline silicon heterojunction solar cells," in *Advances in Photovoltaics: Part 3*, ser. Semiconductors and Semimetals, G. P. Willeke and E. R. Weber, Eds., vol. 90, Elsevier, 2014.

[28] S. De Wolf, A. Descoeudres, Z. C. Holman, and C. Ballif, Green **2**, 1, 2012.

[29] W. G. J. H. M. Sark, L. Korte, and F. Roca, "Introduction – physics and technology of amorphous-crystalline heterostructure silicon solar cells," in *Physics and Technology of Amorphous-Crystalline Heterostructure Silicon Solar Cells*. Springer, 2011.

[30] A. Louwen, W. van Sark, R. Schropp, and A. Faaij, Solar Energy Materials and Solar Cells **147**, 2016.

[31] W. Shockley, G. L. Pearson, and J. R. Haynes, Bell System Technical Journal **28**, 3, 1949.

[32] W. Fuhs, K. Niemann, and J. Stuke, 1, vol. 20, May 1974.

[33] Y. Hamakawa, K. Fujimoto, K. Okuda, Y. Kashima, S. Nonomura, and H. Okamoto, Applied Physics Letters **43**, 7, Oct. 1983.

[34] K. Okuda, H. Okamoto, and Y. Hamakawa, Japanese Journal of Applied Physics **22**, 9A, 1983.

[35] M. Tanaka, M. Taguchi, T. Matsuyama, T. Sawada, S. Tsuda, S. Nakano, H. Hanafusa, and Y. Kuwano, Japanese Journal of Applied Physics **31**, 11R, 1992.

[36] M. Taguchi, K. Kawamoto, S. Tsuge, T. Baba, H. Sakata, M. Morizane, K. Uchihashi, N. Nakamura, S. Kiyama, and O. Oota, Progress in Photovoltaics: Research and Applications **8**, 5, 2000.

[37] T. Kinoshita et al., in *26th EU PVSEC*, 2011.

[38] M. Taguchi, A. Yano, S. Tohoda, K. Matsuyama, Y. Nakamura, T. Nishiwaki, K. Fujita, and E. Maruyama, IEEE Journal of Photovoltaics **4**, 1, 2014.

[39] K. Masuko et al., IEEE Journal of Photovoltaics **4**, 6, 2014.

[40] D. Adachi, J. L. Hernández, and K. Yamamoto, Applied Physics Letters **107**, 23, Dec. 2015.

[41] K. Yoshikawa et al., Nature Energy **2**, 5, 2017.

[42] H. Lin et al., Nature Energy **8**, 8, 2023.

[43] H. Wu et al., Nature **635**, 8039, 2024.

[44] Z. Xie et al., Nat Commun **16**, 1, 2025.

[45] W. Liu et al., Nature **617**, 7962, 2023.

[46] B. Liang, X. Chen, X. Wang, H. Yuan, A. Sun, Z. Wang, L. Hu, G. Hou, Y. Zhao, and X. Zhang, Journal of Materials Chemistry A **13**, 4, 2025.

[47] W. Duan, A. Lambertz, K. Bittkau, D. Qiu, K. Qiu, U. Rau, and K. Ding, Progress in Photovoltaics: Research and Applications **30**, 4, 2021.

[48] C. Ballif, F.-J. Haug, M. Boccard, P. J. Verlinden, and G. Hahn, Nature Reviews Materials **7**, 8, 2022.

[49] D. Qiu, "Development of industry-scalable processes for nanocrystalline silicon oxide in silicon heterojunction solar cells," Ph.D. thesis, RWTH Aachen University, Aachen, Germany, 2023. [Online]. Available: `https://publications.rwth-aachen.de/record/973466/files/973466.pdf`

[50] M. Tanaka, S. Okamoto, S. Tsuge, and S. Kiyama, in *3rd World Conference on Photovoltaic Energy Conversion, 2003. Proceedings of*, vol. 1, 2003.

[51] G. M. Wilson et al., Journal of Physics D: Applied Physics **53**, 49, 2020.

[52] C. A. Deline, S. Ayala Pelaez, W. F. Marion, W. R. Sekulic, M. A. Woodhouse, and J. Stein, National Renewable Energy Lab. (NREL), Golden, CO (United States), 2019.

[53] E. Aydin, T. G. Allen, M. De Bastiani, A. Razzaq, L. Xu, E. Ugur, J. Liu, and S. De Wolf, Science **383**, 6679, 2024.

[54] K. T. VanSant, A. C. Tamboli, and E. L. Warren, Joule **5**, 3, 2021.

[55] M. He, M. Zhang, Z. Li, X. Liu, K. Sun, Z. Liu, and X. Hao, Adv Mater **37**, 40, 2025.

[56] O. M. Saif, A. H. Zekry, M. Abouelatta, and A. Shaker, Silicon **15**, 15, 2023.

[57] S. Li et al., Joule **5**, 6, 2021.

[58] D. D. Tune, N. Mallik, H. Fornasier, and B. S. Flavel, Advanced Energy Materials **10**, 1, 2019.

[59] G. Makrides, B. Zinsser, M. Norton, and G. E, "Performance of photovoltaics under actual operating conditions," in *Third Generation Photovoltaics*. 2012, ch. Chapter 9.

[60] V. Sharma, A. Kumar, O. S. Sastry, and S. S. Chandel, Energy **58**, 2013.

[61] Q. Tang et al., Solar Energy Materials and Solar Cells **251**, 2023.

[62] A. Czanderna and F. Pern, Solar Energy Materials and Solar Cells **43**, 1995.

[63] M. C. C. d. Oliveira, A. S. A. Diniz Cardoso, M. M. Viana, and V. d. F. C. Lins, Renewable and Sustainable Energy Reviews **81**, 2018.

[64] J. Tracy, D. R. D'Hooge, N. Bosco, C. Delgado, and R. Dauskardt, Progress in Photovoltaics: Research and Applications **26**, 12, 2018.

[65] R. F. M. Lange, Y. Luo, R. Polo, and J. Zahnd, Progress in Photovoltaics: Research and Applications **19**, 2, 2011.

[66] C. Hirschl et al., Solar Energy Materials and Solar Cells **116**, 2013.

[67] G. Oreski, A. Rauschenbach, C. Hirschl, M. Kraft, G. Eder, and G. Pinter, Journal of Applied Polymer Science **134.2017**, 23, 2017.

[68] S.-H. Schulze, A. Apel, D. Daßler, and C. Ehrich, Solar Energy Materials and Solar Cells **143**, 2015.

[69] M. Jaunich, M. Böhning, U. Braun, G. Teteris, and W. Stark, Polymer Testing **52**, 2016.

[70] W. Stark and M. Jaunich, Polymer Testing **30**, 2, 2011.

[71] S. Jonai, K. Hara, Y. Tsutsui, H. Nakahama, and A. Masuda, Japanese Journal of Applied Physics **54**, 8S1, 2015.

[72] "Assessment of photovoltaic module failures in the field: report IEA-PVPS T13-09:2017.," IEA PVPS, Report, 2017.

[73] M. Kempe, Solar Energy Materials and Solar Cells **90**, 16, 2006.

[74] Polymer Degradation and Stability **55**, 3, 1997.

[75] M. D. Kempe, G. J. Jorgensen, K. M. Terwilliger, T. J. McMahon, C. E. Kennedy, and T. T. Borek, Solar Energy Materials and Solar Cells **91**, 4, 2007.

[76] C. Peike, P. Hülsmann, M. Blüml, P. Schmid, K.-A. Weiß, and M. Köhl, International Scholarly Research Notices **2012**, 1, 2012.

[77] U. Weber, R. Eiden, C. Strubel, T. Sögding, M. Heiss, P. Zachmann, K. Nattermann, H. Engelmann, A. Dethlefsen, and N. Lenck, Jan. 2012.

[78] S. Pop, R. Schulze, X. Wang, B. Yuan, J. Kapur, K. Stika, C. Westphal, H. Antoniadis, and A. Meisel, Sep. 2014.

[79] B. M. Habersberger, P. Hacke, and L. S. Madenjian, in *2018 IEEE 7th World Conference on Photovoltaic Energy Conversion (WCPEC) (A Joint Conference of 45th IEEE PVSC, 28th PVSEC & 34th EU PVSEC)*, 2018.

[80] K. Hara, S. Jonai, and A. Masuda, Solar Energy Materials and Solar Cells **140**, 2015.

[81] J. Kapur, K. M. Stika, C. S. Westphal, J. L. Norwood, and B. Hamzavytehrany, IEEE Journal of Photovoltaics **5**, 1, 2015.

[82] G. Oreski, G. Wallner, and P. Randel, English, (EUPVSEC ; Conference date: 01-09-2008 Through 04-09-2008), 2008.

[83] K. R. McIntosh, N. E. Powell, A. W. Norris, J. N. Cotsell, and B. M. Ketola, Progress in Photovoltaics: Research and Applications **19**, 3, 2011.

[84] K. Hara, H. Ohwada, T. Furihata, and A. Masuda, Japanese Journal of Applied Physics **57**, 2, 2018.

[85] B. Adothu, P. Bhatt, S. Chattopadhyay, S. Zele, J. Oderkerk, H. P. Sagar, F. R. Costa, and S. Mallick, Solar Energy **194**, 2019.

[86] M. López-Escalante, L. J. Caballero, F. Martín, M. Gabás, A. Cuevas, and J. Ramos-Barrado, Solar Energy Materials and Solar Cells **144**, 2016.

[87] B. Adothu, P. Bhatt, S. Zele, J. Oderkerk, F. R. Costa, and S. Mallick, Materials Chemistry and Physics **243**, 2020.

[88] S. Yamaguchi, S. Jonai, K. Hara, H. Komaki, Y. Shimizu-Kamikawa, H. Shibata, S. Niki, Y. Kawakami, and A. Masuda, Japanese Journal of Applied Physics **54**, 8S1, 2015.

[89] V. Chapuis, S. Pélisset, M. Raeis-Barnéoud, H.-Y. Li, C. Ballif, and L.-E. Perret-Aebi, Progress in Photovoltaics: Research and Applications **22**, 4, 2014.

[90] G. Oreski and G. M. Wallner, Solar Energy **79**, 6, 2005.

[91] C. Yang, X. Xing, Z. Li, and S. Zhang, Polymers **12**, 1, 2020.

[92] G. Oreski, B. Ottersböck, and A. Omazic, "6 - degradation processes and mechanisms of encapsulants," in *Durability and Reliability of Polymers and Other Materials in Photovoltaic Modules* (Plastics Design Library), H. E. Yang, R. H. French, and L. S. Bruckman, Eds., Plastics Design Library. William Andrew Publishing, 2019.

[93] Y. Bai et al., Energy Technology **11**, 7, 2023.

[94] A. J. Steiner, W. Krumlacher, H. Muckenhuber, M. Plank, K. Sundl, and E. Ziegler, in *28th EU PVSEC*, 2013.

[95] R. Cheacharoen, C. C. Boyd, G. F. Burkhard, T. Leijtens, J. A. Raiford, K. A. Bush, S. F. Bent, and M. D. McGehee, Sustainable Energy & Fuels **2**, 11, 2018.

[96] A. Uddin, M. B. Upama, H. Yi, and L. Duan, Coatings **9**, 2, 2019.

[97] R. K. Raman, S. A. Gurusamy Thangavelu, S. Venkataraj, and A. Krishnamoorthy, Renewable and Sustainable Energy Reviews **151**, 2021.

[98] G. Stollwerck, W. Schoeppel, A. Graichen, and C. Jaeger, in *28th EU PVSEC*, 2013.

[99] J. Berghold, S. Koch, B. Frohmann, P. Hacke, and P. Grunow, in *2014 IEEE 40th Photovoltaic Specialist Conference (PVSC)*, 2014.

[100] S. Pingel, O. Frank, M. Winkler, S. Daryan, T. Geipel, H. Hoehne, and J. Berghold, in *2010 35th IEEE Photovoltaic Specialists Conference*, 2010.

[101] B. Luo et al., Solar Energy Materials and Solar Cells **273**, 2024.

[102] B. Voß, J. Knobloch, and A. Goetzberger, in *Sonnenenergie: Photovoltaik: Physik und Technologie der Solarzelle*, 2. Revised and expanded edition. Teubner Verlag, 1997.

[103] B. Fufa, C. Zhao-Bo, and M. Wensheng, Information Technology Journal **9**, 2010.

[104] N. Baldock and M. Mokhtarzadeh-Dehghan, Aircraft Engineering and Aerospace Technology **78**, 3, 2006.

[105] H. Ross, "Fly around the world with a solar powered airplane," in *The 26th Congress of ICAS and 8th AIAA ATIO*.

[106] M. Yamaguchi et al., Progress in Photovoltaics: Research and Applications **29**, 7, 2020.

[107] A. C. Martins, V. Chapuis, A. Virtuani, and C. Ballif, in *2017 IEEE 44th Photovoltaic Specialist Conference (PVSC)*, 2017.

[108] A. C. Martins, V. Chapuis, A. Virtuani, L.-E. Perret-Aebi, and C. Ballif, in *33rd European Photovoltaic Solar Energy Conference and Exhibition*, 2017.

[109] C. Kutter, F. Basler, L. E. Alanis, J. Markert, M. Heinrich, and D.-H. Neuhaus, in *37th EU PVSEC*, 2020.

[110] J. Govaerts et al., EPJ Photovoltaics **13**, 2022.

[111] A. S. Budiman, G. Illya, S. Anbazhagan, S. K. Tippabhotla, W. J. Song, R. Sahay, and A. A. O. Tay, Solar Energy **235**, 2022.

[112] "IEC 61215-2: Terrestrial Photovoltaic (PV) Modules - Design Qualification and Type Approval - Part 2: Test Procedures," International Electrotechnical Commission (IEC), Standard, 2021, Edition 2.0.

[113] B. Luo et al., Solar Energy Materials and Solar Cells **259**, 2023.

[114] H. Park, J. Jeong, E. Shin, S. Kim, and J. Yi, Microelectronic Engineering **216**, 2019.

[115] A. Ndiaye, C. M. F. Kébé, A. Charki, V. Sambou, and P. A. Ndiaye, Energy Procedia **74**, 2015.

[116] T. Ishii and A. Masuda, Progress in Photovoltaics: Research and Applications **25**, 12, 2017.

[117] E. L. Meyer and E. E. van Dyk, IEEE Transactions on Reliability **53**, 1, 2004.

[118] A. Pozza and T. Sample, Progress in Photovoltaics: Research and Applications **24**, 3, 2015.

[119] E. D. Dunlop and D. Halton, Progress in Photovoltaics: Research and Applications **14**, 1, 2006.

[120] A. Skoczek, T. Sample, and E. D. Dunlop, Progress in Photovoltaics: Research and Applications **17**, 4, 2008.

[121] K. Zhang, H. Han, W. Huang, X. Dong, Z. Liang, and H. Shen, Japanese Journal of Applied Physics **57**, 8S3, 2018.

[122] C. E. Chamberlin, M. A. Rocheleau, M. W. Marshall, A. M. Reis, N. T. Coleman, and P. A. Lehman, in *2011 37th IEEE Photovoltaic Specialists Conference*, 2011.

[123] K. O. Davis, S. R. Kurtz, D. C. Jordan, J. H. Wohlgemuth, and N. Sorloaica-Hickman, Progress in Photovoltaics: Research and Applications **21**, 4, 2012.

[124] E. Lorenzo, R. Zilles, R. Moretón, T. Gómez, and A. Martínez de Olcoz, Progress in Photovoltaics: Research and Applications **22**, 12, 2013.

[125] D. Polverini, M. Field, E. Dunlop, and W. Zaaiman, Progress in Photovoltaics: Research and Applications **21**, 5, 2012.

[126] H. Han, X. Dong, B. Li, H. Yan, P. J. Verlinden, J. Liu, J. Huang, Z. Liang, and H. Shen, Solar Energy **170**, 2018.

[127] G.-H. Kang, K. S. Kim, H.-e. Song, G. Yu, H. K. Ahn, and D.-Y. Han, in *25th EU PVSEC/WCPEC-5*, 2010.

[128] M. Quintana, D. King, F. Hosking, J. Kratochvil, R. Johnson, B. Hansen, N. Dhere, and M. Pandit, in *Conference Record of the Twenty-Eighth IEEE Photovoltaic Specialists Conference*, 2000.

[129] E. Dunlop, D. Halton, and H. Ossenbrink, in *Conference Record of the Thirty-first IEEE Photovoltaic Specialists Conference, 2005.*, 2005.

[130] S. A, S. T, D. E, and O. H, München (Germany): WIP-Renewable Energies, 2007.

[131] F. De Lia, S. Castello, and L. Abenante, in *Proceedings of 3rd World Conference on Photovoltaic Energy Conversion*, vol. 2, 2003.

[132] W. Luo, Y. S. Khoo, P. Hacke, D. Jordan, L. Zhao, S. Ramakrishna, A. G. Aberle, and T. Reindl, 1, vol. 9, 2019.

[133] L. Abenante, F. D. Lia, and salvatore castello, in *25th EU PVSEC/WCPEC-5*, 2010.

[134] I. Saleh, I. Abouhdima, and M. Gantrari, in *24th EU PVSEC*, Sep. 2009.

[135] Y. Tang, B. Raghuraman, J. Kuitche, G. TamizhMani, C. E. Backus, and C. Osterwald, in *2006 IEEE 4th World Conference on Photovoltaic Energy Conference*, vol. 2, 2006.

[136] D. C. Jordan and S. R. Kurtz, Progress in Photovoltaics: Research and Applications **21**, 1, 2011.

[137] T. Ishii, Y. Chiba, M. Akitomi, R. Sato, S. Choi, and A. Masuda, Progress in Photovoltaics: Research and Applications **33**, 8, 2025.

[138] T. Ishii, T. Takashima, and K. Otani, Progress in Photovoltaics: Research and Applications **19**, 2, 2011.

[139] M. Vázquez and I. Rey-Stolle, Progress in Photovoltaics: Research and Applications **16**, 5, 2008.

[140] J. E. Granata, W. E. Boyson, J. A. Kratochvil, and M. A. Quintana, 2009 34th IEEE Photovoltaic Specialists Conference (PVSC), 2009.

[141] D. C. Jordan, T. J. Silverman, J. H. Wohlgemuth, S. R. Kurtz, and K. T. VanSant, Progress in Photovoltaics: Research and Applications **25**, 4, 2017.

[142] D. C. Jordan et al., IEEE Journal of Photovoltaics **8**, 1, 2018.

[143] C. S. Jiang, D. B. Sulas-Kern, H. R. Moutinho, et al., in *2020 47th IEEE Photovoltaic Specialists Conference (PVSC)*, 2020.

[144] T. Ishii, S. Choi, R. Sato, Y. Chiba, and A. Masuda, in *2018 IEEE 7th World Conference on Photovoltaic Energy Conversion (WCPEC) (A Joint Conference of 45th IEEE PVSC, 28th PVSEC & 34th EU PVSEC)*, 2018.

[145] M. Schweiger, J. Bonilla, W. Herrmann, A. Gerber, and U. Rau, Progress in Photovoltaics: Research and Applications **25**, 12, 2017.

[146] D. Jordan, D. B. Sulas-Kern, S. Johnston, H. R. Moutinho, C. Xiao, C. S. Jiang, M. Young, A. G. Norman, C. Deline, I. Repins, et al., in *37th EU PVSEC*, 2020.

[147] K. Zhang et al., Applied Energy **400**, 2025.

[148] W. Liu et al., Joule **4**, 4, 2020.

[149] J. Zhu et al., Progress in Photovoltaics: Research and Applications **24**, 10, 2016.

[150] J. H. Wohlgemuth, D. W. Cunningham, P. Monus, J. Miller, and A. Nguyen, in *2006 IEEE 4th World Conference on Photovoltaic Energy Conference*, vol. 2, 2006.

[151] P. Hacke, K. Terwilliger, S. Glick, D. Trudell, N. Bosco, S. Johnston, and S. Kurtz, in *2010 35th IEEE Photovoltaic Specialists Conference*, 2010.

[152] M. Quintana, D. King, T. McMahon, and C. Osterwald, in *Conference Record of the Twenty-Ninth IEEE Photovoltaic Specialists Conference, 2002.*, 2002.

[153] G. Jorgensen, K. Terwilliger, J. Delcueto, S. Glick, M. Kempe, J. Pankow, F. Pern, and T. McMahon, Solar Energy Materials and Solar Cells **90**, 16, 2006.

[154] Y. Voronko, G. C. Eder, M. Knausz, G. Oreski, T. Koch, and K. A. Berger, Progress in Photovoltaics: Research and Applications **23**, 11, 2015.

[155] C. Peike, S. Hoffmann, P. Hülsmann, B. Thaidigsmann, K. A. Weiß, M. Koehl, and P. Bentz, Solar Energy Materials and Solar Cells **116**, 2013.

[156] C. Kutter, F. Basler, L. E. Alanis, J. Markert, M. Heinrich, and D.-H. Neuhaus, in *37th EU PVSEC*, 2020.

[157] J. Govaerts et al., in *40th EU PVSEC*, 2023.

[158] N. Bosco, S. Moffitt, and L. T. Schelhas, Progress in Photovoltaics: Research and Applications **27**, 4, 2019.

[159] C. Han, Solar Energy Materials and Solar Cells **210**, 2020.

[160] M. Jankovec, E. Annigoni, C. Ballif, and M. Topič, in *2018 IEEE 7th World Conference on Photovoltaic Energy Conversion, WCPEC 2018 - A Joint Conference of 45th IEEE PVSC, 28th PVSEC and 34th EU PVSEC*, 2018.

[161] O. K. Segbefia, A. G. Imenes, and T. O. Sætre, Solar Energy **224**, 2021.

[162] F. D. Novoa, D. C. Miller, and R. H. Dauskardt, Solar Energy Materials and Solar Cells **120**, 2014.

[163] C. Ballif, H.-Y. Li, E. Annigoni, F. Galliano, J. Escarré, F. Meillaud, and L.-E. Perret, in *IEEE Photovoltaics*, vol. 4, 2014.

[164] J. H. Wohlgemuth and M. D. Kempe, in *2013 IEEE 39th Photovoltaic Specialists Conference (PVSC)*, IEEE, 2013.

[165] G. C. Eder, Y. Voronko, S. Dimitriadis, K. Knöbl, G. Újvári, K. A. Berger, M. Halwachs, L. Neumaier, and C. Hirschl, Progress in Photovoltaics: Research and Applications **27**, 11, 2018.

[166] M. D. Kempe, G. J. Jorgensen, K. M. Terwilliger, T. J. McMahon, C. E. Kennedy, and T. T. Borek, Solar Energy Materials and Solar Cells **91**, 4, 2007.

[167] T. J. Peshek, J. S. Fada, and I. T. Martin, "4 - degradation processes in photovoltaic cells," in *Durability and Reliability of Polymers and Other Materials in Photovoltaic Modules* (Plastics Design Library), H. E. Yang, R. H. French, and L. S. Bruckman, Eds., Plastics Design Library. William Andrew Publishing, 2019.

[168] S. Hoffmann and M. Koehl, Progress in Photovoltaics: Research and Applications **22**, 2, 2014.

[169] P. Hülsmann, K.-A. Weiß, and M. Köhl, Progress in Photovoltaics: Research and Applications **22**, 4, 2012.

[170] Y. Hu and R. H. French, "5 - degradation and failure mechanisms of pv module interconnects," in *Durability and Reliability of Polymers and Other Materials in Photovoltaic Modules* (Plastics Design Library), H. E. Yang, R. H. French, and L. S. Bruckman, Eds., Plastics Design Library. William Andrew Publishing, 2019.

[171] H. E. Yang, "2 - overview: Durability and reliability of common pv module and polymers/materials," in *Durability and Reliability of Polymers and Other Materials in Photovoltaic Modules* (Plastics Design Library), H. E. Yang, R. H. French, and L. S. Bruckman, Eds., Plastics Design Library. William Andrew Publishing, 2019.

[172] G. Mon, L. Wen, R. G. Ross, Jr., and D. Adent, in *18th IEEE Photovoltaic Specialists Conference*, 1985.

[173] F. P. La Mantia, V. Malatesta, M. Ceraulo, M. C. Mistretta, and P. Koci, Polymer Testing **51**, 2016.

[174] J. Morse, M. Thuis, D. Holsapple, R. Willis, M. D. Kempe, and D. C. Miller, Progress in Photovoltaics: Research and Applications **30**, 7, 2022.

[175] A. Ndiaye, A. Charki, A. Kobi, C. M. F. Kébé, P. A. Ndiaye, and V. Sambou, Solar Energy **96**, 2013.

[176] M. Aghaei et al., Renewable and Sustainable Energy Reviews **159**, 2022.

[177] B. Adothu, F. R. Costa, and S. Mallick, Polymer Degradation and Stability **201**, 2022.

[178] O. Hasan and A. F. M. Arif, Solar Energy Materials and Solar Cells **122**, 2014.

[179] H. Ye et al., Solar RRL **7**, 15, 2023.

[180] J. Ren et al., Solar Energy Materials and Solar Cells **272**, 2024.

[181] B. Fischer, A. Lambertz, M. Nuys, W. Beyer, W. Duan, K. Bittkau, K. Ding, and U. Rau, Adv Mater **35**, 47, 2023.

[182] Y. Chen et al., Progress in Photovoltaics: Research and Applications **27**, 10, 2019.

[183] S. Ma et al., Solar Energy Materials and Solar Cells **275**, 2024.

[184] Z. Yang et al., Solar Energy Materials and Solar Cells **257**, 2023.

[185] C.-K. Wu, S. Zou, C.-W. Peng, S.-W. Gu, M.-F. Ni, Y.-L. Zeng, H. Sun, X.-H. Zhang, and X.-D. Su, Journal of Energy Chemistry **81**, 2023.

[186] K. R. McIntosh, G. Lau, J. N. Cotsell, K. Hanton, D. L. Bätzner, F. Bettiol, and B. S. Richards, Progress in Photovoltaics: Research and Applications **17**, 3, 2008.

[187] B. Xu et al., Advanced Energy and Sustainability Research **6**, 1, 2024.

[188] J. Y. Hartley, D. C. Miller, S. Uličná, N. Bosco, and P. Hacke, Progress in Photovoltaics: Research and Applications **33**, 10, 2025.

[189] "ASTM G173-03(2020), Standard Tables for Reference Solar Spectral Irradiances: Direct Normal and Hemispherical on 37° Tilted Surface," Advancing Standards Transforming Markets (ASTM), Standard, 2020, Edition 3.0.

[190] "IEC 60904-3:2016 – Photovoltaic devices – Part 3: Measurement principles for terrestrial photovoltaic (PV) solar devices with reference spectral irradiance data," International Electrotechnical Commission (IEC), Standard, 2016, Edition 3.0.

[191] Deutscher wetterdienst (dwd). `https://www.dwd.de/EN/ourservices/solarenergy/maps_globalradiation_mvs.html`.

[192] A. Beer, Solid-State Electronics **9**, 5, 1966.

[193] R. A. Smith, "Semiconductors," in CAMBRIDGE AT THE UNIVERSITY PRESS, 1959.

[194] S. Eriksson, "Electronics letters," in Institution of Engineering and Technology IET, 1985.

[195] L. J. v. d. PAUW, "A method of measuring specific resistivity and hall effect of discs of arbitrary shape," in *Semiconductor Devices: Pioneering Papers*.

[196] In *Physics of Semiconductor Devices*, John Wiley & Sons, Ltd, 2006.

[197] I. Martil and G. G. Diaz, European Journal of Physics **13**, 4, 1992.

[198] O. Breitenstein, Opto-Electronics Review **21**, 3, 2013.

[199] W. Shockley, The Bell System Technical Journal **28**, 3, 1949.

[200] C.-t. Sah, R. N. Noyce, and W. Shockley, Proceedings of the IRE **45**, 1957.

[201] K. R. McIntosh, "Three detrimental effects in the current-voltage curve of silicon solar cells," Ph.D. thesis, University of New South Wales, Sydney, Austria, 2001.

[202] S. Steingrube, O. Breitenstein, K. Ramspeck, S. Glunz, A. Schenk, and P. P. Altermatt, Journal of Applied Physics **110**, 1, 2011.

[203] O. Breitenstein, J. P. Rakotoniaina, M. H. Al Rifai, and M. Werner, Progress in Photovoltaics: Research and Applications **12**, 7, 2004.

[204] M. Wolf and H. Rauschenbach, Advanced Energy Conversion **3**, 2, 1963.

[205] P. P. Altermatt, G. Heiser, A. G. Aberle, A. Wang, J. Zhao, S. J. Robinson, S. Bowden, and M. A. Green, Progress in Photovoltaics: Research and Applications **4**, 6, 1996.

[206] U. Rau, IEEE Journal of Photovoltaics **2**, 2, 2012.

[207] T. Kirchartz, A. Helbig, B. E. Pieters, and U. Rau, in *Advanced Characterization Techniques for Thin Film Solar Cells*, John Wiley & Sons, Ltd, 2011, ch. 3.

[208] K. Ramspeck, K. Bothe, D. Hinken, B. Fischer, J. Schmidt, and R. Brendel, Applied Physics Letters **90**, 15, 2007.

[209] M. Kasemann, M. C. Schubert, M. The, M. Köber, M. Hermle, and W. Warta, Applied Physics Letters **89**, 22, Nov. 2006.

[210] P. Würfel, T. Trupke, T. Puzzer, E. Schäffer, W. Warta, and S. W. Glunz, Journal of Applied Physics **101**, 12, Jun. 2007.

[211] O. Breitenstein, J. Bauer, T. Trupke, and R. A. Bardos, Progress in Photovoltaics: Research and Applications **16**, 4, 2007.

[212] D. Hinken, K. Ramspeck, K. Bothe, B. Fischer, and R. Brendel, Applied Physics Letters **91**, 18, 2007.

[213] K. Bothe, K. Ramspeck, D. Hinken, and R. Brendel, ECS Transactions **16**, 6, 2008.

[214] M. Kasemann, D. Grote, B. Walter, W. Kwapil, T. Trupke, Y. Augarten, R. A. Bardos, E. Pink, M. D. Abbott, and W. Warta, Progress in Photovoltaics: Research and Applications **16**, 4, 2008.

[215] T. Fuyuki and A. Kitiyanan, Applied Physics A **96**, 1, 2008.

[216] T. Kirchartz, A. Helbig, W. Reetz, M. Reuter, J. H. Werner, and U. Rau, Progress in Photovoltaics: Research and Applications **17**, 6, 2009.

[217] U. Rau, Physical Review B **76**, 8, 2007.

[218] J. Haunschild, M. Glatthaar, M. Kasemann, S. Rein, and E. R. Weber, physica status solidi (RRL) – Rapid Research Letters **3**, 7-8, 2009.

[219] T. Trupke, R. A. Bardos, M. C. Schubert, and W. Warta, Applied Physics Letters **89**, 4, 2006.

[220] M. D. Abbott, J. E. Cotter, F. W. Chen, T. Trupke, R. A. Bardos, and K. C. Fisher, Journal of Applied Physics **100**, 11, 2006.

[221] M. D. Abbott, J. E. Cotter, T. Trupke, and R. A. Bardos, Applied Physics Letters **88**, 11, 2006.

[222] H. Kampwerth, T. Trupke, J. W. Weber, and Y. Augarten, Applied Physics Letters **93**, 20, 2008.

[223] R. A. Bardos, T. Trupke, M. C. Schubert, and T. Roth, Applied Physics Letters **88**, 5, 2006.

[224] R. A. Sinton, A. Cuevas, and M. Stuckings, Conference Record of the Twenty Fifth IEEE Photovoltaic Specialists Conference - 1996, 1996.

[225] J. I. Goldstein, D. E. Newbury, J. R. Michael, N. W. Ritchie, J. H. J. Scott, and D. C. Joy, "Scanning electron microscopy and x-ray microanalysis," in Springer New York, NY, 2017.

[226] N. Brodusch, H. Demers, and R. Gauvin, "Field emission scanning electron microscopy," in Springer New York, NY, 2017.

[227] K. Dzieciol, Y. E. Durmus, H. Tempel, H. Kungl, A. Bauer, and R. A. Eichel, iScience **26**, 7, 2023.

[228] M. D. Kempe, A. A. Dameron, and M. O. Reese, Progress in Photovoltaics: Research and Applications **22**, 11, 2013.

[229] "ASTM F1249-20: Standard Test Method for Water Vapor Transmission Rate Through Plastic Film and Sheeting Using a Modulated Infrared Sensor," Advancing Standards Transforming Markets (ASTM), Standard, 2003, Edition 1.

[230] "Plastics - Film and sheeting - Determination of water vapour transmission rate. Part 1: Humidity detection sensor method," International Organization for Standardization (ISO), Standard, 2020.

[231] J. Moulder and J. Chastain, "Handbook of x-ray photoelectron spectroscopy: A reference book of standard spectra for identification and interpretation of xps data," in Physical Electronics Division, Perkin-Elmer Corporation, 1992.

[232] P. van der Heide, "X-ray photoelectron spectroscopy: An introduction to principles and practices," in WILEY, 2011.

[233] M. Wendt, P. Wessel, R. Gottschalg, A. Mordvinkin, and R. Heidrich, Progress in Photovoltaics: Research and Applications, 2024.

[234] J. L. Koenig, Applied Spectroscopy Reviews **4**, 2, 1971.

[235] C. V. Raman, Current Science **74**, 4, 1998.

[236] C. Peike, T. Kaltenbach, K. A. Weiß, and M. Koehl, Solar Energy Materials and Solar Cells **95**, 7, 2011.

[237] R. Goodacre and D. B. Kell, Current Opinion in Biotechnology **7**, 1, 1996.

[238] P. M. Peacock and C. N. McEwen, Analytical Chemistry **78**, 12, 2006, PMID: 16771534.

[239] R. Heidrich, A. Mordvinkin, and R. Gottschalg, Polymer Testing **118**, 2023.

[240] J. I. Kim et al., Solar Energy Materials and Solar Cells **122**, 2014.

[241] T. P. Dhakal, M. M. Hamasha, A. S. Nandur, D. Vanhart, P. Vasekar, S. Lu, A. Sharma, and C. R. Westgate, IEEE Transactions on Device and Materials Reliability **12**, 2, 2012.

[242] M. Theelen, T. Boumans, F. Stegeman, F. Colberts, A. Illiberi, J. van Berkum, N. Barreau, Z. Vroon, and M. Zeman, Thin Solid Films **550**, 2014.

[243] T. Tohsophon, J. Hüpkes, S. Calnan, W. Reetz, B. Rech, W. Beyer, and N. Sirikulrat, Thin Solid Films **511-512**, 2006.

[244] Y. S. Liu, C. Y. Hsieh, Y. J. Wu, Y. S. Wei, P. M. Lee, H. M. Hsieh, and C. Y. Liu, Applied Surface Science **282**, 2013.

[245] D. Qiu, W. Duan, A. Lambertz, A. Eberst, K. Bittkau, U. Rau, and K. Ding, Solar RRL **6**, 10, 2022.

[246] D. B. Sulas, S. Johnston, and D. C. Jordan, Solar RRL **3**, 8, 2019.

[247] D. Wisniewski, R. Lv, S. V. Nair, J.-N. Jaubert, T. Xu, and H. E. Ruda, Progress in Photovoltaics: Research and Applications **27**, 2, 2018.

[248] A. Murillo, A. Buceta, A. Urbina, and J. Bengoechea, Solar Energy Materials and Solar Cells **294**, 2026.

[249] S. R. Wenham, M. A. Green, M. E. Watt, R. Corkish, and A. Sproul, "Applied photovoltaics," in 3rd Edition. London: Routledge, 2011.

[250] S. V. Spataru, D. Sera, P. Hacke, T. Kerekes, and R. Teodorescu, Progress in Photovoltaics: Research and Applications **24**, 4, 2015.

[251] G. Li, M. W. Akram, Y. Jin, X. Chen, C. Zhu, A. Ahmad, R. H. Arshad, and X. Zhao, Energy **168**, 2019.

[252] M. T. Zarmai, N. N. Ekere, C. F. Oduoza, and E. H. Amalu, Robotics and Computer-Integrated Manufacturing **47**, 2017.

[253] G. Oreski and G. M. Wallner, Solar Energy **83**, 7, 2009.

[254] A. Sinha, H. Gopalakrishna, A. Bala Subramaniyan, D. Jain, J. Oh, D. Jordan, and G. TamizhMani, IEEE Journal of Photovoltaics **10**, 4, 2020.

[255] D. D. Haillant and O., *Environmental durability of pv modules - a model for accelerated testing*, Conference Paper, 2011.

[256] P. Hacke, R. Smith, K. Terwilliger, S. Glick, D. Jordan, S. Johnston, M. Kempe, and S. Kurtz, IEEE Journal of Photovoltaics **3**, 1, 2013.

[257] P. Hacke, S. Spataru, K. Terwilliger, G. Perrin, S. Glick, S. Kurtz, and J. Wohlgemuth, IEEE Journal of Photovoltaics **5**, 6, 2015.

[258] Ö. Hallberg and D. S. Peck, Quality and Reliability Engineering International **7**, 3, 1991.

[259] X. Li et al., Solar Energy Materials and Solar Cells **247**, 2022.

[260] Timeanddate. `https://www.timeanddate.com/weather/@6557321/climate`.

[261] D. C. Miller et al., Progress in Photovoltaics: Research and Applications **27**, 5, 2019.

[262] R. Heidrich, N. Babić, O. Lacroix-Andrivet, C.-E. Dutoit, C. Bainier, A. Mordvinkin, R. Gottschalg, H. Vezin, C. Afonso, and S. Pondaven, Solar RRL **8**, 10, 2024.

[263] M. Babics et al., in *41st EU PVSEC*, 2024.

[264] J. Yang et al., Solar Energy Materials and Solar Cells **276**, 2024.

[265] P. Würfel, "Physics of solar cells from principles to new concepts," in WILEY-VCH Verlag GmbH & Co. KGaA, 2005.

[266] K. Vandewal, K. Tvingstedt, A. Gadisa, O. Inganas, and J. V. Manca, Nat Mater **8**, 11, 2009.

[267] N. C. Park, J. S. Jeong, B. J. Kang, and D. H. Kim, Microelectronics Reliability **53**, 9-11, 2013.

[268] C. Kutter, F. Basler, L. E. Alanis, J. Markert, M. Heinrich, and D.-H. Neuhaus, in *37th EU PVSEC*, 2020.

[269] A. C. Martins, V. Chapuis, A. Virtuani, L.-E. Perret-Aebi, and C. Ballif, in *33rd EU PVSEC*, 2017.

[270] M. Heinrich, A. J. Beinert, P. Romer, L. C. Rendler, F. Basler, S. Wendlandt, and D. H. Neuhaus, in *38th EU PVSEC*, 2022.

[271] H. Yao and Q. Tang, Solar Energy **211**, 2020.

[272] 34.85%! longi breaks world record for crystalline silicon-perovskite tandem solar cell efficiency again. `https://www.longi.com/en/news/silicon-perovskite-tandem-solar-cells-new-world-efficiency/?utm_source=chatgpt.com`.

Acknowledgements

I would like to express my deepest gratitude to the following people for their contribution to this work:

• Prof. Dr. Uwe Rau for his supervision of my doctoral thesis. From the overall structure of the dissertation to the formulation of the research questions and the preparation of figures and diagrams, you have provided me with careful and insightful guidance. Your rigorous scientific spirit and scholarly attitude have once again shown me the true charm of research. Although our opportunities to communicate in person were limited, every in-depth discussion with you helped to illuminate the direction of my work and resolve my doubts.

• Dr. Andreas Lambertz for his dedicated supervision and generous support during the latter two years of my PhD. Your rigorous research attitude and extensive industrial experience have benefited me greatly. Your patience and friendliness always created a relaxed atmosphere in which I felt comfortable discussing problems and asking questions. Your care and support have made me feel warmly welcomed, even while living and working far from home.

• Dr. Kaining Ding for providing me with the opportunity to come to IMD-3 to study and work. Thank you for your guidance and strong support during the first two years of my PhD, for allowing me to pursue topics that truly interest me, and for providing numerous opportunities to collaborate and communicate with other research institutions and companies.

• Dr. Karsten Bittkau for his constant help and support. You always answered my questions patiently and shared your perspectives generously. Your unexpected cold jokes added a touch of humor and lightness to many otherwise serious and sometimes tedious discussions.

• Henirke Gattermann for the valuable suggestions on my thesis writing and for the help with language polishing.

• I would like to thank Yaqin Muhammad Ainul for the collaboration on the investigation of the DH stability of AZO SHJ solar cell and module. I am also grateful to Dr.

Oleksandr Mashkov from HIERN for assistance with DH testing and characterization of lightweight solar modules, and Dr. Krzysztof Dzięcioł from IET-1 for assistance with the XCT characterization of lightweight solar modules. Many thanks to Dr. Anton Mordvinkin and Jishnu Ramachandran Nair from Fraunhofer CSP; through our collaboration, I gained a much deeper understanding of the degradation mechanisms of UV downshifting encapsulant films.

• My sincere appreciation goes to Volker Lauterbach for his continuous help and support for measurements in the LOANA system. I also thank Christoph Zahren for his assistance with solar module testing, and Thomas Birrenbach and Niklas Bongartz for their strong support with DH and UV-accelerated aging tests. Dr. Benjamin Klingebiel for his support in perovskite and tandem device measurements, and Dr. Timon Vaas for his guidance and assistance with PL measurements.

• I am grateful to my Master's student, Rongda Zhang, for his assistance in the experiments, which contributed significantly to the efficient and successful progress of our research project.

• My warmest thanks go to Binbin Xu, my flatmate and close friend, for accompanying me over these four years. I am also thankful to my fellow students and colleagues for their support at work and their companionship in daily life. The PhD journey can sometimes be lonely and monotonous, but it is your companionship that adds so much color to these four years. I would also like to thank my office mates, Dr. Chris Dreeßen and Sung-Chi Chang; our small talks during breaks helped to dispel the dullness of long working days.

• I would like to thank all my colleagues at IMD-3. It has been a pleasure and a privilege to spend four happy and rewarding years here, and I am truly grateful that our paths have crossed.

• I also want to thank all the collaborators who provided materials and technical support for my experiments. Your contributions were essential to the successful completion of this work.

• Finally, I would like to express my deepest gratitude to my parents. I seldom say "thank you" or openly express my love, but I am profoundly grateful for your constant support and companionship. Thank you for giving me a free and nurturing environment in which to grow, allowing me to pursue the life I truly want. My heartfelt thanks also go to my wife, Lu Liu, for her understanding, support, and trust. We are both striving to become better versions of ourselves. Despite living apart for most of the past four years, I firmly believe that our love has remained unchanged. I look forward to walking the road ahead together with you.

Aber alle Wasser der Welt finden sich wieder,
und Eismeer und Nil vermischen sich im feuchten Wolkenflug.
Das alte schöne Gleichnis heiligt mir die Stunde.
Auch uns Wanderer führt jeder Weg nach Hause.

— From Hermann Hesse, *Wanderung. Aufzeichnungen*, "Bergpaß"

Band / Volume 701
Accelerating the discovery of alkaline-stable anion exchange membrane materials via computational exploration
F. P. Tipp (2026), xii, 135 pp
ISBN: 978-3-95806-900-8

Band / Volume 702
Methods for Investigating the Structure-Performance Correlation in Membrane Electrode Assemblies
N. Utsch (2026), XIII, 138, LXVII pp
ISBN: 978-3-95806-901-5

Band / Volume 703
Hot-Spot Formation in Cu(In,Ga)Se_2 Thin Film Solar Cells
S. Nofal (2026), xvii, 131 pp
ISBN: 978-3-95806-903-9

Band / Volume 704
Machine Learning Guidance of Manufacturing Process of Solid Oxide Cells
T. Le Dinh (2026), xxi, 122 pp
ISBN: 978-3-95806-904-6

Band / Volume 705
Drivers of spatiotemporal variability of European terrestrial ecosystem processes
C. Poppe Téran (2026), 254 pp
ISBN: 978-3-95806-905-3

Band / Volume 706
Characterization of Nitrogen Reduction Reaction Catalysts for the electrochemical Ammonia Synthesis
D. Sachse (2026), xi, 235, 6 pp
ISBN: 978-3-95806-907-7

Band / Volume 707
Autonomous Image Analysis to Accelerate the Discovery and Integration of Energy Materials
A. Colliard Granero (2026), xiv, 156 pp
ISBN: 978-3-95806-910-7 (Print)
ISBN: 978-3-95806-911-4 (E-Book)

Band / Volume 708
Effect of Soil Mechanical Properties, Root Tip Geometry, and Mucilage on Penetration Restistance to Root Growth
R. K. Janakiram (2026), xxviii, 98 pp
ISBN: 978-3-95806-914-5 (Print)
ISBN: 978-3-95806-915-2 (E-Book)

Band / Volume 709
European Energy Transition – Germany in the Heart of Europe
T. Klütz, P. Dunkel, T. Busch, J. Linssen, D. Stolten (2026), V, 54 pp
ISBN: 978-3-95806-916-9 (Print)
ISBN: 978-3-95806-917-6 (E-Book)

Band / Volume 710
Development of High-Efficiency Perovskite/Silicon Tandem Solar Cells
Q. Yang (2026), 264 pp
ISBN: 978-3-95806-920-6 (Print)
ISBN: 978-3-95806-921-3 (E-Book)

Band / Volume 711
No-Regret-Maßnahmen der integrierten Netzplanung mit Fokus auf Wasserstoff
T. G. Busch (2026), xx, 325 pp
ISBN: 978-3-95806-922-0 (Print)
ISBN: 978-3-95806-923-7 (E-Book)

Band / Volume 712
Data-Driven Modeling for Digital Representations in Energy Systems
M. C. Zimmer (2026), xv, 166 pp
ISBN: 978-3-95806-926-8 (Print)
ISBN: 978-3-95806-927-5 (E-Book)

Band / Volume 713
Towards integrated PV applications: development of lightweight silicon heterojunction solar modules and their damp-heat and UV stability
K. Zhang (2026), iii, 179 pp
ISBN: 978-3-95806-928-2 (Print)
ISBN: 978-3-95806-929-9 (E-Book)

Weitere ***Schriften des Verlags im Forschungszentrum Jülich*** unter
http://wwwzb1.fz-juelich.de/verlagextern1/index.asp

Energie & Umwelt / Energy & Environment
Band / Volume 713
ISBN 978-3-95806-929-9

Mitglied der Helmholtz-Gemeinschaft

JÜLICH
Forschungszentrum